The Pennsylvania State University

The Graduate School

Department of Physics

MEASURING THE ELECTRON ELECTRIC DIPOLE MOMENT USING LASER-COOLED CESIUM ATOMS IN OPTICAL LATTICES

A Dissertation in

Physics

by

Kunyan Zhu

Submitted in Partial Fulfillment
of the Requirements
for the Degree of

Doctor of Philosophy

December 2013

The dissertation of Kunyan Zhu was reviewed and approved* by the following:

David S. Weiss
Professor of Physics
Associate Head, Department of Physics
Dissertation Advisor
Chair of Committee

Kurt Gibble
Professor of Physics

Dezhe Jin
Associated Professor of Physics

Mary Beth Williams
Associate Dean for Undergraduate Education, Eberly College of Science
Professor of Chemistry

Richard W. Robinett
Professor of Physics
Director of Graduate Studies

*Signatures are on file in the Graduate School

ABSTRACT

Discrete symmetries have played a vital role in the development of the standard model of particle physics. Electric dipole moments (EDM's) of elementary particles are sensitive probes of discrete symmetry violations. The standard model predicts a permanent electron electric dipole moment (eEDM) that is 10^{-37}~$10^{-38}\ e \cdot cm$. Most proposed standard model extensions, like supersymmetry, predict a larger eEDM that is comparable to or slightly smaller than the current experimental limit, $|d_e| \leq 1.05 \times 10^{-27}\ e \cdot cm$. Observation of a permanent eEDM in the foreseeable future would imply new CP violating effects not captured by the standard model. This dissertation is a project report of the Penn State eEDM search using laser-cooled Cesium atoms in optical lattices. In particular, I will describe experimental progress in apparatus development, quantum state preparation and state-selective fluorescence detection, and magnetometry using Larmor precession of spin-polarized atoms. I will also describe theoretical studies of low frequency spectroscopy that will be used in the eEDM measurements. In our experiment, Cesium atoms are guided into a measurement chamber, where they are laser-cooled and trapped in a pair of far-detuned, high quality linearly polarized, parallel one-dimensional optical lattices. The lattice beams thread three specially coated fused silica electric field plates. The measurement chamber is passively shielded by a four layer mu-metal magnetic shield, inside of which eight magnetic field coils actively control the bias and gradient magnetic fields, based on sensitive atomic magnetometry measurements. A series of high fidelity microwave adiabatic fast passage pulses and specially engineered low frequency magnetic pulses transfer the atoms into a superposition state that is sensitive to the eEDM signal. Combining unprecedented precision made possible by cold atoms with engineering, our experiment has a projected precision that is 400-fold improvement of the current measured limit.

TABLE OF CONTENTS

LIST OF FIGURES

LIST OF TABLES

ACKNOWLEDGEMENTS

I am very grateful to Prof. David S. Weiss for being my adviser and mentor during my PhD career. He taught me more than physics and engineering skills that have been and will be lifetime beneficial. His guidance, prolific experience, logical reasoning and scientific passion have been very inspiring and tremendous helpful in the lab.

I would like to thank my fellow coworker, Dr. Neal Solmeyer for being perfectly "mode matched" with me over the past 6 years. As two graduate students we have played well together to our strengths on many projects of the challenging experiment. His work is structurally significant and I have learned a lot from him.

I would also like to thank a nice group of people over the course of my graduate study:

- Professors Kurt Gibble, Ken O'Hara, and Nate Gemelke for using their lab equipment;
- Dr. Fang Fang, Matthew Ebert, Cheng Tang, Dr. Karl Nelson, Dr. Xiao Li, Dr. Ted Corcovilos, Yang Wang, Dr. Jean-Felix Riou, Dr. Aaron Reinhard, Laura Adams, Dr. Xia Lin, Dr. Eric Hazlett, Yi Zhang for direct help in certain types of lab work: from aligning optics, to forming an electronics pipeline, to locating equipment for immediate use.
- The electronics shop and the machine shop in physics department for sharing engineering ideas and solutions;
- Committee members: Professors Kurt Gibble, Dezhe Jin, Mary Beth Williams, and of course David S. Weiss, for their generous contributions;
- All members in the Friday journal club for giving beneficial presentations and insightful conversations.

I owe a great deal to my wife Xiaolin He for her love, encouragement and dedication. I also thank my parents for raising me in the farmland with their conscience, perseverance and wisdom.

Chapter 1

Introduction

Electric dipole moments (EDM's) of fundamental particles are sensitive probes of discrete symmetries and of new physics beyond the standard model [1, 2]. The history of EDM searches dates back to 1950, when Dr. E. M. Purcell and Dr. N. F. Ramsey proposed and started a neutron beam magnetic resonance experiment to probe parity violation [3], prior to the experimental observation of parity non-conservation in beta decays [4], which altered the general belief that discrete symmetries are all individually good symmetries. Over the past half a century, many sensitive EDM searches have been carried out in neutrons, nuclei, and electrons [5]. For instance, the upper limit of the electron EDM has been pushed down by 14 orders of magnitude to $|d_e| \leq 1.05 \times 10^{-27}\ e \cdot cm$ [6]. Still, no permanent EDMs have been found.

The recently matured technologies of laser manipulation of atoms [7] provide a revolutionary afterburner to classical atomic physics, enabling ground-breaking advancement in the fields of quantum computation and information processing [8], quantum simulations of condensed matter systems [9], precision measurement applications like atomic clocks [10] and more. Combining unprecedented precision made possible by cold atoms with engineering, we are carrying out EDM searches based on laser-cooled cold atoms, which are table-top, interdisciplinary experiments in the low energy sector that bridge atomic physics and particle physics. Our work is complementary to searches for new physics in costly, large-scale high energy accelerators like the Large Hadron Collider (LHC) [11].

1.1. Electric dipole moments as probes of new physics

The search for violations of discrete symmetries including charge conjugation C, parity P and time-reversal T, has played a central role in the development of the standard model throughout the mid to late 20th century. In particular, the 1957 discovery of parity violation in beta decays [4], followed shortly by the observation of both P and C violation in pion decays [12], lead to introduction of chirality in matter fields as an important part of the theory of weak interactions [13]. The observations of the decay of neutral kaons and B-mesons in 1964 [14] identified CP violation by the strong force, so that CP violation was incorporated in the strong sector of the Standard Model.

Existing measurements of CP asymmetries in K and B meson decays can be explained using a single source of CP violation from the Cabibbo-Kobayashi-Maskawa (CKM) mechanism [15] within the standard model that describes the electromagnetic, weak and strong interactions. Nevertheless, the CKM source of CP violation is itself too small to explain the observed matter anti-matter asymmetry of the universe [16]. Searches for other sources of CP violation, which constitute new physics beyond the standard model, are very active areas of research in the high energy particle physics community [17, 18] as well as AMO physics community (see section 1.2).

Because CPT is conserved in all quantum field theories according to the CPT theorem [19], CP violation implies that T is not good standard model symmetry. T-violation motivates the prediction of permanent EDMs of fundamental particles, and makes them possible. To illustrate this point, consider a spin 1/2 particle with magnetic and electric dipole moments. The interactions between the particle and electromagnetic fields can be described by the Hamiltonian

$$H = -\vec{\mu} \cdot \vec{B} - \vec{d} \cdot \vec{E} = -\mu\vec{\sigma} \cdot \vec{B} - d\vec{\sigma} \cdot \vec{E} \qquad (1.1)$$

with $\vec{\mu}$ the magnetic dipole moment, $\vec{d}$ the electric dipole moment and $\vec{\sigma}$ the angular momentum of the particle. Both $\vec{\mu}$ and $\vec{d}$ are proportional to $\vec{\sigma}$, according to the Wigner-Eckart theorem [20].

The transformation properties of the dipole moments, the electromagnetic fields and the interactions under discrete symmetry operators and their combinations are given by Table 1-1 [5]. Since $\vec{d}$ is an axial vector and only even under P, $\vec{E}$ is even under T (and CP), the EDM interaction term is odd under P or T. Therefore a non-zero EDM is a direct signature of both T and P violation.

Discrete symmetry	Yr. of discovery of violation	$\vec{E}$	$\vec{B}$	$\vec{\sigma}$ ($\vec{\mu}$ or $\vec{d}$)	$\vec{\mu} \cdot \vec{B}$	$\vec{d} \cdot \vec{E}$
C	1957 [4]	-	-	-	+	+
P	1957 [12]	-	+	+	+	-
T		+	-	-	+	-
CP	1964 [14]	+	-	-	+	-

Table 1-1. Transformation properties of electromagnetic fields and interactions.

The standard model predicts a permanent electron EDM that is about 10^{-37} ~10^{-38} e-cm [21], which is 10 orders of magnitude smaller than the current upper limit [6]. The very small EDM is due to cancellations of CP-violating terms at the one and two loop level in the standard model [21]. Most proposed extensions to the standard model predict much larger EDMs than the standard model due to new CP violating, EDM-generating interactions from additional particles [21]. For instance, Super-symmetric (SUSY) models predict electron EDMs that are just one or two orders of magnitude smaller than the current upper limit. At a level of 10^{-28} ~10^{-30} e-cm, should an electron EDM be observed, it would be the first measurement that actually contradicts an explicit standard model prediction. Alternatively, a more stringent upper limit will put some extensions of the standard model in question.

1.2. Recent and on-going searches for the electron EDM

Searches for permanent EDMs are very active areas of research. According to Dr. Klaus Kirch's count [22], as of 2013 there are a total of 33 active EDM experimental groups worldwide, using a wide range of systems including atoms (13), molecules (6), neutrons (7), solid state systems (3), muons (1), protons (1) and deuterons (1), where the number in ( ) denotes the total number of distinct EDM groups.

For the case of the permanent electric dipole moment of the electron, experiments are commonly carried out in atoms or molecules. This is simply because electrons are charged particles and it is challenging to trap many electrons in a large DC electric field. According to the Schiff's theorem [23], one could naively imagine that in a classical (nonrelativistic) atom, the atomic charge would adjust to shield the electric field experienced by any proton, neutron or electron such that the atom would be insensitive to the EDMs of its constituents. Nevertheless, this is often not the case because atoms and molecules are relativistic and the subatomic electrostatic equilibrium is never reached.

Consequently, the eEDM in an atom or molecule is most often enhanced by a large factor according to [21]

$$d_A = R d_e + c_N \tag{1.2}$$

Where R is the enhancement factor and c_N accounts for permanent nuclear EDMs and T-violating electron-nucleon interactions. For heavy paramagnetic alkali atoms, the atomic EDM is dominated by the term Rd_e, the relativistic enhancement factor scales approximately as $R \propto Z \cdot (Z\alpha)^2$, with α the fine structure constant and the Z the atom number [2]. State-of-art *ab initio* calculations yield $R \approx 120.5$ for Cs and $R \approx 25.7$ for Rb, with less than 0.7% uncertainty [24]. For close-shell atoms like ^{199}Hg, electronic contributions are suppressed and the atomic EDM is dominated by c_N. Paramagnetic molecules such as YbF are easily polarized in small electric

fields, which results in a very large internal electric field, with an effective enhancement factor as large as 10^6 [6]. However, due to the complicated molecular structure, the extraction of the electron EDM from measured molecular EDMs are at best only accurate to ~10%.

A figure-of-merit comparison for representative eEDM experiments, including the recent results with thermal Tl beams by Dr. E. Commins [25] and thermal YbF beams by Dr. E. Hinds [6], and several on-going searches with molecules, molecular ions, and neutral atoms, is given in Table 1-2.

eEDM Groups (PI, system)	V (m/s)	E_{eff} (GV/m)	τ (s)	$\dot{N}$ (s^{-1})	$\lvert d_e \rvert$ $(e \cdot cm)$
Commins, Tl beam [25]	420	7.2	2.4×10^{-3}	10^9	1.6×10^{-27} (M)
Hinds, YbF beam [6]	590	1450	6.4×10^{-4}	6×10^4	1.05×10^{-27} (M)
Weiss, trapped Cs	0.02	1.8	3	2×10^7	2.4×10^{-30} (P)
ACME, ThO beam [26]	200	10000	1.5×10^{-3}	10^5	3.7×10^{-29} (P)
Cornell, trapped HfF+ [27]	26	2400	0.2	≤100	3×10^{-28} (P)

Table 1-2. Comparison between different eEDM searches.

Comparison between eEDM searches using atoms, molecules and molecular ions as an example, for a full list of eEDM searches worldwide, see ref. [22] . E_{eff}: effective electric fields (applied electric fields multiplied by enhancement factors); τ: coherence time; $\dot{N}$: number of particles measured in unit time; $\lvert d_e \rvert$: sensitivity to the electron EDM for an integration time of a day, (M) represents upper limits of recently completed experiments, (P) stands for projected sensitivity of on-going eEDM searches for one day integration time, which are only accurate at an order-of-magnitude level and are certainly subject to change.

In short, three key factors determine the ultimate sensitivity in an eEDM experiment (see detailed discussions in Chapter 7): the effective electric fields, the coherence time and the total number of particles measured per unit time. Compared to the completed EDM experiments, on-going EDM searches are upgrading the key factors one way or the other while improving the combined overall sensitivity. Thermal beams of molecules have the big advantage of large internal electric fields, but the EDM interaction time is limited to less than 3 milliseconds [6, 26]. The advantage of using laser-cooled heavy atoms is the very long coherence time on the order of a few seconds, but the effective electric field is smaller due to the enhancement factors.

Molecular ions have a fairly large effective electric field and coherence time, but the maximum number of trapped ions are 2~5 orders of magnitude smaller than the other systems [27]. With all the three key factors combined, all on-going eEDM searches have comparable projected sensitivities that are 1~2 orders of magnitude smaller than the current upper limit [6].

1.3. Our EDM measurement with laser-cooled Cesium atoms

The EDM of a Cs atom is proportional to the total angular momentum of the atom [20]. In our experiment, similar to the Zeeman shifts in a magnetic field due to the magnetic dipole moment of an atom, the EDM of a Cs atom results in linear frequency shifts of $m_F = \pm 3$ Zeeman sublevels in an applied DC electric field. In particular, for the Cs F=3 hyperfine ground state, the linear frequency shifts can be written by

$$f = \frac{g_F m_F}{h}(\boldsymbol{d} \cdot \boldsymbol{E} + \mu_{\boldsymbol{B}} \cdot \boldsymbol{B}) \tag{1.3}$$

Where h is the Planck constant, $g_F = -1/4$ is the Landé g-factor, $\boldsymbol{d}$ is the EDM of a Cs atom (~120.5 d_e) and $\mu_{\boldsymbol{B}}$ is the Bohr magneton. For an electron EDM d_e of 2.4×10^{-30} e-cm, the frequency shift is 1.6×10^{-8} Hz for Cs, and the equivalent magnetic field is $7.5 \times 10^{-15}\ G$.

To be maximally sensitive to the EDM, we apply a very large electric field $|\boldsymbol{E}| = 150\ kV/cm$. The electric field will induce a quadratic DC Stark shift $\sim 45 m_F^2\ Hz$ in the F=3 hyperfine manifold (Figure 1-1 (a)). With well controlled small magnetic fields, the DC Stark shift will be the dominant energy term and define the quantization axis. The energy shifts described in Eq. (1.1) will be a small perturbation to the quadratic energy structure.

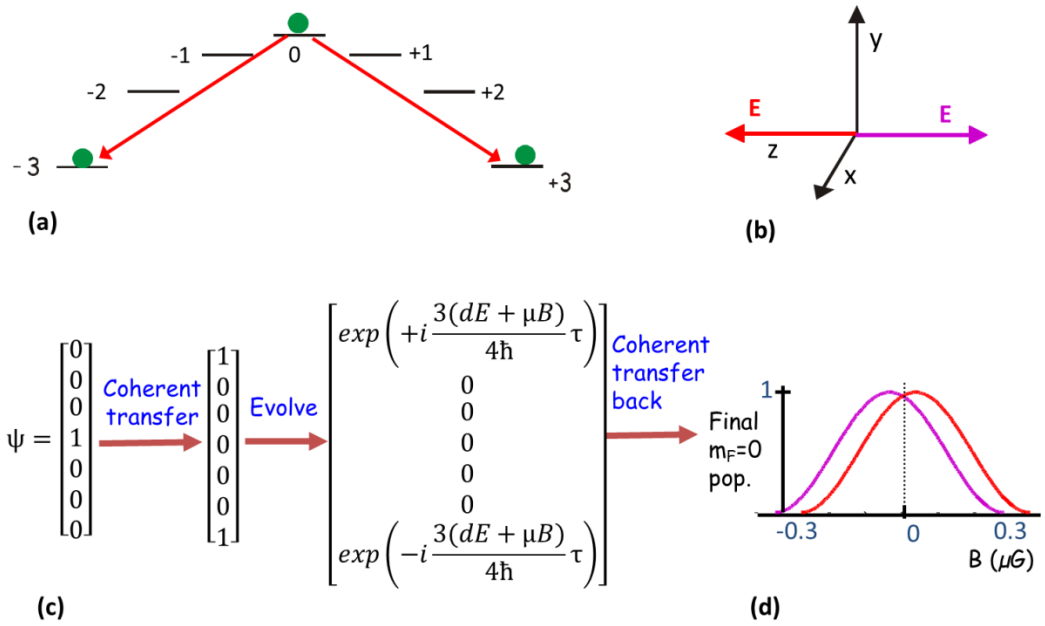

Figure 1-1. Principle of our EDM measurement.

(a) Energy level structure of the Cs F=3 hyperfine ground state relevant to our EDM measurement. (b) Coordinate system for electric field polarity reversal. (c) State evolution during an EDM measurement. (d) Ramsey-like fringe when a bias magnetic field is scanned. The difference between two fringes with electric fields reversed is a direct measurement of the EDM interaction term.

We use the separated oscillatory fields method [28], invented by Norman F. Ramsey, Jr., to measure the EDM induced small frequency shifts. The powerful technique and its variations have been widely used in precision measurements like atom interferometers [29, 30] and atomic clocks [31, 32]. The three-step measurement procedure is illustrated in Figure 1-1 (c). Cs atoms are initially prepared in the $|F = 3, m_F = 0>$ state. A 3-photon low frequency pulse (see Chapter 6) coherently drive the atoms from $|3,0>$ to a superposition state $(|3,+3> + |3,-3>)/\sqrt{2}$. Next we let the atoms freely evolve in the applied electric field for a time τ, during which the interferometric states $m_F = \pm 3$ pick up a relative phase $\phi = \frac{3\tau}{2\hbar}(\boldsymbol{d}\cdot\boldsymbol{E} + \mu_{\boldsymbol{B}}\cdot \boldsymbol{B})$. Finally we coherently transfer atoms back to the $|3,0>$ state and let them interfere. The fractional number of atoms returning to the $|3,0>$ state will be proportional to $cos^2\left(\frac{\phi}{2}\right)$, namely

$$\frac{n_0}{n} = cos^2\left[\frac{3\tau}{4\hbar}(\boldsymbol{d}\cdot\boldsymbol{E} + \mu_{\boldsymbol{B}}\cdot\boldsymbol{B})\right] \quad (1.4)$$

Experimentally, one would like to scan the bias magnetic field B in order to build a Ramsey-like interference fringe, as shown in Figure 1-1 (d). From shot to shot, one would also reverse the sign of the DC electric field for common-mode noise rejection (see Chapter 2, section 2.2). The differential shift in the two sets of Ramsey-like fringes during a bias magnetic field scan is a direct measurement of the EDM interaction term, $\boldsymbol{d}\cdot\boldsymbol{E}$. Using modern atomic theory predictions [24], one can finally divide the measured atomic EDMs by the enhancement factors ($R = 120.5 \pm 0.8$ for Cs) to precisely extract the electron EDM.

1.4. Core features of the experiment

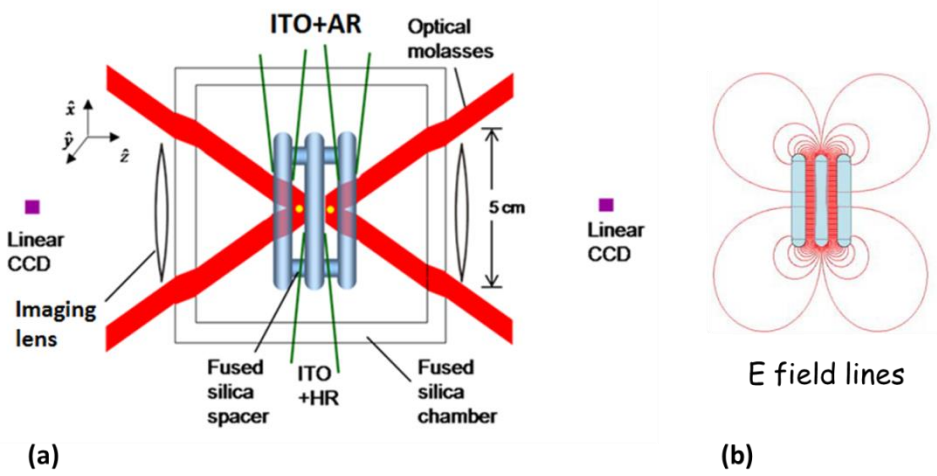

Figure 1-2. Schematic of the measurement chamber.

(a) Top view of the measurement chamber showing the glass cell, specially coated electric field plates (HR: high reflection; AR: anti-reflection; ITO: indium tin oxide, a transparent conductor), and optics for laser cooling, laser trapping (yellow dots are atoms trapped in optical lattices), and fluorescence imaging. (b) Electric field lines around the field plates when high voltage is applied to the center plate and the two outer plates are electrically grounded.

The heart of our experiment is the two simultaneous atom interferometers, designed specifically to minimize noises and systematic errors. The schematic top view of the measurement chamber is shown in Figure 1-2(a). Two 10 cm-long atom pancakes stacks, separated by 1 cm, are trapped in two parallel one-dimensional far-detuned optical lattices, which are made in power built-up cavities.

The two lattice beams thread through 3 fused silica electric field plates. Transparent conductive coatings with indium-tin-oxide (ITO) on all surfaces of the field plates support electric fields for the atoms, and provide optical access for laser cooling and fluorescence imaging. In particular, the center plate has a high reflection coating and the two outer ground plates have anti-reflection coatings in the wavelength regions of interest, which allows three-dimensional polarization gradient cooling [33] at both lattice locations (+Z and –Z sides). The field plates are mounted with titanium mounting structures inside a fused silica glass cell (Chapter 6 in ref. [34]), with 4 mm-thick precision fused silica spacers. The glass field plates suppress magnetic Johnson noises which otherwise would be very large if metal plates were used. Fluorescence signals from atoms are collected with two 10 cm-long, 25 pixel nonmagnetic linear CCD arrays.

For EDM measurements, either positive or negative high voltage is applied to the center plate, and the two outer plates are electrically grounded, which generate equal but opposite directional electric fields on the two lattice sides for every shot of EDM measurement. The simultaneous electric field reversal is a powerful feature for common-mode noise rejection (see Chapter 2, section 2.2). The electric field lines around the field plates are depicted in Figure 1-2 (b).

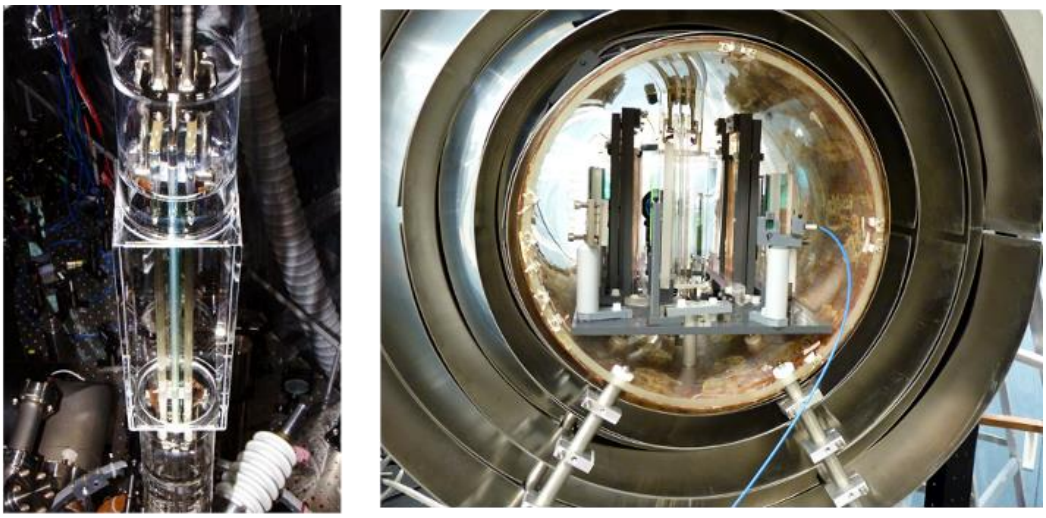

Figure 1-3. Core part of the EDM apparatus.

(a) Photograph of the electric field plates mounted inside the glass cell. (b) Side view (along x direction) of the measurement chamber when the magnetic shields are open. From inside out: the glass cell and field plates, optics for laser cooling and fluorescence imaging, magnetic bias and gradient coils, and 4-layer magnetic shields.

Figure 1-3 (a) is a photograph of the glass cell and field plates. Surrounding optics, together with magnetic coils and magnetic shields are shown in Figure 1-3 (b). The optical components are mostly custom made of nonmagnetic materials like glass and plastics, with some use of nonmagnetic, commercially pure titanium mounts at least 20 cm away from the atoms to minimize the effect of Johnson noise. Four-layer mu-metal magnetic shields provide passive magnetic shielding of the science chamber, and the residual magnetic bias fields and gradients are actively cancelled and controlled with 8 sets of coils using in-situ atomic magnetometry (Chapter 5). The comprehensive experimental design provides precision control of the electric and magnetic fields needed for the EDM measurements.

1.5. Structure of the dissertation

This is the 3rd PhD dissertation from the eEDM lab in the Weiss group at Penn State, following Dr. Fang Fang (December 2007) [35] and Dr. Neal Solmeyer (May 2013) [34]. A large portion of projects and results presented in this dissertation were done in collaboration with, and/or based on the work of Dr. Neal Solmeyer. I will refer to their important work including experimental steps and apparatus developments when appropriate, summarize the key concepts and results wherever necessary and minimize redundant descriptions. I have attempted to write this dissertation with enough details to ease the work of people continuing with the experiment, especially when it comes to engineering and technical contents.

The dissertation is organized as follows: in Chapter 2, I will first give an overview of 4 milestone steps of the EDM measurement procedure, and summarize the unique and powerful features of the experiment. Details of the apparatus development including hardware design and control software engineering, will be addressed in Chapter 3. Chapter 4 describes techniques for state preparation and state-selective fluorescence detection using microwaves. In-situ atomic magnetometry, which is used to zero out the residual magnetic fields in the science chamber priori to EDM measurements, together with measurements of small vector light shifts due to the lattice beams, will be discussed in Chapter 5. Theoretical studies of physics of atoms in large electric fields, and numerical search and optimization of 3-photon low frequency waveforms for EDM spectroscopy, will be presented in Chapter 6. The effects of possible sources of noises and systematic errors in our EDM measurements are studied in Chapter 7. Finally, in Chapter 8, I will describe the on-going work to replace and improve the high voltage field plates, and the effort in progress for an EDM measurement. References for each Chapter are listed at the end of the corresponding Chapter.

1.6. References

[1] M. Pospelov and A. Ritzd, *Electric dipole moments as probes of new physics*, Annals of Physics **318**, 119 (2005).

[2] L. R. Hunter, *Tests of time reversal invariance in atoms, molecules, and the neutron*, Science **252**, 73 (1991).

[3] E. M. Purcell and N. F. Ramsey, *On the Possibility of Electric Dipole Moments for Elementary Particles and Nuclei*, Phys. Rev. 78, 807 (1950).

[4] C. S. Wu et al., *Experimental Test of Parity Conservation in Beta Decay*, Phys. Rev. **105**, 1413 (1957).

[5] B. L. Roberts and W. J. Marciano, *Lepton Dipole Moments*, World Scientific, (2009).

[6] J. J. Hudson et al., *Improved measurement of the shape of the electron*, Nature 473, 493 (2011).

[7] S. Chu, *The manipulation of neutral particles*, Rev. Mod. Phys. **70**, 685 (1998).

[8] K. D. Nelson, X. Li and D. S. Weiss, *Imaging single atoms in a three-dimensional array*, Nature Physics 3, 556 (2007).

[9] I. Bloch, J. Dalibard, and W. Zwerger, *Many-body physics with ultracold gases*, Rev. Mod. Phys. **80**, 885 (2008).

[10] J. Guéna et al., *Progress in Atomic Fountains at LNE-SYRTE*, IEEE Transactions on Ultrasonics, Ferroelectrics, and Frequency Control **59**, 391 (2012).

[11] CDF Collaboration, D0 Collaboration, *Evidence for a Particle Produced in Association with Weak Bosons and Decaying to a Bottom-Antibottom Quark Pair in Higgs Boson Searches at the Tevatron*, Phys. Rev. Lett. **109**, 071804 (2012).

[12] R. L. Garwin, L. M. Lederman, and M. Weinrich, *Observation of the failure of conservation of parity and charge conjugation in meson decays, the magnetic moment of the free muon*, Phys. Rev. **105**, 1415 (1957).

[13] S. L. Glashow, *Partial-symmetries of weak interactions*, Nuclear Physics **22**, 579 (1961).

[14] J. H. Christenson et al., *Evidence for the 2π Decay of the K20 Meson*, Phys. Rev. Lett. **13**, 138 (1964).

[15] M. Kobayashi and T. Maskawa, *CP violation in the renormalizable theory of weak interaction*, Prog. Theor. Phys. **49**, 652 (1973).

[16] A. G. Cohen, D. B. Kaplan, and A. E. Nelson, *Progress in electroweak baryogenesis*, Annu. Rev. Nucl. Part. Sci. **43**, 27 (1993).

[17] The Belle Collaboration, *Difference in direct charge-parity violation between charged and neutral B meson decays*, Nature **452**, 332 (2008).

[18] LHCb Collaboration, *Evidence for CP violation in time-integrated D0 -> h-h+ decay rates*, Phys. Rev. Lett. **108**, 111602 (2012).

[19] T. D. Lee, R. Oehme and C. N. Yang, *Remarks on Possible Noninvariance under Time Reversal and Charge Conjugation*, Phys. Rev. **106**, 340 (1957).

[20] Cohen-Tannoudji, C.; Diu, B.; and Laloë, F., *Vector Operators: The WIgner-Eckart Theorem*, Quantum Mechanics, Vol. 2. New York: Wiley, pp. 1048-1058, (1977)

[21] W. Bernreuther and M. Suzuki, *The electric dipole moment of the electron*, Rev. Mod. Phys. **63**, 313 (1991).

[22] http://nedm.web.psi.ch/EDM-world-wide/.

[23] P. G. H. Sandars, *Electric dipole moments of charged particles*, Contemporary Physics **42**, 97 (2001).

[24] H. S. Nataraj et al., *Intrinsic Electric Dipole Moments of Paramagnetic Atoms: Rubidium and Cesium*, Phys. Rev. Lett. **101**, 033002 (2008).

[25] B. C. Regan et al., *New Limit on the Electron Electric Dipole Moment*, Phys. Rev. Lett. **88**, 071805 (2002).

[26] A. C. Vutha et al., *Search for the electric dipole moment of the electron with thorium monoxide*, J. Phys. B **43**, 074007 (2010).

[27] A.E. Leanhardt et al., *High-resolution spectroscopy on trapped molecular ions in rotating electric fields: A new approach for measuring the electron electric dipole moment*, J. Molecular Spectroscopy **270**, 1 (2011).

[28] N. Ramsey, *Molecular beams*, Oxford U. Press, New York (1985).

[29] M. Kasevich and S. Chu, *Measurement of the Gravitational Acceleration of an Atom with a Light-Pulse Atom Interferometer*, Appl. Phys. B **54**, 321 (1992).

[30] D. S. Weiss, B. C. Young, and S. Chu, *Precision measurement of ℏ/mCs based on photon recoil using laser-cooled atoms and atomic interferometry*, Appl. Phys. B **59**, 217 (1994).

[31] R. Wynands and S. Weyers, *Atomic fountain clocks*, Metrologia 42, S64 (2005).

[32] W. Maineult et al., *Spin Waves and Collisional Frequency Shifts of a Trapped-Atom Clock*, Phys. Rev. Lett. **109**, 020407 (2012).

[33] C. J. Foot, Atomic Physics, Oxford University Press, (2005).

[34] N. Solmeyer, *Progress toward an electron electric dipole moment measurement With laser-cooled atoms*, PhD dissertation, Penn State University, (2013).

[35] F. Fang, *Progress toward a measurement of the electron electric dipole moment using ultra-cold atoms*, PhD dissertation, Penn State University, (2007).

Chapter 2

Overview of our eEDM experiment

The core part of this EDM measurement is the performance of EDM spectroscopy using two simultaneous atom interferometers with extremely well controlled electric and magnetic fields. Many experimental steps, which are made possible by associated apparatus development, must be taken in order to make the spectroscopic measurement happen. In this Chapter, we will first give an overview of 4 milestones that are necessary steps in a typical EDM measurement procedure (section 2.1), then we will discuss the unique experimental features (section 2.2) that are very powerful, and very effective in suppressing experimental noise and minimizing systematic errors.

2.1. The EDM measurement procedure

Broadly speaking, the EDM measurement procedure contains 4 steps: (i) atom processing, which focuses on getting atoms into the measurement chamber and subsequent laser cooling/trapping; (ii) state preparation and detection, which aims to prepare the atoms in the correct internal spin state for a measurement to begin; (iii) atomic magnetometry, which is not necessary for every shot of EDM measurements, but must be frequently performed to ensure that the magnetic fields in the science chamber are small enough that a EDM measurement is feasible; (iv) EDM spectroscopy, which is the measurement to extract the EDM.

From the prospective of experimental sequences, atom magnetometry has a lot of similarities to the EDM measurement. Using combinations of the above 4 steps, we have envisioned the concept of automatic EDM measurement (Figure 3-33 and Figure 3-34 in Chapter

3) that is ultimately needed for in our experiment. The conceptual combination, including associated hardware/software realizations of the automatic control architecture are discussed in details in Chapter 3, section 3.5. In this section, I will give a brief overview of every milestone.

2.1.1. Atom processing

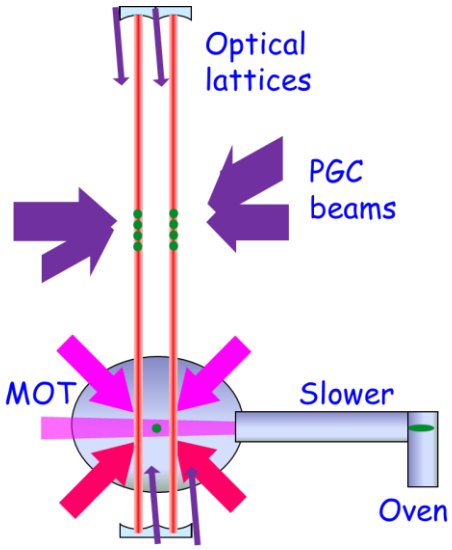

Figure 2-1. Schematic of atom processing.

Atoms (indicated as green) are collected in a magneto-optic trap (MOT) and launched into two parallel 1D optical lattices. Before top of atom trajectories they are stopped and cooled with 3D polarization-gradient cooling (PGC) beams. Alternative launches build up a ~10cm long atom pancake stack on both lattice sides. Arrows with different colors represents laser beams with different frequencies.

Atom processing has already been described in details in the dissertation of Dr. Fang (see Chapter 5 in ref. [1] for launching atoms into one optical lattice) and Dr. Solmeyer (see Chapter 3 in ref. [2] for alternative and multiple launches into two optical lattices). As illustrated in Figure 2-1, we start by slowing a thermal Cs beam in a Zeeman slower from a 100 ^{o}C oven, and collecting atoms in the center of a magneto-optic trap (MOT) at a rate of 2×10^8 atoms/s for 300 ms. The MOT beams have an $1/e^2$ radius of 1 cm. The Cs atoms are then shifted by 5 mm along

+Z (or -Z) direction to overlap with either of the two parallel 1D optical lattices, by adjusting MOT magnetic coil current settings.

When the atoms are loaded into the optical lattices, the MOT beams are frequency chirped to create a vertical "moving molasses" [3], which first accelerate the atoms for 2.5 ms, then cool the atoms in a moving frame at a velocity of 4.4 m/s for 0.9 ms. The MOT beams are then abruptly turned off to avoid heating near the low intensity edges of MOT beams [4].

The atoms travel upwards over a distance of ~0.9 m into the measurement chamber. The launches are transversely guided by the optical lattices which have a spatially averaged trap depth of 50~80 μK. Compared to free-space launches, the guiding optical lattices add alignment tolerances for the ballistic launch velocity vectors and most importantly, prevent transverse expansion of atom packets.

Before the atoms reach top of their trajectories, a series of polarization gradient cooling (PGC) [5] pulses first capture ~80% of the atoms and then cool them in the measurement chamber down to a temperature of 10 μK. The PGC pulses are separated by approximately a quarter of the trap oscillation period (~9 ms) and are pulsed on when atoms are near the center of optical lattice traps. The PGC pulses reduce the amplitudes of dipole oscillations and breathing modes of the stack of pancake-shaped atom clouds.

The launch and re-trap sequence are repeated alternatively on the two lattice sides. On each lattice side, after 2~3 launches, we fill up a ~6 cm-long atom pancakes with 5×10^6 atoms in the measurement chamber. A fluorescence image of the atoms in the measurement chamber is shown in Figure 2-2 (with 3 field plates (not visible) in between). To reduce experimental dead time associated with atom processing, while atoms are travelling upward on one lattice side, the MOT is collecting atoms for the subsequent launch into the other lattice. The total atom number is limited by the beam powers of the MOT beams and the horizontal PGC beams in the measurement chamber. With a power upgrade of the diode lasers (i.e., using a fiber-coupled

taper amplifier) and by adding transverse cooling to the atomic beam in the Zeeman slower, we expect that the total atom number could be improved by at least a factor of 10.

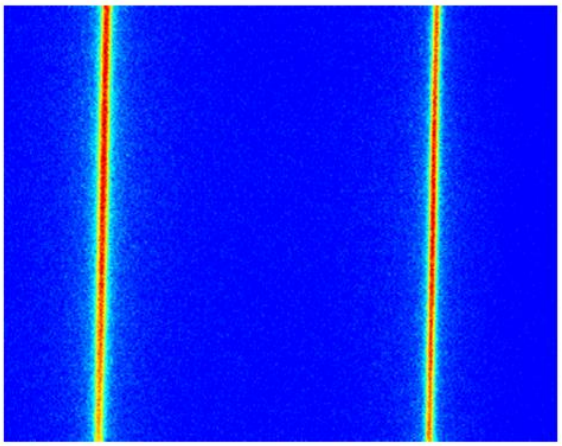

Figure 2-2. Fluorescence image of atoms in the measurement chamber.
The image was taken with a PULNIX CCD camera. The distance between the two atom pancake stacks is 1 cm. Transverse width of the atom stacks yield a temperature of ~10 μK.

2.1.2. State preparation and detection

State preparation has been largely discussed in Dr. Solmeyer's dissertation (Chapter 7 in ref. [2]). Additional technical aspects of state preparation like the microwave launcher and microwave propagations, together with state-selective fluorescence detection using the nonmagnetic imaging system are given in Chapter 3 (section 3.3) and Chapter 4.

Laser-cooled atoms are first optically pumped to the dark state $|4, -4>$ using a σ^- polarized optical pumping beam resonant with the $F = 4 \rightarrow F' = 4$ transition and a σ^- polarized repumping beam resonant with $F = 3 \rightarrow F' = 4$ transition. A bias magnetic field is precisely aligned to be parallel with the k-vector of the optical pumping beam to ensure that more than 99.9% of the atoms end up in the dark state. The alignment of the magnetic bias field is performed by minimizing atom loss after pulsing on a low intensity optical pumping beam for a few seconds. Depending on the handedness of the optical pumping beam or the sign of the bias

magnetic field, we can also optically pump into $|4,+4>$. The optical pumping scheme minimizes heating of the atoms, since once in dark state the atoms no longer scatter photons [5].

Starting from the dark state, we apply a series of microwave adiabatic fast passage (AFP) [6] pulse to transfer atoms to $|3,0>$ for the EDM measurements (Figure 2-3). The AFP microwave pulses are necessitated by the microwave intensity inhomogeneity inside the glass cell and field plates structure (Chapter 4, section 4.1 and 4.2). Using the AFP pulse, we have transferred more than 99% of the atoms to $|3,0>$ in ~ 10ms. For atomic magnetometry experiments, only the first microwave AFP pulse ($|4,-4> \rightarrow |3,-3>$) is necessary for state preparation.

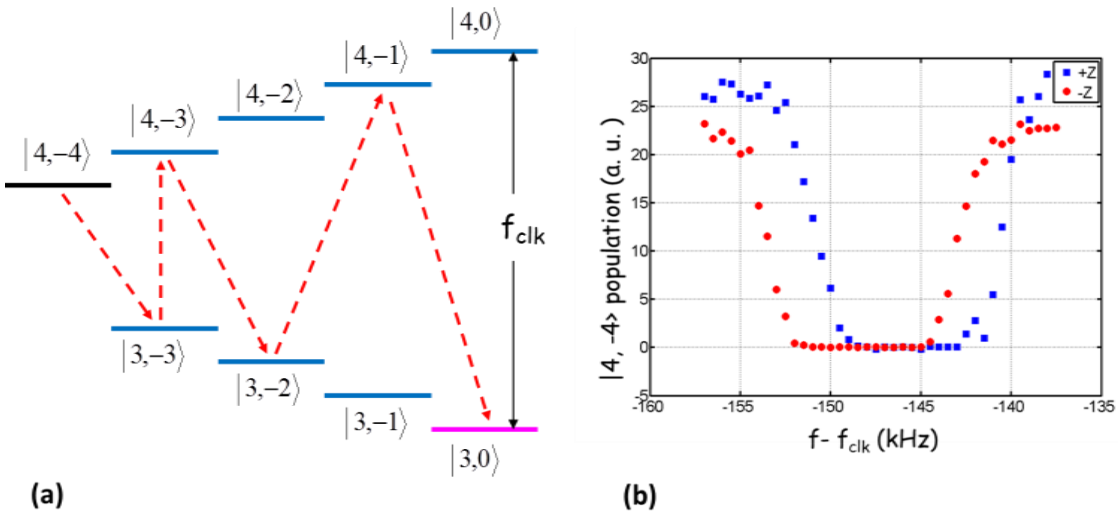

Figure 2-3. State preparation using microwaves.

(a) Energy level diagram of the Cs hyperfine ground states in a bias magnetic field, only half of the Zeeman sublevels are shown for simplicity. Depend on the handedness of the optical pumping beams we can start either from either |4,-4> (σ+ polarized) or |4,+4> (σ- polarized). (b) Robustness of microwave transitions using adiabatic fast passage pulses, the first transition (|4,-4> → |3,-3>) is shown as an example. The atoms are microwave transferred to |3,-3> and the population left in |4,-4> is detected.

State-selective fluorescence detection is accomplished using a microwave AFP pulse which transfer atoms from $|3,m_F>$ to $|4,m_F>$, followed by a circularly polarized, well saturated probe pulse which is resonant with the $F = 4 \rightarrow F' = 5$ optical transition (Chapter 4,

section 4.3). For atomic states which are not initially prepared along the k-vector of probe beams, the quantization axes can be adiabatically rotated to this axis before fluorescence detection begins. The state-selective fluorescence detection of all 7 Zeeman sublevels of Cs F=3 hyperfine ground state can be carried out in an arbitrary order, and the detection scheme can be applied to both the atomic magnetometry experiments and the EDM measurements.

2.1.3. Atomic magnetometry

In-situ atomic magnetometry using a variation of the Hanle effect [7, 8] is performed to measure and cancel residual magnetic fields along all three directions in the science chamber. Using spatial information from the vertical atom pancake stacks and from the two lattice sides, we can also map out all magnetic field gradients. As an example but without loss of generality, we will show the measurement of a bias magnetic field y direction.

The evolution of state vectors for atomic magnetometry experiments is shown in Figure 2-4(a). Atoms are initially prepared in state $|3,-3>$ in a $B_x = 20\ mG$ bias magnetic field along x direction. The Hanle measurement starts by shutting off the bias field B_x, leaving the atoms in a much smaller B_y field. The switch takes less than 5 μs, much quicker than the shortest time scale for Larmor precession out of x. In the new bias field, the fractional populations of each Zeeman sublevel are shown in Figure 2-4(b), which agree with predictions using Wigner-D rotation matrices [9].

The new basis defined by B_y is the eigen-basis for spin precession. We let the atoms freely evolve for a duration t, during which each sublevel m_F picks up a phase $m_F\phi$ (with $\phi = \frac{t}{\hbar} g_F m_F \mu_B B_y$) that is proportional to the residual field B_y.

Finally, we quickly turn on a bias magnetic field $B_z = 20\ mG$, and detect populations for all 7 Zeeman sublevels $n_m|_z(\phi)$ in the basis of B_z. Using Winger-D matrices, it is straight-forward to prove that the average spin measured along z is $\langle S\rangle|_z = sin(\phi)$, which follows the classical picture of Larmor precession (Chapter 5, section 5.1). An example of spin precession as a function of evolution time t is shown in Figure 2-4(c). We can extract the bias magnetic field B_y from the Larmor precession frequency.

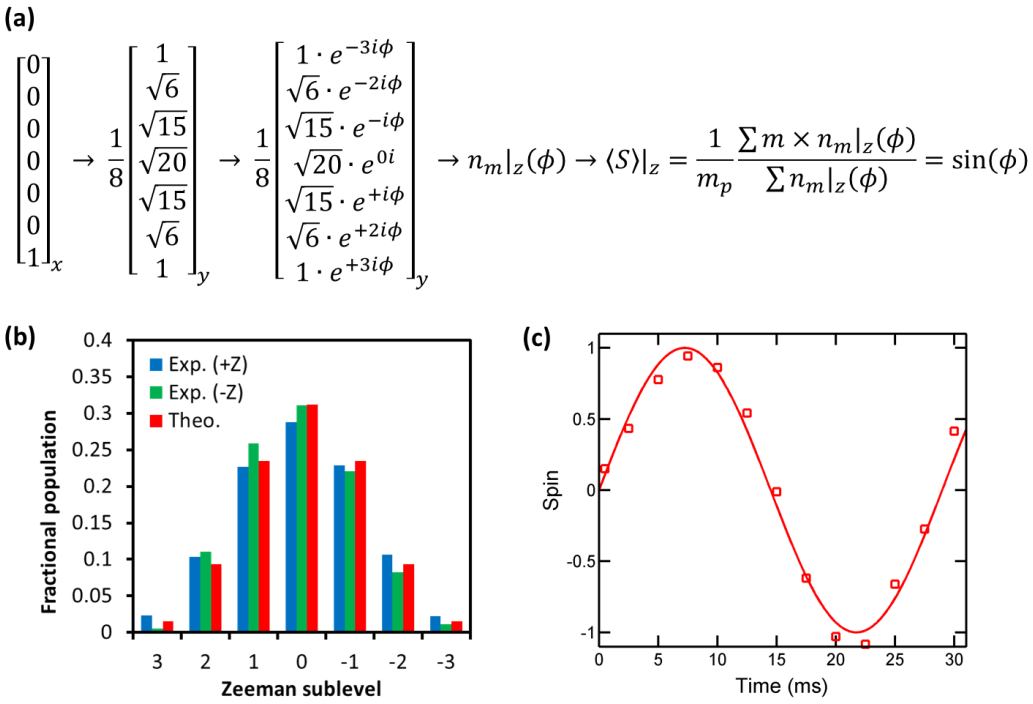

Figure 2-4. Atomic magnetometry using a variation of the Hanle effect.

(a) State vector evolution of the Cs F=3 hyperfine ground state during an atomic magnetometry experiment. (b) Fractional population of each Zeeman sublevel when atoms are prepared in |3,-3> along x and the quantization axis is diabatically switched to y direction. Experimental data for the +Z (blue) and –Z (green) sides are compared with theoretical predictions (red). (c) The average spin precession of the atom ensemble as measured along z.

The measurement can be repeated for the other two directions using cyclic permutations, and can be iterated for higher sensitivity of the magnetic fields. More details on zeroing magnetic fields along all 3 directions starting from a general case of bias magnetic fields are described in

Chapter 5. With this technique, we have managed to zero out the residual magnetic fields down to a 3 μG level, limited by the inhomogeneous vector light shifts (section 5.4) induced by a small residual circular polarization component of the optical lattice beams.

2.1.4. EDM spectroscopy

Spectroscopic measurements of the EDM as described in Chapter 1, section 1.3 are performed in large DC electric fields which define the quantization axis (Figure 2-5). Since the quadratic Stark shift for a m_F level is only $\sim 45 m_F^2\ Hz$ [10] in a $E = 150\ kV/cm$ field, coherent transfer of atoms from $|3,0>$ to $(|3,+3> + |3,-3>)/\sqrt{2}$ using regular π pulses is a nontrivial process. Generic waveforms for rapid and robust population transfer are needed. An ansatz waveform which contains all the frequency components of the 3 magnetic dipole transitions will be studied in Chapter 6, section 6.2. As an example, Figure 2-5(c) shows the population evolution for all sublevels in a numerically optimized, a few-cycle-long 3-photon low frequency magnetic field, which achieves better than 99% fidelity.

After a free evolution time τ, the number of atoms coherently transferred back to $|3,0>$ will be determined by the relative phase between the two interferometric states $|3,+3>$ and $|3,-3>$. Figure 2-5(d) shows the fractional population as a function of the relative phase for all 7 Zeeman sublevels at the end of the time-reversed, 3-photon low frequency pulse. Ideally, the $m_F = 0$ atom signal is a cosine function; the signals for the other m_F levels are sinusoidal functions, with amplitudes determined by the matrix elements of the magnetic dipole transitions and the 3-photon low frequency pulse parameters. In the presence of modest transverse magnetic fields (see section 6.2.4), the contrast for the $m_F = 0$ fringe is negligibly affected; the final populations for $m_F \neq 0$ levels can be used for interferometer signal ($m_F = 0$) normalization and as a measure for the size of transverse magnetic fields.

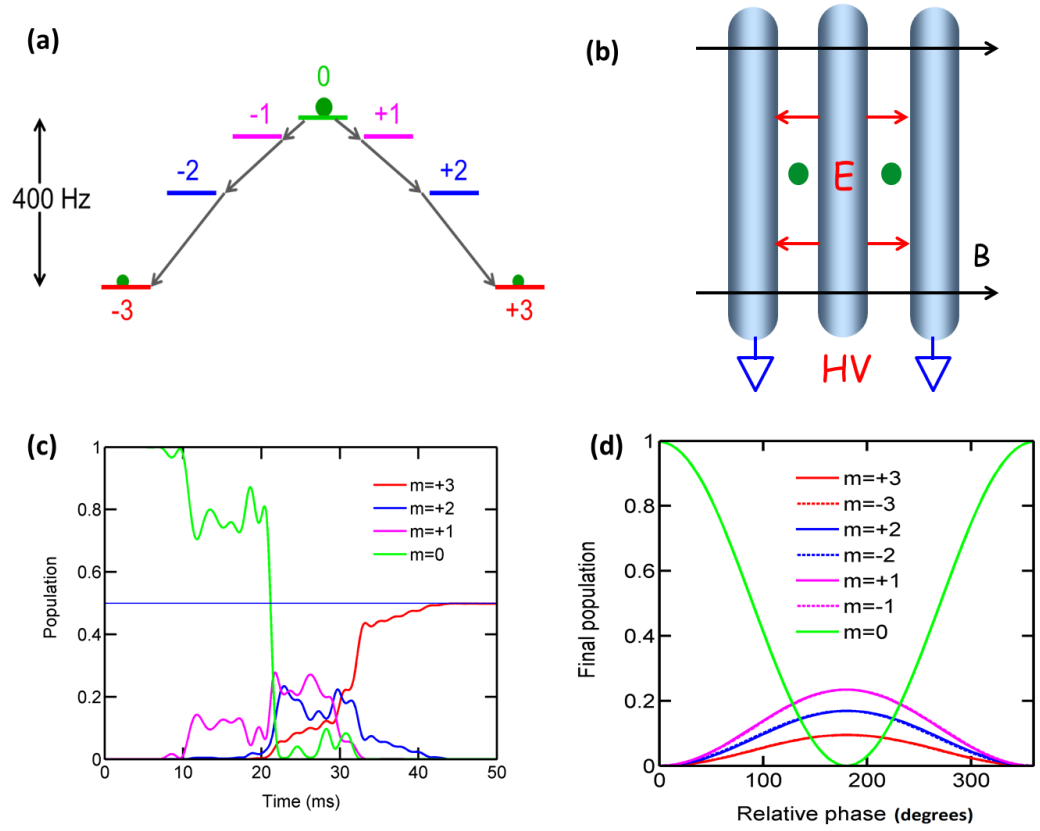

Figure 2-5. EDM spectroscopy.

(a) Energy level structure of the Cs F=3 hyperfine ground state in a ~150 kV/cm DC electric field. (b) Schematic of the electric and magnetic fields during an EDM measurement. The two outer plates are grounded and the center plate is maximally charged to either +60 kV or -60 kV. (c) Population evolution in an optimized 3-photon low frequency waveform which drives the $|3,0> \rightarrow (|3,+3> + |3,-3>)/\sqrt{2}$ *transition. (d) Final population of all 7 Zeeman sublevels as a function of interferometer phase after a 3-photon low frequency waveform coherently transfer atoms back to* $|3,0>$.

2.2. Special features of the experiment

We will now discuss and summarize the most important features of this EDM experiment. The special features are integrated to enhance eEDM sensitivity and suppress noise and systematic errors, and distinguish our experiment from previous or ongoing eEDM searches. In particular, we will discuss the advantage of using laser-cooled atoms, the common mode noise

rejection with simultaneous interferometers, control of electric and magnetic fields, and the ultimate check of systematic errors using alternating measurements with two alkali species, Cs and Rb.

2.2.1. Cold atoms in optical lattices

Using laser-cooled atoms trapped in a one-dimensional far-detuned (1064 nm) optical lattice which have a long coherence time [11], the EDM interaction time can be as large as a few seconds. This affects the interferometer phase linearly and enhances the eEDM sensitivity (Chapter 7). In contrast, eEDM searches based on thermal beams of atoms [12] or molecules [13, 14] have an interaction time on the order of 1 ms.

When atoms move at a velocity $\boldsymbol{V}$ in a DC electric field $\boldsymbol{E}$, they experience a motional magnetic field, $\boldsymbol{B}_m \propto \boldsymbol{V} \times \boldsymbol{E}$. Because $\boldsymbol{B}_m$ changes sign when the electric field polarity is reversed, the motional magnetic field was the dominant systematic source in previous Thallium eEDM experiment [12]. With Cs atoms laser-cooled to a 10 μK temperature and confined in pancake traps with aspect ratios greater than 3000:1 (section 3.1.1), motional field effects are greatly suppressed for three reasons: the average velocity of atoms is reduced to about 2 cm/s (in comparison to a thermal beam of atoms travelling at a few hundred m/s); the alignment and tight confinement of the 1D optical lattices ensure that both $\boldsymbol{V}$ and $\boldsymbol{E}$ are in the same plane; finally, the velocity averaged across every pancake stack for ~1000 atoms per stack is close to zero.

The advantage of trapping atoms in far-detuned optical lattices for eEDM measurements comes at the cost of unwanted light shifts, which needs to be handled properly (see detailed discussions in section 7.1.2 and section 7.2.3). In our experiment, we use two built-up standing wave optical cavities (section 3.1) with polarization optics for desired intensity balance and high quality linear polarization of the lattice traps. Furthermore, we precision align the lattice beam

polarization axis to be parallel to the direction of the electric fields. Those steps help us to control systematic errors associated with light traps to a level less than or comparable to the projected eEDM sensitivity.

2.2.2. Common mode noise rejection

The second powerful feature of our experiment is common mode noise rejection with two simultaneous interferometers (Figure 1-3), at the significant technical cost of three electric field plates, two parallel 1D optical lattices and nearly doubled cooling and detection optics. Performing two simultaneous measurements in two parallel traps for every shot with a given applied high voltage, we are insensitive to uniform and mirror-symmetric magnetic field fluctuations; frequently reversing the high voltage polarities with a particular pattern, we are insensitive to constant and linear drift magnetic field gradients.

To illustrate the common mode noise rejection in more details mathematically, let us consider an example where the most critical z component of the magnetic field in the science chamber is described as

$$\begin{aligned} B(n,z,t) = (B_0 + n\Delta) + (a_1 t + a_2 z) + (b_1 t^2 + b_2 z^2 + b_3 tz) \\ + (c_1 t^3 + c_2 z^3 + c_3 t^2 z + c_4 t z^2) \\ + (d_1 t^4 + d_2 z^4 + d_3 t^3 z + d_4 z^3 t + d_5 t^2 z^2) + \cdots \end{aligned} \tag{2.1}$$

With Δ the increment of magnetic field during a EDM scan (index n) to build a Ramsey-like fringe, and $a, b, c, d, \ldots$ the coefficients for 1st to 4th-order Taylor expansions of the magnetic field as a function of time t and position z (for two lattice traps, $z = \pm L$, $L = 5\,mm$). After re-organizing all the terms, we can rewrite the magnetic field in the following form

$$B(n,z,t) = (B_0 + n\Delta) + \delta B(t) + \Delta B(z) + B_L(z,t) + B_M(z^2,t) + B_R(z^{2p-1}t^q) \ldots \quad (2.2)$$

Where the abbreviated terms are defined as:

$\delta B(t) = (a_1 t + b_1 t^2 + c_1 t^3 + d_1 t^4)$ *-Uniform magnetic field fluctuations*

$\Delta B(z) = (a_2 z + b_2 z^2 + c_2 z^3 + d_2 z^4)$ *-Constant magnetic field gradients*

$B_L(z,t) = (b_3 z + c_4 z^2 + d_4 z^3)t$ *-Magnetic field gradients that linearly drift in time*

$B_M(z^2,t) = d_5 t^2 z^2$ *-Mirror-symmetric magnetic gradient fluctuations*

$B_R(z^{2p-1}t^q) = (c_3 t^2 z + d_3 t^3 z);\ p \geq 1, q \geq 2$ -A*symmetric magnetic gradient fluctuations*

According to Eq. (1.4) in Chapter 1, the interferometer phases for atoms in $z = \pm L$ optical lattices in the k-th EDM shot ($k \geq 0$) can then be defined as

$$\phi_k^{\pm} = \frac{3}{2\hbar}\int_{kT}^{kT+\tau} \left\{ \pm dE \cdot (-1)^{k+\left\lfloor \frac{k}{2} \right\rfloor} + \mu B\left(\left\lfloor \frac{k}{2} \right\rfloor, \pm L, t \right) \right\} dt \quad (2.3)$$

Where $\left\lfloor \frac{k}{2} \right\rfloor$ is the floor of $k/2$, T is the total experiment duration per shot and τ is the EDM interaction time per shot. The pre-factor $(-1)^{k+\left\lfloor \frac{k}{2} \right\rfloor}$ for the EDM interaction term dE describes an alternating electric field polarity switching pattern (+HV→-HV) → (-HV→+HV) that is an optimal measurement strategy for common mode noise rejection and effective suppression of linear drift errors [15]. The interferometer phase extraction for 4 successive EDM shots yields

$$\frac{1}{8}\{[(\phi_0^+ - \phi_0^-) - (\phi_1^+ - \phi_1^-)] + [(\phi_3^+ - \phi_3^-) - (\phi_2^+ - \phi_2^-)]\} = \frac{3\tau}{2\hbar}\left\{ dE + \mu T^2 L\left[c_3 + \frac{3}{2} d_3 (3T + \tau) \right] \right\}. \quad (2.4)$$

Asymmetric magnetic gradient fluctuations $B_R(z^{2p-1}t^q)$ are the only terms that are not cancelled in the above electric field polarity switching pattern for 4 shots. Similar to Eq. (3.4), by evaluating partial terms such as $\frac{1}{2}(\phi_0^+ - \phi_0^-)$ and $\frac{1}{4}[(\phi_0^+ - \phi_0^-) - (\phi_1^+ - \phi_1^-)]$, it is straight-forward to show that:

(i) Both uniform magnetic field fluctuations $\delta B(t)$ and mirror-symmetric magnetic gradient fluctuations $B_M(z^2,t)$ are cancelled within each shot using two simultaneous interferometers located at $z = \pm L$;

(ii) Constant magnetic field gradients $\Delta B(z)$ are cancelled from shot to shot when electric field polarity is reversed, namely (+HV→-HV) or (-HV→+HV);

(iii) Magnetic field gradients that linearly drift in time $B_L(z,t)$ are cancelled within 4 successive shots with electric field polarity switching pattern (+HV→-HV) → (-HV→+HV);

Higher order drifts can be cancelled by implementing a maximally reversed E polarity pattern for 2^{n+1} shots with the following recursion rule: $P_1 = \{+,-\};\ P_{n+1} = \{P_n, -P_n\}$ for $n \geq 1$ [15]. For instance, to cancel a 2nd order magnetic field drift, a minimal number of SHOTs is $2^3 = 8$ and the respective E polarity pattern is $P_3 = \{+,-,-,+,-,+,+,-\}$.

Employing the above common mode noise rejection technique does not necessarily imply that the cancelled terms can be left arbitrarily large in our experiment. For instance, in order to suppress systematic errors from atoms shifting in problematic magnetic field gradients during imperfect electric field reversal (Chapter 7, section 7.2.2), the magnetic field gradients have to be smaller than a certain level.

From the prospective of data analysis, in the case of magnetic field fluctuations that are so large that we cannot reliably park near the maximally sensitive place on the Ramsey-like fringe, an elliptical fitting method can be implemented for effective and rapid differential phase extraction between coupled interferometers [16]. To illustrate the concept, suppose we have two sinusoidal signals described by

$$x = A\cos^2\left(\frac{\phi}{2}\right) + B, y = C\cos^2\left(\frac{\phi + \Delta\phi}{2}\right) + D \tag{2.5}$$

By plotting a Lissajous curve (y versus x), we get an ellipse such that the differential phase $\Delta\phi$ can be directly extracted from fitting parameters of the ellipse

$$X^2 - 2cos(\Delta\phi)XY + Y^2 + cos^2(\Delta\phi) - 1 = 0 \quad (2.6)$$

with rescaled coordinates $X = \frac{x-(B+A/2)}{A/2}, Y = \frac{y-(D+C/2)}{C/2}$. Using Eq. (2.5) and Eq. (2.6), one can derive an elliptical fitting function that explicitly contains the differential phase $\Delta\phi$ as a free fitting parameter independent of ϕ, from which numerical methods for direct least-square fitting [17] can then be employed straightforwardly. Common mode phase noises on ϕ, which could otherwise compromise direct fittings to signals in Eq. (2.5) with sinusoidal functions, do not affect the differential phase extraction from the elliptical fitting method. Numerical examples can be found in ref. [16] and [2] (p.139).

It is straightforward to generalize the elliptical fitting method to the case of more complex electric field polarity switching patterns by keeping track of the polarity of the applied high voltage. For instance, within a single SHOT (+HV) we plot the data from +Z lattice side on y-axis vs that from the –Z lattice side on x-axis for the EDM signal. Using a pattern like (+HV→-HV) → (-HV→+HV), the differential phase in Eq. (2.4) for the EDM signal with common mode noise rejected can be automatically obtained by plotting $\phi_0^+, \phi_1^-, \phi_3^+, \phi_2^-$ on the y-axis vs $\phi_0^-, \phi_1^+, \phi_3^-, \phi_2^+$ on the x-axis.

2.2.3. Control of electric and magnetic fields

Precision control of the electric fields in the measurement chamber is achieved by interferometric measurements of field plate separations (section 3.4.2) with a fractional uncertainty of 2.9×10^{-5}, and active stabilization of the high voltage applied to the electric field plates (section 3.4.1) to better than 2×10^{-5} using a precision high voltage divider. The high

voltage servo also enables us to reverse the electric field from shot to shot to a comparable accuracy, which suppresses systematic errors related to imperfect electric field reversal below our projected sensitivity level (section 7.2.2).

The measurement chamber is passively shielded from the laboratory environment with 4-layer mu-metal magnetic shields (Chapter 4 in ref. [2]), with a shielding factor of 100K along z, 35K along y and 12K along the x direction after degaussing (section 3.4.3). The residual magnetic fields are measured in-situ using atomic magnetometry as described in Chapter 5, and cancelled with 8 sets of magnetic field coils (including 3 bias coils and 5 linear gradient coils, see Chapter 5 in ref. [2]) inside the inner-most magnetic shield layer.

With the ability to image ~25 subgroups of atoms on each lattice side with linear CCD arrays (section 3.3), we can map out magnetic field gradients and potential local systematic effects and cancel them.

2.2.4. Ultimate check of systematic errors

The final special experimental feature is to measure the eEDM using both Cs and Rb atoms, with the two species used in alternating measurements, not trapped simultaneously. If the atomic EDMs result from the electron EDM, Cs and Rb will differ by a factor of 4.7 [18]. eEDM sensitivities for the two species are about the same, because the higher Rb density allowed by its smaller collision rates, allowing a factor of ~40 more Rb atoms, makes up for the smaller EDM enhancement factor. Although all of our optics and optical paths have been designed for both species, we plan to first implement a complete Cs measurement. Throughout this dissertation we will only focus on Cs. At the price of technical complication, measuring two species will ultimately provide a strong final check against systematic errors.

2.3. References

[1] F. Fang, *Progress toward a measurement of the electron electric dipole moment using ultra-cold atoms*, PhD dissertation, Penn State University, (2007).

[2] N. Solmeyer, *Progress toward an electron electric dipole moment measurement With laser-cooled atoms*, PhD dissertation, Penn State University, (2013).

[3] F. Fang and D. S. Weiss, *Resonator-enhanced optical guiding and trapping of Cs atoms*, Opt. Lett. **34**, 169 (2009).

[4] T. W. Hodapp et al., *Three-dimensional spatial diffusion in optical molasses*, Appl. Phys. B **60**, 135 (1995).

[5] C. J. Foot, Atomic Physics, Oxford University Press, (2005).

[6] M. Khudaverdyan et al., *Adiabatic quantum state manipulation of single trapped atoms*, Phys. Rev. A **71**, 031404(R) (2005).

[7] W. Hanle, *Magnetic influence on the polarization of resonance fluorescence*, Z. Phys. **30**, 93 (1924).

[8] D. Budker et. al., *Resonant nonlinear magneto-optical effects in atoms*, Rev. Mod. Phys. **74**, 1153 (2002).

[9] M. A. Morrison and G. A. Parker, *A guide to rotations in quantum mechanics*, Aust. J. Phys. **40**, 465 (1987).

[10] S. Ulzega *et. al.*, *Measurement of the forbidden electric tensor polarizability of Cs atoms trapped in solid ^{4}He*, Phys. Rev. A **75**, 042505 (2007).

[11] S. L. Winoto, et al., *Laser cooling at high density in deep far-detuned optical lattices*, Phys. Rev. A **59**, R19 (1999).

[12] B. C. Regan et al., *New Limit on the Electron Electric Dipole Moment*, Phys. Rev. Lett. **88**, 071805 (2002).

[13] J. J. Hudson et. al., *Improved measurement of the shape of the electron*, Nature **473**, 493 (2011).

[14] A. C. Vutha et al., *Search for the electric dipole moment of the electron with thorium monoxide*, J. Phys. B **43**, 074007 (2010).

[15] V. V. Yashchuk, *Optimal measurement strategies for effective suppression of drift errors*, Rev. Sci. Instrum. **80**, 115101 (2009).

[16] G. T. Foster et al., *Method of phase extraction between coupled atom interferometers using ellipse-specific fitting*, Opt. Lett. **27**, 951 (2002).

[17] A. Fitzgibbon, M. Pilu, and R. B. Fisher, *Direct Least Square Fitting of Ellipses*, IEEE Trans. on Pattern Analysis and Machine Intelligence **21**, 476 (1999).

[18] H. S. Nataraj et al., *Intrinsic Electric Dipole Moments of Paramagnetic Atoms: Rubidium and Cesium*, Phys. Rev. Lett. **101**, 033002 (2008).

Chapter 3

The apparatus development

Apparatus development is central to this complex experiment. From both the physics and perhaps more the engineering prospective, in this Chapter we discuss some of the key components of the experiments that have been developed over the past few years. In particular, I will describe some key engineering issues related to one-dimensional optical lattices for atom trapping (section 3.1), the design and characterization of microwave systems for quantum state manipulation (section 3.2), custom made nonmagnetic fluorescence imaging systems (section 3.3), electric and magnetic field precision control (section 3.4), and finally the mastermind software control architecture and implementations for the ultimate automatic EDM measurements (section 3.5). Those components are the invaluable subsystems of the EDM apparatus which make current experimental progress possible.

3.1. One-dimensional optical lattices

The one-dimensional optical lattices are present throughout the entire experiment procedure for atom guiding and trapping. A schematic of the two far-detuned 1D optical lattices is shown in Figure 3-1. A more complete map of the optical lattice system including nearly every piece of optic and electronic components can be found in Appendix A (Figure A-1). The lattice beams are parallel to each other to within 0.5 mrad, separated by 1 cm and thread through the three electric field plates. Each optical lattice is made of a 2.1-m-long nearly confocal cavity, which has a finesse of $F \approx 300$ and a power build-up factor of $Q \approx 25$. Atoms are trapped near the center of the confocal cavities, where the spread in wave vectors of the lattice beams are the

smallest. At a maximum input power of 4 Watts per cavity from a 10 Watt fiber amplifier, the cavities have a maximum one-way power of ~100 Watt, or equivalently a trap depth of 200 μK.

The intensity of the lattice beams is given by $I(y,\rho) = I_0 cos^2(ky) exp(-\rho^2/w^2)$, where $k = \frac{2\pi}{\lambda}$ is the wave vector ($\lambda = 1064\ nm$), $w = 580\ \mu m$ is the transverse beam waist radius. Using the harmonic approximation, the trapping frequencies at a typical trap depth of $U_0 = 100 \mu K$ is

$$\omega_y = k\sqrt{\frac{2U_0}{m}} = 2\pi \times 105.3kHz, \omega_\rho = \sqrt{\frac{2U_0}{mw^2}} = 2\pi \times 30.7Hz \quad (3.1)$$

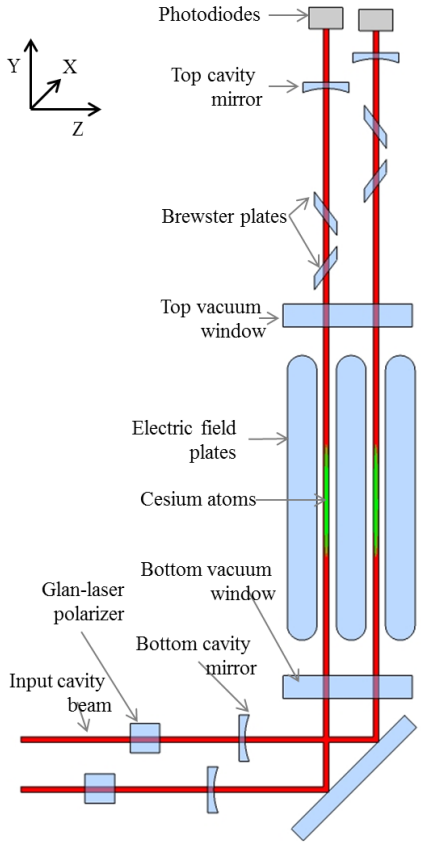

Figure 3-1. Schematic of the optical lattice setup.

The schematic is not to scale. Laser cooled atoms are trapped in two parallel 1D optical lattices made in 2.1 m-long build-up cavities, separated by 1 cm. The 90^o cavity-folding mirror is necessitated by geometric constraints.

We use a standard two-band, Pound-Drever-Hall technique [1] to lock the two cavities to a YAG laser. Each cavity contains a pair of Brewster plates for cavity locking in the low frequency range (below 100~200 Hz), and a piezoelectric transducer (PZT) epoxied to the top cavity mirror which primarily takes care of frequency noises higher than 100Hz. In the presence of optical table mechanical vibrations and PZT induced mechanical resonances, the 2 m-long, vertically mounted cavities present great challenges in frequency stabilization. Section 3.1.1 discusses an effective solution that emerged after a long march of engineering and developments.

To minimize the vector light shifts induced by the residual circular component of the lattice beams, which acts like a fictitious magnetic field for the atoms (see section 5.4), we have developed a set of polarization purification techniques that improve the linear polarization quality of our optical lattice beams to a level better than that one could get using the best available Glan-laser polarizers. Detailed implementations for the high quality linear polarizations will be addressed in section 3.1.2.

3.1.1. Cavity stabilization and anti-resonances

Figure 3-2 shows a photograph of the top cavity mirror for the +Z lattice. The mirror is cut into a D-shape to leave space for the –Z lattice that is just 1 cm away. The cavity mirror is glued onto a ring PZT (Noliac part# CMAR04), which is then epoxy attached to an ultra-stable industrial mirror mount plate (Siskiyou part# IXM100.P3). Special care is taken avoid excess of epoxy onto the side of the PZT stacks, which could otherwise degrade their mechanical response.

The industrial mirror mounts are selected based on their flat electro-mechanical transfer function measured with a Michelson interferometer over a wide range of acoustic frequencies, which out performs similar products from various vendors (see detailed transfer functions in Figure A-2). To monitor the cavity power from the top cavity mirror transmission, we cut a 9 mm

diameter hole on the mirror mount plate, an inevitable step that introduces new resonances. The best solution to this added problem is to fill the hole with a glass spacer, which transmits optical signals as well as preserves the mechanical advantage of an intact mirror mount plate (see detailed transfer functions in Figure A-3).

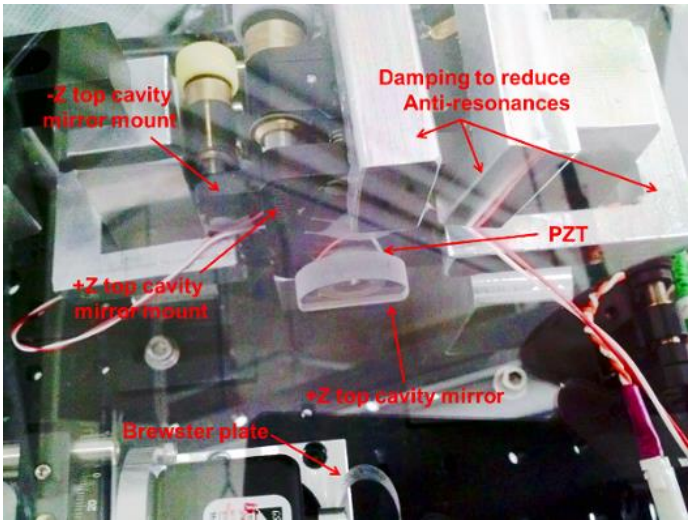

Figure 3-2. Aerial view of the top cavity mirrors.

The PZT has an unloaded resonance frequency of 500 kHz. With our D-shaped mirror the resonance frequency is shifted by a factor of $\sqrt{\frac{m}{3} / \left(\frac{m}{3} + M\right)}$, down to ~60kHz, where m is the mass the PZT and M is the mass of the D-shaped mirror. Using a twin-T notch filter (Figure A-4) to reduce the effect of the PZT resonance we achieve a bandwidth of ~50 kHz in the cavity feedback circuit. The PZT has a capacitance of 450 nF. We have designed a high power amplifier (Figure A-5) with a capability of +/-15 V voltage swing, and +/-5 A current up to 100 kHz. The voltage range is large enough to cancel the mechanical vibrations in the system, which are typically < 5 V (or equivalently < 1 nm) RMS in the frequency bandwidth of 100 Hz ~50 kHz. The voltage range +/- 15 V is also far away from the PZT depoling limit of -40 V to ensure a linear and bipolar response.

The PZT-mirror system exhibits anti-resonances at 2.5 kHz, which is somewhat counterintuitive and adds complications for the cavity stabilization. The effect is illustrated in Figure 3-3, where we consider the PZT as a hard spring, with a spring constant k~1600N/m that is much larger than the strength of mirror mount springs. When the PZT expands, both the mirror mount plate and the cavity mirror will move accordingly (note the mirror mount base is assumed to be locked in place with 1.5 inch diameter post). If the cavity mirror move downwards ΔL while the mirror mount plate move upwards by more than ΔL, the effective change in cavity length is 180^{o} out-of-phase compared to one would expect.

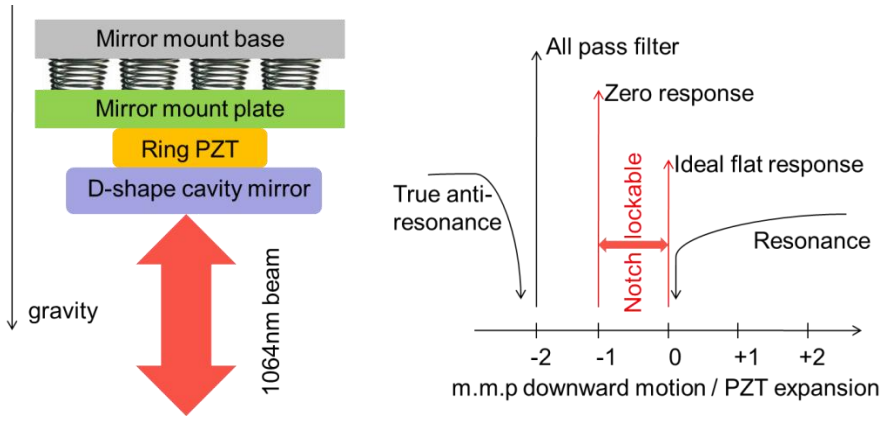

Figure 3-3. Schematic of anti-resonances and effects on cavity stabilization.

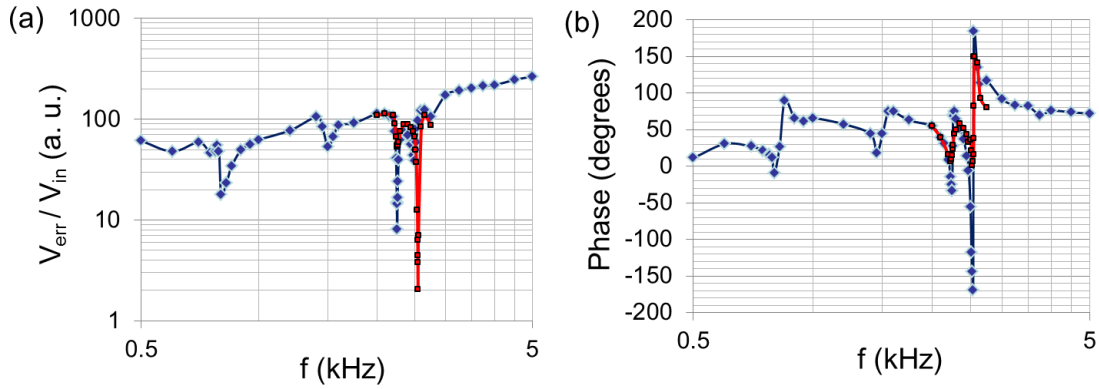

Figure 3-4. Transfer function and mechanic response of the PZT-mirror system.

The blue (red) points are the electro-mechanical response of the original (damped) PZT-mirror system. The damped system (Figure 3-2) does not have a 180^{o} *phase shift at 2.5 kHz.*

We have measured the electro-mechanical response of the PZT-mirror system, by intentionally adding a sinusoidal signal to the lock circuit and measuring the amplitude and phase of the error signal while the cavity is marginally in-lock with a low gain setting. The results are shown in Figure 3-4 (blue points). The 180^o phase shift at 2.5 kHz is in fact the limiting factor for a tighter lock (the lock circuit will oscillate at this frequency if the gain is raised), even though the amplitude response at this frequency looks flatter than that at 2.2 kHz.

We have reduced the effects of anti-resonances very effectively by adding 3 C-clamps with ultra-soft polyurethane to damp out the motion of the mirror mount plate (Figure 3-2). The corresponding transfer function is shown in Figure 3-4 (red points) for comparison. The damped system no longer has the 180^o phase shift at 2.5 kHz; right at the resonance frequency the cavity mirror moves in phase with respect to the driven signal. The damping can evolve 1~3 days after the initial alignment, which requires further minor adjustments by adjusting the tightening strength on the C-clamps. The process converges after a few days until the polyurethane eventually settles down to its minimal energy state. Provided that no further mechanical changes are made, the damping can last for a very long time.

3.1.2. Polarization purification

We optimize the linear polarization of the lattice beams in several ways. The cavity input beams pass through Glan laser polarizers (GLP, Thorlabs # GL10-C26) that filter out the incorrect polarization to better than 2 ppm. The GLPs are mounted on precision Goniometers (Thorlabs # GNL18) which have a 0.05^o minimal increment. To prevent the dielectric 90^o cavity-folding mirror from mixing S and P polarizations, we align the ($\mathbf{k}$, $\boldsymbol{\epsilon}$) plane of the cavity beams to be perpendicular the mirror surface to better than 0.2^o by monitoring the beam polarization before

the top cavity mirrors and rotating the residual birefringence axis of the low-birefringence vacuum windows [2] to be along ϵ.

The measured wrong polarization component due to S-P mixing as a function of GLP angle is shown in Figure 3-5, which is well fitted to quadratic functions. From the quadratic coefficients we estimated that the relative phase shift for S and P polarizations at the dielectric surface is $0.35^{o} \pm 0.01^{o}$ for the both +Z and –Z lattice beam locations. The 11 ppm offset is dominated by the residual stress-birefringence of the vacuum windows, and the offset does not change more than 50% if ϵ is rotated by $< 5^{o}$ with respect to the optimal vacuum window birefringence axis [2]. The optimal GLP angles for the two lattices differ by 0.2^{o}, which can be improved in the future by making the two input lattice beams more parallel.

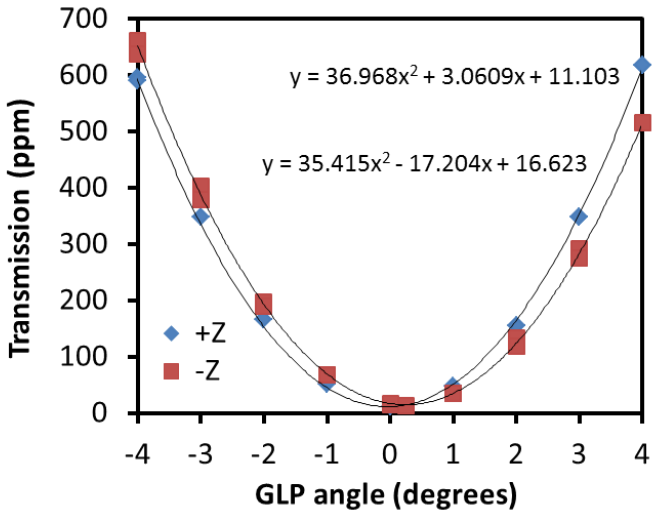

Figure 3-5. Precision alignment of the input lattice beam polarization.

We actively purify the intra-cavity polarization by using precision aligned Brewster plates, which are also employed in the cavity lock. To this end we have built a compact goniometer-based 3-axis precision rotation mount for each Brewster plate (Figure 3-6). All axes are aligned to better than 0.2^{o} by minimizing the Brewster reflection when the cavities are in lock.

An example optimization curve for rotation Ω_Y along Y direction is shown Figure 3-7(a), where a clear minimum is found. During this alignment the galvanometer (General scanning # G108) DC offset is controlled to within 80 mV (Figure 3-7(b), equivalently 0.1^o Brewster rotation) to minimize the reflections of P polarization components that could otherwise mimic the reflected signal from the S polarization.

The total intensity-averaged angular spread of the lattice beams wave vectors at the Brewster plates is 0.03^o, so it does not limit our alignment sensitivity. Scattering from the 11 cavity surfaces can degrade polarization quality [3] since non-parallel momentum components, when superposed with unscattered light, can give elliptical polarization. The four Brewster surfaces (uncoated) filter out 66% of the wrong component per round trip.

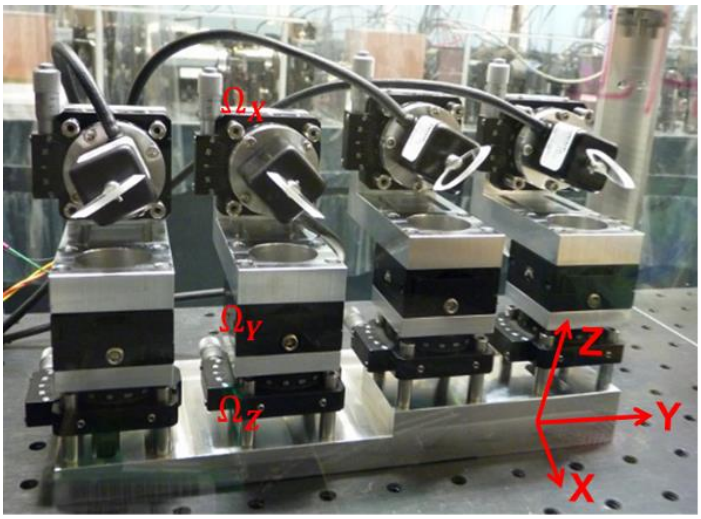

Figure 3-6. Precision rotation mounts for the Brewster plates.
The wave vector is along Y. All axes (with angular rotations $\Omega_X, \Omega_Y, \Omega_Z$) are aligned to better than 0.2^o by minimizing the Brewster reflection when the cavity is in lock.

The typical RMS Brewster plate rotation angle Ω_X used to cancel out mechanical vibrations of the cavity system in the frequency range below 100 Hz is about 0.06^o, or equivalently 1.8 μm change in cavity length. On a time scale of a day, due to small temperature

variations (<0.2 ^{o}C) of the lab, the thermal expansion of the 2 m high tower can change the cavity length by up to 20 free spectral ranges (10.6 μm), leaving a large galvanometer offset. Because of the imperfectness of the Brewster plate mount, this could effectively misalign Ω_Y and Ω_Z by a small amount, which could degrade the lattice beam polarization to 2nd order. To avoid this effect, the cavity can be relocked if a large galvanometer offset is observed. If necessary, perhaps a more elegant solution would be to use the galvanometer DC offset and feedback to the slow temperature tuning port of the 1064 nm YAG laser.

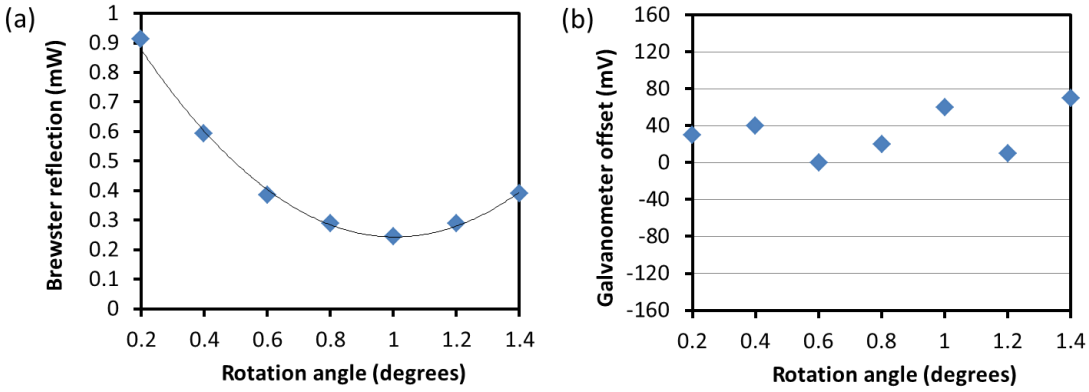

Figure 3-7. Precision alignment of the Brewster plates for optimal lattice polarization.
The one-way cavity power is 90W (or equivalently 180 μK) for this alignment and the measured power accounts for reflections from two surfaces of each Brewster plate.

3.2. Microwave system

3.2.1. RF electronics design

Our experiment utilizes microwaves pulses for quantum state manipulation of atoms. The microwave pulses must be frequency chirped and amplitude modulated to ensure high fidelity population transfer (see Chapter 4). We have designed a robust microwave system that has been integrated into the user-friendly mastermind hardware architecture (section 3.5).

A schematic of our microwave system with the key components is shown in Figure 3-8. A complete map with more technical details regarding electrical connections, RF power matching/characterization and manufacture information can be found in Appendix-B. The microwave frequency is obtained by mixing the local oscillator signal from the 9.152 GHz constant frequency synthesizer (CFS) and ~40MHz control signal from a homemade direct digital synthesizer (DDS) [4]. Both the CFS and the DDS are referenced to a 10 MHz GPS clock signal from Dr. Gibble's lab. The frequency of the CFS can be set by the D15 GUI program on the EDM2 computer via a Line Print Terminal (LPT) interface. The DDS is arbitrarily controlled in real time for frequency chirping and amplitude modulation (see details in section 3.3.2) from the Mastermind computer using a 32-channel digital PCI card. The output from the single sideband mixer (frequency sum of the CFS and DDS) has the right frequency (near the clock transition at 9.192631770 GHz) for magnetic dipole transitions between Cs F=3 to F=4 hyperfine manifolds. The microwave signal is then amplified by a 10 W amplifier and delivered to the science chamber with a nonmagnetic, rectangular horn antenna. Details for the microwave power distribution in the science chamber can be found in Chapter 4, section 4.1.

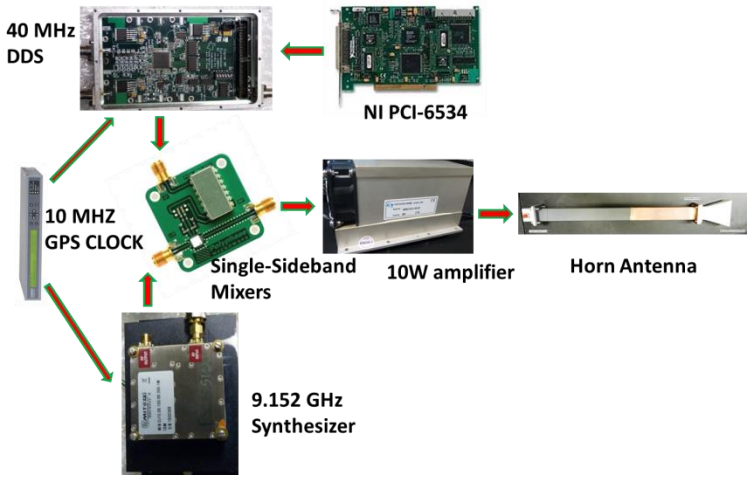

Figure 3-8. Schematic of the microwave system.

3.2.2. Programming microwave pulses

The central part of the microwave control programs the DDS core chip AD9852 from Analog Devices, Inc [5]. The specifications of the DDS and our real-time DDS control system (using National Instruments digital card PCI-6534) can be found in Table 3-1. Pulse control data is preloaded to the PCI-6534 on-board first-in-first-out (FIFO) memory and transferred to the DDS chip in real-time at the rate of 2 million samples per sec, which is assisted by a 167 ns Strobe pulse series generated from one of the PCI-6534 digital channel.

Global constants		
GPS reference clock	10 MHz	GPSCLK
PCI-6534 FIFO update clock	2 MHz (EDM specific)	External function generator
DDS system clock	300 MHz	SYSCLK=GPSCLK x30
Ramp rate clock	100 MHz (10 ns)	RRC=GPSCLK x10
DDS sample and data transfer		
Unit sample size	32 bits	6 bits not in use
Max sample size	8 Million, 4 seconds long	Limited by the 32MB FIFO
Data transfer rate with Strobe	2 Million samples per sec	0.5 μs per DDS register
Strobe pulse width	167 ns	1/3 of the 0.5 μs period
DDS tuning parameters and resolution		
Frequency Tuning Word	6 Registers, 48 bits	FTW = $f \times 2^{48} / SYSCLK$
Delta Frequency Word	6 Registers, 48 bits	DFW = $\delta f \times 2^{48} / SYSCLK$
Phase Adjust Register	2 Registers, 14 bits	PAR = $\phi \times 2^{14} / (2\pi)$
Output Shaped Keying Multiplier	2 Registers, 12 bits	OSKM = $V \times 2^{12}$, V=[0,1]
AFP pulse parameters		
Linear section minimal duration	4 μs	DFW and OSKM
Pulse switching time	7 μs	FTW, DFW and OSKM
Pulse duration (typ.)	5 ms	>1000 linear ramps
Frequency sweep range (typ.)	12 kHz	

Table 3-1. Specifications of the DDS and the real-time DDS control system.

Up to now we have implemented three modes of operation:

(i) Blackman π pulse mode: each microwave pulse has a constant frequency, but the amplitude of the pulse is varied in time with a Blackman function;

(ii) Adiabatic fast passage (AFP) pulse mode: both the frequency and the amplitude of each pulse are varied nonlinearly in time according to the functions defined in Chapter 4, section 4.2. This is the most frequently used mode.

(iii) Single tone mode: the output is continuous, both the amplitude and frequency are fixed in time. This mode is designed for troubleshooting purpose only and should be used cautiously, because a continuous high power microwave could potentially damage the conductive coatings of the electric field plates. Special instructions operating in this mode are given in the DDS control program. Users are required to power off or disconnect the 10 Watt high power amplifier and apply a special 4-digit pass code to the DDS pulse parameter file. The pass code is the manufacturing serial number of the high power amplifier and can be found on the backside of the amplifier.

We now focus on the important programming features related to microwave AFP pulses in type **(ii)** mode. To program a nonlinear chirp, we first divide a typical microwave pulse into more than 1000 linear sections, as shown in Figure 3-9. Each linear section is 4 μs long and the frequency is linearly ramped at a rate of 100 MHz internally on the chip AD9852. By dynamically changing the slope of the linear section via the 48-bit Delta Frequency Word (DFW) throughout the AFP pulse, we approach a nonlinear chirp with more than 1000 linear chirps, and the approximation has less than 10 ppm relative frequency error compare to an ideal nonlinear chirp. We can also arbitrarily modulate the pulse amplitude via the 12-bit Output Shaped Keying Multiplier (OSKM) for each linear section. Programming code for the DDS can be found as a subsection of the Mastermind control software (section 3.5) on the EDM mastermind computer.

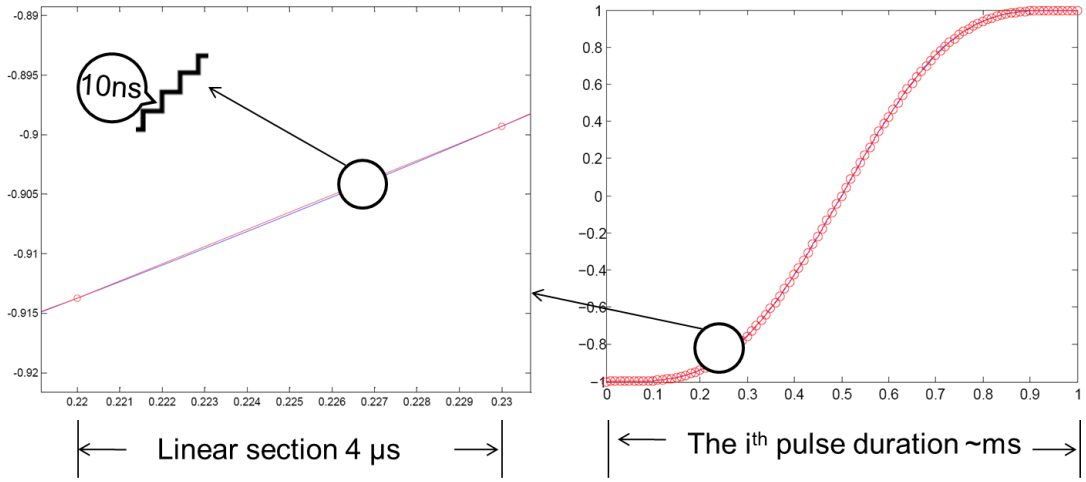

Figure 3-9. Implementation of a nonlinear chirp.

Plot of frequency (a. u.) as a function time (a. u.) for an AFP pulse. The left plot is zoom in view of the right plot.

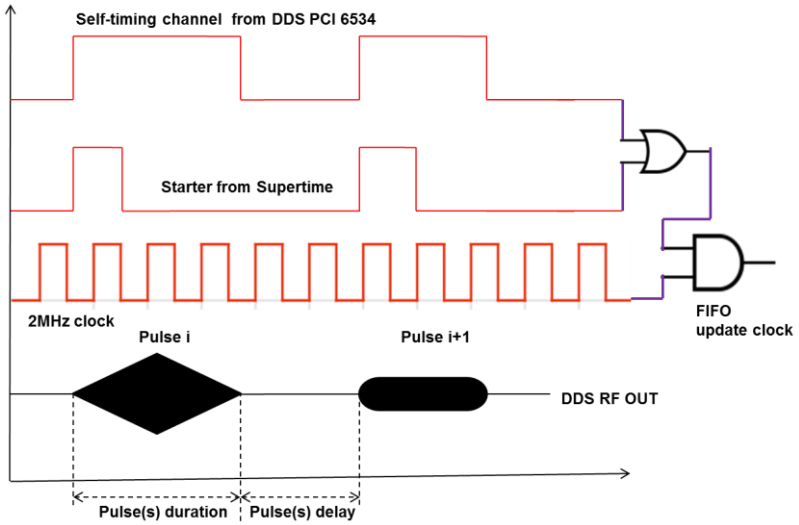

Figure 3-10. Timing control for a microwave pulse train.

The diagram for timing control of a series of microwave pulses is conceptually shown in Figure 3-10. Using a trigger channel from the experimental timing control (Supertime) as a start trigger of every microwave AFP pulse, a self-timing channel from the real-time DDS control system (PCI-6534) as a stop trigger at the end of every microwave AFP pulse, and an external

FIFO update clock for PCI-6534, we are able to bin all pre-calculated DDS control data samples for a train of microwave pulses together in the FIFO and conveniently control the delays between AFP pulses directly in the experimental timing sequence. The logic circuit for the timing control shown in Figure 3-10 and the Strobe pulse generator are made by Yang Wang from the Quantum Computation lab.

3.3. Imaging systems

The experiment uses two types of imaging systems: CCD cameras and linear photodiode arrays (PDA). With a 8 μm resolution along two dimensions, the CCD cameras mounted near the MOT chamber and the science chamber (during early phases of the experiment) helps troubleshooting, and more importantly improving the launching efficiency and polarization-gradient cooling of the atoms in the glass cell (Chapter 3 in ref. [6]). The linear PDA is used in atomic magnetometry (Chapter 5) and the final EDM measurement because it is nonmagnetic, which was the key design constraint for this highly specialized homemade imaging system.

3.3.1. 2D imaging with PULNIX camera

The CCD camera imaging system consists of two major components, a PULNIX camera (JAI part# TM-7AS, and a newer version # CV-A55IR) and a Frame Grabber (Data Translation part# DT-3155) for digitizing and acquisition of video signals. The PULNIX camera has 640 x 480 pixels, with a pixel size of 7.8 μm by 7.8 μm. It takes a total time of ~15ms to acquire one CCD image. The C/C++ programs for the Frame Grabber data logging and a large collection MATLAB programs for 2D image analysis can be found on the EDM2 computer, which include basic functions such as selecting a particular region of an image, integration along one dimension

and fitting the integrated atom signal to a Gaussian function. From the CCD images we can extract the total atom number and temperature both in the MOT chamber and in the glass cell.

3.3.2. Nonmagnetic photodiode arrays and amplifiers

The nonmagnetic PDA is motivated by a need to detect light from a linear array of atoms in the extremely well magnetically shielded region of space. Commercial off-the-shelf photodiodes and photodiode arrays contain ferromagnetic materials from connector pins and on-board circuitry, making them unacceptable magnetic field sources. The conventional way to avoid magnetic fields from light detectors is to place them far from the low magnetic field region and direct light to them either through free space when paths are available, or in a light guide which has a limited acceptance angle and can lead to intensity noise from etaloning. When a light source needs to be spatially resolved, a fiber bundle can be used, with all the problems of light guides plus only 50% source area coverage.

Our solution to this problem is the nonmagnetic PDA (Figure 3-11) connected by 2 m long mini-coaxial cables to a set of bootstrapped, low noise, high gain trans-impedance amplifiers (Figure 3-12). The 10 cm long, nonmagnetic PDA contains 25 identical, closely packed single photodiodes modeled on the commercial Advanced Photonix photodiode, 150-25-002D. Due to volatile nature of wire-bonding and die attachment, the entire PDA board, the front surface in particular, is NOT subject to any chemical exposure for cleaning purposes, which could otherwise either damage the PDA or leave unacceptably large leakage currents on the PDA board. Technical details on PDA manufacturing, electric connections and amplifier noise analysis regarding this novel design of separating photodiode front-end and transimpedance amplifiers by a long distance and handling large photodiode/cable capacitances have been published in ref. [7].

Key specifications of the PDA imaging system, which fulfill the experiment's requirement, are summarized in Table 3-2.

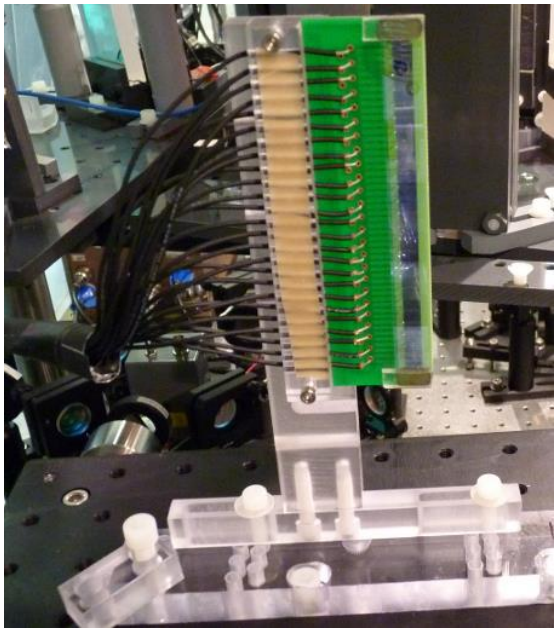

Figure 3-11. The 25-pixel nonmagnetic photodiode array.

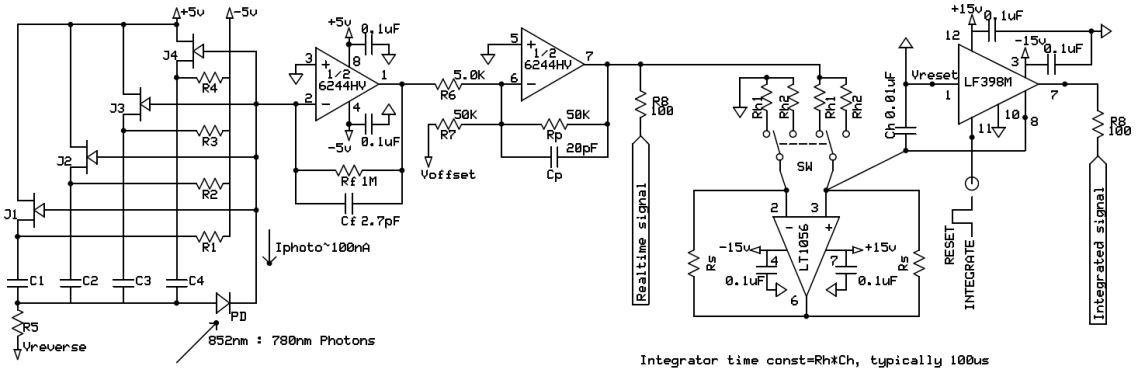

Figure 3-12. One-channel circuit of the PDA amplifier.

To minimize electronic pick-up noises, the 2 m-long coaxial cables and the transimpedance amplifier are completely electromagnetically shielded and grounded to the GND of imaging system, which is ultimately define by the DAQ card analog input ground. The interior and exterior view of the PDA amplifier enclosed by the electromagnetic shielding is shown in

Figure 3-13. The convention for connecting the mini-coaxial cables to amplifier input channels can be found in Appendix-C. A 11" x 7" motherboard capable of holding 56 identical amplifier channels (including 6 spare channels) reorganize the PDA signals to a 100-pin interface that can be directly connected to commercial DAQ card, National Instruments part # PCI 6071E.

Nonmagnetic photodiode arrays		
Imaging area	92 mm x 4.7 mm	25 pixels for each lattice side
Effective pixel size	3.2 mm x 4.7 mm	
Dead space	13.5%	Gap between adjacent pixels
Dark current	< 2 nA	
Spectral response	0.585 A/W at 852 nm	85.1% quantum efficiency
Transimpedance amplifiers		
Transimpedance	10^7 V/A	10 Mega-Ohms
Volumetric capacity	56 identical channels distributed on 7 PCB boards	
Bandwidth	150 kHz	
Total output noise ($\mu V/Hz^{1/2}$)	10 @ 100kHz (peak), 1.8 @ 10kHz, 1.4 @ <3kHz	
light-equivalent spectral noise	1 $\mu V/Hz^{1/2}$ = 0.17 $pW/Hz^{1/2}$	
Output RMS voltage noise (mV)	0.16 (3.3) for 10 kHz (150 kHz) bandwidth	
Power consumption	25.6 W (for a total of 2072 electronic components)	
Integration/Reset function		
Integration time constant	0.1 ms typ.	10kHz integration bandwidth
Hold Step (Sample/Hold)	-98 mV	
Hold Step noise (successive shots)	< 0.3 mV	
Data acquisition		
DAQ time	50 μs	1 Mega-samples per sec
Analog input type	Serial, arbitrarily programmable channel read in order	
Voltage resolution	12 bit	2.5 V voltage range

Table 3-2. Specifications of the PDA imaging system.

The amplifier has a direct output port with atom signals in real-time and an integrated output, which integrates the real-time signal for a fixed amount of time and can be reset to 0. An example of the integration/reset output for just one amplifier channel is shown in Figure 3-14. The integration with a sample/hold circuit causes a -98 mV hold step, which can be avoided using

a differential measurement, or can be done automatically in all experiments with background subtraction.

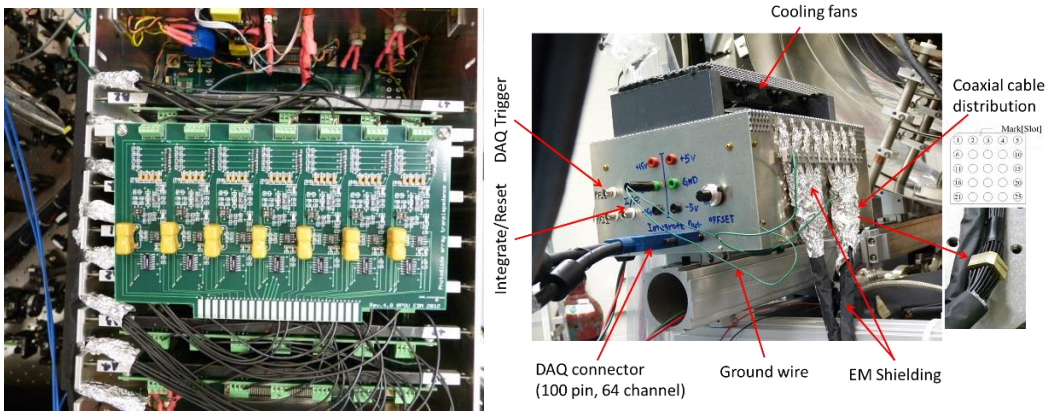

Figure 3-13. The interior and exterior view of the PDA amplifier.

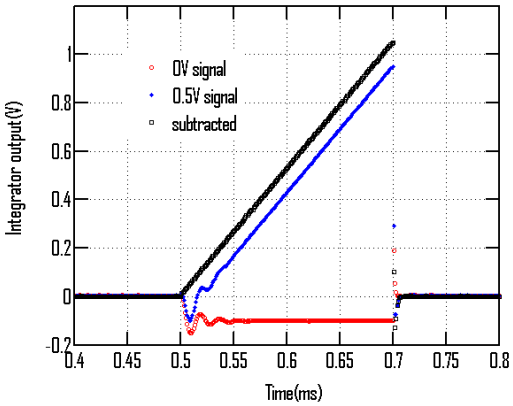

Figure 3-14. The integration/reset functions of the PDA amplifier.

Without atom signal (red), the integrated output shows the dynamics of the Hold Step typically seen in Sample/Hold circuit. A new measurement with nonzero atom signal (blue) leads to a clean subtraction (black) that is linear in time when the atom signal is constant.

The timing diagram for the PDA imaging system is shown Figure 3-15. All signals for 50 channels of the two PDAs (for both +Z and –Z lattice side) are digitized in a serial order in 50 μs. The serial order can be programmed arbitrarily. To this end we have used an alternative pattern between the +Z and –Z lattice side to minimize any possible systematic errors associated with priority of reading in any particular lattice side. The integrated signal is given by

$$V_n = \frac{1}{\tau_n}\int_0^{T+n\cdot\Delta}[s_n(t) + g_n(t)]dt \tag{3.2}$$

With the terms defined as the following:

n: pixel index from 1 to 50. Indices are odd for the +Z side and even for –Z side

τ: integrator time constant, 100 μs

T: probe on time, typically ~200 μs

Δ: time for DAQ to read one pixel, 1 μs

s(t): atom fluorescence signal, which is only nonzero during the probe on time, T

g(t): background signal

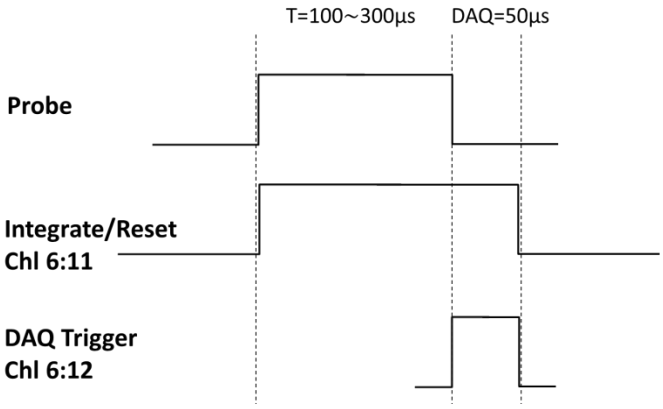

Figure 3-15. The timing diagram of the PDA imaging system.

The background can be subtracted by taking an additional shot without atoms. If the background fluctuates during a measurement, it can be a statistical error source. At this moment the dominate source of background signals comes from the unblocked lattice light diffuse-scattered from the field plate titanium mounting structure. With a more centered structure in the new plate mounting scheme, in particular tilted high voltage cap being fixed, together with an additional 1064 nm filter in front of the PDA, the background from the lattice light should be reduced. Due to the geometry of the measurement chamber, the vertical probe beams do not cause measureable background even at their maximum intensity.

We now estimate the signal to noise ratios (SNR) of our PDA imaging system. From the specifications (Table 3-2), the detector has an overall RMS voltage noise of ~0.3 mV. We used a 10 cm x 3.5 cm Fresnel lens to connect fluorescence light from the atoms. The averaged signal size per pixel is 0.5 V for 0.3 ms integration time (Chapter 4, section 4.3) and total atom number $N_A = 5 \times 10^6$. This leads to a SNR~1.7x10^3. An increase in total atom number will increase the SNR linearly. In comparison, the atom shot noise per group (for effectively 10 subgroups) limited SNR is 7.1x10^2 for $N_A = 5 \times 10^6$ and 2.2x10^3 for $N_A = 5 \times 10^7$.

3.3.3. Transfer function of the imaging system

The imaging quality of the PDA system with a Fresnel lens set (10 cm x 3.5 cm collecting area with effective focal length f =3.3 cm) has been measured in-situ with atoms. We begin by preparing Cs atoms in F=3 hyperfine manifold, which can be done by first optically pumping laser cooled atoms to the dark state |F=4, m_F=+4> and then transferring them to |F=3, m_F=+3> using a microwave AFP pulse (Chapter 4). We then turn on a σ^--polarized vertical probe beam that is resonant with $F = 4 \rightarrow F' = 5$ optical transition and cover all the trapped atoms in the measurement chamber, and a 2 mm diameter, σ^--polarized horizontal repumping beam that is resonant with $F = 3 \rightarrow F' = 4$ optical transition and only selectively illuminates a 2 mm section of atoms, and collect fluorescence signals from the 2 mm spot with the PDA. We repeat the procedure from shot to shot while translating the vertical location of the horizontal repumping beam on a translation stage to map out the entire atom distribution, the result of which is shown in Figure 3-16.

Signal sizes measured by the PDA from a horizontal repumping beam at various locations from H=14.6 cm to H=19.0 cm is shown in Figure 3-16 and analyzed in Figure 3-17, from which we have built the transfer function matrix of the imaging system (Figure 3-17 (b))

and calculated the spatial distribution of atoms over a vertical distance of 5 cm (Figure 3-17 (d)). In comparison, the imaging matrix for an ideal imaging system with 1:1 conjugate ratio is an identity matrix. Due to the poor quality of the existing Fresnel lens set, which is particularly severe for objects that are more than 2 cm away from the center of the lens, each 2 mm section of illuminated atoms results in an approximately 2 cm (5 pixels) image on the PDA with a characteristic long tail (see Figure 3-16). This type of optical crosstalk between many nearby pixels makes the imaging matrix singular; therefore it is not feasible to back out the spatial distribution of atoms in the glass cell from an arbitrary PDA signal distribution.

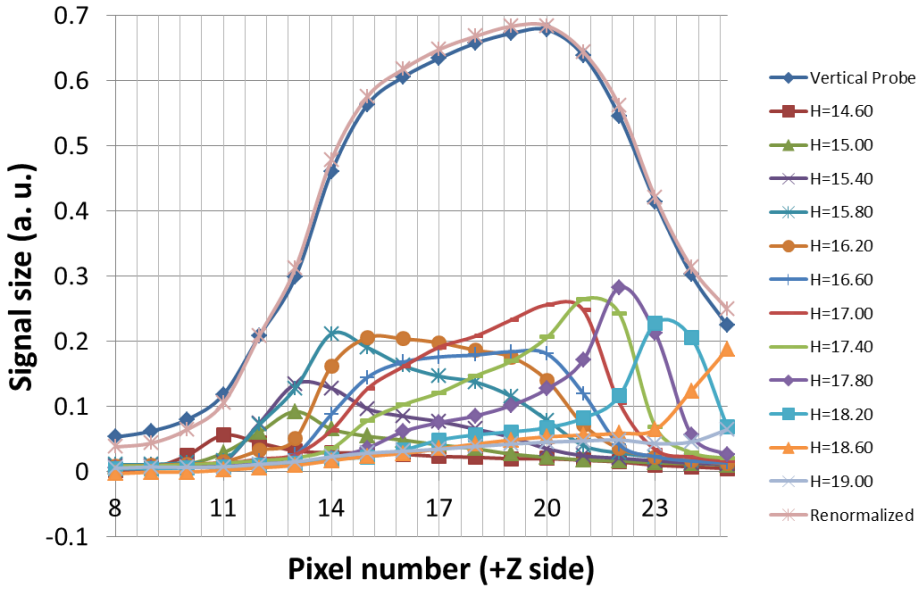

Figure 3-16. Raw data for mapping atom distribution to a PDA image.

Signal sizes measured by the PDA from a horizontal repumping beam at various locations from H=14.6 cm to H=19.0 cm. The raw data is analyzed in Figure 3-17.

An upgrade of the imaging lens is tested in progress by Cheng Tang. Given the very tight space constraint imposed by the cooling optics neat the glass cell, an immerging solution is to replace the large Fresnel lens set with two smaller, Cooke triplet lens vertically mounted on top of each other. The improvement should lead to an image RMS spot size of a point source that is

better than the vertical resolution of the PDA (3.7 mm) by effectively imaging atoms closer to the center of the Cooke triplet lens, at a manageable cost of ~50% decrease in collection efficiency.

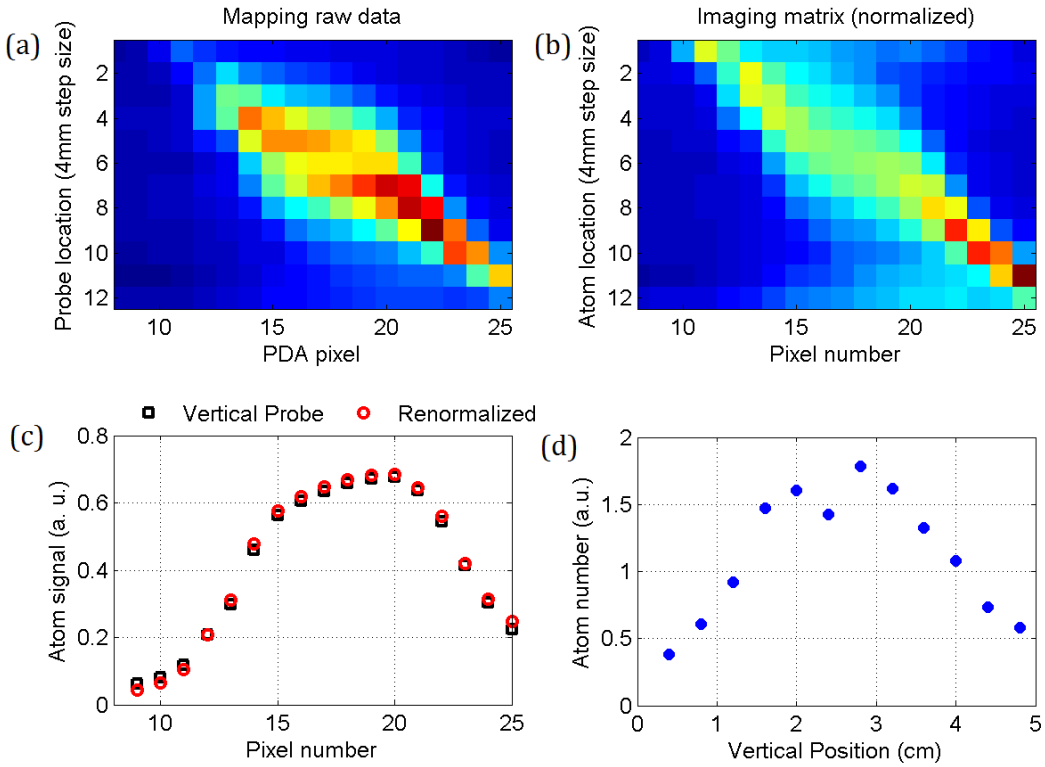

Figure 3-17. The transfer function of the PDA imaging system.

(a) Raw data from Figure 3-16, replotted in a matrix format. (b) The imaging matrix from the signal normalized by the total atom number at every measured vertical location. (c) The renormalized curve for all signals integrated over all locations is compared to the direct measurement using a vertical repumping beam that is co-propagating with the probe beam and shows excellent agreement. (d) Atom number (a. u.) as a function of vertical position, which is also used as the normalization vector for the imaging matrix in (b).

3.4. E and B field control

The control of electric fields and magnetic fields are central to the eEDM measurement. In our experiment, the large DC electric field E is generated by applying a high voltage $V_{max} = \pm 60\ kV$ to the field plates which are separated by a distance $d \approx 4\ mm$

$$E = \frac{V}{d} \tag{3.3}$$

The technical challenges regarding the design and high voltage tests of the electric field plates have been well addressed in Chapter 6 of Dr. Solmeyer's dissertation [6]. In this section, I will describe servos to precisely control and reverse the high voltage V (section 3.4.1) to an absolute level of $\leq 0.3\ V$, and a broadband laser interferometer to measure the separation d of the electric field plates (section 3.4.2) to an absolute level of $116\ nm$. With the precise knowledge of V and d we expect the DC electric field E is controlled to within $30\ ppm$ fractional uncertainty.

We use 4 layer mu-metal magnetic shields to passively shield the science chamber from environmental magnetic fields, and 8 sets of magnetic coils (3 biases and 5 gradients) to actively cancel out the residual magnetic fields in the science chamber, using trapped atoms as a precision magnetometer (Chapter 5). The mechanical design and characterization of the magnetic shields and magnetic coils are described in Chapter 4 and Chapter 5 of Dr. Solmeyer's dissertation [6], respectively. I will discuss the degaussing technique in section 3.4.3, which helps eliminating the remnant magnetization of the magnetic shields whenever mechanical changes have been made (i.e. shield mounting). I will then briefly introduce and summarize two types of currents sources for the 8 sets of magnetic coils, and electro-mechanical switching with high electric-isolation between these current sources in our experiments. The degaussing and current source switching techniques have been used in atomic magnetometry experiments (Chapter 5).

3.4.1. High voltage stabilization and perfect field reversal

The high voltage servo is necessitated by stringent requirements of the experiment: first, the high voltage must be stable within each measurement shots, or namely over a few seconds free evolution time; second, the high voltage must be stable and nearly perfectly reversed from

shot to shot to enable common mode noise cancellation (see section 2.2). The initial setup of the high voltage system did not meet the requirements, due to insufficient dynamic voltage regulation of the high voltage power supplies (Glassman High Voltage Inc., part # EH60P1.5 and # EH60N1.5). Because of lack of fine tuning from the high voltage power supplies, it is also tricky to precisely control the high voltage to sub-Volt levels using just a 10-turn pot with a calibration of 6 kV per turn, or 17 V per degree.

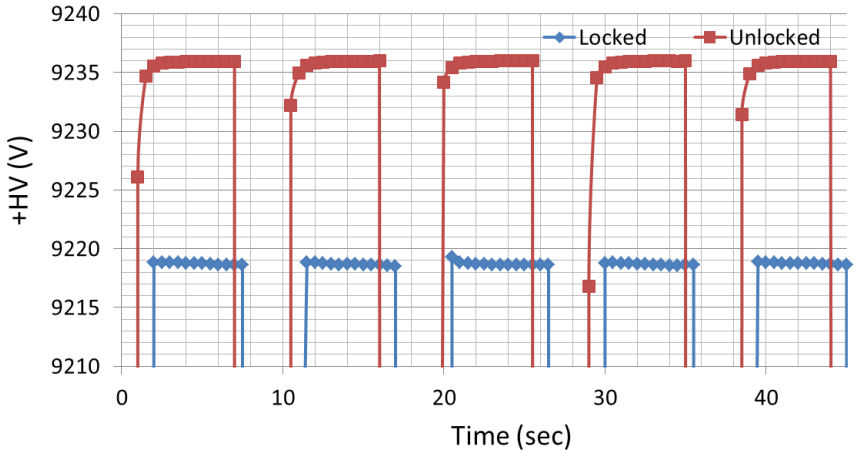

Figure 3-18. The switching characteristics of the high voltage system.
Successive measurements have an interval of 0.5 second, limited the by bandwidth of the DMM.

We measure the high voltage near the field plates using a precision high voltage divider (HVD, Ross Engineering Corp. part # 60-6.2Y-BD-LD-ALBD) and a 6.5 digit digital multimeter (DMM, Agilent part# 34401A). Best effort is made to match the capacitance of the electric path to the field plates and to the HVD, in order to minimize the voltage difference between these two places, which is expected to be smaller than the voltage fluctuations measured on the HVD. The bipolar HVD has an internal resistance of 240 MΩ and two cascaded impedance-matched outputs with dividing ratios 1000:1 and 15:1 respectively, the primary output ($\pm$ 60 V) is connected to the DMM directly and the secondary output ($\pm 4\ V$) goes to the high voltage servo. The complete set of high voltage measurement system, including the HVD, the DMM and impedance matched

cable/connector accessories are NIST calibrated in situ to an absolute fractional accuracy of 8.4×10^{-5}. To maintain the accuracy, users are required to keep the existing setup as it is. Re-calibration should be performed upon part replacements.

An example of the measured positive high voltage is shown in Figure 3-18. During a typical high voltage switching that will be used in the EDM measurement, the high voltage power supplies are always kept on. Using high voltage replays (Jennings Technology, part# RGH5-26S) we can switch to ON/OFF position and switch between two polarities from shot to shot in less than 20 ms. Since our high voltage system has a total capacitance of 1 nF due to 10 m-long coaxial cables and the field plates (see Figure 6-13 in ref. [6]), turning on the high voltage triggers a capacitor charging process, which has a peak charging current of $1\ \mu A/kV$ and a RC time constant of 40 ms. In the free running (unlocked) mode, the high voltage power supplies fail to provide the necessary charging current in a short time and result in a long charging time constant on a time scale of 10 seconds. As a result, 0.5 second after the high voltage is switched on, the charging current is still as large as $50\ pA/kV$ while in comparison the steady state leakage current is typically $1\sim2\ pA/kV$ (see Figure 6-14 in ref. [6]), and the voltage is still $\geq$3 V off with respect to the set point. The long time charging behavior is not acceptable, since it will mimic the leakage current measurements right after switching on the high voltage, and more importantly it is varying during a few seconds-long free evolution time. Using a high voltage lock servo, as we will describe below, we can reach the set point to within 0.3 V in less than 0.5 seconds (see data in Figure 3-18 for Locked mode), which should suppress long term charging current by more than a factor of 10.

Figure 3-19 is a photograph of the high voltage servo, with the corresponding electronic circuit diagram shown in Figure D-1 (Appendix D). The circuit contains 4 major sections: (i) *Precision voltage set point*. This is accomplished by using a 4.096 V precision voltage reference with 1 ppm-level voltage stability and low TCR (thermal coefficient of resistance) 20-

step resistor ladder, which can be selected using a mechanical switch and gives discrete high voltage values at an interval of ~3 kV. The selected reference is then sent to the error signal summing section. In the case of positive high voltage, the selected reference is reversed using a precision inverter, which can exactly match the high voltage magnitudes between positive and negative polarities.

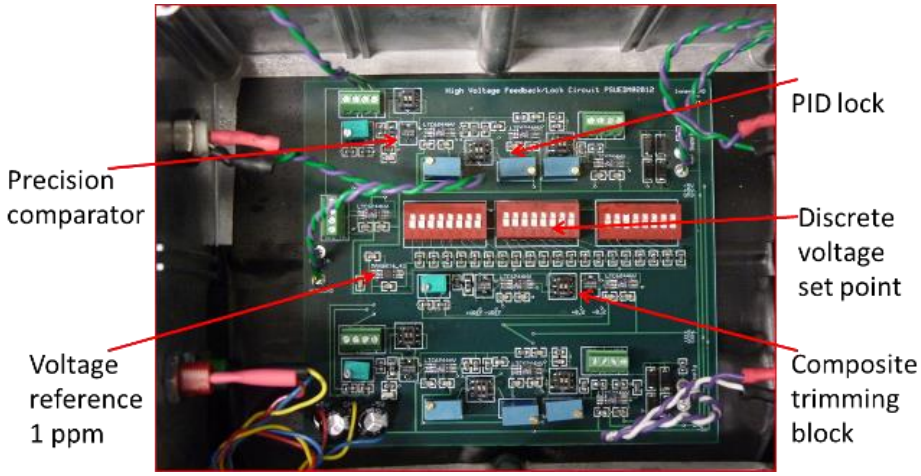

Figure 3-19. The key components of the high voltage lock circuit.

(ii) *Error signal summing section*. On either side of the feedback circuit (positive and negative polarities), we use the sum of the secondary HVD output and the selected reference from step (i) as the error signal. The error signal is then amplified by a factor of 100 using a low noise, offset-trimmed op-amp, with precision balanced resistor network connected to the inputs. The output of the amplifier is sent to a standard PID servo.

(iii) *PID feedback servo*. Three potentiometers are used to adjust PID gain settings.

(iv) *Range limiting servo output with fly-back protection*. The output is limited to $\pm 30\ V$ and is connected to the control interface of the high voltage power supplies (see Figure D-2). The $\pm 30\ V$ "capture range" implies that, if one need to lock the system to a particular high voltage, the front panel 10-turn pot must be adjusted to within 30 V to begin with, which is readily achievable without much effort. When the system is locked to one high voltage polarity, the servo

responsible for the other polarity simply runs into a 30 V rail (5V output from the PID servo). When the system is switched to OFF, both servos run into a 30 V rail.

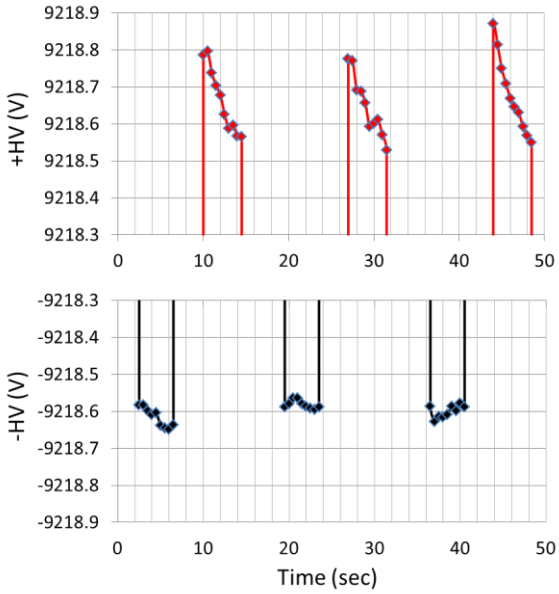

Figure 3-20. Demonstration of a nearly perfect high voltage polarity reversal.

A demonstration of nearly perfect voltage reversal near $|V| \approx 9.2\ kV$ is shown Figure 3-20. The switching pattern is similar to what we will use in a standard eEDM measurement. After the high voltage is switched on, the positive high voltage has an initial overshoot, followed by 10-second-long drift at a rate of $\sim 0.05\ V/s$ and then settles to a steady set point value. The origin of the linear drift has not been identified and understood. The same drift rate also occurs near $+3\ kV$ and $+6\ kV$, suggesting the source is independent of the high voltage set point. The negative side has a much better performance, with less than 0.1 V change in 4 seconds. The variations correspond to a fractional high voltage stability and polarity reversal to within 10 ppm.

Figure 3-21 shows the long time stability of the high voltage system. The absolute voltage stability is about 0.1 V in locked mode (also checked near $+3\ kV$ and $+6\ kV$), which is probably determined by the μV-level voltage drift in the voltage reference of the servo. The high voltage drift in the free running mode is about 3 times worse.

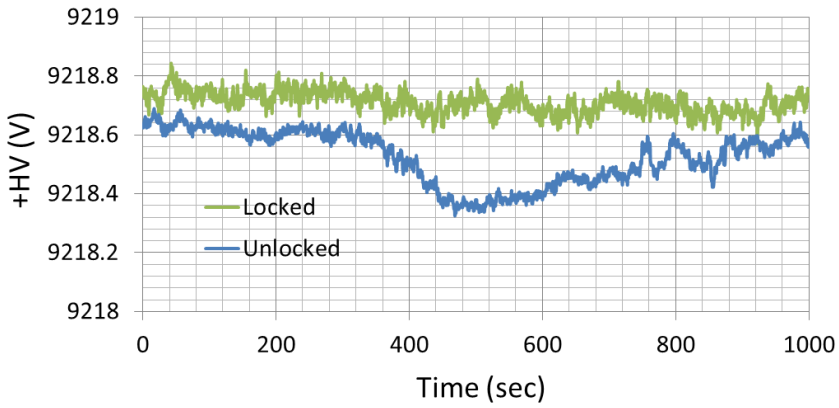

Figure 3-21. Long term drift of the high voltage system.

3.4.2. Interferometric measurements of field plate separations

Interferometric measurement of the field plate separations in situ provides precise knowledge of the DC electric fields for the eEDM experiment, which will be used to calculate the quadratic Stark energy structure and will also be used to extract the EDM (section 1.2, Chapter 1). Spatial inhomogeneity of the DC electric fields leads to shift of atoms in the optical lattices when the electric fields are not reversed perfectly. This becomes a systematic error source in the presence of magnetic field gradients (section 7.2.2, Chapter 7). Gradients of the DC electric fields can be used to estimate the tolerances of magnetic field gradients.

3.4.2.1 Principle of the broadband interferometer

We use a broadband Michelson interferometer [8, 9] to measure the ~4mm distance between field plates (Figure 3-22). The broadband laser (O/E Land Inc., part # OEBLS-200) has a wavelength centered at $\lambda_0 = 830\ nm$ and a FWHM of $\Delta\lambda \approx 50\ nm$, which gives a coherence length of

$$L = \frac{\lambda_0^2}{\Delta\lambda} \approx 14\ \mu m, \tag{3.4}$$

or equivalently an interference envelope with a FWHM of about 34 fringes. The beam from the broadband laser (red lines) is shown in Figure 3-22, which passes through an auxiliary beam splitter and is sent to the glass cell - field plate structure. The wave-fronts of the reflections from the inner surface of a ground plate (G) and the nearby high reflection surface of the center plate (V) are separated by d, which is the distance we are trying to measure.

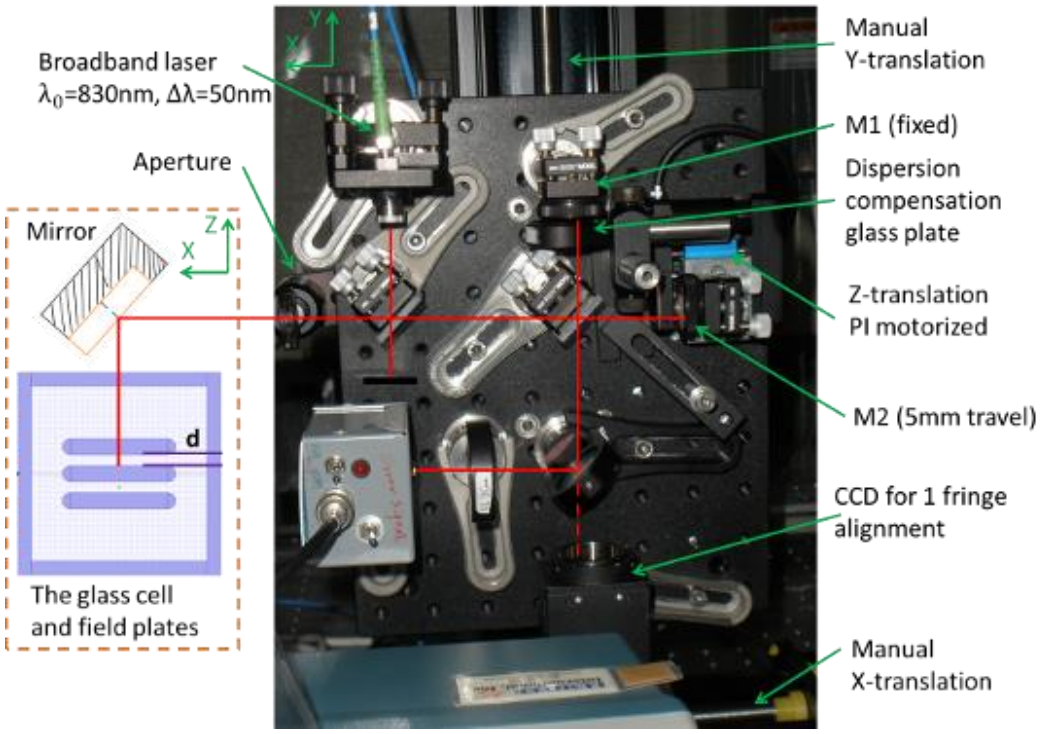

Figure 3-22. The white light interferometer for plate separation measurement.

Note both the side view of the interferometer (X-Y plane, right) and the top view of the glass cell-field plates structure (X-Z plane, left) are rotated by 90 degrees with respect to each other and drawn on the same plane for convenience. The compact interferometer is mounted on a Velmex manual translation stage (X and Y translation) to cover the regions of interest of the field plates.

The reflected beams (G and V) first go through the auxiliary beam splitter and are then separated by the primary beam splitter of this broadband laser interferometer, creating two sets of wave fronts on the two interferometer arms, (G'/2, V'/2) and (G"/2, V"/2), as shown in Figure 3-

23. The mirror on the first arm of the Michelson interferometer M1 is fixed in position, and the mirror on the second arm is mounted on a precision motorized micro translation stage (Physik Instrumente GmbH, part # M-110.1DG). The translation stage has a maximum travel range of 5 mm and minimum incremental motion of 50 nm. The wave-fronts from the two arms are then combined by the primary beam splitter and the interfering signals are recorded by a photodiode. To maximize the interference signal size, we first use a CCD camera (Figure 3-22) to align the interferometer so that there is only approximately half a fringe across the entire output beam (either bright or dark) and then collect all the output light with a lens.

With the broadband laser input, interference fringes can merge only when the separation of the interfering wave fronts is comparable to or less than the coherence length ($14\ \mu m$). When we translate the mirror M2, there are three positions [8] when interference fringes are observed (Figure 3-23): the position at which (i) G"/2 overlaps with V'/2; (ii) G"/2 overlaps with G'/2, and simultaneously V"/2 overlaps with V'/2; (iii) G"/2 overlaps with G'/2. Given the limited range of the precision translation stage, we use the position (ii) and the position (iii), which from now on are abbreviated as d0 and d4, respectively, to measure the plate separation, d=d4-d0.

The reflection coefficient from the center (ground) plate is about 99% (1%) at 830 nm. Thus the fringe contrast at the d4 position is only about $\sqrt{0.99 \times 0.01} \approx 10\%$ of that at the d0 position. Reflections from two surfaces of the fused silica glass cell (thickness $a = 5\ mm$) do not interferer because of the fused silica dispersion, which leads to an extremely low contrast [8]

$$\Gamma_{max} = exp\left\{-\pi\left[\frac{a}{\lambda_0}\frac{dn}{d\lambda}\Delta\lambda\right]^2\right\} \approx e^{-310} \tag{3.5}$$

Similarly one can also verify that reflections form the two sides of the ground plate do not interferer as well. Interference could occur from the inner surface of the glass cell and outer surface of ground plates, separated by about 2.5 cm. Nevertheless, with a 5 mm travel range in the geometric configuration, this does not affect our measurement.

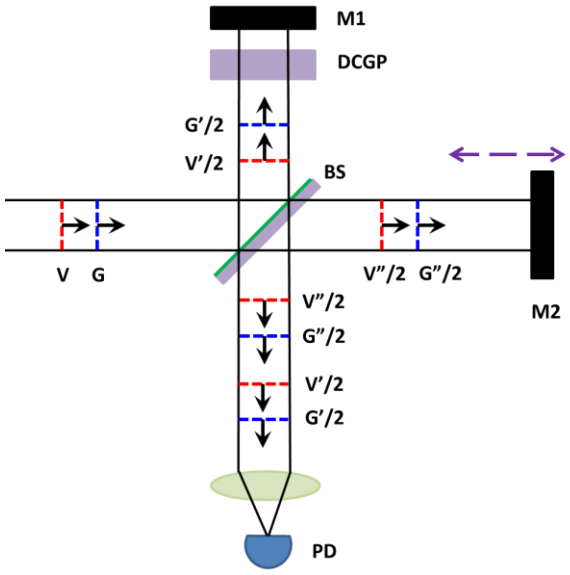

Figure 3-23. Principle of the broadband interferometer.

The wavefront components reflected from a target with two surfaces as they pass through the interferometer. 'V' denotes the wavefront from the surface of the center high voltage plate and 'G' denotes that of one ground plate, as shown in Figure 3-22. The upper surface (green) of the primary beam splitter is the beam-splitting surface and the lower surface is AR coated. The thickness of the dispersion compensation glass plate (DCGP) on the first arm is approximately $\sqrt{2}$ *times the thickness of the primary beam splitter.*

An important feature of our interferometer which was absent in previous designs [8, 9] is the addition of a dispersion compensation glass plate (DCGP), as shown in Figure 3-23. Without the DCGP, the photodiode signal size $I(z)$ as function of the M2 position z follows [10]

$$I(z) \propto \left| exp\left[-\left(\frac{\lambda - \lambda_0}{\sqrt{2}\Delta\lambda} \right)^2 \right] \times \left\{ 1 + exp\left[i \frac{2\pi}{\lambda} \left(z + n(\lambda) \cdot 2\sqrt{2} l_{BS} \right) \right] \right\} d\lambda \right|^2 \tag{3.6}$$

Where the term in front of the multiplier is the laser spectrum and the following term is the interference term; $n(\lambda)$ is the wavelength-dependent refractive index of the primary beam splitter (BK7 glass), which has a thickness of l_{BS}. Because the beam on the second arm (M2) goes through the primary beam splitter effectively 3 times, while the beam on the M1 arm only goes through once, the dispersion of the beam splitter leads to an asymmetric interference envelop that

could complicates data analysis and limit our ability to reliably find the center of interference fringes. Using a $\sqrt{2}l_{BS}$-thick DCGP made of the same material (BK7) as the primary beam splitter, the dispersion on the two interferometer arms can be compensated and the resulting interference envelops are symmetric around the center.

An example interference data set for a d4 measurement is shown Figure 3-24 (a), where we plot the photodiode signal (offset-subtracted) as a function of time, as we scan the position of the mirror M2 at a speed of 0.2 mm/s. The fringes for a d0 measurement are similar to that of d4 except the amplitude is approximately 10 times larger. The maximum and minimum of the interference envelops are well fit to Gaussian functions, as indicated by Figure 3-24(c) and (d). A scan without the DCGP will result in a fitting residual function that is an odd function around the center, in contrast to the plot like Figure 3-24(d). In our compact interferometer, the addition of the DCGP gave confusing measurement results at an early stage of the experiment, because the distance between the DCGP and M1 (Figure 3-23) is 4.2 mm. Now that we have identified the source, it no longer affects our measurement of d~4.0 mm.

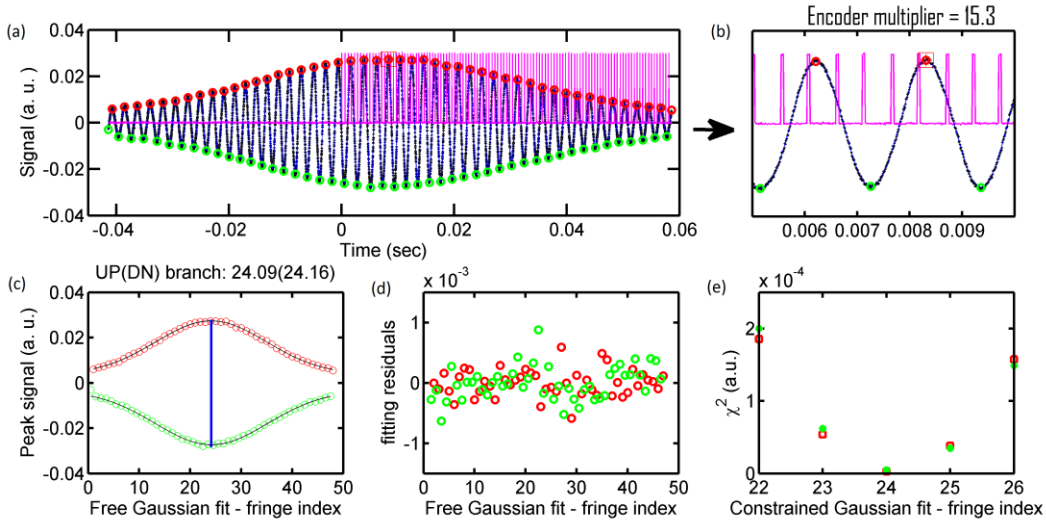

Figure 3-24. Methods to locate the center of interference fringes.

3.4.2.2 Absolute position measurement

We now focus on the methods of extracting the absolute centers of interference envelops which are used for the d4 position measurements. We start by resetting the translation stage at one end, and scanning toward the other end. The translation stage has a <100 nm error accumulated over a full distance of 5 mm travel and a minimum incremental motion 50 nm. The scan in all cases is unidirectional to avoid ~2 μm backlashes. The scan speed is typically between 0.2~0.5 mm/s to ensure that the travel speed is constant across an entire interference envelop, which contains a total of ~70 fringes. Each fringe separation is approximately $\lambda_0/2 \approx 415\ nm$.

The translation stage can be programmed to send out encoder clicks which represent the absolute position of the stage in real time. We command the stage to send out one click every 103 nm, which is about a quarter of a fringe. The minimal encoder resolution is ~6.85 nm. An example of encoder clicks for a typical d4 scan is shown in Figure 3-24 (a) (magenta lines), with a center zoomed in version shown in Figure 3-24 (b).

Both the interference signals and encoder clicks are recorded by a 4-channel oscilloscope (Tektronix, part # TDS3014B). The encoder clicks are first broadened by a digital delay generator (Stanford Research Systems, part #DG535) before being sent to the oscilloscope. We then run numerical algorithms written in MATLAB to locate the center peak of the interference envelop (Figure 3-24 a-e). From the analysis of the phase shifts from the mirror (M1 and M2) and the primary beam splitter (BS) surfaces, we conclude that the interference signal should be constructive when the wave-fronts from the two interferometer arms are perfectly matched. We run a peak/valley search to identify all recorded fringes, and perform a local quadratic fitting to find the exact time stamp and amplitude for each peak/valley, which are marked as circles in (a).

We perform two types of Gaussian fits to the interference peaks and valleys as a functioned of fringe index: the first type is a center-free Gaussian fit (c) to find the center index

(note the Gaussian fits to the valleys have been offset by 0.5 fringes), which gives 24.09 and 24.16 from the peak (UP) and valley (DN) branches, respectively. The second type is a center-constrained Gaussian fit (e), where we fix the center of the Gaussian to an integer (again, offset by 0.5 for the valley branch) and plot the fitting χ^2 as a function of fringe index. The center-constrained fit also gives a best fit at fringe index 24.

Finally we mark the time stamp of the 24th fringe peak and calculate the encoder multiplier for this time stamp (Figure 3-24 (b)) to be 15.3. The measurement for d4 then reads in the following format: $d4 = 4.218474 + 0.000103 \times 15.3 = 4.220050\ mm$, where the first term is the absolute position of the first encoder.

Following the above measurement procedure we can measure d0 in a similar way. Figure 3-25 shows 10 successive measurements at a fixed field plate location. Each point is a single measurement. The $\pm 100\ nm$ error bars for d0 and d4 are the maximum error accumulated over a full distance of 5 mm travel according to the manufacturer specifications. The measurements give $d = 4.001882 \pm 0.000029(stat.)\ mm$, as shown in Figure 3-25 (c), and the 29 nm statistical error is smaller than the $\pm 100\ nm$ manufacturer specified error accumulation.

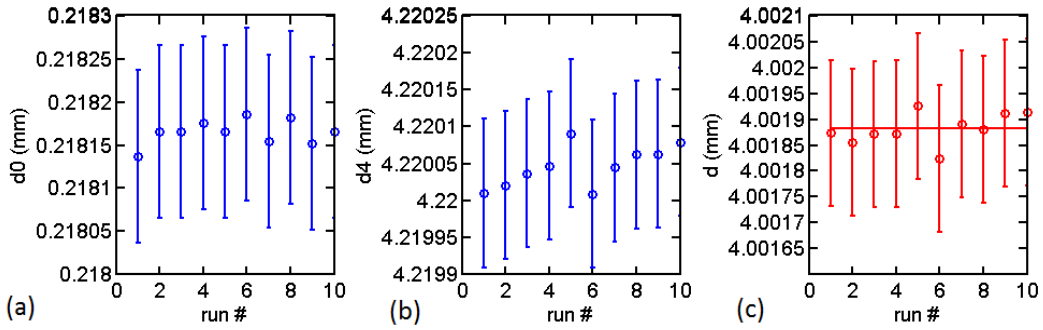

Figure 3-25. Repeatability of the interferometer.

If two-color laser inputs were used for this interferometer (for instance, in addition one combines a 600 nm broadband laser with the 830 nm laser as the input), the center peak could potentially be identified directly without using any numerical algorithm as suggested above,

because the two sets of interference fringes will overlap only at the center peak and start to deviate from each other away from the center peak. Nevertheless, this comes at the cost of an additional laser. Furthermore, at the new wavelength one will start to get reflections from the other lattice side of plates, which is also very close to 4.0 mm and might potentially make the measurement challenging.

3.4.2.3 Speeding up measurements of plate separations

In order to measure the plate separations at multiple locations, we perform a series of differential measurements to map out the differential changes of plate separations. This is motivated by the time-saving nature of differential measurements, as well as the fact that in center regions of the plates the interference fringe contrasts for d4 measurements is demonstrably low by factor of ~2 (potentially due to better AR coating on the ground plates with <1% reflection). The differential measurement contains four steps:

(i) Perform an absolute d0 and d4 measurement using the technique described in section 3.4.2.2 at a plate location where the contrast for d4 measurement is large;

(ii) Start from the location in step (i), move by a small distance to a new plate location at which the plate separation changes less than half a fringe, and perform a short range scan with a typical range of 10 μm. Start first encoder trigger 200 nm before the expected peak position. Such a scan usually starts 8 μm before the expected peak position and end 2 μm after. All scans are in the same direction to avoid backlashes.

(iii) For a new scan, find the position of the first peak after first encoder trigger, by directly reading from the scope using the average position of two zero-crossings around the peak of a fringe. Repeated measurements during this step agree within 30 nm.

(iv) Move the Velmex translation stages (Figure 3-22) along vertical or horizontal directions to cover the regions of interest of the plates. Depending on the spatial wedge of the plates, the step size may vary as one move along to ensure that one always moves less than half a fringe. Test data shows after moving 1 cm horizontally or 5 cm vertically, and come back to the original position and measure the plate separation again after half a day, the answers agree within 50 nm. This is most likely due to temperature dependent drifts.

The measurement traces and results for the two sides of field plates are shown in Figure 3-26 (+Z side) and Figure 3-27 (-Z side). The positions in the graphs are referenced to the center of field plates, which are $1.5 \pm 0.2\ cm$ above and $3.5 \pm 0.5\ mm$ shifted to the –X side with respect to the center of the glass cell. For the +Z side, we have measured 1 vertical and 6 horizontal traces. The vertical trace shows a parabolic bowing of the field plate with a maximum change of 6.5 μm over a distance of 5 cm (27 arcsec). Plate separations for horizontal traces are well fit to linear functions and the maximum wedge along X direction is less than 40 ppm (8 arcsec). For the –Z side, we have measured 2 vertical traces and 3 horizontal traces, which gives a maximum parabolic bowing of 3 μm over a distance of 5 cm (13 arcsec) and a maximum wedge along the X direction of 150 ppm (31 arcsec). The measured separations suggest the field plates marginally meet the 30 arcsec design specifications. A comparison of plate separations between the two sides yields a $18\ \mu m$ maximum difference, which corresponds to an electric field amplitude imbalance of 4.5×10^{-3}. Apart from the $8\ \mu m$ measured parabolic bowing of the plates, we are replacing the glass spacers with precisely characterized and matched thickness (to within $1\ \mu m$) to minimize this imbalance.

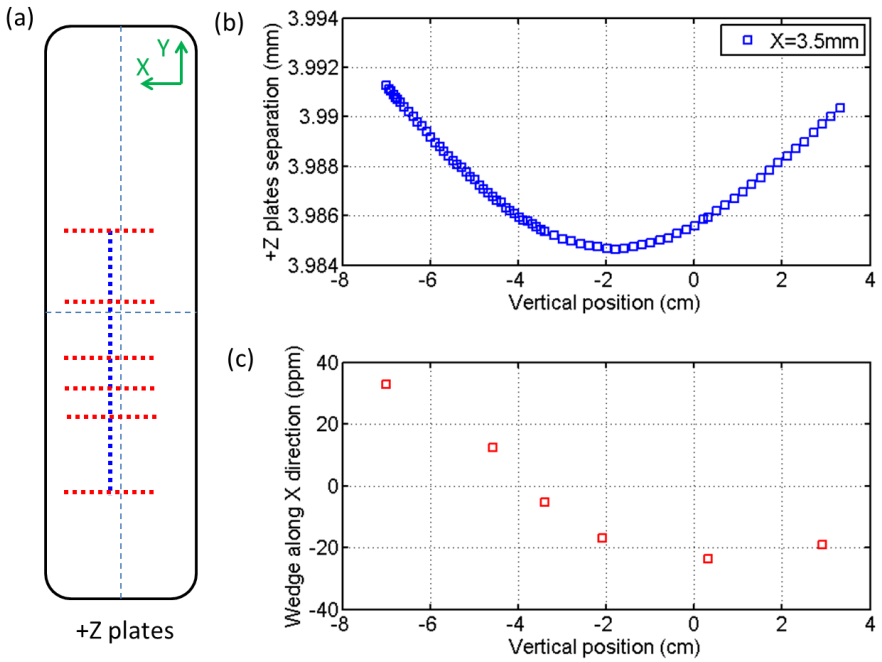

Figure 3-26. Measurement of +Z side plate separation.

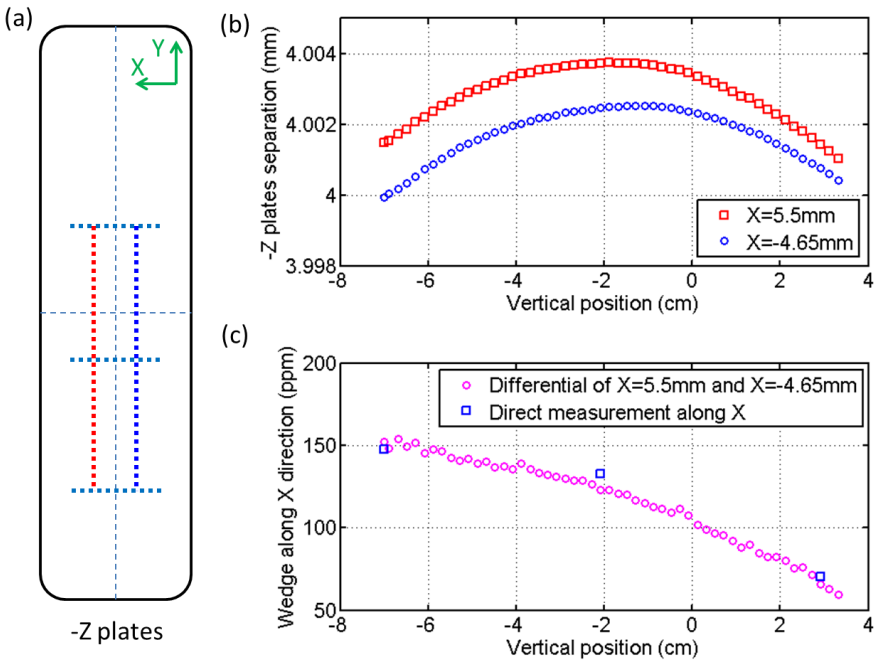

Figure 3-27. Measurement of -Z side plate separation.

3.4.2.4 Calibration and specials issues

We calibrate the interferometer by replacing the broadband laser input with a narrow linewidth ($< 0.1\ MHz$, ~852 nm) diode laser output, which is -2.7 MHz detuned from the Cs $F = 4 \rightarrow F' = 5$ transition. This turns the broadband interferometer into a standard narrow band Michelson interferometer with which we can precisely calibrate the precision motorized translation stage. In this configuration, as we travel over a 4.0 mm distance, we use a counter (LabJack U12 from Dr. O'hara) to count the total number of fringes (~9388) as well as to monitor the starting and ending points. With this technique, we found that the precision translation stage gives distances that are small by a factor of $1.000365(5)$ and gives an absolute error of 1.5 μm over a 4 mm travel. The data presented in Figure 3-26 and Figure 3-27 are plotted after this calibration error was corrected.

Throughout the measurement and calibration procedure we have monitored the temperatures of the glass cell and the interferometer board. The temperature of the glass cell was 23.00 ± 0.03 ℃. Future quotation of the plate separation data should be corrected by the thermal fused silica thermal expansion coefficient ($0.5 \times 10^{-6}\ /K$) if the temperature setting is significantly different from 23.00 ℃. The temperature of the interferometer board is within $22.86 \sim 22.97$ ℃. Given that the two arms of the compact interferometer are only ~5 cm long, the differential temperature drift is < 0.06 ℃. Using the thermal expansion of aluminum ($22.2 \times 10^{-6}\ /K$), we estimate that the maximum differential change in the length of interferometer arms is less than 67 nm.

For the –Z side, it happens that as one moves from the bottom to the top along the field plates, the contrast at d4 gradually decreases, which initially was a serious problem for the measurement. A spatially dependent reflection coefficient of the –Z ground plate is not sufficient to explain a more than a factor of 10 change in contrast. Sample area has been identified to be the

major problematic source. Since we can primarily align the interferometer using the retro-reflection from the center high voltage plate, as one move along the plates, the plate differential wedge is large enough to change the interference fringes across the 2 mm beam. We initially start with half an interference fringe (either bright or dark). A differential wedge along the vertical direction results in 1 or 2 fringes across the beam. When the photodiode averages out the signal across the entire beam, the "contrast" appears very low even if the real interference contrast stays about 2/3 of its original value. The solution is to use an aperture (~1 mm diameter when closed to minimum size, see Figure 3-22), after which d4 contrast only changes about 30% when we move over a 10 cm region. There is about 90 nm systematic error due to this sample area limiting aperture. This can be seen from the –Z plates reference data; the plates separation measured when the aperture is closed is about 90 nm greater than when the aperture is open. Nevertheless, we keep this aperture closed for all measurements and during absolute PI stage calibration with 852 nm laser to minimize this systematic error.

To sum up, accounting for the 30 nm statistical uncertainty of repeated measurements, the <67 nm uncertainty in differential expansion of interferometer arms and the <90 nm systematic error due to this sample area limiting aperture, the total uncertainty of the plate measurements is less than 116 nm, or equivalently a fractional uncertainty of 2.9×10^{-5}.

3.4.3. Magnetic shields degaussing

Because the shields are so easily magnetized, it is usually necessary to degauss the shields whenever they are opened, or whenever the applied internal magnetic field is grossly changed. In our experiment, we use a simple geometric layout for the degaussing coils [11] as shown in Figure 3-28. A rectangular 23-turn coil bundle threads through the 4 layer magnetic shields, carrying a degaussing current waveform as below

$$I(t) = s(t)I_{max}\sin(2\pi f t), \tag{3.7}$$

where $I_{max} \approx 7\ A$ is the peak current which saturates the entire shields completely, $f = 5\ Hz$ is the frequency of the degaussing waveform, and $s(t)$ is the arbitrarily programmable waveform shaping function. The degaussing procedure contains three steps:

(i) Ramp $s(t)$ from 0 to 1 in 100 cycles. Because the degaussing coil is primarily inductive (effectively a transformer), instantaneous turning on a large AC current could potentially damage the degaussing driver electronics.

(ii) Keep $s(t) = 1$ for 100 cycles. At the peak current, the magnetic shields are completely staturated and all local magnetic domains are forced to follow the driven signal. During this step, immense low frequency sound can be heard from the shield end-cap holes.

(iii) Ramp $s(t)$ from 1 to 0 in 1000 cycles. By slowly reducing the amplitude of the applied AC magnetic field, one effective gradually shrinks the area of the shield hysteresis loop to zero, which means the magnetic shields are demagnetized.

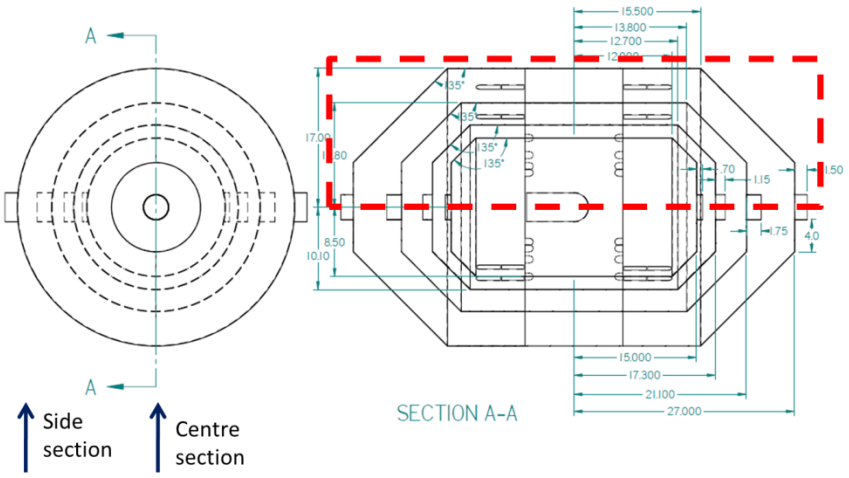

Figure 3-28. The geometric layout of the magnetic shields degaussing coil set.

Side view of the 4 layer shields are shown on the right. Red dashed lines are 23-turn, 0.43 m x *1.45 m rectangular degaussing coils, the applied magnetic fields of which can be calculated using the model from ref. [12].*

We have built a degaussing amplifier as shown in Figure 3-29. The mu-metal shields have a saturation threshold at $B_s = 8000\ G$ and a practical relative permeability of $\mu_r = 15000$ counting all imperfections. The system is over engineered by a factor of 3 in terms of maximum current rating needed to saturate the shields. A critical feature of the degaussing electronics is the 1 Hz high pass filter, which is used to block any small DC offset on the applied magnetic fields and is accomplished a pair of 4 Faraday car audio capacitors and a pair of high performance Schottky diodes for bipolar operation. We have measured the harmonics of the bipolar switching at $2f$, which is 40 dB smaller than the main AC signal at f. Therefore the bipolar switching does not show problematic nonlinear characteristics. When the degaussing waveform output completes, a mechanical switch shorts the BOP amplifier output first, and then the BOP amplifier is powered off. This step protects the magnetic shields from being re-magnetized due to potential current spikes when the BOP amplifier is turned off.

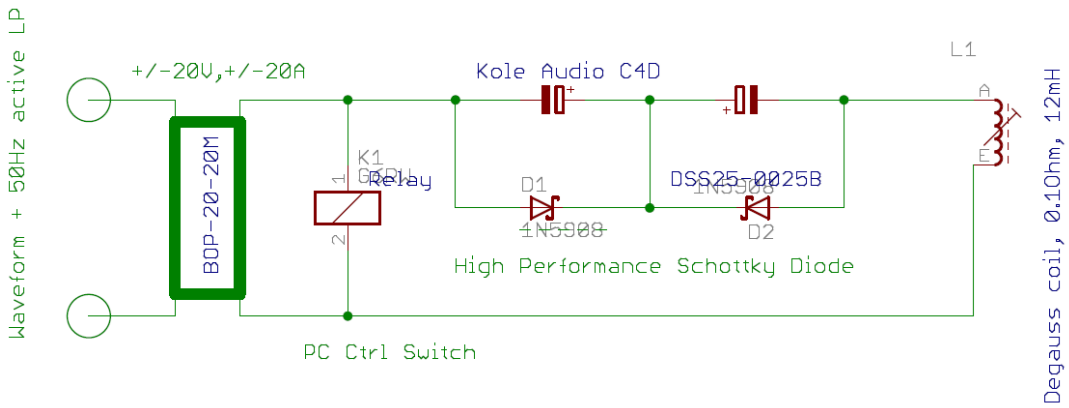

Figure 3-29. The degaussing circuit with 1 Hz high pass filter.

Throughout the degaussing procedure, we use two 1-turn pick-up coils to monitor and make sure the shields are completely saturated. One pick-up coil encloses the inner-most layer and the other encloses the 4 layers all together [13]. An example of the pick-up signals during step (ii) of the degaussing procedure is shown in Figure 3-30. The saturated shape of the pick-up can be understood in the following manner

$$I(t) \rightarrow B(t) \propto I(t), \leq B_s \rightarrow \phi(t) \propto B(t) \rightarrow I_{pkup}(t) = \frac{d}{dt}\phi(t) \tag{3.8}$$

Where the applied current $I(t)$ generates a magnetic field $B(t)$ in the magnetic shields, which is determined by the hysteresis loop and has an upper bound B_s. The magnetic flux enclosed by the pick-coils is $\phi(t) \propto B(t)$, the derivative of which is the pick-up current. Experimentally we observed signal sizes for the two pick-up coils that differ by a factor of 4 approximately.

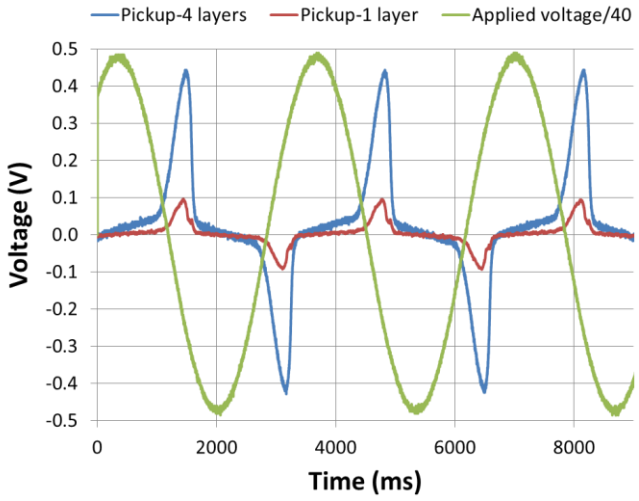

Figure 3-30. The pick-up signal characteristics during shields degaussing.

The magnetic shields after degaussing have a total residual field of ≤ 10 μG in the center region, and an approximately 8 μG/cm vertical gradient from the center of the measurement chamber to the innermost shield hole. Shielding factors are measured as the ratio of the 5 Hz applied external field amplitude over the 5 Hz residual magnetic field amplitude in the center of the shields, which gives 100,000 along z, 35,000 along y and 12,000 along x. Due to the geometry of the magnetic shields, the shielding factors are not always orthogonal. When the applied field is along y, the residue inside is primarily along x. The cross-term is possibly due to the effect of vertical shield holes threaded by the glass cell.

3.4.4. Magnetic coil current control and switching

Two distinct types of current sources are used in the experiment: the first type is a high current version for bias coils (Figure 3-31), which generates typically ~20 mG magnetic bias for optical pumping, microwave state-preparation and state-selective detection. The second type is a low current version for both bias coils and gradient coils, primarily developed by Matthew Ebert [14], with special emphasize on ultralow noise and long term stability. The low current version is used is atom magnetometry and will be used in the EDM measurements, which are very sensitive to magnetic field noises and requires very small field amplitudes (typically $\leq 100\ \mu G$).

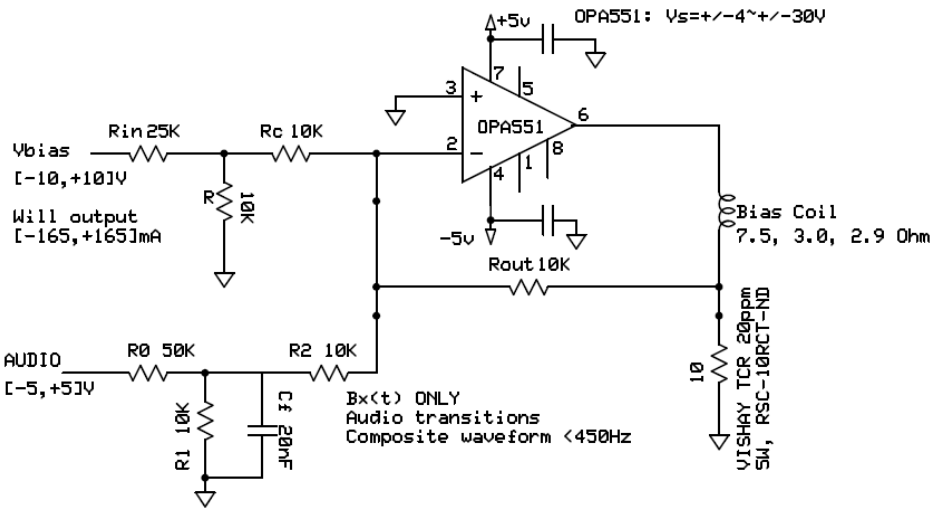

Figure 3-31. The circuit diagram for high current source.

We use 6 Reed relays (Coto Technology part # 8041-05-111) to switch between the two types of current sources (including both the signals and grounds for the 3 bias coils) during the experiment. A reed relay consists of a coil wrapped around a reed switch. The switch is composed of two overlapping ferromagnetic blades that are hermetically sealed within an inert-gas-filled glass capsule. As a result of the $10^{12}\ \Omega$ insulation resistance [15], the two current sources do not have measurable cross-talks. When current flows through the coil, a magnetic field is produced that pulls the two reeds together. This completes a signal path through the relay. When the coil is

de-energized, the spring force in the reeds pulls the contacts apart. The switching characteristics are shown in Figure 3-32, with a typical switching time less than 0.4 ms [15].

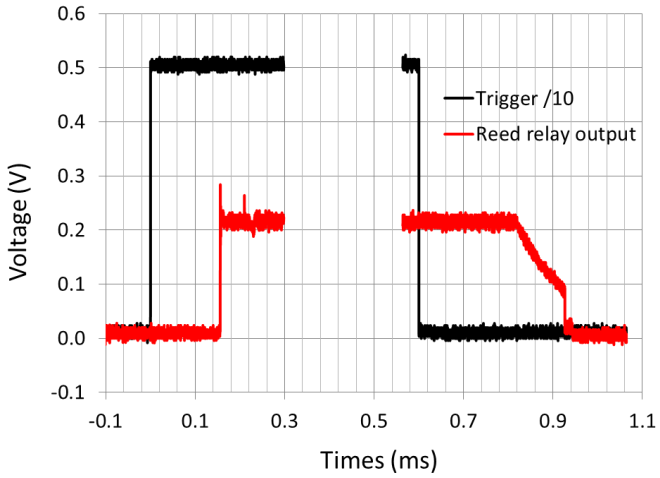

Figure 3-32. The current switching time scales for Reed relays.

3.5. Mastermind control architecture

The complexity of the EDM experiment dictates that essentially all aspects of the experimental operations are computer controlled. We have developed a control architecture nicknamed Mastermind, based on the commonly used timing software Supertime in Prof. Weiss' labs, which was initiated by Akira Villar in 1999, significantly modified by Trevor Wenger, and most recently overhauled by Karl Nelson. The Supertime software incorporates convenient data input and control functions. It is an effective experimental timing program, but the EDM experiment requires more sophisticated control architectures than just a timing sequence, as we will describe in section 3.5.1.

Direct upgrade of the Supertime software to meet our requirements seems a daunting task for two main reasons: first, due to lack of direct conversion of LabVIEW 6.1 (released in 2002) to up-to-date versions (LabVIEW 2012), and more importantly incompatibility of hardware

interfaces (LabVIEW 6.1 is based on NI DAQ and most recent versions are using more advanced NI DAQmx [16]), upgrade of Supertime essentially means significant reworking of Supertime; second, additional hardware needed by the EDM experiment, like the microwave DDS, require real-time control and intensive computation, which may add an extra unsustainable load to Supertime; third, for the ease of the overall EDM experiment control flow, it is more natural to use two separated systems. Mastermind efficiently addresses the technical challenges associated with software upgrade, hardware interface and device integration (section 3.5.2), while the existing Supertime is used as a sublevel of the control architecture (section 3.5.2 and 3.5.3).

The Mastermind software is written in Microsoft Visual Studio® and uses C++/VC++ as the core language. It is equipped with up-to-date hardware interfaces (text-based NI DAQmx) that is free of upgrade hurdles, affords more flexibility than LabVIEW, is more robust in terms of code reuse and sophisticated data structures, and is certainly more appropriate for developing a complicated control and acquisition scheme [17]. The software provides interfaces to Supertime, as well as other commonly used software packages for data analysis and visualization. The compromise is that the development of these systems requires an intermediate to advanced level of programming. From a user's point of view, graphical interfaces built in VC++ provide convenient access. The complexity of the core structure is straightforwardly illustrated with visualization tools provided by Visual Studio® for code developers.

3.5.1. Concept of automatic EDM measurements

The control and data structure of the automatic EDM measurements are illustrated in Figure 3-33. From bottom up, core elements of the 4-level infrastructure are:
(i)SHOT: a single shot of EDM measurement as described in Chapter 2, section 2.1, which includes atom processing, state preparation, EDM measurement, state-selective fluorescence

detection and pre-analysis of the EDM data. Key experimental elements for each step are detailed in Figure 3-33. From SHOT to SHOT, as an optimal measurement strategy for effective suppression of linear drift errors [18], the polarity of the DC electric fields for EDM interaction might be alternated in a pattern as follows (see also Chapter 2, section 2.2.2)

$$\cdots(+E,-E) \rightarrow \Delta B(-E,+E) \rightarrow \Delta B(-E,+E) \rightarrow \Delta B(+E,-E)\cdots \qquad (3.9)$$

Where ΔB is an increment of the bias magnetic field during a SCAN. The electric field is the core element that will be frequently reversed throughout EDM measurements to minimize systematic errors. Many other parameters (such as bias magnetic fields, etc.) also have to be reversed in combination with the electric fields in order to look for correlations among data sets (see examples in ref. [19] and ref. [17]) in the final EDM data analysis.

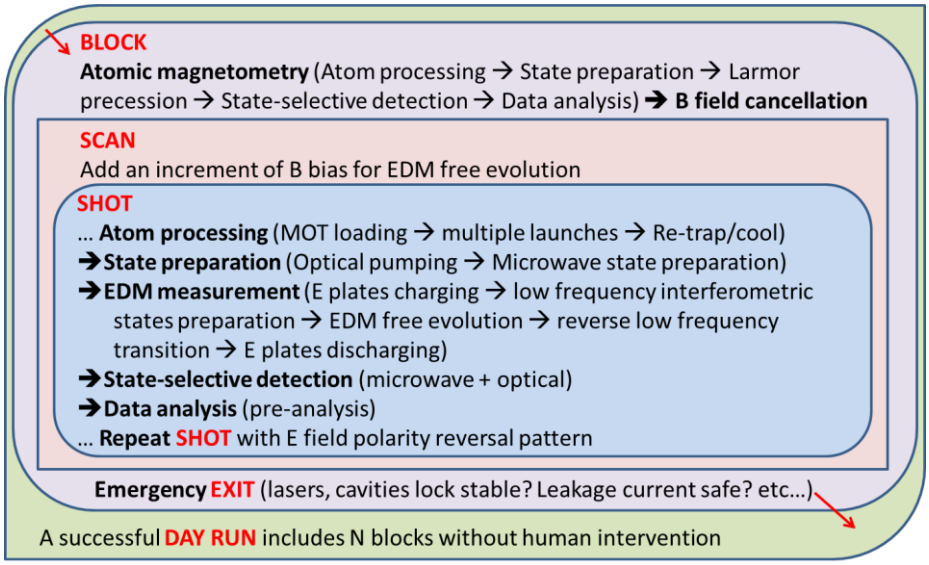

Figure 3-33. The hierarchy of automatic EDM measurements.

(ii)SCAN: a series of EDM SHOTs where the bias magnetic field is scanned (an increment ΔB is added) to build a Ramsey-like interference fringe (Chapter 1, Figure 1-1).

(iii)BLOCK: a BLOCK contains a series of continuous SCANs during which no further magnetic cancellation is necessary. At the beginning of each BLOCK, an atomic magnetometry experiment

(see Chapter 5) is performed to measure and zero the residual magnetic fields in the measurement chamber. As shown in Figure 3-33, many steps of atomic magnetomtery experiments are conceptually identical or similar to that of EDM measurements.

(iv)DAY RUN: a successful DAY RUN contains many BLOCKs without human interruption.

An emergency check runs throughout the experiments to determine whether the experiment can successfully continue. Possible experimental interrupts may include: loss of lock of the Cs lasers and/or built-up cavities (which occurs occasionally once over half a day), leakage currents of the high voltage system exceed a safe level, uncontrolled environmental sources such as power surge, etc. Depending on the nature of an emergency exit, either an automatic or a manual emergency fix can be employed to address the problem and bring the experiment back to normal.

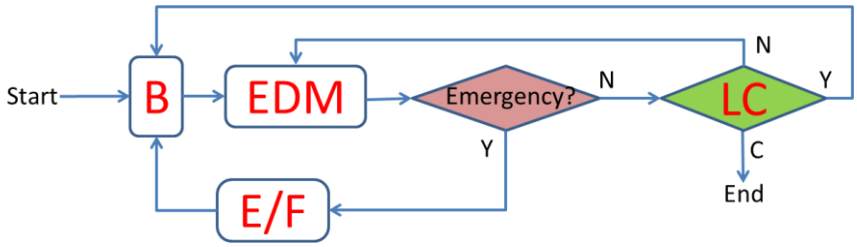

Figure 3-34. Control flow chart of automatic EDM measurements.

***B**: atomic magnetometry to measure and cancel residual magnetic fields; **S**: single shot EDM measurement during a SCAN; **LC**: loop counter; **E/F**: emergency exit and fix; **Y(N)**: if the condition is (not) satisfied; **C**: conditional exit.*

The control flow to realize the 4-level structure of automatic EDM measurements as described above is shown in Figure 3-34. The flow chart is a graphical and miniature version of the Mastermind programming logic for the EDM measurements. A daily entry begins with atomic magnetometry. Once the residual magnetic fields are iteratively nulled, EDM measurements can start. For every single EDM SHOT, an emergency check is performed to ensure that subsequent SHOTs are safe and feasible. An emergency flag might be raised when lasers occasionally jump

lock, or leakage currents of the high voltage system exceed a critical level; in that case a corresponding emergency fix is needed to start the experiment again. Otherwise, the EDM measurement can continue. Depending on the time scale and magnitude of magnetic field fluctuations, a loop counter determines the number of SHOTs after which a magnetometry experiment is needed. The magnetic field measurements not only give critical information for EDM SHOTs performed between two successive counter resets, but also can be used to zero out the residual magnetic fields. The value for the loop counter will be ultimately determined experimentally. The entire control flow stops when data from a desired number of BLOCKs are acquired.

3.5.2. Mastermind control architecture and device integration

To physically realize the 4-level infrastructure of the automatic EDM measurements, the Mastermind hardware architecture is built in corporation with the existing Supertime (documented in the PhD theses of Dr. Wenger, Dr. Fang and Dr. Li from the Weiss group). The new architecture shown in Figure 3-35 is a hybrid of hardware on two computers, Supertime and Mastermind, controlled by LabVIEW and C++ programs, respectively.

The communications between Mastermind and Supertime are achieved with a simple TCP/IP messaging system, the details of which will be described in section 3.5.3. Whenever Mastermind decides what to do next (EDM measurement, atomic magnetometry, or stop), it sends a message to Supertime such that Supertime will load and run the selected timing sequence. When the commanded task finishes, Supertime sends a message back to Mastermind for cross checking.

The Supertime contains a 32-channel digital output (DO) card (National Instrument # PCI-6534) and five 8-channel analog output (AO) cards (National Instrument # PCI-6713). The

DO card controls laser beam shutters, RF and high voltage switches, and triggers for various devices. The AO card controls acoustic-optic-modulators (AOM) for laser beam intensity and frequency adjustments, MOT coil currents, built-up cavity power and lock, etc.

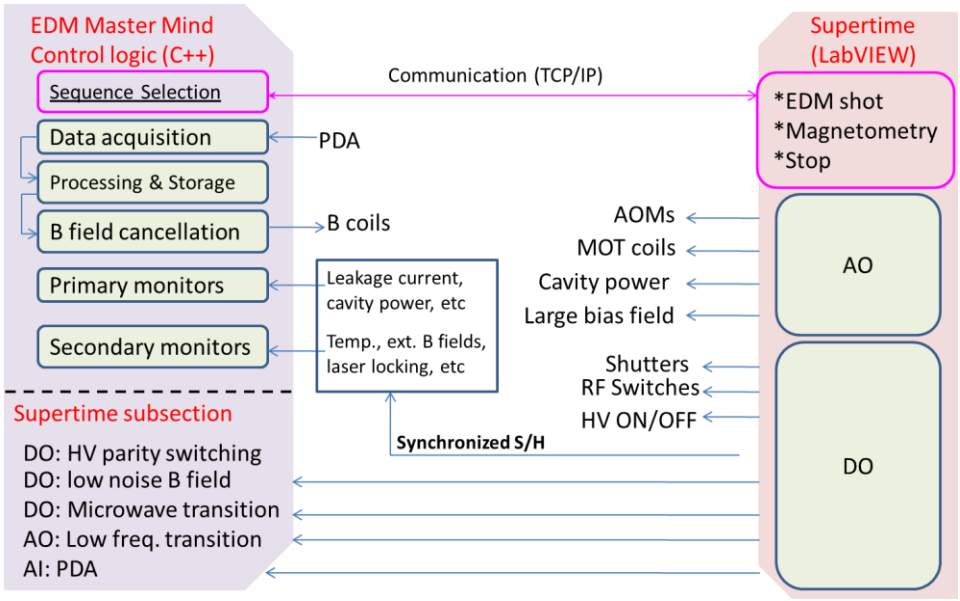

Figure 3-35. Mastermind hardware control architecture and device integration.

The Mastermind has a Supertime subsection which is triggered by Supertime. The functionality of the subsection partially falls in the category of Supertime, but is implemented on Mastermind because of (i) computation intensive work load like real-time microwave pulse control; (ii) convenience of data access from Mastermind, such as the atom signal measured by the PDA which is directly analyzed in Mastermind; (iii) convenience of parameter sweep in Mastermind to avoid the sequence re-calculation downtime in Supertime, such as scanning the magnetic fields; (iv) Limited number of timing edges in Supertime hardware (finite Analog card FIFO size).

The second part of hardware on Mastermind computer is a series of monitors, such as room temperature, which are elements that do not control the experiment directly, but keep track

of the state of the lab. Critical monitors at a particular edge of the EDM measurement (i.e. free evolution) can measure and store data through a sample/hold function (Soft[S/H]).

A full list of existing and functioning devices on Mastermind computer is enumerated in Table 3-3. All the hardware and devices are controlled by Mastermind software using C or C++ based interfaces.

Task	**Device [Interface]**	**Protocol[flow]**	**Trigger**
Timing programmable delay	PCI6601 [PCI]	DAQmx [DO]	Supertime
DDS control	PCI6534 [PCI]	DAQmx [DO]	Supertime
PDA data acquisition	PCI6071E [PCI]	DAQmx [AI]	Supertime
Low frequency waveform	PCI6713 [PCI]	DAQmx [AO]	Supertime
Low noise B field control	USB6501 [USB]	DAQmx [DO]	Software
HV Parity control	PCI6713 [PCI]	DAQmx [DO]	Software
HV Leakage current monitor	pA6485 [RS232]	VISA [DI]	Software
HV Divider monitor	AT34401A [RS232]	VISA [DI]	Software
Temperature tracker	TSci506F [USB]	Excel/libxl [DI]	Software
Cavity power/lock monitor	NI9205 [USB]	DAQmx [AI]	Soft[S/H]
External B field monitor	Optional	DAQmx	Soft[S/H]
Cs laser lock monitor	Atom signal	Data analysis	NA
Atom number monitor	Atom signal	Data analysis	NA

Table 3-3. Hardware on the Mastermind computer.

Data flow in various devices: DO – digital output, DI – digital input, AO – analog output and AI – analog input. Most of the devices are from National Instruments, except the picoammeter (Keithley # pA6485), the digital multimeter (Agilent # AT34401A) and the temperature tracker (Innovative Sensor Technology # TSci506F).

3.5.3. Interactions with Supertime

A cross-platform (C++11 and LabVIEW 6.1) communication link has been built so that Mastermind computer tells Supertime to switch between any of the existing experimental sequences and to loop for any number of times. Assuming both computers have no other internet load, it takes 10 ms to send/receive a sequence select command. Switching between different sequences takes about 1 sec, largely due to data calculation of ~6 sec-long timing sequences in Supertime.

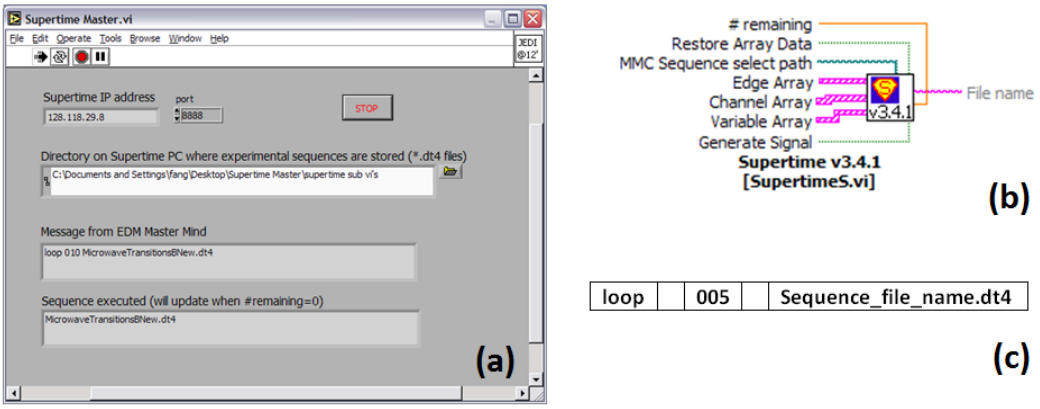

Figure 3-36. Supertime Master messaging system.

A LabVIEW program on the Supertime computer nicknamed "Supertime Master" is the communication medium between Supertime and Mastermind. The front panel of "Supertime Master" is shown in Figure 3-36(a), the underlying program utilizes Supertime as a SubVI ("SupertimeS.vi", Figure 3-36(b)). Upon receiving a message with the format described in Figure 3-36(c), Supertime will select a user-defined sequence (an existing *.dt4 file), loop for a finite number of times and return the sequence name to Mastermind when the sequence finishes output. Due to the complexity of the Supertime program, the detailed modification of Supertime (with step-to-step screen shots) to implement the Supertime Master is not given here, but is posted on the AMO wiki instead [21].

Another important extension of Supertime program is the capability to programmably sweep the time parameter (arbitrary delay between nearby timing edges) in the Mastermind software, just like sweeping any other parameters in the Supertime subsection. This saves time during a parameter scan in Supertime, since it can simply loop the same sequence without recalculation. The implementation is a simple "hack" to the existing timing system as illustrated in Figure 3-37, where we replace the Supertime internal 1 MHz clock with an external, Mastermind-controllable paused 1MHz clock. The start of the "pause" is triggered by Supertime

and the duration of the “pause” is controlled by Mastermind (via a timing card, National Instrument # PCI6601). The minor modification of Supertime to accommodate the time parameter sweep is also documented in details in [21].

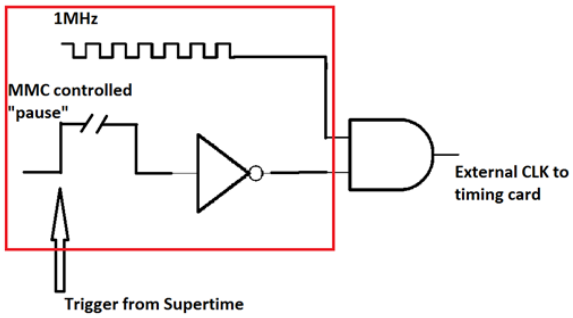

Figure 3-37. Programmable delay of a timing sequence.

3.5.4. Mastermind control software

Mastermind is a C++11-based, user-friendly lab automation software written in Visual Studio to realize the hardware control and data functions described in section 3.5.1 and 3.5.2. The software features:

(i) Adaptive hierarchy to meet variable requirements, in particular, the software is designed to work with multiple formats of atom signals and monitor data acquisitions. Universal functional interfaces enable convenient serialization and parallelization to build up complex control loops.

(ii) Multithreading routines to control hardware. Devices running in parallel (using the new C++11 “pthread” library) on the Mastermind computer (DELL # T3500, quad core, 6GB RAM) fully utilize available computation power and reduce experimental dead time.

(iii) Communications with remote LabVIEW programs (section 3.5.3).

(iv) Data analysis and management with STL and ALGLIB, a C++ based numerical analysis open source with nonlinear fitting packages, matrix toolboxes, etc.

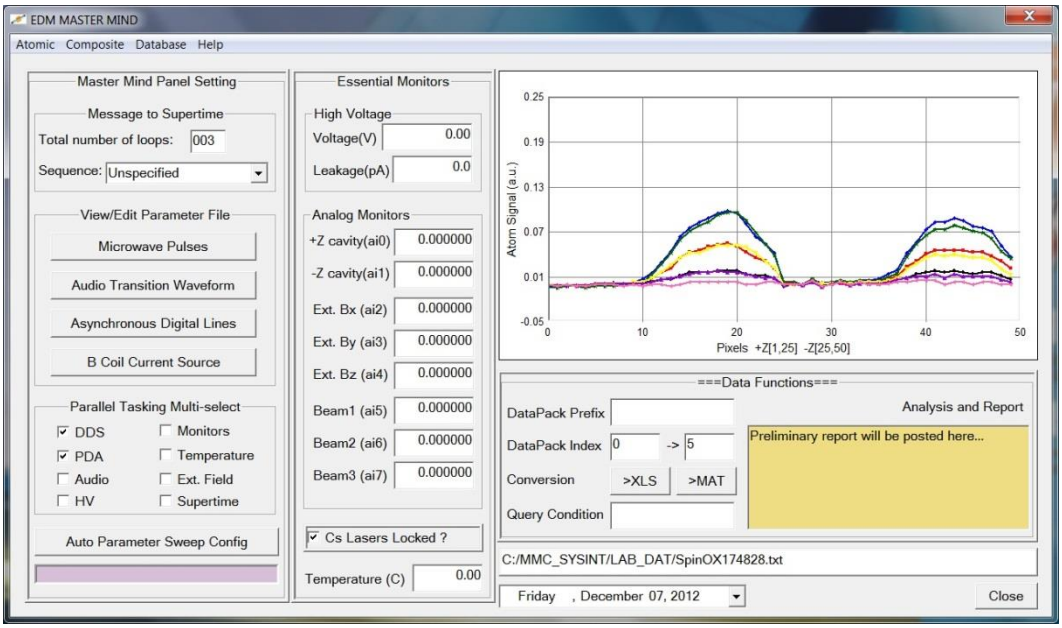

Figure 3-38. Mastermind control software main panel.

The estimated hand-typed C++ source lines of codes (SLOC) for Mastermind software functions is about 12,000 as of July 2013, excluding source code of commercial and open source packages (see “Help” menu in Table 3-4). A full listing of the codes are omitted due to complexity. Two Mastermind software manuals (~22 pages) are posted on the AMO wiki [21], including the user manual describing software functions and menus, and the developer manual on underline software architectures, data structures, and nontrivial algorithms.

The main panel of Mastermind software is shown in Figure 3-38. The buttons in the left column are links to Excel files with experimental settings for various tasks, the middle column displays both essential and non-essential monitor data that we may need to keep track of in real time, and the right panel displays atom signals that are updated for each shot. All experimental data taken for a single SHOT is formatted and packaged as a “DataPack”, the most fundamental data unit for further analysis and query functions (lower part of the right panel). The basic “DataPack” format is a user-defined text file which allows fast I/O operations and can be

conveniently viewed in Mastermind only. When necessary they can be converted in Mastermind into Excel files and/or MATLAB structured arrays.

Data structures built upon a series of "DataPacks" provides direct information of important experimental observables such as atom state population maps and average spins ("SpinPacks") used in atomic magnetometry, which have been transferrable to EDM measurements ("EDMSignalPacks"). Special panels to display and analyze the upper level data are given in Appendix-E.

Menu	Submenu	Function
Atomic	Supertime Communication	Communication via Supertime Master
	Microwave DDS	Calculate DDS data and output μw pulses
	Audio Transitions	Calculate and output low frequency pulses
	PDA Imaging	Data acquisition from the PDA amplifier
	Current Source	Update low noise current sources for B coils
	High Voltage	Measure high voltage and leakage current
	Update Asyn Digital Lines	Set asynchronous lines, i.e. HV polarity
	Analog monitors	Primary and secondary monitors input
	Temperature	Measure science chamber temperature
	1 MHz CLK On	Turn on 1 MHz clock for pause timing
	Pause Timing	Programmable delay of a Supertime sequence
	Hardware Pattern Match	Compare patterns of two NI9205 AI channels
Composite	Parallel Tasking	Test multithreaded tasking of atomic operations
	Magnetometry: Bias Scan	Analyze spin data for a bias scan
	Load/Analyze Spin - Bias	Load/display analyzed spin for a bias scan
	Magnetometry: Grad Scan	Analyze spin data for a gradient scan
	Load/Analyze Spin - Grad	Load/display analyzed spin for a gradient scan
	Spin Sweep Truncate	Truncate the DataPack list for a parameter scan
	Auto Magnetometry*	Stand-alone Auto Magnetometry Loop
	EDM Single Scan*	A single EDM BLOCK
	Automated EDM Block*	Automated DAY RUN with N BLOCKs
Database	Save Panel Data	Save current single shot data to DataPack
	Load Panel Data	Load DataPack to front panel
	DataPack Listing	List analyzed DataPack for a parameter scan
	DataPack Averaging	Load and average multiple DataPacks
	Magnetometry Histogram*	Histogram of B fields for a N BLOCK data set
	Analyze EDM Scan*	Load/Analyze EDM from a single BLOCK
	Query EDM Databases †	Conditional display EDM data among BLOCKs
Help	Source Code	Mastermind Visual Studio source code
	Documentation	Documentation for Mastermind developers

	Protocols – MFC	Microsoft Foundation Classes for Visual C++
	Protocols – Excel Link	Libraries for linking Excel to C++
	Protocols – NI DAQmx	PCI & USB device communication interface
	Protocols – NI VISA	RS232 device communication interface
	Protocols – WinSock	Windows Sockets for TCP/IP communication
	Protocols – NTGraph	Libraries for 2D plot as ActiveX controls
	Protocols – ALGLIB	Libraries for numerical analysis

Table 3-4. Mastermind control software menus.

*All functions (unless otherwise noted) have been implemented and tested in situ in most recent atomic magnetometry experiments. Menu items marked with * have been implemented in software and tested with simulated data. Menu item marked with † has not been implemented.*

Four types of menus are built into Mastermind, the detailed functionalities of which are summarized in Table 3-4. The **Atomic** operations allow one to trouble shoot each device or run any individual hardware related task. A **Composite** selection includes sequential and parallel execution of different tasks in a typical experimental control flow. The **Database** deals with pulling up structured data and post data analysis. Finally, the **Help** links to the Mastermind source code and documentation, as well as various frequently used commercial or open source protocols.

3.6. References

[1] R. W. P. Drever et. al., *Laser phase and frequency stabilization using an optical resonator*, Appl. Phys. B **31**, 97 (1983).

[2] N. Solmeyer, K. Zhu, and D. S. Weiss, *Mounting ultra-high vacuum windows with low stress-induced birefringence*, Rev. Sci. Instrum. **82**, 066105 (2011).

[3] G. N. Birich et al., *Precision laser spectropolarimetry*, J. Russian Laser Res. **15**, 455 (1994).

[4] T. P. Meyrath and F. Schreck, *Digital RF Synthesizer: DC to 135 MHz*, Univ. of Texas at Austin, (2005).

[5] AD9852 datasheet, *CMOS 300 MSPS Complete DDS*, Analog Devices, Inc., (2007).

[6] N. Solmeyer, *Progress toward an electron electric dipole moment measurement With laser-cooled atoms*, PhD dissertation, Penn State University, (2013).

[7] K. Zhu, N. Solmeyer and D. S. Weiss, *A low noise, nonmagnetic fluorescence detector for precision measurements*, Rev. Sci. Instrum., **83**, 113105 (2012).

[8] R. A. Patten, *Michelson Interferometer as a Remote Gauge*, Applied Optics **10**, 2717 (1971).

[9] I. Kozyryev, *Michelson Interferometer Remote Gauge with Sub-micrometer Resolution for the ThO eEDM Experiment*, technical report from the ThO eEDM group, Yale University, (2010).

[10] Z. Hu and A. M. Rollins, *Theory of two beam interference with arbitrary spectra*, Optics Express **14**, 12751 (2006).

[11] B. Heckel, private communication, the Hg EDM group, University of Washington, (2009).

[12] M. Misakian, *Equations for the Magnetic Field Produced by One or More Rectangular Loops of Wire in the Same Plane*, J. Res. Natl. Inst. Stand. Technol. **105**, 557 (2000).

[13] K. Kirch, technical report from the Neutron EDM Collaboration, Paul Scherrer Institut, (2009).

[14] M. Ebert, *Progress towards a measurement of the electron electric dipole moment using cold Cs and Rb atoms in a 1D optical trap*, BS dissertation, Penn State University, (2010).

[15] Data sheet for The Coto 8L Spartan Series relays, Coto Technology.

[16] National Instruments, Inc., see http://www.ni.com/white-paper/8387/en for details regarding conversion between LabVIEW versions and http://www.ni.com/white-paper/4342/en for documentation of hardware interface.

[17] H. Ashworth, *Towards an improved measurement of the electron electric dipole moment*, Chapter 2, PhD dissertation, Imperial College London, (2008).

[18] V. V. Yashchuk, *Optimal measurement strategies for effective suppression of drift errors*, Rev. Sci. Instrum. **80**, 115101 (2009).

[20] J. J. Hudson et. al., *Improved measurement of the shape of the electron*, Nature **473**, 493 (2011).

[21] More details of Mastermind software are available upon request, and can be found under the "Hardware Control and Code Developing" section from the AMO wiki (only accessible in the phys@PSU network)

https://amo.phys.psu.edu/WeissLabWiki/index.php/EDM:EDM_Experiment

Chapter 4

Quantum state manipulation and detection

Microwaves enable quantum state manipulation and state-selective detection of the Cs ground state manifolds. The method of driving magnetic dipole transitions between $F = 3$ and $F = 4$ hyperfine Zeeman sublevels (Figure 4-1) is a widely used for various stages of this experiment, which include state preparation (Chapter 2), atomic magnetometry (Chapter 5) and the final EDM measurement (Chapter 6).

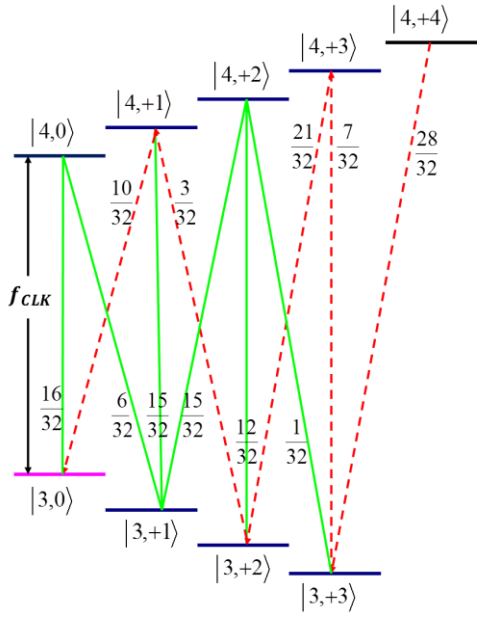

Figure 4-1. Energy levels and matrix elements relevant to microwave transitions.

Only half of the Cs ground state manifold is shown for simplicity. The transition frequency between the clock states is $f_{CLK} = 9.192631770\ GHz$, the current definition of a second. Fractional numbers near each transition line are squared matrix elements [1]. The red dashed path is used for state preparation, and all π transitions ($\Delta m_F = 0$) are used for state-selective fluorescence detection.

Due to the geometric constraints of our science chamber, the microwaves have a complex power distribution, which leads to a large imbalance between Rabi flopping rates at the two

lattice locations. A robust technique, adiabatic fast passage, is then implemented for high fidelity population transfer. With the success of the deterministic microwave spin flop, we have also worked out a clean state-selective detection scheme which provides a complete picture of Cs atoms in the F=3 hyperfine ground state.

4.1. Microwave power distributions

Given the importance of microwave transitions, in this section we perform a systematic study of microwave intensity distributions inside our science chamber. The initial step of the study is to simulate the microwave propagations inside the glass cell structure, which serves as a technical guide as well as a feasibility analysis for physically implementing the microwave system. The final step of the study utilizes atoms as microwave analyzers. By measuring Rabi flopping rates for three fundamental transitions, we can back out the microwave amplitudes and polarizations at the two lattice locations. This in turn helps us to improve the Rabi flopping rates by finding the optimal quantization axis for controlling atoms with microwaves.

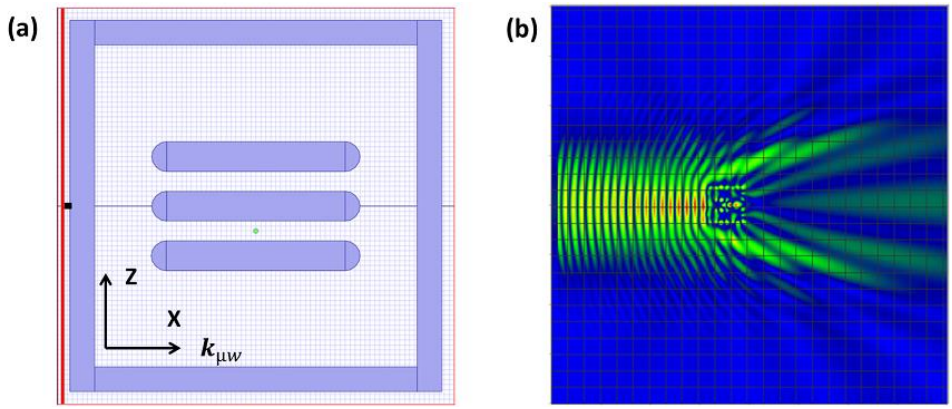

Figure 4-2. Geometric layout for microwave propagation.

3D OptiFDTD simulations of microwave propagation through the measurement chamber, the cross section (top view) of which is shown in (a). The microwaves are sent along x direction for experimental convenience. (a) Central area of interest ($8\ cm \times 8\ cm$*). (b) Microwave intensity map around an area of* $40\ cm \times 40\ cm$.

Figure 4-2 (a) shows the geometric layout of our glass cell/field plates structure. For experimental convenience, we prefer to send microwaves along the x direction. The complexity of the microwave power distributions inside the glass cell can be seen straightforwardly, by comparing the wavelength of the microwaves $\lambda_{\mu w} \approx 3.26\ cm$ to the characteristic size ($\sim 4\ mm$) of the electric field plates. In the microwave frequency band ($9.2\ GHz$), fused silica has a refractive index $n_{fs} \approx \sqrt{3.82}$ [2] and a skin depth $\delta_{fs} = \sqrt{2/\mu\sigma\omega} \approx 7.4\ km$ [3]. The $30\ nm$-thick [4] conductive ITO coating has $n_{ITO} \approx \sqrt{3.8}$ [5] and $\delta_{ITO} \approx 20.3\ \mu m$ [6]. Thus the glass cell structure as a whole is an object with refractive index ~1.95, which leads to significant reflections and refractions, with negligible absorptions.

We use the commercial software OptiFDTD [7], a 3D photonic product from Optiwave Systems Inc., to simulate microwave propagations near the sub-wavelength structure. Figure 4-2 (b) is an example of the field distributions for a computed area of $40\ cm \times 40\ cm$. The glass cell has an area of $7.5\ cm \times 7.5\ cm$, shown in the center. In our experiment, the rectangular microwave horn antenna is placed approximately $25\ cm$ away from the center of the glass cell, which can be considered as a point source in the far-field limit. The antenna has a 3dB beam-width of 64^o in the E-plane and 28^o in the H-plane [8], which covers the two $10\ cm$-long atom pancake stacks with 1 cm separation. Along the vertical direction, the microwave power variation is less than 8% over a distance of $10\ cm$. Therefore, the simulation problem can be approximately reduced to 2D (x-z plane) with translational invariance along the y direction. Furthermore, from comparison of simulated intensity maps, we find that the microwave intensity distributions are primarily determined by the field plates' structure, regardless of the geometry of the radiation source, i.e., whether we use point sources or plane waves.

Figures 4-3 (a) to (c) show the microwave field amplitude maps in the central regions of interest when the antenna is orientated in the transverse-electric (TE) mode. In the TE

configuration, the microwave electric field is along y direction (the direction of the field plates). With reflections and refractions there are two microwave magnetic field components, H_x and H_z. A clear feature from the field maps is the microwave lensing due to the field plates, which results in field maximum (and minimum) spots with a characteristic size of a few millimeters. The separations between the field spots along the z direction approximately coincide with the geometry of the field plates. The corresponding field maps for the transverse-magnetic (TM) mode are shown in Figure 4-3(d) to (f). The field plates are a poor waveguide in the TM configuration, where the magnetic component is along y, and the electric fields are in the x-z plane. The structure of the field plates is even more evident, especially in the field map of E_z.

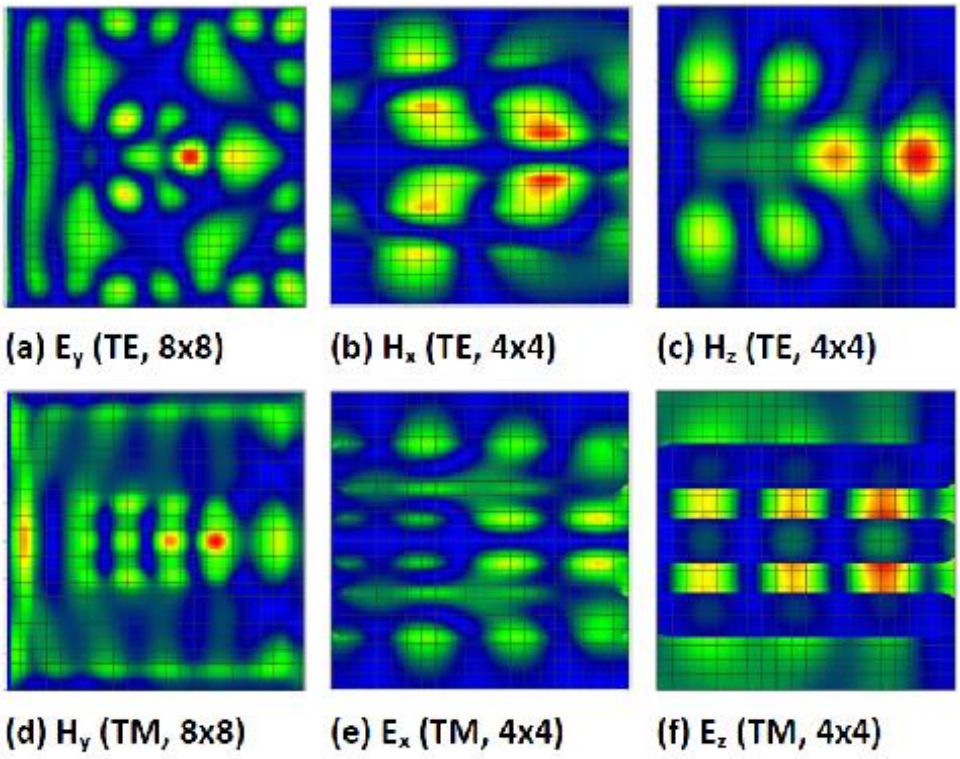

Figure 4-3. Microwave distributions inside the glass cell.

(a) to (c): microwave amplitude map near atoms for the transverse-electric mode, which has an electric field along y, and two magnetic field components in the x and z plane due to reflections and refractions. The numbers in brackets represent a central area of $8\ cm \times 8\ cm$ *in (a) and* $4\ cm \times 4\ cm$ *in (b) and (c). (d) to (f): the equivalence of (a) to (c) for the transverse-magnetic mode. On the false color scale, red (blue) indicates high (low) filed points.*

The microwave magnetic field amplitudes are closely related to magnetic dipole transition rates. Field amplitudes sliced along x direction at locations where atoms are trapped are plotted in Figure 4-4. Comparison of the TE mode (a) and TM mode (b) implies that the former is more robust for spin flips, since in the TM mode the microwave magnetic field amplitude has nearly complete destructive interference near the center ($x \approx 40\ mm$). Given a few-millimeter uncertainty on centering the field plates with respect to the glass cell, the TE mode gives a smaller power imbalance between the two lattice sides.

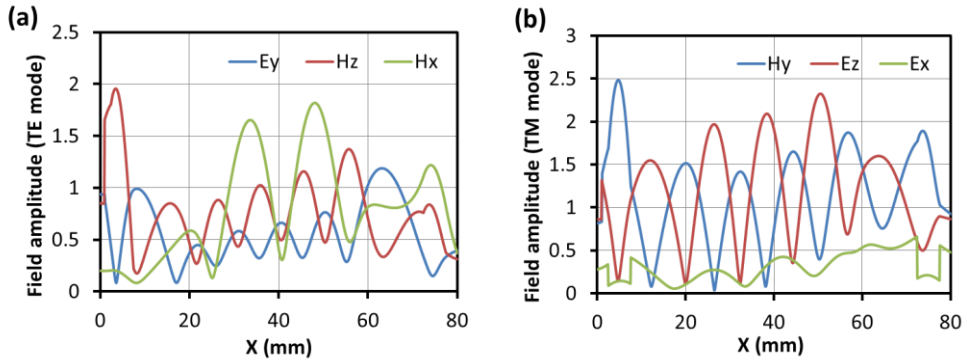

Figure 4-4. Microwave field amplitudes inside the glass cell.

A line cut of field amplitudes along x direction from Figure 4-3. Atoms are located at x=40 mm. For comparison, all field amplitudes are renormalized the corresponding field values at x=0mm (2.5mm before the edge of the glass cell) for free space propagation (without the glass cell/plates structure).

We have measured Rabi frequencies for microwave spin flips in differential configurations. The results are summarized in Table 4-1. In the TM configuration, we experimentally observed a 5-fold difference in Rabi frequencies, or equivalently, a 25-fold difference in microwave intensities. The imbalance is improved by about a factor of 2 in the TE configuration, which qualitatively agrees with the FDTD simulations.

Other constraints also contribute to the imbalance of the measured Rabi frequencies. In particular, a 1 cm-thick fused silica beam-splitter orientated at about 15^o with respect to the glass

cell (see red arrow in Figure 4-5), which is necessary for polarization gradient cooling of atoms in the science chamber, is partially in the way on the –Z lattice side and leads to power loss.

Transition	Location	TM	TE	TE (cut horn)	TE ($\boldsymbol{e} = \hat{\boldsymbol{y}}$)
$\boldsymbol{\sigma}^+$ (3,3)→(4,4)	+ Z	6.0	19.8	13.2	9.5
	- Z	1.2	7.3	10.8	8.0
$\boldsymbol{\pi}$ (3,3)→(4,3)	+ Z		1.2	8.5	8.0
	- Z		2.4	3.3	3.4
$\boldsymbol{\sigma}^-$ (3,3)→(4,2)	+ Z		2.4	1.2	
	- Z		1.2	2.4	

Table 4-1. Measured Rabi frequencies for the three types of microwave transitions.

The listed numbers are in unit of 2π kHz, for instance, as the final configuration (cut horn), +Z lattice side has a Rabi frequency of $2\pi \times 13.2$ kHz for the (3,3)→(4,4) transition. TM stands for transverse-magnetic mode, and TE stands for transverse-electric mode. The Rabi frequencies are measured with an optimal quantization axis $\boldsymbol{e} \approx (\hat{\boldsymbol{y}} + \hat{\boldsymbol{x}})/\sqrt{2}$ unless otherwise indicated. The last column list Rabi frequencies for $\boldsymbol{e} \approx \hat{\boldsymbol{y}}$, which are used in state-selective fluorescence detection.

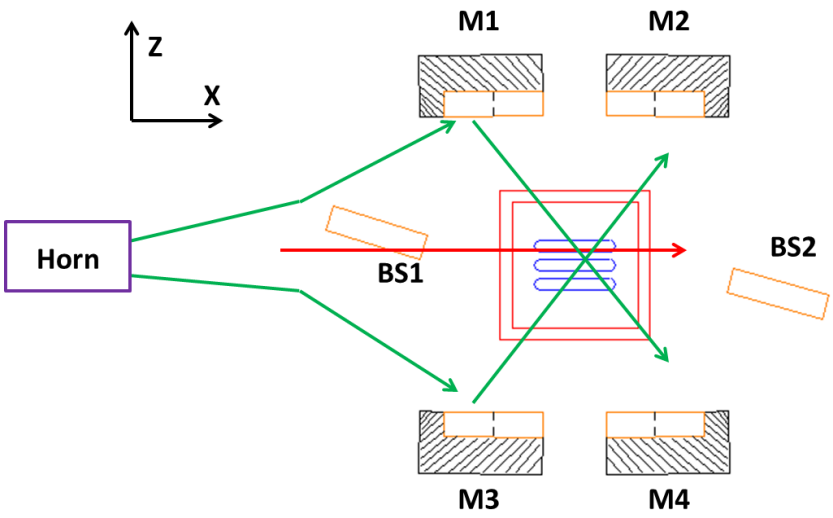

Figure 4-5. Schematic of optical elements in the path of microwave propagation.

The geometric layout is not to scale. M1~M4 are cooling mirrors, BS1 and BS2 are beam-splitters. The BS1 is partially blocking the microwaves on the –Z side (red arrow). When the horn antenna is shortened, the H-plane 3dB beam-width is increased, which reduces the antenna gain, and leads to possible reflection paths (green arrows) for the microwaves to enter along z direction and potentially improves power uniformity.

During the installation of the magnetic shields, we cut the far-end of the microwave antenna by $\sim 20\%$ in length to best fit through the holes on the shield end caps. The cut magically improves the imbalance between the two sides (see Table 4-1). We believe the shortened antenna has a larger 3dB beamwidth, in particular along the z direction (the H-plane). Due to the reflections from the cooling mirrors (see green arrows in Figure 4-5) that can easily go through the glass cell and the field plates without microwave lensing, the uniformity of microwaves between the two lattice sides is improved.

We now move to the final step of the microwave distribution study and focus on the technique of measuring microwave fields using Rabi flopping rates of atomic spins. Cold atoms are versatile tools for microwave field imaging, which are very useful for microwave integrated circuits, which can be used as building blocks for superconducting quantum processors [9]. Using ^{87}Rb atoms trapped on an atom chip, Dr. Theodor Hänsch's group has recently demonstrated 2D microwave imaging with micrometer spatial resolution [10].

In our experiment, due to the approximate translational invariance along the y direction, we only need to measure the microwave fields at the two lattice locations on the x-z plane for the selected TE mode. In general, microwave magnetic fields can be written as $\boldsymbol{B}(\boldsymbol{r},t)=\left[\boldsymbol{B}(\boldsymbol{r})e^{-i\omega t}+\boldsymbol{B}^{*}(\boldsymbol{r})e^{-i\omega t}\right]/2$, with the spatial dependence of the field amplitudes and phases described by

$$\boldsymbol{B}(\boldsymbol{r})=\begin{pmatrix} B_x(\boldsymbol{r}) \\ 0 \\ B_z(\boldsymbol{r})e^{-i\phi(\boldsymbol{r})} \end{pmatrix} \xrightarrow{R(\boldsymbol{z}\to\boldsymbol{e})} \begin{pmatrix} B'_x(\boldsymbol{r})e^{-i\phi'_x(\boldsymbol{r})} \\ B'_y(\boldsymbol{r})e^{-i\phi'_y(\boldsymbol{r})} \\ B'_z(\boldsymbol{r})e^{-i\phi'_z(\boldsymbol{r})} \end{pmatrix} \tag{4.1}$$

The y component is approximately zero given the translational invariance of the setup. Thus only three parameters need to be measured, namely two field amplitudes $B_{x,z}(\boldsymbol{r})$ and their relative phase $\phi(\boldsymbol{r})$. To measure the Rabi frequencies in the presence of the microwave fields, we first apply a bias magnetic field along the direction the quantization axis, $\boldsymbol{e}$. Then we measure Rabi

frequencies for three fundamental magnetic dipole transitions $\Delta = 0, \pm 1$. Using the 3D rotation matrix $R(\boldsymbol{z} \rightarrow \boldsymbol{e})$ [11], the microwave fields in the new frame (x',y',z') is given in Eq.(4.1), where the quantization axis $\boldsymbol{e} = \boldsymbol{z}'$ is the z' axis the new frame. In the new frame, the Rabi frequencies for Cs atoms starting from state (3,+3) are

$$\Omega_+ \equiv \Omega_{3,3}^{4,4} = \sqrt{7}\frac{\mu_B}{\hbar} \cdot B_+ e^{-i\phi_+}$$

$$\Omega_\pi \equiv \Omega_{3,3}^{4,3} = \sqrt{\frac{7}{4}}\frac{\mu_B}{\hbar} \cdot B_\pi e^{-i\phi_\pi} \tag{4.2}$$

$$\text{and } \Omega_- \equiv \Omega_{3,3}^{4,2} = \sqrt{\frac{1}{4}}\frac{\mu_B}{\hbar} \cdot B_- e^{-i\phi_-}.$$

With the matrix elements recalled from Figure 4-1, and the normal definition of three eigenmode polarized fields defined as [10]

$$B_+ e^{-i\phi_+} \equiv \frac{1}{2}\left(B_x' e^{-i\phi_x'} - iB_y' e^{-i\phi_y'}\right)$$

$$B_\pi e^{-i\phi_\pi} \equiv B_z' e^{-i\phi_z'} \tag{4.3}$$

$$B_- e^{-i\phi_-} \equiv \frac{1}{2}\left(B_x' e^{-i\phi_x'} + iB_y' e^{-i\phi_y'}\right),$$

Eq.(4.1)-(4.3) provide a complete set. One can solve for three unknown field parameters from three experimentally measured Rabi frequencies for each lattice location.

Figure 4-6 is a Lissajous plot of the measured microwave magnetic fields, which contains information about the field amplitudes and field polarizations. It is evident that the –Z side has less microwave power and that the major-axes of the two sides are rotated with respect to each other by nearly 60^o as a result of the microwave reflections and refractions from the complex structure of the measurement chamber. If the y component of microwave magnetic fields is not zero (which results in 5 unknown field parameters), then one needs to measure at least two more Rabi frequencies along a different quantization axis to map out all microwave magnetic field amplitudes and phases [10].

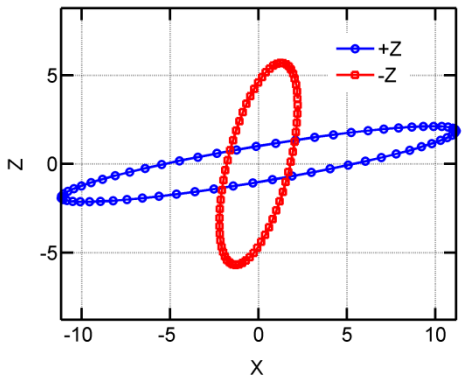

Figure 4-6. Lissajous plot of the measured microwave amplitude and polarization.

Example of reconstruction of microwave field amplitudes and polarizations from measured Rabi frequencies for the transverse-electric mode. The magnetic field components of microwaves (both the horizontal and the vertical axes) are in unit of $h \cdot kHz/\mu_B$.

From the measured microwave fields, we have optimized the Rabi frequencies for all types of transitions and found that the best quantization axis is approximately along $(\hat{\boldsymbol{y}} + \hat{\boldsymbol{x}})/\sqrt{2}$. The optimization procedure runs backwards compared to the measurement, where we numerically select an optimized quantization axis from the measured microwave fields, and experimentally verify all Rabi frequencies in that axis. The global optimization objective is to maximize Rabi frequencies for all three fundamental transitions, and equalize the Rabi frequencies at the two lattice locations.

4.2. Adiabatic fast passage

The technical challenges of driving population transfer in two-level systems in the presence of inhomogeneous fields can be understood by considering the effective Rabi frequency [12]

$$\Omega_{eff} = \sqrt{\Omega^2 + \delta^2}, \tag{4.4}$$

which is a quadrature sum of on-resonant Rabi frequency Ω and detuning δ. In our experiment, inhomogeneous effective Rabi frequencies limit the microwave transition fidelity to 80% when we use a standard Blackman π pulse [13].

There are three types of inhomogeneities in our system. First, as described in section 4.1, microwave power differs by nearly a factor of 4 at the two lattice locations, which gives a factor of 2 in on-resonant Rabi frequency Ω. The microwave power imbalance is thus the dominant source for inhomogeneous Rabi flopping rates. Second, in each pancake trap, atoms sample a range of AC-Stark shifts due to the red-detuned 1064 nm lattices, which leads to differential AC-Stark shifts between the two ground state hyperfine levels. The differential AC-Stark shifts are approximately

$$\Delta\delta_{AC} \cong \sum \delta_{AC} \cdot \frac{\Delta_{HFS}}{\delta_{YAG}} \approx 2\pi \times 0.9\ kHz \tag{4.5}$$

where $\delta_{YAG} \approx -2\pi \times 70(56)THz$ is the detuning of the 1064 nm YAG trap with respect to the Cs D2 (D1) line, $\Delta_{HFS} \approx 2\pi \times 9.2\ GHz$ is the hyperfine splitting, $\delta_{AC} = -2\pi \times 3.1(2.9)MHz$ is the AC-Stark shifts for a $150\ \mu K$ deep trap, and the sum accounts for both the D2 and D1 lines. Finally, magnetic field gradients cause inhomogeneous Zeeman shifts. Nevertheless, with well controlled magnetic fields in the science chamber, the dominant source of magnetic gradients comes from the ~5%-level non-uniformity of applied bias fields for microwave transitions, which in turn gives $\leq 2\pi \times 1\ kHz$ spread in detuning δ. The magnetic bias field inhomogeneity can be corrected using gradient coils but the correction is currently not employed.

Composite pulse techniques, which are widely used in the field of Nuclear Magnetic Resonance (NMR) [14], replace the standard π pulse with a sequence of pulses with variable pulse areas and relative phases. For instance, using a $\pi/2\ -\pi_{90^o}-\pi/2$ pulse sequence for a Cs (3,0)→(4,0) microwave transition (the subscript 90 °indicates that the phase of the center π pulse is shifted 90 °relative to the $\pi/2$ pulses), Dr. Mark Kasevich's group has demonstrated an

improvement of the transfer efficiency from 80% with a regular π pulse to 95% [15]. Like a standard π pulse, the composite pulse sequence preserves the phase coherence across the atomic sample, but is still not robust enough due to its sharp transition lineshapes.

Adiabatic fast passage (AFP) pulses exhibit a high degree of robustness against inhomogeneties [16-18], at the cost of slightly longer pulse durations. For an AFP pulse, both the instantaneous pulse amplitude and frequency are varied slowly in time. In particular, we use the following pulse function in our experiment

$$\begin{aligned} \Omega(\tau) &= \Omega_{max} sin^2(\pi\tau) \\ \delta(\tau) &= \delta_c + sgn(\tau - 1/2)\delta_{max}\sqrt{1 - sin^4(\pi\tau)}, \end{aligned} \tag{4.6}$$

where Ω_{max} is the maximum Rabi frequency as tabulated in Table 4-1, $\tau = t/T_p$ is the time rescaled by the pulse duration T_p (typically a few ms), δ_c is the frequency offset and δ_{max} is the half of the maximum frequency sweeping range (typically a few kHz). This functional form is the result of a AFP pulse optimization procedure, in which the Rabi frequency and the detuning form an eigenenergy ellipse to minimize non-adiabatic corrections [17],

$$\left[\frac{\Omega(\tau)}{\Omega_{max}}\right]^2 + \left[\frac{\delta(\tau)}{\delta_{max}}\right]^2 = 1. \tag{4.7}$$

It is intuitive to understand the robustness of the AFP pulses using the Bloch picture [12]. The state vector closely follows (precesses around) the torque vector, or equivalently the effective Rabi frequency, which is rotated slowly in time from the initial state to the final state. At the beginning and the end of the AFP pulse when the microwave power is the smallest, the torque vector is primarily determined by the largest detuning δ, which forms a unique state vector for the atoms to be aligned to, regardless of the spread in the effective Rabi frequencies.

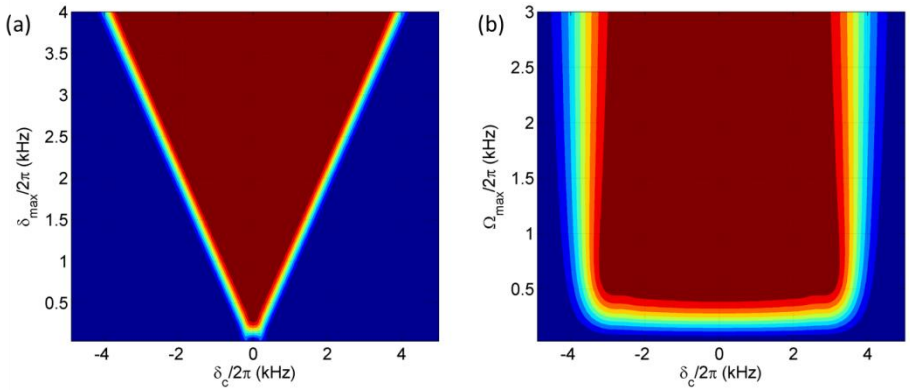

Figure 4-7. Robustness of microwave AFP pulses.

Calculated transition fidelities (red=100%, blue=0%) as a function of frequency offset δ_c for different frequency sweep ranges δ_{max} (a), and Rabi frequencies Ω_{max} (b). The other pulse parameters are $T_p = 5\ ms$, $\Omega_{max} = 2\pi \times 1\ kHz$ (a) and $\delta_{max} = 2\pi \times 3\ kHz$ (b).

Figure 4-7 shows calculated transition fidelity maps using the AFP pulse defined in Eq. (4.6). The flat-top lineshape is a signature of robustness against inhomogeneous frequency offsets, and a fidelity of >99.9% can be achieved with a factor of 5 difference in on-resonance Rabi frequency as illustrated in Figure 4-7(b).

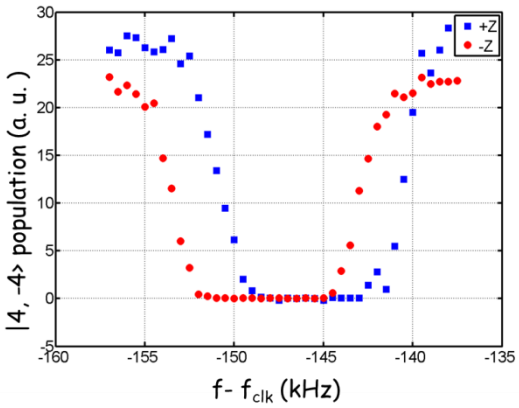

Figure 4-8. Microwave transition in a large bias magnetic field.

Experimentally, the AFP pulses can drive microwave transitions with a high fidelity of 99.8% for atoms in the two parallel lattices (Chapter 7 in ref. [13]). Figure 4-8 shows an example

of the population left in state (4,-4) as a function of center frequency of the AFP microwave pulse which transfer atoms to (3,-3). For this experiment we began with atoms optically pumped to the state (4,-4). The applied bias magnetic field, which defines the quantization axis for the microwave transition, is 60 mG along the optimal direction $\mathbf{e} \approx (\hat{\mathbf{y}} + \hat{\mathbf{x}})/\sqrt{2}$ that is used during state preparation. The bias field corresponds to a Zeeman shift of 21 kHz between adjacent sublevels, which is about 3.5 times larger than the optimal frequency sweeping parameter δ_{max}=2π×6 kHz.

Performance of microwave AFP pulses in a more interesting regime with low applied magnetic field bias is studied in Figure 4-9. The motivation is that large applied bias magnetic fields could potentially lead to small hysteresis in the magnetic shields. Although we have not seen hysteresis of a 60 mG applied field at a few μG level, it is likely that nG level hysteresis could affect the EDM measurement as a potential statistical error (since the applied bias fields are unlikely to correlate with E field reversal). Thus it is useful to demonstrate the dynamic working range for the bias fields and to operate at the low field regime when necessary. With an applied bias magnetic field of 23 mG (reduced by nearly a factor of 3), or equivalently a Zeeman shift of 8.1 kHz between adjacent sublevels, which is only slightly larger than the optimal frequency sweeping parameter δ_{max}=2π×6 kHz and marginal for resolving each Zeeman sublevel, the transition fidelity is slightly degraded to 98.5%. The infidelity is attributed is to off-resonant transitions to nearby sublevels. For instance, in Figure 4-9(c), the microwave AFP pulse primarily drives atoms from (4,+4) to (3,+3), but also slightly populates (4,+3) levels, especially when the microwave amplitudes are large. The infidelity can be avoided with a larger applied bias to further separate the Zeeman sublevels, if the low level hysteresis is found to not to be a problem in the future.

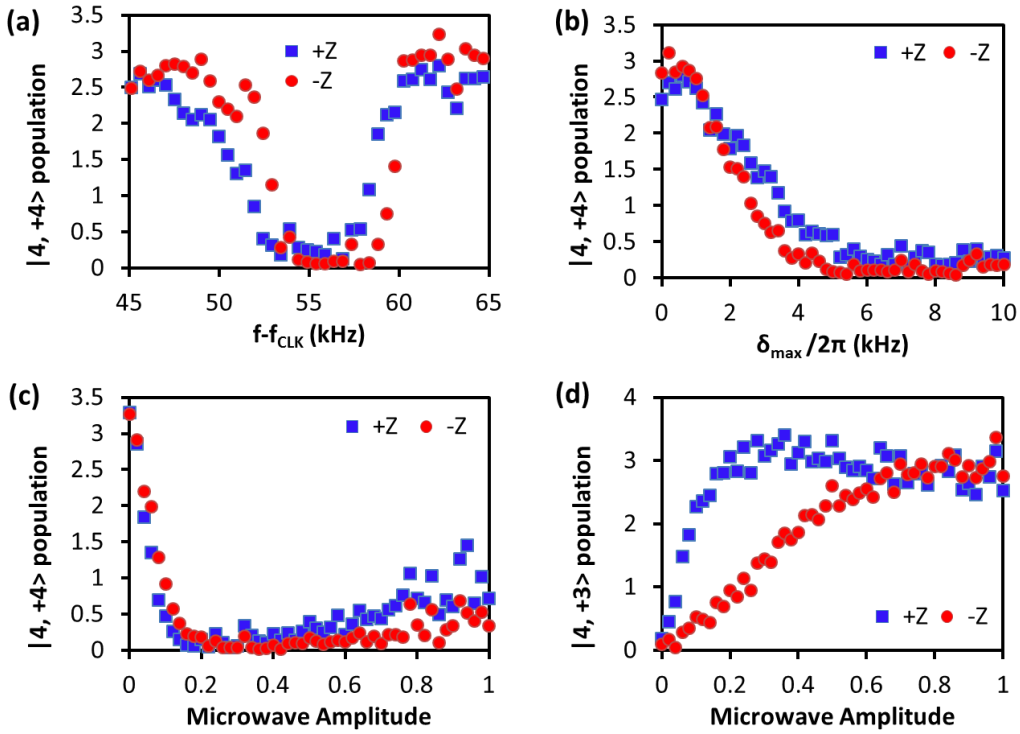

Figure 4-9. Microwave transitions in a small bias magnetic field.

(a) to (c): Population (a. u.) left in state F=4 after a microwave pulse which transfer atoms to (3,+3). The various pulse parameters are scanned to optimize transition fidelity. (d): Population (a. u.) of atoms transferred from (3,+3) to (4,+3) as a function of peak microwave amplitude (proportional to Ω_{max}), which differs by nearly a factor of two for the +Z and –Z side.

Data in Figure 4-9 is taken with the applied bias field along $\boldsymbol{e} \approx \hat{\boldsymbol{y}}$, which is less ideal than the optimal direction $\mathbf{e} \approx (\hat{\mathbf{y}} + \hat{\mathbf{x}})/\sqrt{2}$ for microwave transitions during state preparation stage due to slightly smaller Rabi frequencies (see section 4.1). Nevertheless, there is a big advantage to use this quantization axis for state-selective fluorescence detection, as we will discuss in next section, since it is the natural direction for the σ^+ polarized probe beams and we do not have to adiabatically rotate the quantization axis frequently during subsequent detections of all 7 Zeeman sublevels of the Cs F=3 hyperfine state, which takes about 150 ms per sublevel (see section 4.3). Using the quantization axis $\boldsymbol{e} \approx \hat{\boldsymbol{y}}$ thus minimizes experimental dead time and avoids possible signal degradation during a second long detection sequence.

An extension of the AFP pulses, composite adiabatic passage (CAP), has been suggested in ref. [19], which utilizes a composite sequence of AFP pulses with specific relative phases in-between. It can potentially do better than a single AFP pulse. The lowest order for the CAP pulse is $AFP - AFP_{120^o} - AFP$, where the phase of the center AFP pulse is shifted 120 °relative to the initial and final AFP pulse. This type of waveform control is also readily achievable with our microwave DDS using a phase shift register (see section 3.2.2 in Chapter 3), but it is not employed at the moment.

4.3. State-selective fluorescence detection

With state selectivity of microwaves in the frequency domain in hand, we now discuss a fluorescence detection sequence that provides a complete picture of Cs atoms in the F=3 hyperfine manifold. The scheme is generally used for both atomic magnetometry (Chapter 5) and EDM measurements (Chapter 6).

Figure 4-10(a) shows the relevant energy diagram and Figure 4-10(b) lists a typical timing sequence for state-selective fluorescence detection. A 20 mG bias magnetic field is applied along the direction of probe beam to lift the degeneracy of the F=3 hyperfine state. The vertical probe beams are sent from the bottom of the measurement chamber and are nearly along the y direction. The detection of each Zeeman sublevel contains a $\Delta m_F = 0$ microwave AFP pulse that drives atoms from state $|F = 3, m_F\rangle$ to $|F = 4, m_F\rangle$, followed by a 0.3 ms-long σ^--polarized probe pulse which is resonant with the $F = 4 \rightarrow F' = 5$ optical transition, with intensity well above saturation. The nonmagnetic imaging system records and integrates the atom fluorescence signals (see section 3.3.2 in Chapter 3). At the end of each detection pulse, a 2 ms-long clearing pulse (the probe beam) pushes atoms in F=4 hyperfine state out of the optical lattice traps completely. The detection leaves atoms in other Zeeman sublevels of the F=3 hyperfine manifold

untouched. The procedure is repeated to detect all 7 Zeeman sublevels. The microwave π-transition pulse durations for different sublevels are rescaled according to their corresponding matrix elements shown in Figure 4-1.The complete detection takes a total time of ~50 ms.

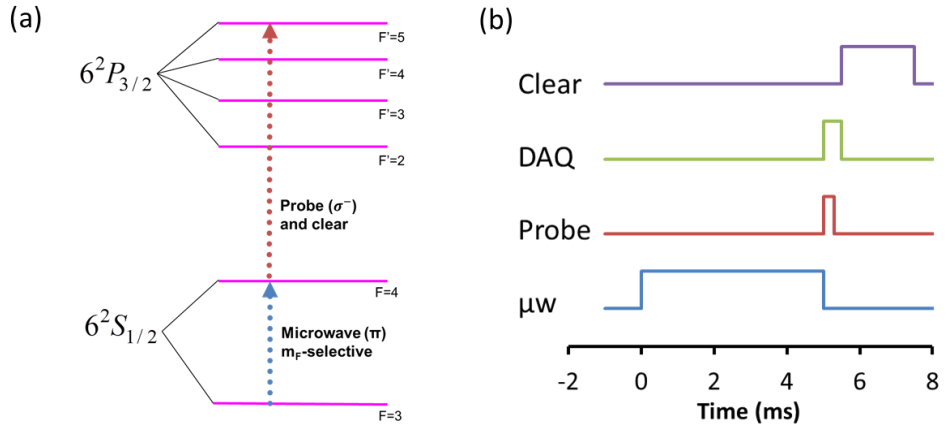

Figure 4-10. Scheme and timing sequence for state-selective fluorescence detection.

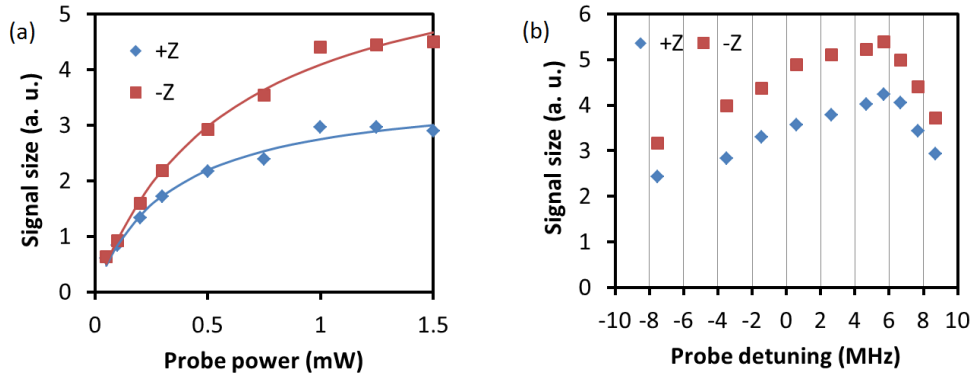

Figure 4-11. Optimizing the parameters of the probe beams.

Integrated signal size as a function of probe beam power (a) and detuning (b) with respect to the $F = 4$ to $F' = 5$ optical transition. Solid lines in (a) are nonlinear fit according to the scattering rate model for a two-level system [12].

The optimization of probe beam parameters is shown in Figure 4-11. To reduce the adverse effect of power fluctuations of the probe beam, which is measured to about 3% over a 50 ms time scale, we set the probe beam at an intensity well above saturation (with an on-resonant

saturation parameter of $s \approx 10$). In our experiment, the probe beams themselves do not add a measurable level of background in our linear PDA detection system due to the geometry of the measurement chamber. A scan of the probe beam detuning reveals that the signals peak at a detuning around +6 MHz, which is caused by the AC Stark shift of atoms in the red-detuned YAG traps.

A notable aspect of our fluorescence detection of atoms is that the probe will uniformly heat up and heat out the atoms from the lattice traps. The effect is illustrated in Figure 4-12, where we plot atom signal as a function of vertical locations for various probe durations. All measured data sets in Figure 4-12(a) collapse on to one curve when we normalize the signals by the total signal size integrated over all pixels, as seen in Figure 4-12(b). A small upward shift of atoms can be seen for probe durations longer than 1 ms, due to the pushing forces from the vertical probe beams exerted on atoms that have been heated out of the lattice traps.

Each scattering event will deposit 2 photon recoil energy to the atoms, which corresponds to 0.2 μK per scattering event. Nevertheless, in a 150 μK deep optical lattice trap, atoms that initially have a temperature of ~10 μK will still be only be well-confined within the trap for less than 700 scattering events on average until the total accumulated energy exceeds the trap depth. As shown in Figure 4-13, the characteristic time scale for significant atom loss to begin is about 0.3~0.4 ms. Due to the confinement geometry of the pancake traps, atoms have a higher probability to be heat out transversely. Consequently, atom loss for long probe times does not smear out the spatial profile along the pancake stacks. This aspect of robustness is in clear contrast to unconfined geometries, where atoms are free to move right after a few initial scattering events, which would tend to wash out spatial information along the probe direction.

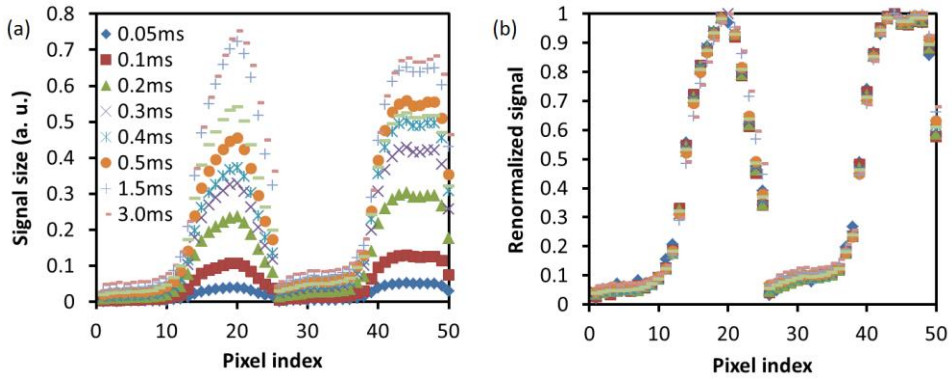

Figure 4-12. Uniform heating of the probe beams.

(a)The signal sizes at various locations (pixel 1~25 for +Z, and 26~50 for -Z) as a function of integration time. (b) Normalized signal sizes in (a), where the normalization factor is the total signal integrated for all pixels.

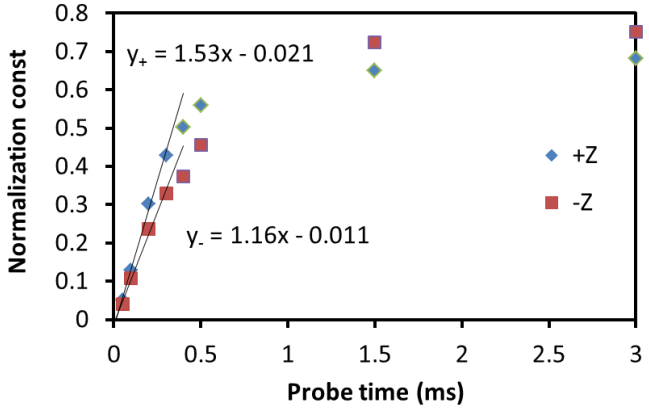

Figure 4-13. Atoms loss from the trap due to probe beam heating.

Integrated signal sizes from Figure 4-11(a). Atoms are significantly lost from the pancake traps if probe durations are longer than 0.3 *ms, as indicated by the linear fit (solid lines) in short-pulse regime.*

After a 0.3 ms-long detection pulse, some portion of the atoms are still trapped, and they must be pushed away for a clean detection of subsequent Zeeman sublevels. The effect of the clearing pulses can be seen in Figure 4-14, where we prepare atoms in state (4,+4), and a series of 7 optical probe pulses separated by 4 ms are applied. All atom signals are normalized to the 1st

pulse. Without the clearing beam, there are about 10% of signals shown from the 2nd detection pulse. Conversely, addition of a 2 ms clearing pulse enables clean detection for each sublevel.

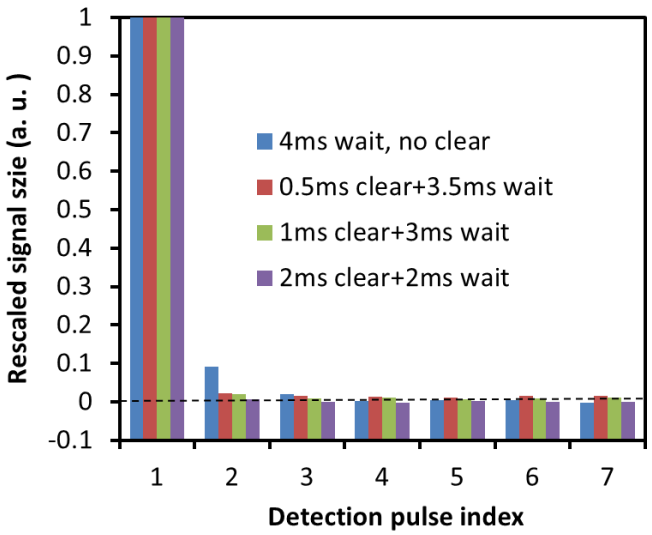

Figure 4-14. The effect of clearing beams.

Since the optimal state-selective detection scheme requires a bias magnetic field along the probe beam direction (nearly along y), if one needs to map out a state that is initially polarized along a direction other than y, for instance a state that is defined by a 20 mG bias magnetic field along z, the quantization axis rotation is used prior to the state-selective detection. The adiabatic condition of quantization axis rotation requires that, the rate of B field changes at any time of the rotation is much smaller (by a factor of $\xi \ll 1$) compared Lamor procession rate

$$\frac{1}{|\boldsymbol{B}(t)|}\frac{d}{dt}\boldsymbol{B}(t) = \xi \times \frac{g_F \mu_B}{\hbar}\boldsymbol{B}(t) \tag{4.8}$$

The solution to Eq. (4.8) results in a waveform (optical function) for B field ramps

$$\boldsymbol{B}(t) \propto \frac{1}{1+t/\tau}, \tag{4.9}$$

where τ is the adiabatic time scale determined by ξ and the size of bias fields. With our typical parameter setting $B{\sim}20$ mG, we found that when $\tau \geq 150$ ms we observe no significant state mixing during quantization axis rotation. Figure 4-15 shows the results of a quantization axis

rotation experiment for an optimal adiabatic time scale. The atoms are prepared in the (3,+3) state along B_y = 20 mG. Then we ramp up B_z= 20 mG with an optical waveform in a time period of T and ramp down B_z to 0 in a time period of T, finally we detection the population for each Zeeman sublevel along B_y= 20 mG. For a short ramp time of T~14 ms, we observe about %10 population in state (3,+2). When T >150 ms, no significant population in state (3,+2) is observed.

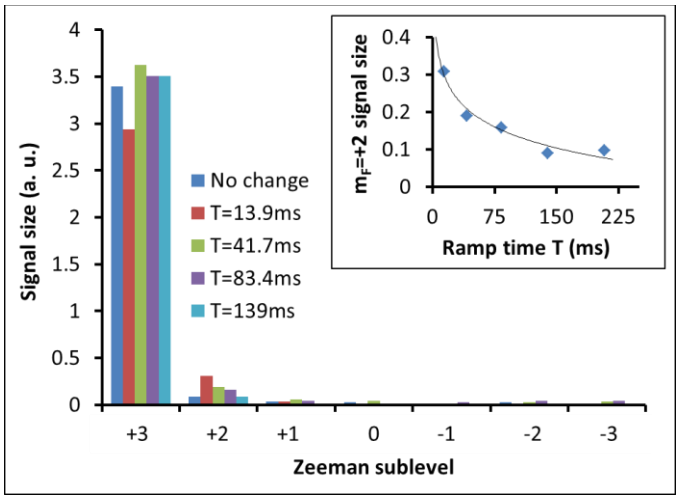

Figure 4-15. Adiabatic quantization axis rotation for state-selective detection.
The signal size of atoms in state (3,+2) is an indication of state mixing due to nonadiabatic quantization axis rotations. Optimal adiabatic time scale is about 150 ms.

4.4. References

[1] S. L. Gilbert et. al., *Measurement of the 6S→7S M1 transition in cesium with the use of crossed electric and magnetic fields*, Phys. Rev. A **29**, 137 (1984).

[2] J. D. Anstie et. al., *Characterization of a spherically symmetric fused-silica-loaded cavity microwave resonator*, Meas. Sci. Technol. **14**, 286 (2003).

[3] M. J. Mortonson et. al., *Effects of electrical charging on the mechanical Q of a fused silica disk*, Rev. Sci. Instrum. **74**, 4840 (2003).

[4] Evaporated Coatings Inc., private communication.

[5] Stefan Franzen, private communication.

[6] S. H. Brewer and S. Franzen, *Optical properties of indium tin oxide and fluorine-doped tin oxide surfaces*, J. Alloys & Compounds **338**, 73 (2002).

[7] Optiwave Inc., http://www.optiwave.com/products/fdtd_overview.html

[8] Chengdu AINFO Inc., specifications of microwave horn antenna.

[9] L. DiCarlo et. al., *Demonstration of two-qubit algorithms with a superconducting quantum processor*, Nature **460**, 240 (2009).

[10] P. Böhi et. al., *Imaging of microwave fields using ultracold atoms*, Appl. Phys. Lett. **97**, 051101 (2010).

[11] C. J. Taylor et. al., *Minimization on the Lie group SO(3) and related manifolds*, Yale Univ. Technical Report No. 9405 (1994).

[12] H. J. Metcalf and P. Van Der Straten, *Laser Cooling and Trapping*, Springer (1999).

[13] N. Solmeyer, *Progress toward an electron electric dipole moment measurement With laser-cooled atoms*, PhD dissertation, Penn State University, Chapter 7, (2013).

[14] M. H. Levitt, *Composite pulses*, Prog. Nucl. Magn. Reson. Spectrosc. 18, 61 (1986).

[15] J. M. McGuirk, *Sensitive absolute-gravity gradiometry using atom interferometry*, Phys. Rev. A **65**, 033608 (2002).

[16] S. Guérin et. al., *Optimization of population transfer by adiabatic passage*, Phys. Rev. A **65**, 023409 (2002).

[17] M. Khudaverdyan et. al., *Adiabatic quantum state manipulation of single trapped atoms*, Phys. Rev. A **71**, 031404(R) (2005).

[18] S. Zhdanovich et. al., *Population Transfer between Two Quantum States by Piecewise Chirping of Femtosecond Pulses: Theory and Experiment*, Phys. Rev. Lett. **100**, 103004 (2008).

[19] B. T. Torosov et. al., *High-Fidelity Adiabatic Passage by Composite Sequences of Chirped Pulses*, Phys. Rev. Lett. **106**, 233001 (2011).

Chapter 5

Atomic magnetometry

Sensitive magnetometry using a variation of the Hanle effect has enabled us to actively cancel out magnetic fields along all directions to a level of $\sim 3\ \mu G$, which is an important step towards the EDM measurement. Since the net circular component of our trapping beams induces a fictitious magnetic field along the direction of wave vectors and gives rise to vector light shifts that are linear in an atom's magnetic quantum number, the same technique also helps us to characterize and improve the linear polarization quality of our optical lattice beams to a level that is at least 10 times better than even the best available Glan-laser prisms.

The inhomogeneity of vector light shifts for atoms spread across pancake traps is the current limitation for coarse magnetic zeroing. The 3 μG level residual magnetic fields along transverse directions (x or y) are good enough for the EDM measurement (see Chapter 6); further zeroing for residual magnetic field along the direction of large DC electric field (z) can be done using low frequency spectroscopy that is identical to EDM measurements.

5.1. Hanle effect and Larmor precession

The Hanle effect was discovered in magnetic depolarization of resonance fluorescence experiments with Hg [1, 2]. The effect can be viewed as a generic example of quantum interference. As illustrated in Figure 5-1, incident linearly polarized light coherently excites atoms from the ground state $m_F = 0$ to different Zeeman sublevels of the upper excited states $m_F' = \pm 1$. In a magnetic field $B \neq 0$, the $m_F' = \pm 1$ sublevels are split and the $\sigma^{\pm}$ components of

the reemitted light acquire a B-dependent relative phase. Consequently the quantum interference reduces the degree of polarization of the Hg fluorescence, which is determined by the size of the magnetic bias and the excited-state lifetime (~100 ns).

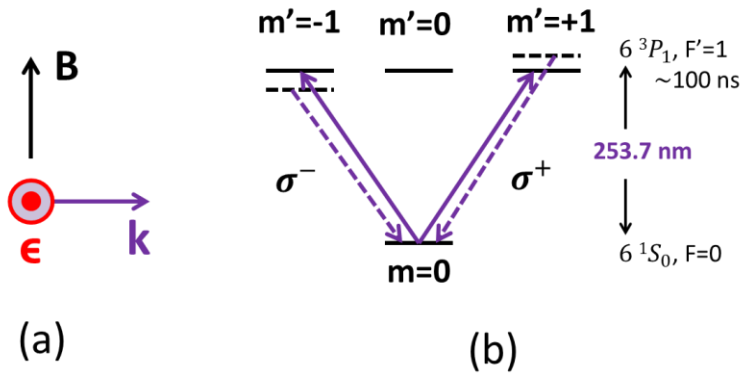

Figure 5-1. The Hanle effect in Hg.

(a)The 253.7 nm light is linearly polarized along a direction $\boldsymbol{\epsilon}$ *that is perpendicular to the quantization axis* $\boldsymbol{B}$*, and (b) couples the ground state with* $F = 0$ *and excited state with* $F' = 1$ *(*$m' = \pm 1$ *levels, solid arrows).The magnetic field introduce a phase difference for the* σ^+ *and* σ^- *circular-polarization components of the reemitted light (dashed arrows), and reduces the degree of polarization.*

We perform magnetic field measurements using Hanle rotations in spin-polarized ground state Cs atoms. The state is stable and not limited by a sub-microsecond lifetime. The long coherence time of laser-cooled atoms results in a very high sensitivity to small magnetic fields.

The objective of our atomic magnetometry is to measure small residual magnetic fields $(b_x, b_y, b_z) \ll 1\ mG$ in the passively shielded measurement chamber. For simplicity but without loss of generality, assume we need to measure the magnetic field b_y first, and the magnetic fields along the other directions are much smaller ($|b_x|, |b_z| \ll |b_y|$). The condition can be readily satisfied by applying a bias along the y direction. The evolution of state vectors throughout our measurement procedure is described in Eq. (5.1). In the following we will address each step successively in detail.

The starting point is laser-cooled Cs atoms in state $|F = 3, m_F = +3\rangle$ (see details in Chapter 4, section 4.2), prepared in a large bias magnetic field along the x direction, $B_x \approx 20\, mG$.

$$\begin{bmatrix}0\\0\\0\\0\\0\\0\\1\end{bmatrix}_x \rightarrow \frac{1}{8}\begin{bmatrix}1\\\sqrt{6}\\\sqrt{15}\\\sqrt{20}\\\sqrt{15}\\\sqrt{6}\\1\end{bmatrix}_y \rightarrow \frac{1}{8}\begin{bmatrix}1\cdot e^{-3i\phi}\\\sqrt{6}\cdot e^{-2i\phi}\\\sqrt{15}\cdot e^{-i\phi}\\\sqrt{20}\cdot e^{0i}\\\sqrt{15}\cdot e^{+i\phi}\\\sqrt{6}\cdot e^{+2i\phi}\\1\cdot e^{+3i\phi}\end{bmatrix}_y \rightarrow n_m|_z(\phi) \qquad (5.1)$$

Next, we quickly turn off B_x, and leaving the atoms in a much smaller b_y field. The field switching speed is less than 5 μs, much quicker than the relevant time scale for Larmor precession out of x; thus the field switching is diabatic.

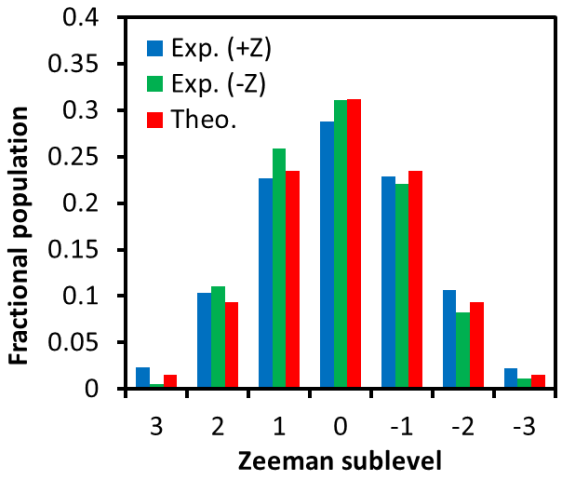

Figure 5-2. State preparation for atomic magnetomtery.

Fractional populations of Zeeman sublevels after preparing atoms in |3,+3> along x and detecting them selectively along y. Experimental data from both lattices (+/-Z sides) are shown and compared to theoretical predictions using Wigner-D rotations (Red).

Along the y direction, each Zeeman sublevel m_F will now be populated, as shown in Eq. (5.1), predicted by the Winger D-rotation matrices for systems with an angular momentum $j = 3\hbar$ [3]

$$D^{j}_{m,n}(\alpha,\beta,\gamma) = \sum_{\lambda}(-1)^{\lambda}\frac{\sqrt{(j+m)!\,(j-m)!\,(j+n)!\,(j-n)!}}{\lambda!\,(j+m-\lambda)!\,(j-n-\lambda)!\,(n-m+\lambda)!} \times e^{in\alpha}\cdot cos^{2j+m-n-2\lambda}\left(\frac{\beta}{2}\right) sin^{n-m+2\lambda}\left(\frac{\beta}{2}\right)\cdot e^{im\gamma} \tag{5.2}$$

Where m, n are Zeeman sublevel indices that go from -3 to +3. α, β, γ are rotation angles between different coordinate systems. For instance, the state mapping indicated by the first arrow in Eq. (5.1) is a result of the rotation matrix $D^{3}_{m,n}\left(0, \frac{\pi}{2}, 0\right)$. The summation is performed over values of λ's that give a finite value denominator. In practice this means any λ that does not result in negative factorials [4].

The measured state populations for the superposition state in the y basis are shown in Figure 5-2, which is in good agreement with theoretical predictions from Eq. (5.1).

To measure the magnetic field b_y, we let the atoms freely evolve for a time interval T, during which a Zeeman sublevel m_F in the eigenbasis y will evolve in phase by $m_F\phi$, where the Hanle interferometer phase $\phi = g_F\mu_B b_y T/\hbar$ is the phase shift of the $m_F = +1$ level.

Finally, we quickly turn on a large magnetic field along the z direction, $B_z \approx 20\ mG$ and map the phase shifted superposition state in the z basis. The rotation is described by the Wigner-D matrix $D^{3}_{m,n}\left(\frac{\pi}{2}, \frac{\pi}{2}, 0\right)$. The state populations in the z basis yield

$$n_m|_z(\phi) = \begin{bmatrix} \frac{1}{64}(-1+\mathrm{Sin}[\phi])^6 \\ \frac{3}{512}(-5\mathrm{Cos}[\phi]+\mathrm{Cos}[3\phi]+4\mathrm{Sin}[2\phi])^2 \\ \frac{15(-2-2\mathrm{Cos}[2\phi]+\mathrm{Sin}[\phi]+\mathrm{Sin}[3\phi])^2}{1024} \\ \frac{5\mathrm{Cos}[\phi]^6}{16} \\ \frac{15(2+2\mathrm{Cos}[2\phi]+\mathrm{Sin}[\phi]+\mathrm{Sin}[3\phi])^2}{1024} \\ \frac{3}{512}(-5\mathrm{Cos}[\phi]+\mathrm{Cos}[3\phi]-4\mathrm{Sin}[2\phi])^2 \\ \frac{1}{64}(\mathrm{Cos}[\frac{\phi}{2}]+\mathrm{Sin}[\frac{\phi}{2}])^{12} \end{bmatrix} \quad (5.3)$$

Which is a complex function of ϕ. We sequentially detect populations for all 7 sublevels using state-selective fluorescence detection (see Chapter 4, section 4.3).

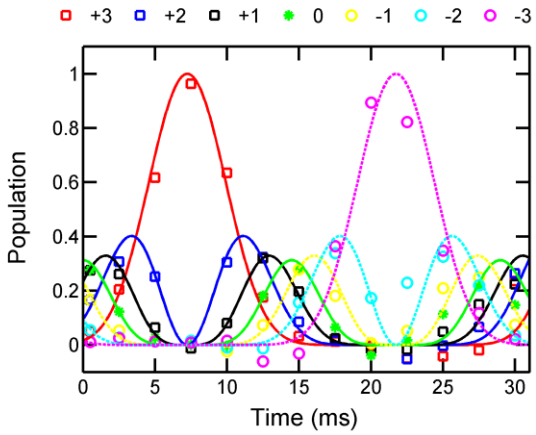

Figure 5-3. Population evolution for all Zeeman sublevels for a Larmor precession cycle.

State evolution for all 7 Zeeman sublevels of the F=3 hyperfine ground state during a Larmor precession cycle in an effective magnetic field of ~100 μG. Theoretical predictions according to Eq. (5.3) without dephasing are also plotted in comparison (solid lines).

An example of state evolution for all 7 Zeeman sublevels of the F=3 hyperfine ground state during a Larmor precession cycle in an effective magnetic field of ~100 μG is shown in Figure 5-3. Theoretical predictions according to Eq. (5.3) without dephasing (which is quantified later in the Chapter) are also plotted in comparison (solid lines). Each set of 7 points is from a

single atom ensemble. The standard deviation of ± 0.05 in fractional population is dominated by fluctuations in the background from scattered trapping light. Imperfect background subtraction due to these fluctuations can lead to an inference of negative populations. These fluctuations can be avoided in future measurements with an additional 1064 nm filter.

We define the normalized total atomic spin as

$$\langle S \rangle|_z = \frac{1}{m_p} \frac{\sum m \times n_m}{\sum n_m} = \sin(\phi) \tag{5.4}$$

Where $m_p = +3$ is the initially prepared spin, used as a normalization factor. The average spin is a sinusoidal function. Compared to Eq. (5.3), $\langle S \rangle$ is a much simpler metric for data analysis to extract the phase shift ϕ, from which the magnetic field b_y can be calculated.

One could also measure the phase shifted superposition state population in the original x basis, using Wigner-D rotation $D^3_{m,n}\left(0, -\frac{\pi}{2}, 0\right)$. It is straight-forward to show that $\langle S \rangle|_x = \cos(\phi)$. Using cyclic permutations of (x, y, z) of the measurement procedure (*preparation, precession, detection*), we are able to measure magnetic fields along all 3 directions.

The classical analog of the quantum interference measurement described above is the Larmor precession. Consider the average spin as a classical unit vector, in a magnetic field $\boldsymbol{B} = B\hat{\boldsymbol{B}}$ (we have separated field amplitude and direction). The spin will precess according the Larmor equation

$$\frac{d}{dt}\boldsymbol{S}(t) = \omega_L \hat{\boldsymbol{B}} \times \boldsymbol{S}(t), \tag{5.5}$$

where $\omega_L = 2\pi \times 0.35 Hz \times \frac{B}{\mu G}$ is the precession frequency of Cs in the $F = 3$ hyperfine state.

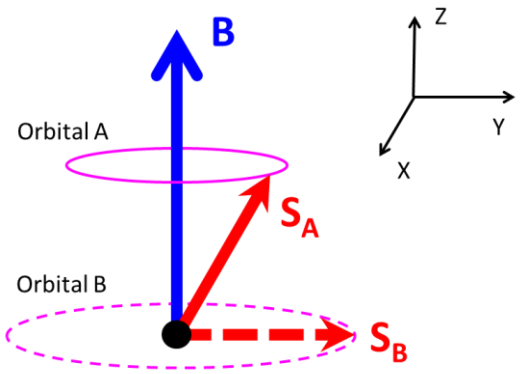

Figure 5-4. Schematic for Larmor precession of atomic spins in bias magnetic field.
The spins will precess around the bias magnetic field. The Larmor precession is driven by the torque vector $\widehat{\boldsymbol{B}} \times \boldsymbol{S}(t)$ and the precession orbitals depend on the initial spin alignment.

The exact solution to the Larmor equation is [5]

$$\boldsymbol{S}(t) = \widehat{\boldsymbol{B}}(\boldsymbol{S}_0 \cdot \widehat{\boldsymbol{B}}) + [\boldsymbol{S}_0 - \widehat{\boldsymbol{B}}(\boldsymbol{S}_0 \cdot \widehat{\boldsymbol{B}})]cos(\omega_L t) + (\widehat{\boldsymbol{B}} \times \boldsymbol{S}_0)sin(\omega_L t). \tag{5.6}$$

A schematic of Larmor precession is shown Figure 5-4. If the initial spin is aligned along the direction of the bias magnetic field, no precession will occur because $\widehat{\boldsymbol{B}} \times \boldsymbol{S}_0 = 0$. For initial spins not along the bias field, Larmor precession will result in an orbital on the unit sphere. In the special case where $\boldsymbol{S}_0 = \hat{y}$ and $\widehat{\boldsymbol{B}} \perp \boldsymbol{S}_0$, the spin precession will follow a circle on the equator. If one measures the spin along the y and x directions, the results will be $S_y = \cos(\omega_L t)$ and $S_x = \sin(\omega_L t)$, respectively.

For simplicity, from now on we will use the classical object, the average spin, to analyze data in atomic magnetometry experiments. Figure 5-5 shows a typical spin precession in a modest magnetic field primarily along x direction. We have prepared the state along y, and measured along all three directions. The spin precession data can be fit globally with the Larmor equation to extract magnetic fields. Nevertheless, the method of measuring spin precession over

an entire precession cycle is time consuming. We will introduce a more efficient and accurate measurement technique in the section 5.2.

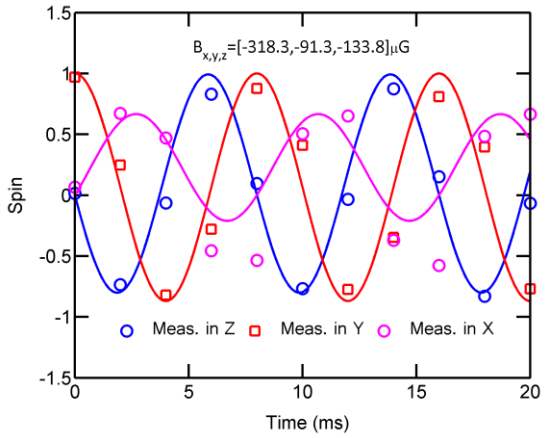

Figure 5-5. Spin precession in large magnetic fields as measured along all 3 directions. *Measured spin precession along all directions with the initial spin prepared along y. The solid lines are a global fit to the Larmor equation to extract magnetic fields.*

A different metric, namely the fractional population difference between $m = +3$ and $m = -3$ sublevel, might be used to boost to the sensitivity of the spin precession signal to the relative phase ϕ. This is in fact very marginal compared to that of the average spin, because from Eq. (5.3), one can show that $n_{+3}(\phi) - n_{-3}(\phi) = [198sin(\phi) - 55sin(3\phi) + 3sin(5\phi)]/198$, which is to the leading order approximately identical to $sin(\phi)$. The maximum slope of the new metric is $\left|\frac{d}{d\phi}[n_{+3}(\phi) - n_{-3}(\phi)]\right|_{max} \approx 1.07$, which is only slightly larger than $\left|\frac{d}{d\phi}sin(\phi)\right|_{max} = 1$. Furthermore, in the presence of measurement noise and large transverse magnetic fields (see section 5.3), the new metric is does not have a straightforward offset error correction due to higher order oscillatory terms and lack of a simple classical analog.

5.2. Measuring and zeroing the magnetic fields

We have measured and cancelled the magnetic fields using an iterative procedure, progressively increasing the sensitivity to magnetic field using longer precession times. Figure 5-6 shows typical Larmor precession data during the iterative procedure. For a given iterative step, the Larmor precession frequency is decreased due to the coarse magnetic field cancellation.

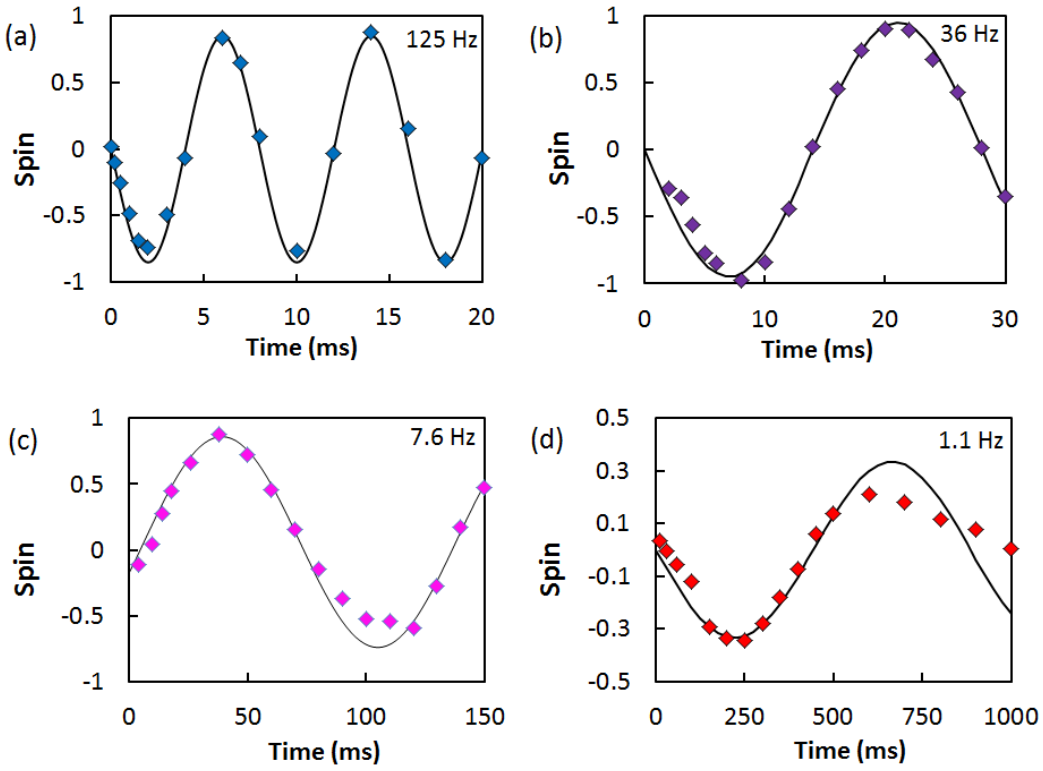

Figure 5-6. Spin precession during the iterative magnetic field zeroing procedure.
During each step, the spin precession is measured only along one direction to extract the precession period, which will be used as set point for a successive measurement.

Suppose the initial fields are $\boldsymbol{b_0} = (b_x, b_y, b_z)$, and we need measure and cancel all three field components. We start by measuring the spin precession along one direction, and extracting the spin precession period $T_1 = 1/(0.35 \times |\boldsymbol{b_0}|)\ sec$, which is determined only by the magnetic field amplitude $|\boldsymbol{b_0}|$ (in μG). There is no preferential direction to choose from as long as we can

measure a precession curve with reasonable contrast, from which we can use a sinusoidal fit or a Fourier transform to obtain the precession frequency. To speed up the measurement, it is enough in practice to measure slightly more than half a precession cycle. The precession period is just twice the time difference between an identified maximum and a nearby minimum of the precession curve.

We begin by measuring b_x using the 3-step procedure described previously, where we prepare the spin along z, let the spin Larmor precess along x, and measure the final populations of each Zeeman sublevel along y. For the free evolution, we set the precession time to be $t_1 = T_1/4$, scan the bias coil current I_x from shot to shot (which will translate into a magnetic field of $B_x \cong \frac{0.22G}{A} I_x$), and measure the average spin $S(B_x)$ or $S(I_x)$ as a function of the bias current. The Hanle interferometer phase will be $\phi = g_F \mu_B (B_x + b_x) t_1/\hbar$. The observed spin signal vs bias current will be a sinusoidal function with an offset that is approximately equal to b_x, as shown in Figure 5-7. The precession time is analogous to a gain knob in control circuit. To illustrate this concept, we have shown that by decreasing the precession time to $t_1 = T_1/8$, the slope of the spin curve near its most sensitive point is reduced by approximately a factor of 2.

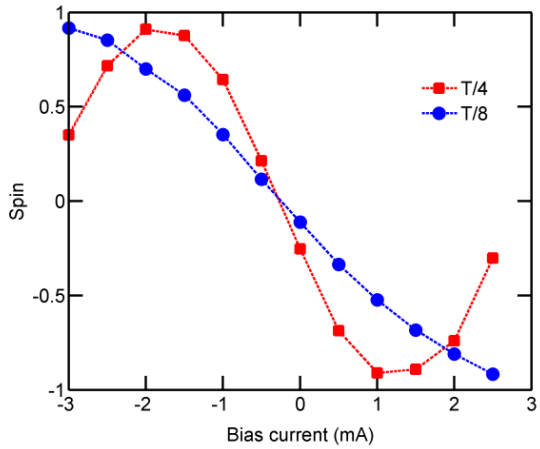

Figure 5-7. Average spin versus bias magnetic coil current for different procession times.

There are a few methods that can be used to extract b_x from the $S(B_x)$ curve. As one might have noticed, the interception of two different $S(B_x)$ curves near the center (a bias current which cancels b_x) gives the offset b_x directly. Nevertheless, one needs to take two experimental curves for each magnetic field measurement. Since each point takes at least a few seconds, this method of direct interception might be less favorable if one needs to measure the magnetic fields quickly. Now we focus on two new numerical methods to extract b_x using the $S(B_x)$ curve at $t_1 = T_1/4$ only.

The method we initially implemented historically is a linear zero crossing technique, as shown in Figure 5-8. We fit the $S(B_x)$ curve to a linear function, using just a few data points near the center. Then we locate the center by solving $S(B_x) = 0$. This method gives accurate measurement of b_x if $S = 0$ when $B_x + b_x = 0$. When the magnetic field amplitudes along the transverse directions b_y, b_z are comparable to that of b_x, the condition $B_x + b_x = 0$ does not necessarily mean $S = 0$, and the linear zeroing crossing method can lead to an offset error as large as 60%. In section 6.4 there is a detailed study of the origin of the offset error and the corresponding post-measurement software corrections.

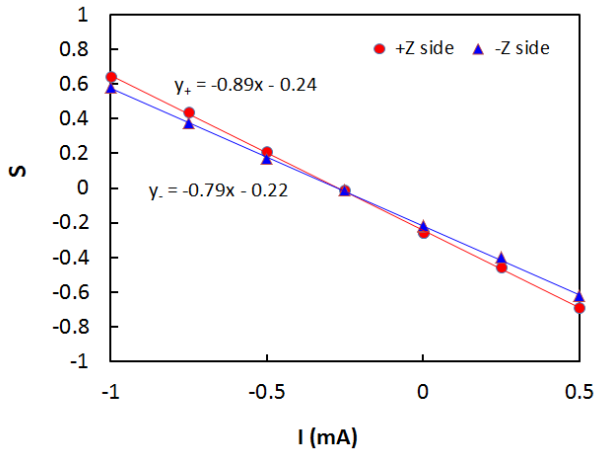

Figure 5-8. The linear zero crossing technique for magnetic field zeroing.
The $S(B_x)$ curve is fit to a linear function, and b_x is extracted by solving $S(B_x) = 0$.

An improved technique termed dSdB utilizes the first order derivative of the $S(B_x)$ curve, namely dS/dB or equivalently dS/dI. An example is show in Figure 5-9 (b). We fit the dS/dI curve with a quadratic function and locate b_x from the parabolic extrema. This method works much better for all combinations of residual magnetic field components. When amplitudes of b_y, b_z are comparable to that of b_x, the dSdB technique will only have an error of 8%. A software error correction for this technique will also be introduced in section 5.3.

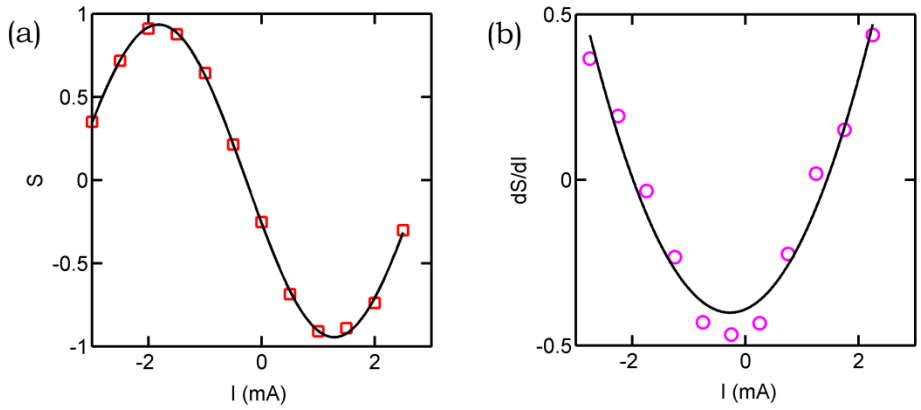

Figure 5-9. The dSdB technique for magnetic field zeroing.

The measurement results in a first order cancellation of $B_x + b_x \approx 0$. The imperfection come from noise in the $S(B_x)$ curve and imperfect offset corrections. We now set the bias coil current along the x direction using the measured value so that $B_x + b_x \approx 0$.

Based on the previous measurement of b_x, we now set the precession time at $t_2 \cong t_1 \times \frac{|\boldsymbol{b_0}|}{\sqrt{|\boldsymbol{b_0}|^2 - |b_x|^2}}$ to increase the sensitivity, since the magnetic field along the x direction has been coarsely cancelled and the spin precession period will be longer. We measure b_y using the dSdB technique as described earlier in this section, by preparing along x, precessing along y and measuring along z. This step leads to first order cancellation of $B_y + b_y \approx 0$. We proceed by measuring and cancelling b_z , using again an increased gain setting $t_3 \cong t_1 \times \frac{|\boldsymbol{b_0}|}{\sqrt{|\boldsymbol{b_0}|^2 - |b_x|^2 - |b_y|^2}}$.

Consequently, we now have cancelled magnetic fields along all three directions. The entire procedure can be iterated for a next order cancellation. The typical spin precession curves during the entire iterative procedure are shown Figure 5-6. It takes 1 to 3 steps to cancel the residual fields to a level of $3\ \mu G$ (in $\sim 100\ \mu K$-deep traps), depends on the initial magnetic fields.

5.3. Offset errors and sensitivity

Throughout our measurement procedure, we have counted on the approximate orthogonality between the initially prepared spins and the residual fields $\boldsymbol{b_0}$, namely precession orbitals close to the equator (i.e. orbital B in Figure 5-4). Transverse magnetic fields, which are perpendicular to the direction of the magnetic field to be measured, have a compound effect on the Larmor precession by driving precession orbitals at higher altitudes (like the orbital A in Figure 5-4). Consequently, this leads to an offset error in both the linear zero crossing and the dSdB measurement techniques described in section 5.2.

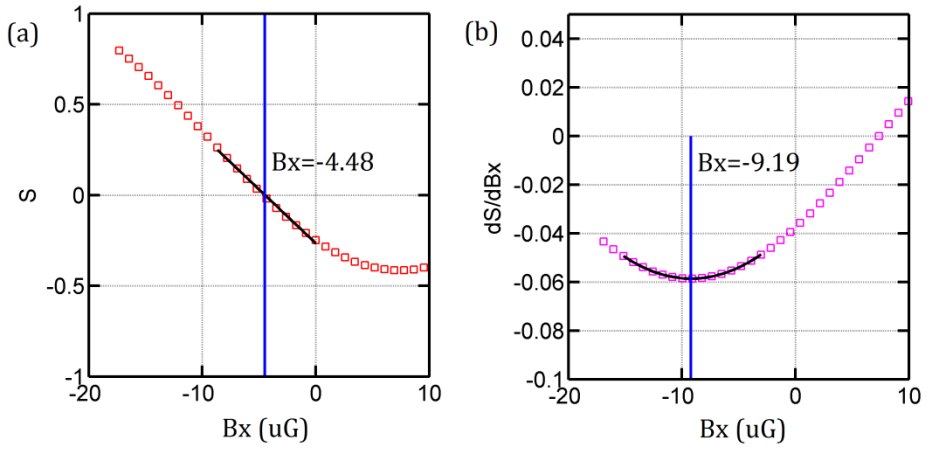

Figure 5-10. The origin of offset errors for the linear and dSdB field zeroing techniques. *(a) The spin precession is calculated numerically and plotted for a bias field* $\boldsymbol{b_0} = (10,10,10)\mu G$. *The linear zeroing crossing method leads to a 55% offset error. (b) The dSdB method for the spin precession in (a), a parabolic fitting (black solid line) gives the correct bias setting (blue line) with about 8% error.*

Figure 5-10 shows the offset error during a zeroing procedure to cancel b_x, with a bias field $\boldsymbol{b_0} = (10,10,10)\mu G$. Since the spin is about $S \approx 0.7$ at the point $B_x + b_x = 0$, the linear zero crossing method is off by almost 55%. The dSdB method is not constrained by spin zero crossing and is sensitive to the slopes of $S(B_x)$. It thus provides an improved extraction of b_x, with an error of only about 8%.

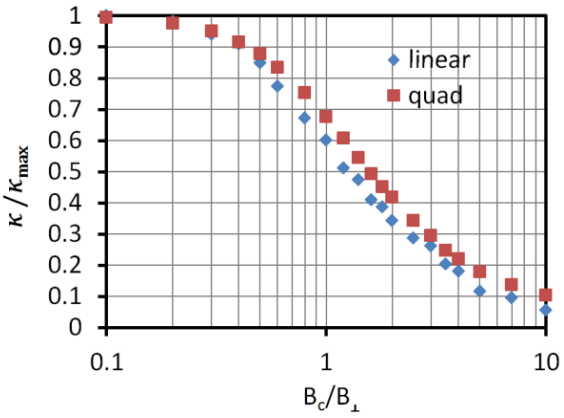

Figure 5-11. Calculated error functions for offset corrections.

The error correction function $\kappa(|B_c|/B_\perp)$ is numerically computed and normalized to it maximum value in the $|B_c|/B_\perp \to 0$ limit: $\kappa_{max} \approx 2.9$ for the linear zeroing crossing method and $\kappa_{max} \approx 0.4$ for the dSdB technique. The functions do not fit well with simple offset erf(x) functions or composite tanh(x) functions.

A detailed study of the Larmor equation shows that a simple and universal error correction function *g* exists for all cases of residual bias fields

$$g(B_c;\, B_p, B_m) \approx sgn(m_F^p)\epsilon_{pcm} \cdot \kappa\left(\frac{|B_c|}{B_\perp}\right) B_\perp sin[2\phi] \cdot \frac{t}{T} \tag{5.7}$$

With parameters defined as follows:

c, p, m : the direction in which one tries to *cancel* the magnetic field, the direction in which one *prepares* the initial spin and the direction in which one *measures* the final population respectively;

m_F^p : the initial prepared spin, +3 or -3 in our experiment;

ϵ_{pcm} : the Levi-Civita permutation symbol, for example, $\epsilon_{xyz} = +1$ and $\epsilon_{xzy} = -1$;

$B_\perp$, ϕ: the transverse magnetic field amplitude and phase, defined as $B_{p,m} = B_\perp(cos\phi, sin\phi)$;

$\kappa\left(\frac{|B_c|}{B_\perp}\right)$: the error function as shown in Figure 5-11, which provides a precise description of transverse field effect;

$\frac{t}{T}$: the precession time set point. Typically we have $t/T = 1/4$.

The error correction function described above provides an efficient way to compensate the offset errors along all three measured directions after every iterative step, which is added in software and requires no extra experimental time. The offset errors are calculated as below

$$\begin{aligned} \Delta B_x &= g(b_x;\ b_z, b_y) \cong g(-B_x; -B_z, -B_y) \\ \Delta B_y &= g(b_y;\ B_x + b_x, b_z\ ) \cong g(-B_y;\ -\Delta B_x, -B_z) \\ \Delta B_z &= g(b_z;\ B_y + b_y, B_x + b_x) \cong g(-B_z;\ -\Delta B_y, -\Delta B_x). \end{aligned} \tag{5.8}$$

In this way we can keep track of the transverse fields during measurement for each magnetic field direction, and recall the error function g in a step-wise manner. After applying the error corrections, the magnetic field zeroing is more precise for all directions ($\alpha = x, y, z$) in every iterative step: $b_\alpha + (B_\alpha + \Delta B_\alpha) \to 0$.

We now compare the offset errors and sensitivities for both zeroing techniques. Figure 5-12 (a) shows the relative error $\Delta B_x/B_\perp$ as a function of the precession time set point t/T. For small precession time, both methods result in a linear function, but the linear zeroing crossing method is worse by nearly a factor of 7. For large t/T, the offset errors grow more rapidly than linear functions, which could potentially make accurate error corrections less straightforward.

The metric of sensitivity for the linear zeroing crossing technique is the slope of the linear fit, namely dS/dB. The metric of sensitivity for the dSdB technique is the quadratic fitting coefficient, namely d^3S/dB^3. The sensitivity for both techniques is shown in Figure 5-12 (b), which are normalized to their corresponding values at $t/T = 1/4$ for comparison. It is evident

that the maximal sensitivity for the linear zeroing crossing technique is near $t/T = 1/4$ and the dSdB technique is near $t/T = 1/2$, which makes the dSdB method inherently more sensitive to magnetic fields because it allows longer precession times for the Hanle interferometer phase accumulation.

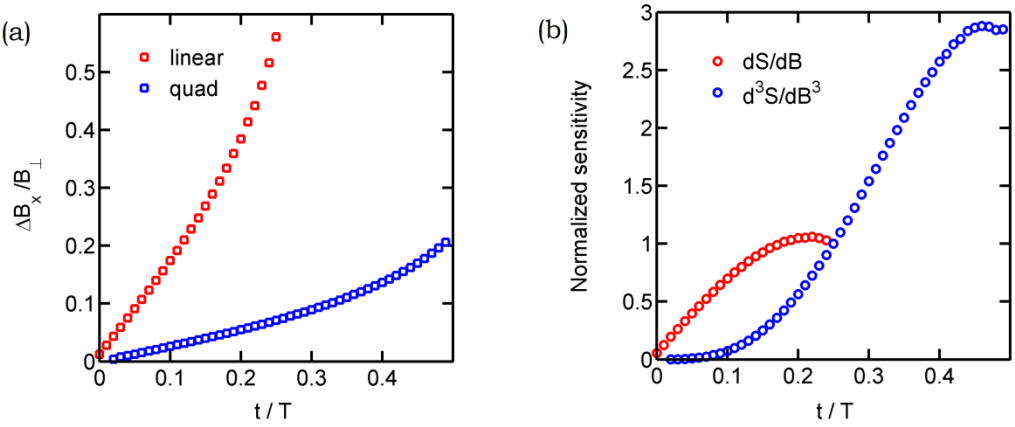

Figure 5-12. Error and sensitivity vs precession time for different techniques.
A comparison between the linear zero crossing technique (linear) and the dSdB (quad) method. Numerical results are obtained with $\phi = \pi/4$ for different precession time set point (t/T).

We have chosen the dSdB technique with a typical set point $t/T = 0.25$ as our final magnetic field zeroing procedure, since it introduces small offset errors that can be accurately corrected using Eq. (5.7) straightforwardly in a simple manner. We have tested the magnetic field zeroing at $t/T = 0.35$ and have not found a measurable gain, possibly due to the high signal to noise ratio in our detection system. A factor of 2 increase in sensitivity might be possible with the setting $t/T \approx 1/2$. Because the offset error is no longer a linear function of t/T when $t/T > 0.3$ (see Figure 5-12 (a)), a more complex error correction function is needed to replace Eq. (5.7).

5.4. Measurement of vector light shifts

Circularly polarized light leads to vector light shifts (VLS's) on atoms, which are ac-Stark shifts that act like fictitious magnetic fields [6-8]. In our linearly-polarized cavity built-up optical lattice beams, a small fraction of net circular polarization induces fictitious magnetic fields which are present throughout our procedure for zeroing the real magnetic fields. Due to the inhomogeneous nature of the trapping geometry, atoms spreading out over the pancake traps experience inhomogeneous fictitious magnetic fields, which in turn lead to sophisticated Larmor precession signals manifested as dephasing. The spatial variations of VLS's limit our ability to further cancel out the magnetic fields.

The VLS's can be minimized either by polarizing atoms perpendicular to the direction of light propagation, or by making the trapping light as linearly polarized as possible. Absolute linear polarization can be created and measured using Glan-laser prisms, but it is hard to do better than 10^{-6} of the wrong intensity, because of residual birefringence in optical elements, including optical coatings [9], and momentum-changing low-level scattering [10]. Differential polarization measurement techniques have been an active area of research in physics and engineering [9-12]. Most progress has been made in sensitivity to polarization changes, but not in absolute polarization measurement.

We measure the VLS's due to the cavity built-up optical lattice using the technique described in section 5.1. The measurement is linearly sensitive to the electric field of the non-linearly polarized light, which allows unprecedentedly accurate measurements of the absolute linear polarization quality, to a level at least 10 times better than that one could even get using the best available Glan-laser prisms [13].

The VLS for a ground state atom in a far off-resonant trap (FORT) is [6, 8]

$$v_V = (\alpha_V \, U \, m_F) \times [i(\boldsymbol{\varepsilon}^* \times \boldsymbol{\varepsilon}) \cdot \boldsymbol{e}] \tag{5.9}$$

Where the constant α_V is 464 Hz/μK for the Cs $F = 3$ hyperfine ground state in a $\lambda = 1064\,nm$ lattice, U is the trap depth in μK, $\boldsymbol{\varepsilon}$ is the polarization vector, and $\boldsymbol{e}$ is the quantization axis for the atom. Maximum sensitivity to polarization quality requires that $\boldsymbol{e}$ be parallel to the wave vector, $\boldsymbol{k}$, the geometry we use. The electric field unit vector for linearly polarized light with a slightly circular component can be described by

$$\boldsymbol{\varepsilon} = sin\left(\frac{\pi}{4} + \theta\right)\boldsymbol{\varepsilon}_L + e^{i\phi}cos\left(\frac{\pi}{4} + \theta\right)\boldsymbol{\varepsilon}_R, \tag{5.10}$$

where the small angle θ characterizes the linear polarization quality, the circular polarization vectors $\boldsymbol{\varepsilon}_L, \boldsymbol{\varepsilon}_R$ are given by $\boldsymbol{\varepsilon}_L = -(\boldsymbol{\varepsilon_1} + i\boldsymbol{\varepsilon_2})/\sqrt{2}$, $\boldsymbol{\varepsilon}_R = (\boldsymbol{\varepsilon_1} - i\boldsymbol{\varepsilon_2})/\sqrt{2}$ in the Cartesian basis, and ϕ is the misalignment of the linear polarization with respect to the axis $\boldsymbol{\varepsilon_1}$. The angular dependence of the VLS and the absolute polarization sensitivity of a Glan-laser prism (GLP) are

$$\begin{aligned} \delta_{VLS} &= i(\boldsymbol{\varepsilon}^* \times \boldsymbol{\varepsilon}) \cdot \boldsymbol{e} \approx 2\theta \\ \delta_{GLP} &= |\boldsymbol{\varepsilon}_1 \cdot \boldsymbol{\varepsilon}|^2 \approx \theta^2 + \frac{\phi^2}{4}. \end{aligned} \tag{5.11}$$

Therefore, the VLS is linearly sensitive to θ and the GLP is quadratically sensitive to θ when it is optimally aligned ($\phi = 0$). The VLS has the sensitivity of the polarization imperfection interfering with each of the two circular polarization components, but the combined effect of the two circular polarization components themselves on the atom gives exactly no VLS, so unlike conventional polarimeters which only measure polarization changes, the linear VLS signal sits on an zero background.

We measure the VLS's using a variation of the Hanle effect as described in section 5.1. During the measurement, we let the atoms Larmor precess at a composite frequency $\omega = \omega_B + \omega_U$, where spatially uniform ω_B could be due to a real residual B-field or a fictitious magnetic field from a beam with uniform intensity, and ω_U is due to the VLS's from the optical lattice light. Note the VLS corresponds to a fictitious magnetic field along the y direction in our

experiment according to Eq. (5.9) and we have zeroed the magnetic fields along transverse directions (x and z) for the VLS measurements.

Figure 5-13 shows spin precessions $S(t)$ when the +Z lattice polarization is misaligned, which makes ω_U greatly exceed ω_B, illustrated by fact that halving the lattice power halves the oscillation frequency. The atoms are prepared in state |3,+3> along x, are allowed to spin precess along y and are then measured along x. Points on the two curves are taken alternately to minimize any effect of small drifts in ω_B. The oscillations quickly damp out because trapped atoms with different energies experience different average VLS's.

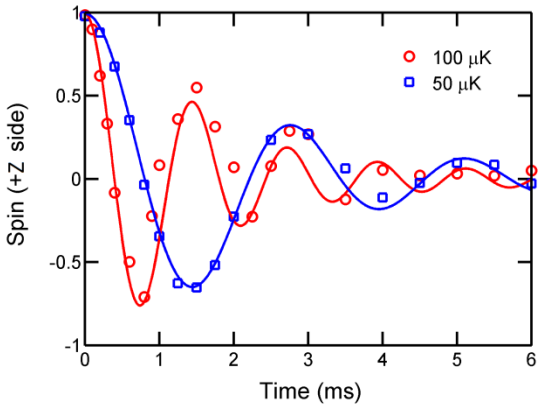

Figure 5-13. Measurement of large vector light shifts when the cavity is misaligned.

We have constructed a theoretical model for $S(t)$ to account for this inhomogeneity. In Figure 5-13, the total precession frequency ω exceeds the transverse oscillation frequency, $\omega_\rho = \omega_x = \omega_z = 2\pi \times 30.7\ Hz$ with $U_0 = k_B \times 100\ \mu K$, and is much less than the axial oscillation frequency, $\omega_y = 2\pi \times 105.3\ kHz$. Atoms are spread out axially according to harmonic oscillator wave-functions, while their transverse positions are essentially fixed during a Larmor precession cycle. The spatial dependence of the precession is given by $\omega_U(n_y, \rho) \approx \omega_{U_0} g(n_y)(1 - \rho^2/w^2)$, where $w = 580\ \mu m$ is the lattice beam waist radius, ω_{U_0} is the peak ω_U and

$$g(n_y) = 1 - \frac{1}{2}\left(n_y + \frac{1}{2}\right)\frac{\hbar\omega_y}{U_0} \tag{5.12}$$

The virial theorem has been used to account for the average intensity in each axial mode, n_y. For the approximately thermal distribution that results from laser cooling [14], the transverse spatial distribution is given by $f(\rho) = exp\left(-\frac{\rho^2}{2\sigma_\rho^2}\right)/\sqrt{2\pi\sigma_\rho^2}$, where $\sigma_\rho = \frac{1}{\omega_\rho}\sqrt{\frac{k_B T}{m}}$ is the transverse width and the axial occupation probabilities are given by

$$p(n_y) = \left(1 - e^{-\frac{\hbar\omega_y}{k_B T}}\right)e^{-n_y\frac{\hbar\omega_y}{k_B T}} \tag{5.13}$$

The observed spin precession is the weighted spatial average,

$$S(t) = \sum_{n_y} p(n_y) \int cos\{[\omega_B + \omega_U(n_y, \rho)]t\} f(\rho) d\rho. \tag{5.14}$$

The integral in Eq. (5.14) can be simplified to yield

$$S(t) = \sum_{n_y} p(n_y) \frac{cos\{[\omega_{U_0} g(n_y) + \omega_B]t - tan^{-1}[bt]\}}{\sqrt{1+[bt]^2}}, \tag{5.15}$$

where $b = (k_B T/U_0) g(n_y) \omega_{U_0}$. Three free parameters are used to simultaneously fit the two precession curves in Figure 5-13 to Eq. (5.15): the normalized peak VLS, ω_{U_0}/U_0; the normalized temperature, $T/\sqrt{U_0}$, which is a constant parameter with adiabatic change of U_0 (fixed phase space density) [15]; and ω_B. The fitting result is listed in Table 5-1. From the fit value of ω_{U_0} we determine that the peak vector light shift is $792 \pm 30\ Hz$, which implies a polarization defect of $\theta = 7.3(3) \times 10^{-3}$ radians. The fit temperature value gives $T = 21.6 \pm 1.3\ \mu K$ (for $U_0 = k_B \times 100\ \mu K$). CCD camera in situ imaging of atoms using the cooling light implies a transverse temperature of $T = 11 \pm 0.8\ \mu K$. The discrepancy suggests that the polarization quality varies across the lattice beams. That the model does not explicitly account for this does not affect the fit value of ω_{U_0} to within our uncertainty.

Spin precession data for our best linear polarization is shown in Figure 5-14 for both optical lattices. The atoms are prepared in |3,+3> along x, spin precess along y and are finally

measured along z. With the best linear polarization quality, the spin signal stays in phase over many Larmor precession cycles. When the trap depth is halved, we observed only a small difference in total precession frequency and the dominate constant precession frequency is $\omega_B \approx 2\pi \times 40\ Hz$ ($\sim$115 μG). The data in Figure 5-14 will be analyzed in detail in the following two sections, 5.4.1 and 5.4.2.

	+Z Full	+Z Half
U_0/k_B (μK)	100	50
$(\omega_{U_0}/2\pi)/(U_0/k_B)$ (Hz/μK) [fit]	7.92(0.30)	
$T/\sqrt{U_0/k_B}$ [fit]	2.17(0.19)	
$\omega_B/2\pi$ [fit]	70.0 (21.8)	
VLS (Hz) at 100 μK [cal]	792(30)	
T (μK) [cal]	21.7(1.9)	15.3(1.3)

Table 5-1. Fitting parameters for large vector light shifts measurement.

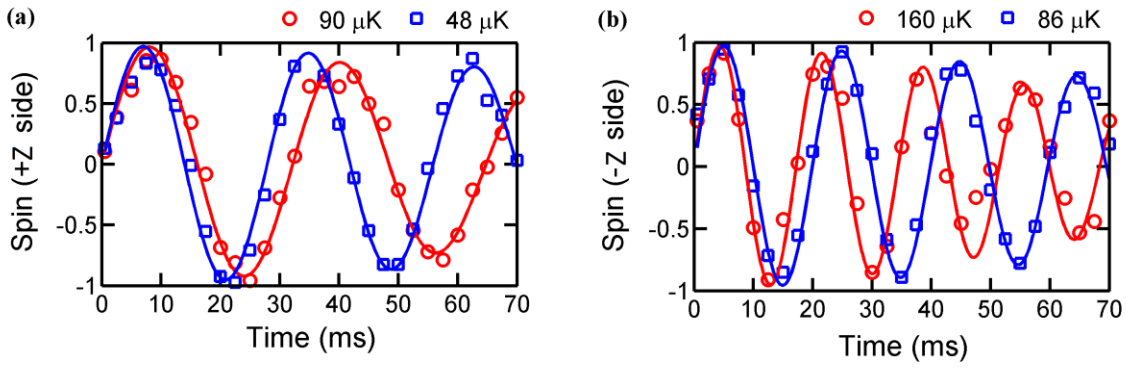

Figure 5-14. Measurement of small vector light shifts.

Blue squares and red circles are experimental data and the solid lines are fits using the model described in section 5.4.1.

5.4.1. Vector light shifts model with uniform effective magnetic fields

Historically, we thought the $\sim$115 μG magnetic field might be due to parts of the magnetic shields (like shield collars or shims) that have not been fully degaussed and behave

ferromagnetically. Since then, we have disassembled the magnetic shields and tested their performance in a different room. Surprisingly, this hypothesis has been proven false. At this point we do not yet have a definitive conclusion about the origin of ω_B. We have constructed two classes of models with many variations to infer possible mechanisms behind Figure 5-14, as detailed in the following sections 5.4.1 and 5.4.2, respectively. The two classes of relevant calculations show what effects we have ruled out and provide insights for future verifications and improvements.

The first class of models assumes the existence of $\omega_B \approx 2\pi \times 40\ Hz$, or equivalently a $\sim 115\ \mu G$ effective and uniform magnetic field along y direction. We will first discuss the models in detail and then describe how we rule out the three possible origins of the $\sim 115\ \mu G$ effective and uniform magnetic field along y direction.

In Figure 5-14, since ω is comparable to ω_ρ and smaller than ω_y, we calculate $S(t)$ in a somewhat different way, assuming that the atoms sample their whole transverse orbits during a spin precession. The result is:

$$S(t) = \sum_{n,n_y} p(n_y)p(n)sin\{[\omega_B + \omega_U(n,n_y)]t\} \tag{5.16}$$

With $n = n_x + n_z$,

$$p(n) = \left(1 - e^{-\frac{\hbar\omega_\rho}{k_B T}}\right)^2 \cdot (n+1)e^{-n\cdot\frac{\hbar\omega_\rho}{k_B T}} \tag{5.17}$$

the Boltzmann distribution of transverse modes, and

$$\omega_U(n,n_y) = \omega_{U_0}\left[1 - \frac{1}{2}(n+1)\frac{\hbar\omega_\rho}{U_0} - \frac{1}{2}\left(n_y + \frac{1}{2}\right)\frac{\hbar\omega_y}{U_0}\right] \tag{5.18}$$

the average ω for the trap vibrational mode numbers (n, n_y). We find that this quantum mechanical approach makes it easy to average over all semiclassical atom trajectories, at the small cost of extra computational time due to the ~60,000 occupied modes. We fit the data in

Figure 5-14 to Eq. (5.16) for both lattice depths of each lattice simultaneously and the fitting parameters are listed in Table 5-2. Since ω_U is much smaller than ω_B, there is little dephasing,

	+Z Full	+Z Half	-Z Full	-Z Half
U_0/k_B(μK)	90	48	160	86
T (uK) [set]	20.6	15.0	27.4	20.1
$\omega_B/2\pi$ (Hz) [fit]	39.51(0.44)		43.09(0.84)	
$(\omega_{U_0}/2\pi)/(U_0/k_B)$ (Hz/μK) [fit]	-0.139(0.0046)		0.123(0.0044)	
θ (radians)	-1.50(5)E-4		+1.33(5)E-4	

Table 5-2. Fitting and derived parameters for small vector light shifts measurement.

and we are not very sensitive to T, getting negligibly different results for ω_{U_0}/U_0 and ω_B if we fit to $T/\sqrt{U_0}$, or keep it fixed at either the value extracted from Figure 5-13 or the directly measured value. The fit values for $\omega_{U_0}/2\pi$ with a 100 μK trap depth are 13.9 $\pm$ 0.5 Hz (+Z) and 12.3 $\pm$ 0.4 Hz (-Z). These correspond to polarization imperfections of $\theta_{+Z} = -1.50(5) \times 10^{-4}$ radians and $\theta_{-Z} = 1.33(5) \times 10^{-4}$ radians, or fractional intensity impurities of $2.2(2) \times 10^{-8}$ (+Z) and $1.8(1) \times 10^{-8}$ (-Z), about two orders of magnitude better than can be measured with a Glan laser prism. The signs are different because the residual circular polarizations of the two lattices have opposite handedness.

We now discuss the possible origins of the ~115 μG effective and uniform magnetic field along y direction. The first possibility is a uniform magnetic field inside the glass cell. During the period when the VLS data is taken, we had not yet tested some aspects of the shields (i.e. shield shims or collars that are used to improve the shielding factors) which were added after the main part of the shield was installed around the measurement chamber. This motivated a more complete magnetic test after we disassembled the shields from the measurement chamber and reassembled it in a different room, where we had enough space and did not have to work around the fragile glass cell. The performance of the shields in various situations that are similar to that near the measurement chamber is listed in Table 5-3. The conclusion is that the magnetic fields

inside the shields are 10 μG at most and the various parts inside the innermost shield layer are not magnetic at a sensitivity level of 5 μG.

Item	Test subject	Conclusion
Parts inside shields	Measure magnetic fields of the following parts at a distance of 1cm away from the sensor: Microwave antenna, cooling optics, plastic mounts and platforms, titanium mirror mounts, entire photodiode arrays and mounts, degaussing coils, entire 8-set bias/gradient coils and plexi-glass cylinders, Pyrex glass cell and Pyrex to fused silica graded seal Parts untested: field plates and titanium-mounting structures	All parts are nonmagnetic at a sensitivity level of 5 μG
Magnetic shields	Shield shims and collars do not contribute to magnetic field inside after degaussing	The shields have about $\leq 10\ \mu G$ after degaussing
	Shields have no measureable larger residues when degaussed in large-scale concentric gradient	
	Response to a 0.3 G at 0.5 m ion pump magnet, the shields have a 60uG field inside. Degauss with the presence of the magnet, the residual field is ⩽10 μG; then remove the magnet, the field inside is about 45 μG; then put the magnet back to its original location, the residual field is again ⩽10 μG	
	Shields do not develop hysteretic magnetization after running a MOT-like pulsed 0.4 G field for more than 8000 cycles (15 hours), along either y or x direction. When the 0.4 G field (in the center location without shields) is on, the field in the center with shields is around 15 μG.	
	The MOT and Zeeman coil have about ⩽0.3 G at the bottom glass cell flange and ⩽50 mG near the unshielded glass cell, which will cause field changes in the glass cell on the order of ⩽1.4 μG with shields	
	Shields have no measureable hysteresis after switching on and off a Bx=20 mG bias field in a pattern similar to microwave transition and detection for 100 cycles	

Table 5-3. Magnetic tests of the measurement chamber using a fluxgate magnetometer.

The second possibility is a uniform fictitious magnetic field of $\sim 115\ \mu G$ (or equivalently 40 Hz VLS) due to diffuse scattered light from MOT beams. Since the all the cooling and detection beams that go into the glass cell are blocked by mechanical shutters, the residual light is would have to come from the MOT chamber. All MOT beams were unblocked at the time of Larmor precession experiment, but were turned off by the acoustic optical modulators (AOM), which allows ~5 $\mu W/cm^2$ per beam to pass through. All MOT beams were not in the direct line of sight of atoms. With the enclosure of the shields, only a small fraction can leak into the glass cell through multiple scatterings on the inner surfaces of the vacuum chamber. The fact that atoms do not heat up and decohere for a time scale of 1 second suggests the diffuse scattering light must be off resonance with respect to the Cs F=3 hyperfine. MOT cooling beams are 9.2 GHz detuned from the F=3 hyperfine, which cannot account for the 40 Hz VLS even if the full 5 $\mu W/cm^2$ was shined at the atoms. The relevant MOT beam is the repumping beam, with a frequency (un-shifted by the AOM) that is -40MHz detuned with respect to the F=3 hyperfine. A 40 Hz VLS corresponds to an intensity of 0.2 $\mu W/cm^2$, a factor of 25 smaller than the residual repumping beam intensity. When the experiment is reassembled in the future, all MOT beams will be blocked by the addition of mechanical shutters and the effect of possible cooling light induced VLS can be directly verified.

The third possibility is a 40 Hz VLS from the 1064 nm light that has spatially uniform and constant intensity. For circularly polarized light, it corresponds to 7.6 mW/cm^2, or equivalently 2×10^{-7} of the maximum lattice beam intensity when the cavities are in lock. Scattering from the optical lattice beams themselves is unlikely, because their intensity is changed when we change the trap depth using a combination of a Pockels cell and a Glan laser prism. Thus, if the uniform and constant 1064 nm light accounts for the total VLS, it must come from locations before the Pockels cell (~10 Watt cavity input beam), so that the unwanted 7.6 mW/cm^2 light remains unaltered when we change the trap depths. A definitive test for the spatially uniform

and constant 1064 nm light is to perform a spin procession experiment at two different trap depths by changing the 10 W fiber amplifier output power directly, instead of using the Pockels cell.

5.4.2. Vector light shifts model with intensity-dependent polarization imperfections

Our second class of models eliminates the essentialness of ω_B and assumes the ~40 Hz Larmor precession is only caused by the optical lattice beams. We will first derive the models with intensity dependent polarization quality in detail. We will then discuss how we estimate and rule out two classes of possible origins of intensity dependent polarization quality in out optical lattice system, nonlinear optical Kerr effects (section 5.4.2.1) and thermally induced birefringence (section 5.4.2.2), respectively.

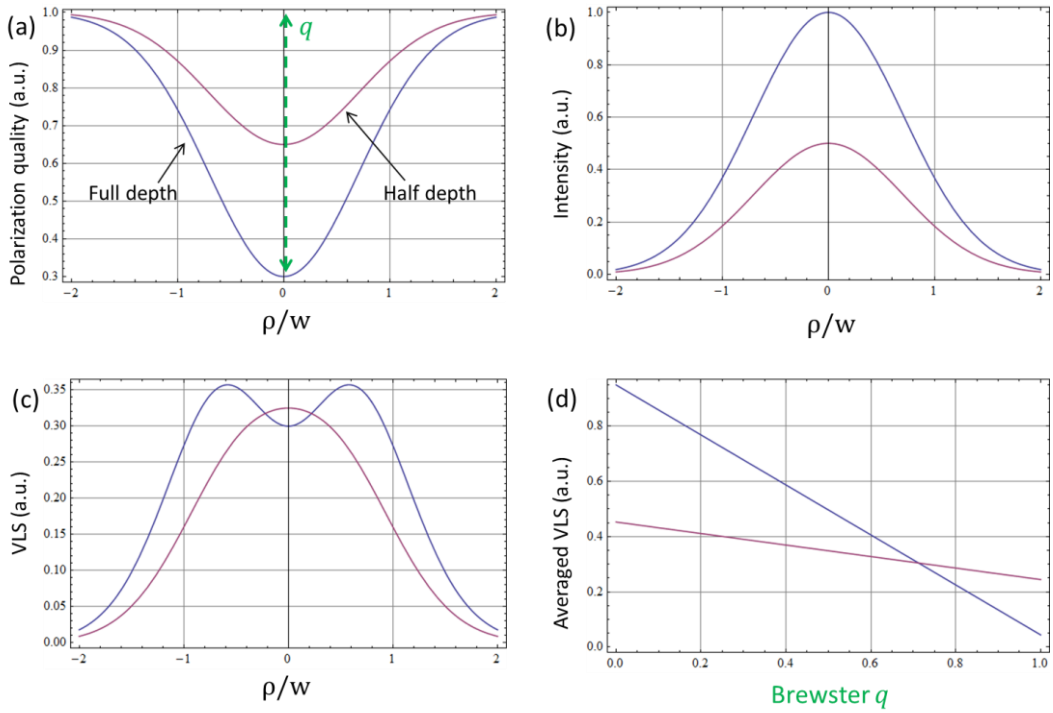

Figure 5-15. Vector light shifts due to nonlinear optical effects.

(a)-(c): polarization quality, intensity and spatially varying VLS as a function of transverse position ρ/w for the Brewster alignment parameter q=0.7; (d) spatially averaged VLS from integration of (c) shown as a function of q.

We begin by assuming an intensity dependent polarization quality across the lattice beams,

$$\theta(\rho, q) \propto 1 - q \cdot \frac{I(\rho)}{I_s(\rho)} \tag{5.19}$$

Where $I_s(\rho)$ is the intensity at which we optimize the Brewster plates to minimize their reflections when the cavities are in lock (see 3.1.2). At the time of the experiment we had optimized this step with the peak intensity available in order to maximize our alignment sensitivity. q is the Brewster alignment parameter that characterizes to what extent the Brewster plates are aligned such that the polarization quality in the center of the lattice beams is better than that away from the center, as shown in Figure 5-15(a). Consequently, for a lower trap depth, the polarization quality in the beam center is worse by $q/2$.

The spatially dependent VLS then yields

$$\omega_U(\rho, q) \propto I(\rho) \times \left[1 - q \cdot \frac{I(\rho)}{I_s(\rho)}\right], \tag{5.20}$$

which is a nonlinear function of the beam intensity, conversely to the model in section 5.4.1. The VLS is plotted in Figure 5-15(c) for two different trap depths. The averaged VLS is $\overline{\omega_U}(q) = \int \omega_U(\rho, q) f(\rho) d\rho$ is shown in Figure 5-15(d). For this nonlinear model with q~0.7, the magnitude of the VLS remains constant when the trap depth is changed by a factor of two. The observed spin precession is the weighted spatial average

$$S(t, q) = \int sin\{[\omega_U(\rho, q)]t\} f(\rho) d\rho \tag{5.21}$$

We fit the measured spin precession data (same as Figure 5-14) to Eq. (5.21) and the results are shown in Figure 5-16. The nonlinear model can qualitatively explain the fact that the measured spin precession frequencies change only slightly when we halve the trap depths, and the precession does not damp out in a few cycles. Nevertheless, because the model predicts that, for

any q, the dephasing time gets longer for a lower trap depth as seen in Figure 5-16(a), it fails to explain the observed change of dephasing time upon a change in the trap depth in Figure 5-16(b).

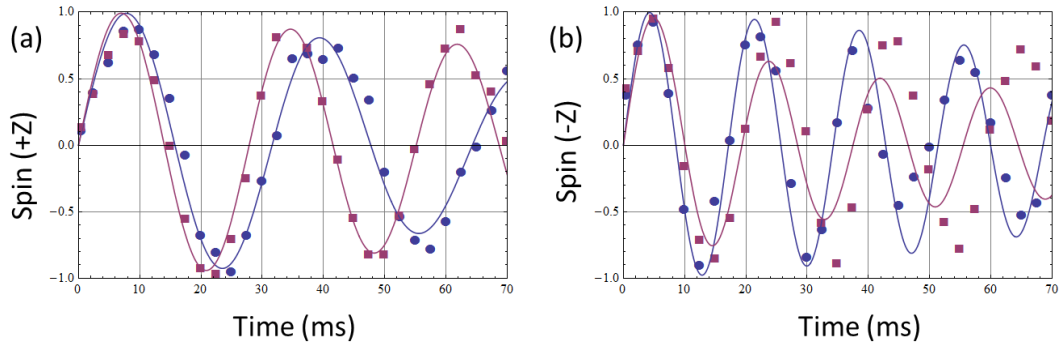

Figure 5-16. Performance of the nonlinear optical effect model.

Magenta squares and blue filled circles are experimental data (same as Figure 5-14) and the solid lines are fits using Eq. (5.21). Data on the +Z side (a) can be fit to the model with q~0.75 and data on the -Z side (b) can be fit to the model with q~0.65 to account for the difference in precession frequency, but the fitting in (b) does not work well since this model gives a unique sign of change on dephasing that agrees with (a), but not (b).

To account for the 40 Hz precession due to the VLS induced by the lattice beams within this hypothesis, the birefringent phase shift is $\theta = 4.3 \times 10^{-4}$, and the wrong polarization component is 1.9×10^{-7} in fractional intensity. The hypothesis can be potentially checked in the future when the experiment is reassembled again by optimizing the Brewster plate alignment at half the trap depth (instead of the maximum trap depth), and looking for difference in Larmor precession when the trap depth is increased, by a factor of 2 for instance. In that case, in contrast to Figure 5-15(a), in the beam center where atoms are trapped, the polarization quality for the higher trap depth will be worse than that of a lower trap depth.

5.4.2.1. Nonlinear optical Kerr effects

We have evaluated nonlinear optical effects that could possibly give rise to a spatial dependence of polarization quality according to Eq. (5.19). Ffor instance, the optical birefringence effect from the 3rd order induced electric dipole moments of the lattice beams through the intra-cavity elements is [16]

$$\boldsymbol{P}^{NL} = 6\epsilon_0\chi_{1122}(\boldsymbol{E}\cdot\boldsymbol{E}^*)\boldsymbol{E} + 3\epsilon_0\chi_{1221}(\boldsymbol{E}\cdot\boldsymbol{E})\boldsymbol{E}^*, \tag{5.23}$$

where $\boldsymbol{E}$ is the electric field of the lattice laser beams and $\chi_{ijkl} = \chi^{(3)}_{ijkl}(\omega_4 = \omega_1 + \omega_2 + \omega_3)$ is the 3rd order susceptibility, a fourth-rank tensor. The nonlinear dipole leads to the optical Kerr effect, with an intensity-dependent refractive index $n(I) = n_0 + n_2 I$. In an isotropic medium like fused silica, the nonlinear Kerr coefficient is $n_2 = 3.2 \times 10^{-20}\ m^2/W$ [16]. As described in Eq. (5.23), the first term produces a nonlinear polarization with the same handedness as $\boldsymbol{E}$, whereas the second terms produces a nonlinear polarization with the opposite handedness. Consequently, the difference in the refractive indices of two circular components ($\boldsymbol{E}_L$, $\boldsymbol{E}_R$), is given by [16]

$$\delta n_{Kerr} = \frac{3\chi_{1221}}{n_0}\left(|\boldsymbol{E}_R|^2 - |\boldsymbol{E}_L|^2\right). \tag{5.24}$$

Only for a perfectly linearly polarized light ($|\boldsymbol{E}_R|^2 = |\boldsymbol{E}_L|^2$) or perfectly circularly polarized light will the optical birefringence (or equivalently the rotation of the polarization ellipse) be zero. For a typical elliptical polarization input, nonlinear Kerr effects lead to an intensity-dependent polarization rotation.

Our inter-cavity elements contain two Infrasil® windows and a pair of fused silica Brewster plates. With a total effective thickness L= 29.5 mm, at maximum lattice beam intensity $I_{max} = 3.8 \times 10^8\ W/m^2$(with a linear polarization quality better than 10^{-6} in fractional intensity), in order to have a birefringent phase shift that can give 40 Hz VLS, the resulting Kerr coefficient would have to be $> 1.3 \times 10^{-11}\ m^2/W$, more than 8 orders of magnitude higher than that of fused silica. We have two high reflective coatings from two cavity mirrors and 4

anti-reflective coatings on the two vacuum windows. The optical coatings can have a Kerr coefficient that is 1~2 orders of magnitude higher than fused silica [17], but their total thickness is less than 20 μm, so the overall birefringent phase shift from optical coatings is unlikely to account for the 40 Hz VLS either.

There is an enhancement of optical nonlinearities for high intensity standing waves. For example, in sodium vapors [18] and fused silica fibers [19], due to additional four-wave mixing processes, substantial depolarization has been observed when the nonlinearity parameter $kn_2 I_{max} L$ is on the order of unity. In our system, $kn_2 I_{max} L = 2.3 \times 10^{-6}$, which is more than 5 orders of magnitude below the threshold for the onset of that enhancement.

5.4.2.2. Thermal effects: thermal lensing and thermal-stress induced birefringence

To estimate the size of thermally induced stress birefringence in our optical lattice system, let's first consider the case where the temperature distribution is cylindrically symmetric. For a high power CW laser beam transmitting through an isotropic window with internal absorption β and thickness l, we estimate the temperature increase, $T(\rho, t)$, from a thermal model that includes volumetric heating and heat conduction [20], to be

$$T(\rho, t) = \frac{\dot{T}_0}{4\kappa/w^2}\left[E_i(-\rho^2/w^2) - E_i\left(-\frac{\rho^2/w^2}{1+4\kappa t/w^2}\right)\right], \tag{5.25}$$

where the temperature changing rate at the center is given by $\dot{T}_0 = \beta I_{max}/\tilde{\rho}c$, with $\tilde{\rho}c \approx 1.6 \times 10^6\ J/(m^3 K)$ the volumetric heat capacity of the window, $\kappa \approx 8.5 \times 10^{-7}\ m^2/s$ is thermal diffusivity of the window, and $E_i(x)$ is the exponential integral of negative arguments, $E_i(x) = -\int_x^\infty t^{-1} e^{-t} dt$. Eq. (5.25) only holds for a thin window (thickness ≪ diameter). We have compared the temperature profile with a more general but slightly computation intensive model

which works for both thin window and long-rod geometries [21], and found negligible differences (< 10%) between the two models with our parameter settings.

At this moment, we have used two 12.7 mm-thick Infrasil® windows (Heraeus Infrasil® 302) with absorption coefficient $\beta \approx 200\ ppm/cm$ (due to metallic impurities), and a pair of 2 mm-thick Brewster plates (Corning glass code 7980) with $\beta \approx 120\ ppm/cm$ (due to $\sim 1000\ ppm$ level OH contents). Eq. (25) gives a worst-case estimate for the temperature distributions, because steady-air surface convection cooling from the outer surface of the vacuum windows and two surfaces of the Brewster plates will lead to a lower temperature in our experiments. The temperature profile of the Brewster plates are not cylindrically symmetric, because of elliptical projection of the lattice beams. We will estimate the possible thermal effects due to anisotropic temperature profile for this special case later on.

The temperature distribution according to Eq. (5.25) for a vacuum window is shown in Figure 5-17(a). For regions within 1.5 beam waists of the center of the lattice beamsthe temperature profile can be approximated as $T(\rho, t) \cong T_0(t) + T_M[1 - (\rho/\rho_c)^2]$, where the term $T_0(t)$ describes a uniform temperature change across the lattice beams, whichincreases in time approximately as $T_0(t) \propto tlog(t)$. One minute after the lattice beams are turned on, the curvature of the temperature is approximately constant, with $T_M \approx 0.37\ K$ and $\rho_c \approx 2w$. The temperature change leads to thermal expansions of the vacuum window. In the most critical regions of interest, in particular within 3 beam waists, the curvature of the temperature profile leads to phase shifts across the lattice beams, which are origins of thermal lensing effects and thermal-stress induced birefringence.

The cylindrically symmetric phase shift relevant to thermal lensing of a thin window is given by [22, 23]

$$\phi_L(\rho) \approx kl \frac{dn_0}{dT}\, T(\rho) \tag{5.26}$$

Where the temperature coefficient of the window is $dn_0/dT \approx 11.5 \times 10^{-6}\ K^{-1}$, $\alpha = 5.1 \times 10^{-7}\ K^{-1}$ is the linear thermal expansion coefficient, $E = 70\ GPa$ is the modulus of elasticity, $\nu = 0.17$ is the Poisson's ratio. The approximation in Eq. (5.26) has ignored thermal stress induced refractive index change [22, 23], which is about 40 times smaller than the dominate linear expansion term dn_0/dT. Figure 5-17(b) shows the thermal lensing phase shift calculated from the temperature profile. The maximum thermal phase distortion is about 0.05 waves across the lattice beam. Similar to a regular lens, we found the effective focal length of the lens from the quadratic coefficients $\phi_L(\rho)$ to be

$$f_T = \frac{\rho_c^2}{2l(dn_0/dT)T_M} \approx 48.5\ m \tag{5.27}$$

Which is about 24 times longer than the focal length of our cavity mirrors ($R = 2\ m$). The effect of a thermal lens near cavity mirrors of a confocal cavity can be seen from the ABCD matrix formulism

$$\begin{pmatrix} 1 & 0 \\ -\frac{1}{f_T} & 1 \end{pmatrix}\begin{pmatrix} 1 & 0 \\ -\frac{2}{R} & 1 \end{pmatrix}\begin{pmatrix} 1 & 0 \\ -\frac{1}{f_T} & 1 \end{pmatrix} = \begin{pmatrix} 1 & 0 \\ -\frac{2}{R^*} & 1 \end{pmatrix}, \qquad R^* = R\frac{f_T}{f_T+R}, \tag{5.28}$$

which is equivalent to reducing the cavity mirror focal length R by 4%, to 1.92 m. Adding a small propagation distance $d \ll R \ll f_T$ between the thermal lens and the cavity mirror does not change the answer to the leading order. In our experiments, we have not observed lattice intensity drifts that are directly correlated to the thermal lensing at this level. The cavity lengths are initially configured to $\sim 2.1\ m$ (10 cm longer than the confocal condition) to lift of the degeneracy of transverse (TEM_{00} and TEM_{01}) cavity modes. Since thermal lensing can only change the transverse cavity mode further away from the confocal condition by an extent which is smaller than our initial configuration, we have not observed intensity drifts that are correlated to thermal lensing at this level. Furthermore, thermal lensing only changes the lattice beam wave vectors in a

cylindrically symmetric way (much less than their initial spread). Thus the intensity averaged vector and the polarization quality remain unaltered.

Anisotropy of the phase shift across the lattice beams would degrade the linear polarization quality if the lattice beam polarization is not perfectly aligned to the axes of anisotropy. For instance, our vacuum window has an averaged mechanical stress birefringent phase shift $\phi_B^* \approx 8.4 \times 10^{-3}\, rad$ [24] and if the input linear polarization is misaligned with respect to one of the birefringent axes by a small angle γ (we typically have a $\gamma \leq 5^o$ misalignment error), the transmitted beam will have a spatially uniform circular polarization component $I_\sigma^*(\rho)/I(\rho) = sin^2(2\gamma)sin^2[\phi_B^*]$ in fractional intensity, which does not depend on the lattice beam intensity. Although both the vacuum windows and Brewster plates are made of isotropic glass, low residual stress resulting from window mounting, and thermal stress due to elliptical projection and the epoxy mounting of one side of the Brewster plate into an aluminum holder, could make these intra-cavity elements slightly anisotropic.

Thermal stress in an anisotropic window results in an intensity-dependent birefringent phase shift that could also degrade the lattice beam linear polarization quality. For a cylindrically symmetric temperature profile, the thermal stress birefringent phase shift is determined by the difference between the radial (σ_ρ) and azimuthal (σ_θ) thermal stress [22-23]

$$\begin{aligned} \phi_B(\rho) &= \frac{kln_0^3}{4}\left(q_{||} - q_\perp\right)\left(\sigma_\rho - \sigma_\theta\right), \\ \sigma_\rho - \sigma_\theta &= \frac{\alpha E}{1-\nu}\left[T(\rho) - \frac{2}{\rho^2}\int_0^\rho T(\rho')\rho' d\rho'\right]. \end{aligned} \tag{5.29}$$

Where the symbols $q_{||}$ and $q_\perp$ refer to the stress-optic coefficients for stress applied parallel and perpendicular to the polarization axis [25]. For fused silica the coefficients are $q_{||} = 0.6 \times 10^{-12}\, m^2/N$, $q_\perp = 5.8 \times 10^{-12}\, m^2/N$ [26]. For a linearly polarized beam, the transmitted beam will have a circular polarization component

$$I_\sigma(\rho,\psi) = sin^2(2\psi)sin^2[\phi_B(\rho)] \times I(\rho), \tag{5.30}$$

with ψ the relative angle with respect to the linear polarization axis [22]. Due to local thermal stress, the output beam thus has a circular polarization component which has a $sin^2(2\psi)$ angular dependence that breaks the cylindrical symmetry [27]. A general model with a detailed explanation of the angular dependence is given in Appedix-F.

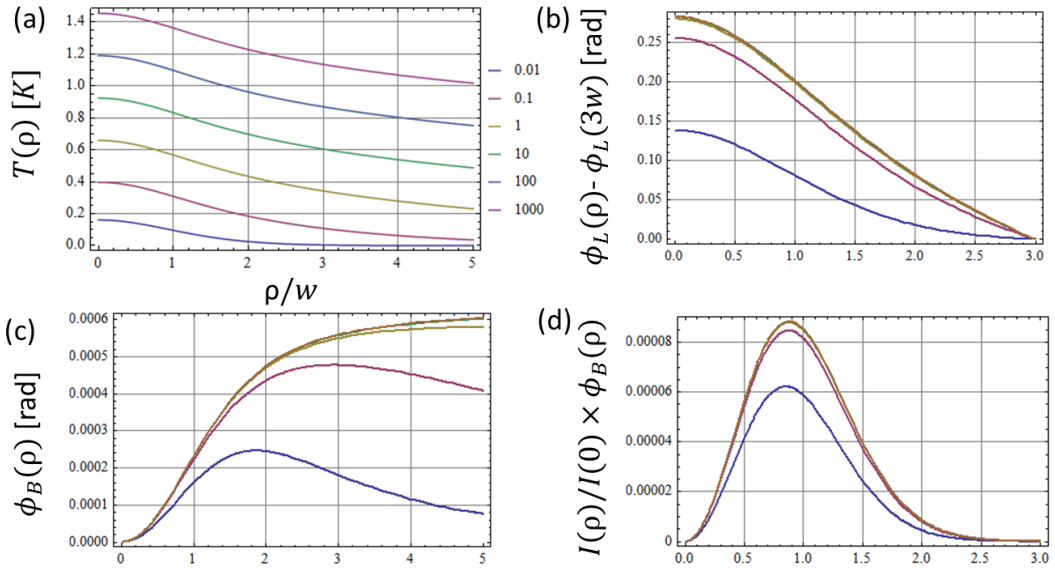

Figure 5-17. Thermal effects of due to vacuum window absorption.

All horizontal axes are in unit of lattice beam waist radius. (a) The temperature distribution for a vacuum window for different lattice turn-on times from 0.01 to 1000 minutes. (b) Cylindrically symmetric thermal lensing phase shift. (c) Thermal-stress induced birefringent phase shift due to window anisotropy. (d) Replot of (c) multiplied by normalized intensity profile as a measure of the VLS.

Plots of $\phi_B(\rho)$ and intensity weighted $\phi_B(\rho)$ for the vacuum window can be found in Figure 5-17(c) and Figure 5-17(d). A striking feature is that the thermal stress birefringence is zero at the center of lattice beams since $\sigma_\rho(0) = \sigma_\theta(0)$ and is peaked at approximately 1 beam waist [27]. This is very interesting since it gives a functional shape of the polarization quality similar to that described by Eq. (5.19). Intensity weighted $\phi_B(\rho)$ is a measure of the VLS similar to Eq. (5.20). Since the distribution of atoms has a transverse size of $w/3$, the maximum

birefringent phase shift relevant to the VLS from Figure 5-17(d) is $2 \times 10^{-5}\ rad$ for the vacuum window, which is about 22 times smaller than what is needed to account for the 40 Hz VLS. Furthermore, birefringence phase distortions (see Eq. (5.30) and Appendix Figure F-2 and F-3) have an intrinsic odd symmetry built into them. So for both the vacuum windows and the Brewster plates, 2 out of 4 quadrants across the beams have opposite signs compared to the other two quadrants. For a symmetrical atom distribution in the pancake traps, the VLS from the thermally induced stress birefringence cancels to the leading order. Only to the extent that the mirror symmetry of temperature distribution is broken or the atoms sample only part of the traps is the net VLS shift nonzero. This level of thermal birefringence will not affect the adjustment of the Brewster plates while the cavities are in lock, since we only have a sensitivity level of 0.5~1 ppm in fractional intensity for the fine adjustment (see section 3.1.2), much larger than the thermally induced fractional depolarization.

For the special case of the Brewster plates, due to the elliptical projection of lattice beams at Brewster's angle, the temperature distribution anisotropy leads to thermal stress birefringence which is not described by Eq. (5.29). The general model as derived in Appendix-F shows that birefringent phase shift of Brewster plates relevant to the VLS of atoms is ~12% of that of vacuum windows, since the vacuum windows are 6 times thicker and have higher internal absorption. Precision alignment of laser beam polarization along the major axis does not avoid the thermally induced birefringent depolarization, because of the spatial dependence of thermal stress across the lattice beams.

Only recently, a new silica grade, isotropic Heraeus Suprasil® 3001 has become commercially available, together with a precisely measurement of absorption at 1064 nm, $\beta \approx 0.5\ ppm/cm$ [28]. Replacement of Brewster plates and vacuum windows with this high quality silica (also with a reduced thickness of 6.2 mm) is in progress, which will reduce the size

of the temperature gradients and suppress any possible thermal effects by more than two orders of magnitude.

5.5. Limitations of the technique and future improvements

Progress is being made to identify the origin of the 40 Hz precession frequency, as described in details in section 5.4.1 and 5.4.2. If the former is verified, or equivalently a 115 μG level (either real or fictitious) magnetic field source has been found, it is then straight forward to either eliminate the magnetic source or block the unwanted light. If the latter is verified, additional effort might be needed to reduce the overall size of the effect by replacing with high quality intra-cavity optics, or to stabilize and equalize the size of the effects on both optical cavities. If that is done, then it can be treated as a constant residual magnetic field along the y direction, which can be cancelled using the bias coil By.

When the magnetic fields are zeroed to a level that is close to the inhomogeneous spread of VLS's, the spin precession signal is significantly smeared out, which makes magnetic fields zeroing to a smaller level very challenging. As an example, Figure 5-18 shows a set of calculated spin precession curves using Eq. (5.15), where we set the VLS to be $10\ Hz$, inhomogeneous spread of the VLS to be $2.5\ Hz$, and vary the bias magnetic field. For small composite precession frequencies $\omega_B + \omega_U \to 0$, the precession no longer behaves like a simple phase accumulation that is linear in time.

An experimental data set when magnetic fields are coarsely zeroed is shown in Figure 5-19. The spin precession along all three directions does not follow a simple Larmor precession model with dephasing, which is partially due to the motion of atoms in the pancake traps. At a $100\ \mu K$ trap depth, the axial (transverse) trapping frequency is $105\ kHz$ ($30.7\ Hz$), over an entire Larmor precession period (approximately $1\ sec$), the atoms will sample a large volume of space in the

presence of inhomogeneous fictitious magnetic fields. It is experimentally impractical to utilize the spin precession in such complex 3D geometries to back out the magnetic fields. It is also impossible to cancel out the inhomogeneous fictitious magnetic fields using a uniform bias or gradients.

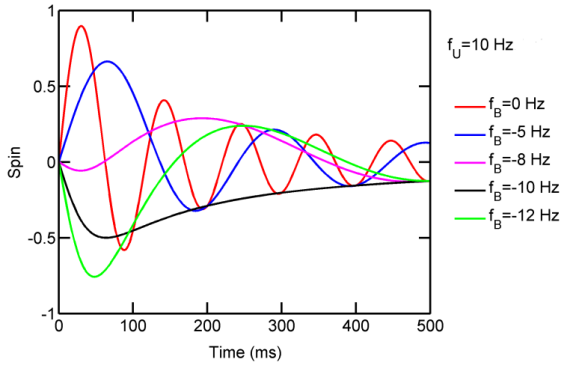

Figure 5-18. Calculated spin precession with inhomogeneous vector light shifts.

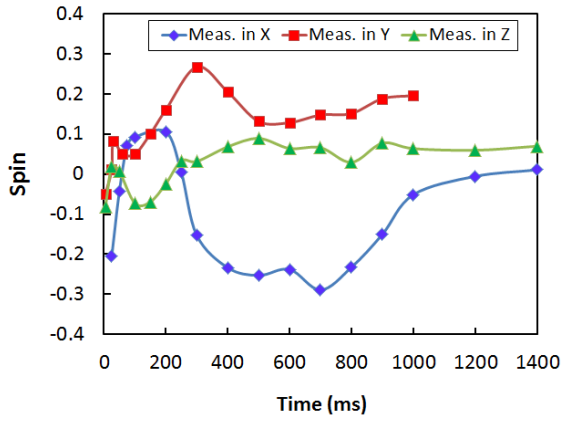

Figure 5-19. Measurement of spin precession in coarsely zeroed magnetic fields.

The current level of nulled magnetic fields that are perpendicular to the DC electric field (E_z) used in the final EDM measurement are good enough, as we will discuss in Chapter 6. A better zeroing for the magnetic field along the DC electric field, which is critical for the final EDM measurement, can be done using a procedure with the Stark energy structure that is identical to the EDM measurement: by setting the bias coil B_z so that the EDM interferometric

phase is close to zero. Using just a few shots of measurements, the technique should allow cancellation of the magnetic field along the z direction to a level that is at least comparable our single shot sensitivity to EDM signals (Chapter 7, Table 7-1), or equivalently down to the *pG* level.

5.6. References

[1] W. Hanle, *Magnetic influence on the polarization of resonance fluorescence*, Z. Phys. **30**, 93 (1924).

[2] D. Budker et. al., *Resonant nonlinear magneto-optical effects in atoms*, Rev. Mod. Phys. **74**, 1153 (2002).

[3] M. A. Morrison and G. A. Parker, *A guide to rotations in quantum mechanics*, Aust. J. Phys. **40**, 465 (1987).

[4] M. Weissbluth, *Atoms and Molecules*, Academic Press, Student edition, (1980).

[5] E. Merzbacher, *Quantum Mechaincs*, John Wiley & Sons, Inc., 2nd edition, p282, (1970).

[6] B. S. Mathur, H. Tang and W. Happer, *Light shifts in the alkali atoms*, Phys. Rev. **171**, 11 (1968).

[7] I. H. Deutsch and P. S. Jessen, *Quantum-state control in optical lattices*, Phys. Rev. A **57**, 1972 (1998).

[8] M. V. Romalis and E. N. Fortson, *Zeeman frequency shifts in an optical dipole trap used to search for an electric-dipole moment*, Phys. Rev. A **59**, 4547 (1999).

[9] J. Morville and D. Romanini , *Sensitive birefringence measurement in a high-finesse resonator using diode laser optical self-locking*, Appl. Phys. B **74**, 495 (2002).

[10] G. N. Birich, et al., *Precision laser spectropolarimetry*, J. Russian Laser Res. **15**, 455 (1994).

[11] M. Durand, et al., *Shot-noise-limited measurement of sub–parts-per-trillion birefringence phase shift in a high-finesse cavity*, Phys. Rev. A **82**, 031803(R) (2010).

[12] G. Zavattini, et al., *Measuring the magnetic birefringence of vacuum: the PVLAS experiment*, Int. J. Mod. Phys. A **27**, 1260017 (2012).

[13] K. Zhu, N. Solmeyer, Cheng T. and D. S. Weiss, *Absolute polarization measurement using a vector light shift*, Phys. Rev. Lett., submitted, (2013).

[14] S. L. Winoto, et al., *Laser cooling at high density in deep far-detuned optical lattices*, Phys. Rev. A **59**, R19 (1999).

[15] A. Kastberg, et al., *Adiabatic Cooling of Cesium to 700 nK in an Optical Lattice*, Phys. Rev. Lett. **74**, 1542 (1995).

[16] R. W. Boyd, *Nonlinear Optics*, Academic Press, 3rd edition, chapter 4 (2008).

[17] R. L. Sutherland, *Handbook of Nonlinear Optics*, CRC Press, 2nd edition (2003).

[18] A. L. Gaeta, et al., *Instabilities and chaos in the polarizations of counterpropagating light fields*, Phys. Rev. Lett. **58**, 2432 (1987).

[19] S. Pitois, G. Millot, and S. Wabnitz, *Nonlinear polarization dynamics of counterpropagating waves in an isotropic optical fiber: theory and experiments*, J. Opt. Soc. Am. B, **18**, 432 (2001).

[20] J. L. Zar, Temperature, *Stress and Optical Phase Difference for a Window Transmitting a CW laser Beam*, Avco Everett Research Laboratorary, Inc., Report 432, ADA042671 (1976).

[21] L. C. Malacarne, N. G. C. Astrath, and L. S. Herculano, *Unified theoretical model for calculating laser-induced wavefront distortion in optical materials*, J. Opt. Soc. Am. B, **29**, 1772 (2012).

[22] C. A. Klein, *Stress-Induced Birefringence, Critical Window Orientation, and Thermal Lensing Experiments*, Laser-Induced Damage of Optical Materials: 1980, Nat. Bur. Stand. U.S. Spec. Pub. 620, Washington, pp. 117–128.

[23] L. C. Malacarne, N. G. C. Astrath, and L. S. Herculano, *Laser-induced wavefront distortion in optical materials: a general model*, J. Opt. Soc. Am. B, **29**, 3355 (2012).

[24] N. Solmeyer, K. Zhu, and D. S. Weiss, *Mounting ultra-high vacuum windows with low stress-induced birefringence*, Rev. Sci. Instrum. **82**, 066105 (2011).

[25] C. A. Klein, *Optical distortion coefficients of high-power laser windows*, Optical Engineering **29**, 343 (1990).

[26] C. A. Klein, *Figures of merit for high-energy laser-window materials: thermal lensing and thermal stresses*, Proc. SPIE 6403, Laser-Induced Damage in Optical Materials: 2006, 640308 (January 15, 2007).

[27] C. E. Greninger and S. E. Rodriguez, *Thermal stress, optical distortion, and birefringence in a heated cylindrical trigonal crystal rod*, J. Appl. Phys. **87**, 8545 (2000).

[28] Heraeus datasheet, *Suprasil® and Infrasil® – Material Grades for the Infrared Spectrum*, (2012).

Chapter 6

EDM spectroscopy for atoms in large electric fields

The core part of our eEDM measurement is the low frequency spectroscopy of atoms in large DC electric fields. In this Chapter, we will numerically explore the physics of atoms when the quantization axis is defined by the DC electric fields, and we will search and characterize the robust three-photon waveforms for EDM-sensitive spectroscopy. The theoretical results not only provide a complete physics picture, but also serve as an experimental guide for pulse design and hardware implementation.

6.1. Physics of electric field quantization

The relevant Hamiltonian for the F=3 hyperfine ground state is

$$H = \frac{1}{2}\alpha E_z^2 m_F^2 + g_F \mu_B B_x \sigma_x + g_F \mu_B B_z m_F \tag{6.1}$$

The first term accounts for the quadratic Stark shift, with $\alpha = (-3.99 \pm 0.03) \times 10^{-3}\ \frac{Hz}{kV/cm}$ the tensor polarizability [1]. The 2nd and 3rd term are Zeeman energy shifts due to magnetic fields perpendicular and parallel to the electric field, respectively. σ_x is the Pauli matrix for a system with angular momentum 3ħ, and couples states with $\Delta m_F = \pm 1$ [2]

$$\sigma_x = \frac{1}{2}\begin{pmatrix} 0 & \sqrt{6} & 0 & 0 & 0 & 0 & 0 \\ \sqrt{6} & 0 & \sqrt{10} & 0 & 0 & 0 & 0 \\ 0 & \sqrt{10} & 0 & \sqrt{12} & 0 & 0 & 0 \\ 0 & 0 & \sqrt{12} & 0 & \sqrt{12} & 0 & 0 \\ 0 & 0 & 0 & \sqrt{12} & 0 & \sqrt{10} & 0 \\ 0 & 0 & 0 & 0 & \sqrt{10} & 0 & \sqrt{6} \\ 0 & 0 & 0 & 0 & 0 & \sqrt{6} & 0 \end{pmatrix} \tag{6.2}$$

For a sanity check, the 2nd term σ_x in Eq. (6.1) can be diagonalized , which gives the typical Zeeman shifts as seen in the eigenbasis that is identical to the 3rd term ($\sigma_z = m_F$). Similarly, a magnetic field along y will introduce a transverse Zeeman shift that is proportional to $B_y\sigma_y$. The spinor matrices obey the angular momentum commutation relation $[\sigma_x, \sigma_y] = i\sigma_z$.

With a designed maximum DC electric field $E_z = 150\ kV/cm$ in our experiment, the quadratic Stark shift is $f_E = 45\ Hz$ for $m_F = 1$ level. In coarsely nulled magnetic fields ($\leq 3\ \mu G$), the quadratic Stark shifts are much larger than the Zeeman shifts ($\leq 1\ Hz$). The quantization axes are then defined by the DC electric fields.

6.1.1. Effect of transverse fields

Since there is a practical limit to the degree to which we can zero out the transverse magnetic fields in the measurement chamber, as discussed in Chapter 5, it is technically important to explore the effects of small transverse magnetic fields on the Stark shifted energy level structure. The most important question is how transverse magnetic fields will affect our EDM measurement.

Figure 6-1 shows the eigenstate energies for all 7 Zeeman sublevels as a function of the transverse magnetic field. At $B_x = 0$, the Zeeman sublevels $\pm m_F$ are completely degenerate. For small B_x , the energy separations for different $\pm m_F$ levels fortunately follow a power scaling law,

$$\Delta E_{\pm m_F} \propto x^{2|m_F|}, \tag{6.3}$$

where $x = \frac{g_F \mu_B B_x}{\frac{1}{2}\alpha E_z^2} \approx \frac{1}{45}$ is the ratio of Stark energy over Zeeman shift for $m_F = \pm 1$ level. The power scaling factor $2|m_F|$ comes from the "multi-photon" coupling between $\pm m_F$ levels. For instance, it takes six $\Delta m = +1$ magnetic dipole transitions to go from $m_F = -3$ to $m_F = +3$.

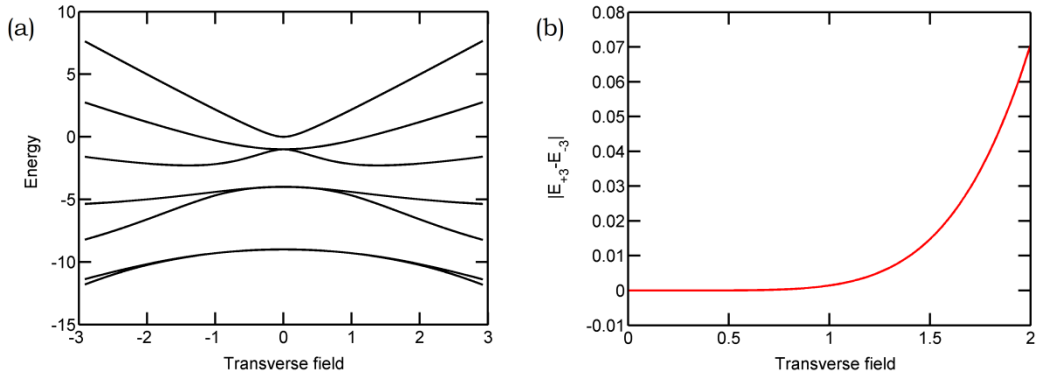

Figure 6-1. Energy levels for Cs in a large electric field and a transverse magnetic field. *(a) Energy for all 7 Zeeman sublevels in a large DC electric field E_z as a function of transverse magnetic field B_x , assuming $B_z = 0$. (b) The energy difference between $m_F = +3$ and $m_F = -3$ as a function of B_x . The energy and B_x are dimensionless and rescaled to the Stark shift of $m_F = 1$ level.*

For the interferometric states $m_F = \pm 3$ used for EDM measurements, the scaling factor is approximately $(1/45)^6 \approx 1.2 \times 10^{-10}$. The ten orders of magnitude suppression factor thus provides the most stringent protection for our atom interferometers from transverse magnetic fields.

As B_x increases, the $\pm m_F$ levels start to separate, and eventually when B_x is very large and the Zeeman shifts dominate, each energy level approaches the usual Zeeman shape that is linear in B_x. By ramping up B_x , $m_F = -3$ stays as $m_F' = -3$, $m_F = +3$ will change to $m_F' = -2$, $m_F = 0$ will become $m_F' = +3$, and so on. In the intermediate field regime, each Zeeman sublevel is a mixed state and is not well defined in either the basis of B_x or the basis of E_z.

6.1.2. Adiabatic B and E field switching

During the state preparation stage of our experiment, the quantization axis of the atoms is defined with magnetic fields. For the Ramsey-like EDM measurement sequence, the DC electric field defines the quantization axis. The final state-selective fluorescence detection needs to be

done in a bias magnetic field again. Because of possible state changing while switching between magnetic and electric fields, it is important to preserve the state in both bases.

Figure 6-2 shows a possible adiabatic switching sequence that is state preserving. Consider atoms initially in state $m_F = 0$, Figure 6-2 (a) indicates that if one keeps the bias magnetic field B_z and adiabatically ramps up the high voltage, the state will be still be in $m_F' = 0$. The same is true for all other 6 sublevels while we switch from a magnetically quantized (B) to an electrically quantized (E) basis. Similarly, as shown in Figure 6-2 (b), as long as we keep the high voltage on while adiabatically ramp up the bias field again, it is possible to map all states from the E basis to the B basis without state mixing.

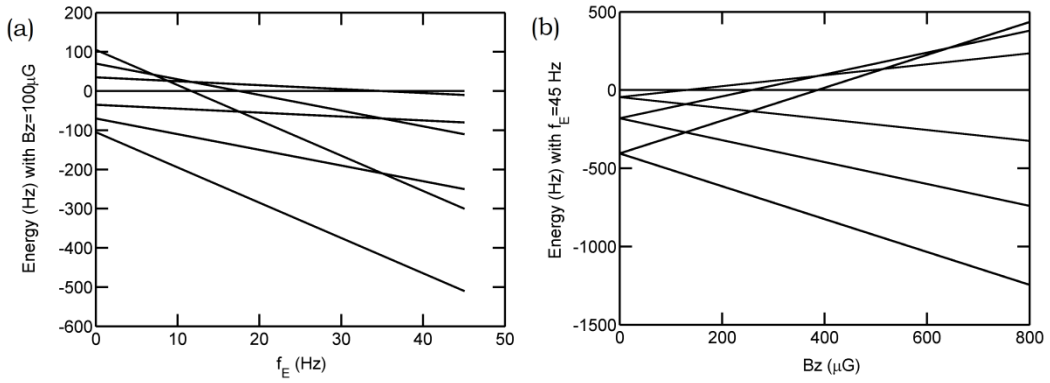

Figure 6-2. Energy levels for adiabatic B and E field switching.

Eigen-energies for all 7 Zeeman sublevels for Cs atoms in (a) a fixed $B_z = 100$ μG bias magnetic field as the DC Stark shift f_E is varied; (b) a fixed DC electric field $E_z = 150\ kV/cm$ when the bias B_z is changed.

6.2. Theoretical study of low frequency transitions

The first step in the core part of our EDM spectroscopic measurement is to drive all the atoms from the initial state $|0\rangle$, to a superposition state $(|+3\rangle + |-3\rangle)/\sqrt{2}$, as shown in Figure 6-3. The population transfer can be achieved by a series of π pulses with frequencies f_E , $3f_E$, and

$5f_E$, respectively, where $hf_E = \frac{1}{2}\alpha E_z^2$ is the energy splitting between the $m_F = 0$ and the $m_F = 1$ level.

For a typical operation, the energies for the three-photon transitions are in the low frequency range, from 20 *Hz* to 400 *Hz*. With the maximum high voltage of 60 *kV*, which has a base frequency is $f_E = 45\ Hz$, a standard π pulse that incorporates many base frequency cycles will take more than 200 *ms*, which leads to a decrease in the experimental duty cycle, and a shortened free evolution time, given the limited lifetime of atoms in optical lattices. A medium high voltage setting (for instance $f_E = 20\ Hz$) requires even longer total pulse duration. A few-cycle pulse will in principle drive the Rabi flops, but to obtain high transition fidelity, precise control of the pulse shape presents a technical challenge. We have answered that challenge, and designed a pulse that is short, robust and can be readily achieved in the lab.

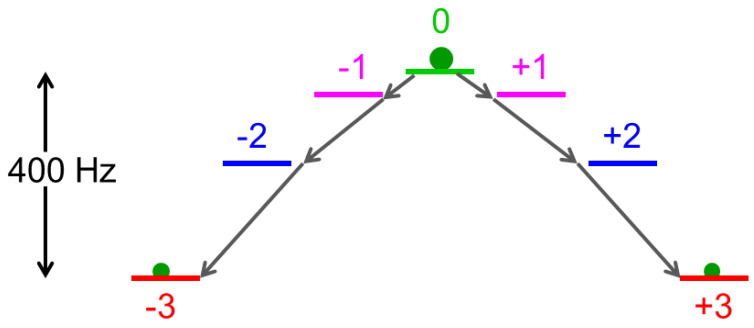

Figure 6-3. Three-photon transition energy level diagram.

6.2.1. Quantum optimal control

Historically, generic pulses obtained from quantum optimal control theory [3] have been widely used in controlling complex laser-driven chemical reactions [4, 5], and more recently constructing general unitary maps for quantum computation and information processing [6, 7].

Numerical searches for control waveforms have performed much better than initially expected. The fidelity of a state preparation is a functional of the control waveform $\boldsymbol{b}(t)$ given by

$$F[\boldsymbol{b}(t)] = \left|\langle \Psi_{target} \left| exp\left[-i\int_0^T H[\boldsymbol{b}(t)]dt\right]\right| \Psi_{initial}\rangle\right|^2 \tag{6.4}$$

Under ideal conditions without decoherence, Rabitz et. al. [8] proved that for an arbitrarily amount of time to perform control, the landscape is surprisingly simple: every local optimum is a global optimum. This implies that for a controllable quantum system [9], a local search of the space of control fields, starting from an initial guess, will find a global maximum of the fidelity $[\boldsymbol{b}(t)] = 1$. Another way to say this is that the topology of quantum transition landscapes does not have local traps, and each local maxima is a global maxima. In cases where a few maxima peaks get close together, it is possible that for part of the parameter settings they may have minimums, but these turns out to be saddle points [10]: optimizing other parameters will lead to global maxima. An important part of numerical waveform searches is to identify and select maximums with flat transition landscapes.

6.2.2. Three-photon waveform search

Inspired by the success in the field of quantum optimal control, we have engineered a nontrivial three-photon waveform with the following shape

$$B_x(t) = s(t)\sum_{n=1}^{3} B_{2n-1} cos[2\pi(2n-1)f_E t + \phi_{2n-1}] \tag{6.5}$$

Where $s(t) = sin^2\left(\pi t/T_p\right)$ is the pulse shaping function that enables smooth pulse switching, and T_p is the total pulse duration. The waveform contains three frequency components that are resonant with the three $\Delta m = +1$ transitions, but they are applied simultaneously with two relative phases among them. This leads to five parameters to be optimized, including three field

amplitudes and two relative phases. The waveform is an educated guess, obtained by considering the Fourier transform of a typical generic waveform from completely numerical optimal control under no constraints, and making up the simplest combination of all frequency components. It is entirely possible that there are better mathematical ansatzes, but it is probably most constructive and effective to first experimentally test the performance of existing waveforms when possible. As we will show in the following sections, the ansatz waveform works well theoretically and will well meet our requirements.

The Schrödinger equation for low frequency transitions is

$$i\hbar\frac{\partial}{\partial t}\boldsymbol{c}(t) = H(t)\boldsymbol{c}(t), \tag{6.6}$$

where $H(t) = -hf_E m_F^2 + g_F \mu_B B_x(t)\sigma_x$ is the time-dependent Hamiltonian, and $\boldsymbol{c}(t)$ is the 7-by-1 state vector $\boldsymbol{c}(t) = [c_{+3}, c_{+2}, c_{+1}, c_0, c_{-1}, c_{-2}, c_{-3}]^T$. The Initial condition for the above 7-level Bloch equation is $\boldsymbol{c}(0) = |\Psi_{initial}\rangle = [0,0,0,1,0,0,0]^T$, and the transition fidelity which accounts for the population in the superposition state $|\Psi_{target}\rangle = [1,0,0,0,0,0,1]^T/\sqrt{2}$ at T_p is defined as

$$F(T_p) = \left|c_{+3}(T_p)\right|^2 + \left|c_{-3}(T_p)\right|^2. \tag{6.7}$$

The waveform is optimized using a simple iterative algorithm written in MATLAB on a single personal computer. It typically takes about half an hour to complete a waveform search. The procedure has 6 steps:

(i) The five parameters are initially randomly generated, within a reasonable range estimated from a fixed pulse duration;

(ii) Sort the five parameters with an arbitrary order. For each parameter, span across its own range with a certain step size while keeping the rest of the four parameters constant. Solve the 7-level Bloch equation for each step and save the final state vector;

(iii) Find a step which gives maximum fidelity $F(T_p)$, and set the parameter to that value;

(**iv**) Repeat step (**ii**) and (**iii**) for the other 4 parameters.

(**v**) Iterate step (**ii**) to (**iv**) until the desired fidelity is reached.

(vi) Plot the time evolution of the state population in the optimized waveform field and check whether the parameter set is on a flat transition landscape. If the population in the last portion of the evolution has a wide flat region that is a signature of insensitivity to pulse duration, exit the optimization loop; otherwise reject the parameter set and start again from step (i).

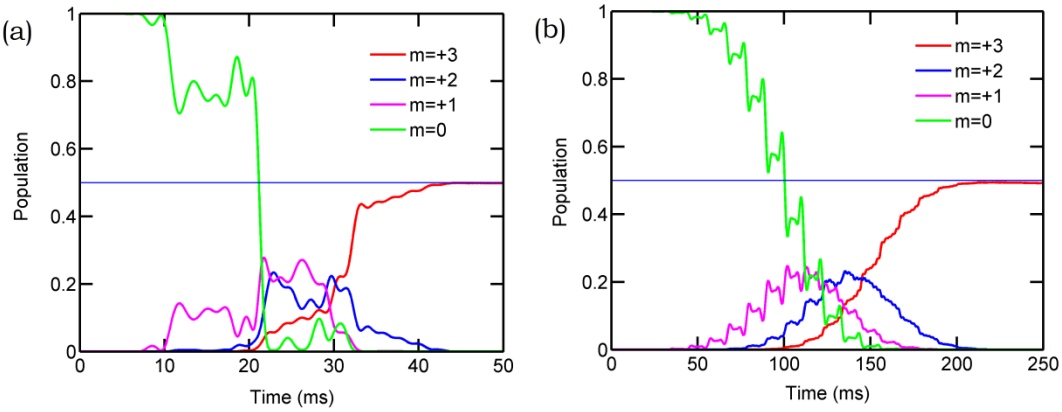

Figure 6-4. Population evolution in the optimized three-photon driven field.

The population evolution is calculated using the optimized pulse parameters from Table 6-1. (a) Result of a 50-ms duration short pulse labeled as "45Hz"; (b) Result of a 250-ms long pulse "45Hz L", which is similar to multilevel stimulated Raman adiabatic passage (STIRAP) with single frequency pulses.

We set the Stark splitting ($f_E = 45\ Hz$) to the maximum applied high voltage for the following sections of this Chapter unless otherwise specified. A population evolution example in the optimized waveform field is shown in Figure 6-4 (a). A nontrivial feature of the transfer is that the target population grows nearly linearly over time, instead of quadratically, as is the case for a standard π pulse. The linearity is a signature of transition robustness against pulse parameters. Furthermore, a fidelity of $F \approx 99.7\%$ is obtained within $T_p = 50\ ms$, which is only slightly longer than two cycles of the Stark shift for $m_F = 1$. In the long pulse duration limit, the optimized ansatz waveform will drive transitions that are similar to multilevel stimulated Raman

adiabatic passage (STIRAP) [11] with single frequency pulses, as shown in Figure 6-4 (b) for $T_p = 250\,ms$.

Label	$f_E(Hz)$	$T_p(ms)$	$B_1(\mu G)$	$B_3(\mu G)$	$B_5(\mu G)$	$\phi_{13}(\pi)$	$\phi_{35}(\pi)$	Pulse Area (π)
45Hz	45	50	42.00	77.00	87.00	0.17	0.56	5.67
45Hz L	45	250	8.05	14.45	16.30	1.86	1.87	5.33
20Hz	20	80	28.40	42.20	42.40	1.26	0.70	5.38

Table 6-1. Optimized pulse parameters for robustness comparison.

Stark shift f_E and pulse duration T_p are preset parameters for iterative optimizations. The pulse area is calculated as the sum of pulse areas of all 3 magnetic dipole transitions, in comparison, a 3-photon π pulse sequence has a total pulse area of 3π.

Table 6-1 lists a complete set of parameters for $f_E = 45\ Hz$ and $f_E = 20\ Hz$ for the robustness study in section 6.2.3. The parameter set fully describes the ansatz waveform in Eq. (6.5). The voltage control signal for the waveforms has been generated from one channel of a programmable National Instrument PCI-6713 analog output card, and the alternating magnetic field along x direction can be readily applied using the corresponding bias magnetic field coil.

6.2.3. Robustness of low frequency transitions

Figure 6-5 shows the dependence of transition infidelity (1-F) on pulse duration while keeping the total effective pulse area fixed. The infidelity from the numerical optimization procedure is approximately a quadratic function of pulse duration, which suggests that as high as 99.9% fidelity can be achieved using a one-cycle-long short pulse. Shorter pulses have a wider Fourier-limited bandwidth, which improve the transition fidelity in the current ansatz waveform construction as demonstrated throughout this section. Nevertheless, shorter pulses also require larger transverse AC magnetic fields. For the best overall performance of the magnetic shields (which might have measureable amount of magnetic hysteresis for large applied fields), and more

importantly for the ease of low-frequency precision pulse parameter control, it is reasonable to use few-cycle-long pulses for low frequency transitions.

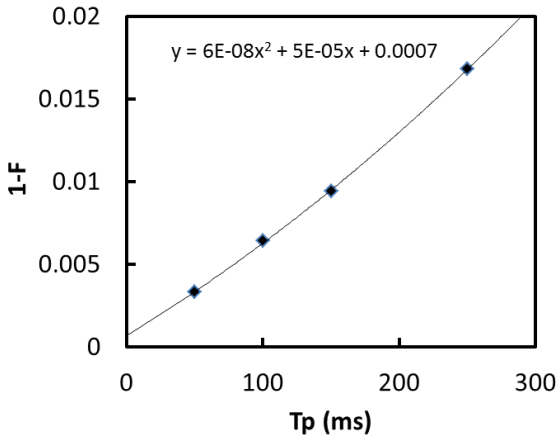

Figure 6-5. Dependence of transition fidelity on pulse duration.

Transition infidelities (1-F) as a function of pulse duration T_p after numerical optimizations with fixed Stark shift $f_E = 45\ Hz$.

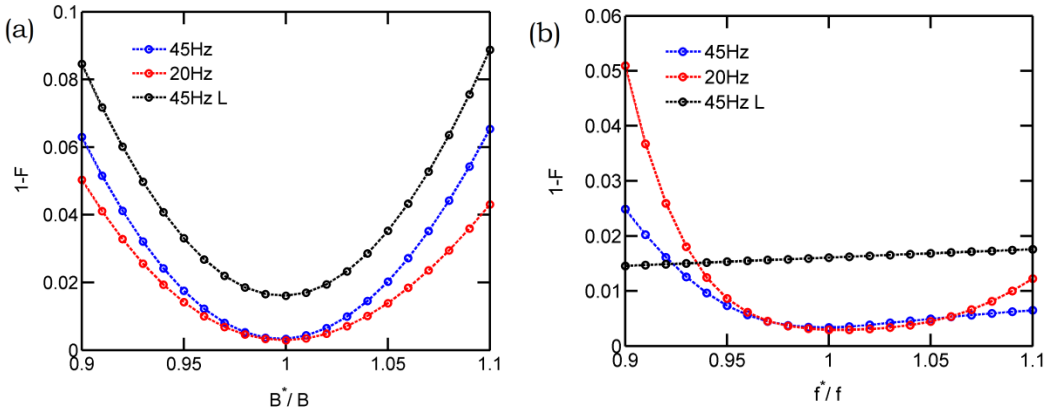

Figure 6-6. Dependence of transition fidelity on pulse amplitude and frequency errors.

Transition infidelities (1-F) using adjusted overall pulse amplitudes (a) and center frequencies (b). The horizontal axes are rescaled to the pulse parameters from Table 6-1.

In the rest of this section, we further study the transition robustness of optimized pulses listed in Table 6-1, where we have included three cases for comparison: a typical short pulse for $f_E = 45\ Hz$, a long pulse for $f_E = 45\ Hz$ and a typical short pulse for $f_E = 20\ Hz$. Figure 6-6

shows the infidelity vs calibration of pulse parameters, including overall amplitudes (a) and pulse frequencies (b). The numerical results indicate that better than 99% fidelity can be obtained if the pulse calibration error is smaller than 3%.

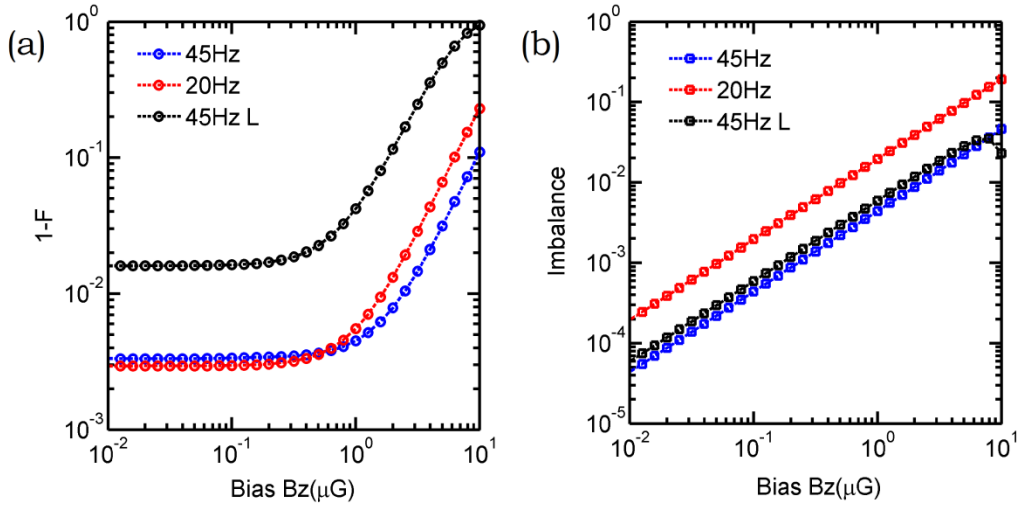

Figure 6-7. Robustness of low frequency transition against bias magnetic fields.

The transition infidelity (1-F) (a) and interferometric states population imbalance (b) as a function of the bias magnetic field B_z (can be zeroed to sub-nG level potentially*) .*

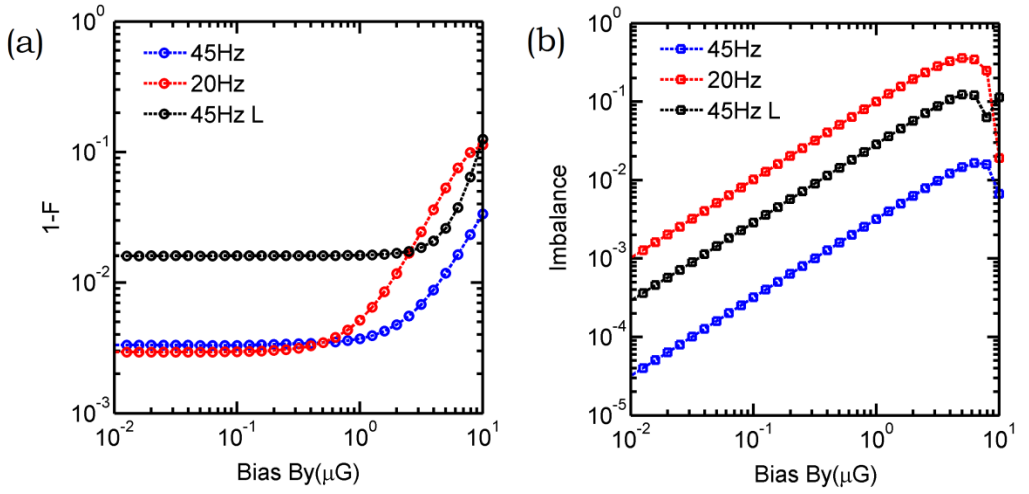

Figure 6-8. Robustness of low frequency transition against transverse magnetic fields.

The transition infidelity (1-F) (a) and interferometric states population imbalance (b) as a function of the bias magnetic field B_y (<3 μG, limited by inhomogeneous vector light shifts).

The effects of bias magnetic fields present during low frequency transitions are shown Figure 6-7 and Figure 6-8. A magnetic field offset will degrade transition fidelities, as well as introduce population imbalance between $m_F = +3$ and $m_F = -3$. Bias along the electric field quantization direction B_z (Figure 6-7) will directly lift the degeneracy between $\pm m_F$ levels, and the transition frequency in the optimized waveform will no longer be resonant. Nevertheless, since B_z can be zeroed to the sub-nG level with experiments using atoms in high electric fields that are similar to EDM measurements (see section 5.5 in Chapter 5), it will have a negligible effect on low frequency transitions. Transverse magnetic fields B_y in our experiment are cancelled only to the level of 3 μG in ~100 μK-deep traps, or slightly less for a lower trap depth, which will have a small effect on low frequency transition fidelity (Figure 6-8), which will still be greater than 99%. B_y can also degrade the population imbalance through nontrivial mechanisms of state mixing as shown Figure 6-1. Figure 6-8 (b) indicates that for a large Stark splitting $f_E = 45Hz$, the imbalance can be controlled to below 2×10^{-3}, which will minimize the collisional frequency shifts below the short noise limited frequency resolution per group of atoms (see Chapter 7, section 7.1.3). For a small Stark splitting $f_E = 20\ Hz$, the imbalance could be slightly problematic for large transverse fields.

60 *Hz* magnetic fields inside the magnetically shielded chamber could in principle degrade the performance of low frequency waveforms as well, as shown in Figure 6-9. The dominant 60 *Hz* will be along the x direction, due to the axial shielding factor (12,000), which is about 8 times smaller than transverse shielding factors (see Chapter 3, section 3.4.3). With an estimated <1 *mG* magnetic field amplitude at 60 *Hz* from various lab equipment, the residual 60 *Hz* field inside the shields should be less than 0.1 μG, which in the worst case could lead to a population imbalance of 3×10^{-3}. Nevertheless, by fine tuning the relative phase between our

low frequency pulses with respect to the 60 *Hz* AC line according to Figure 6-9, this effect of 60 Hz fields could potentially be minimized to a level that does not affect our measurement.

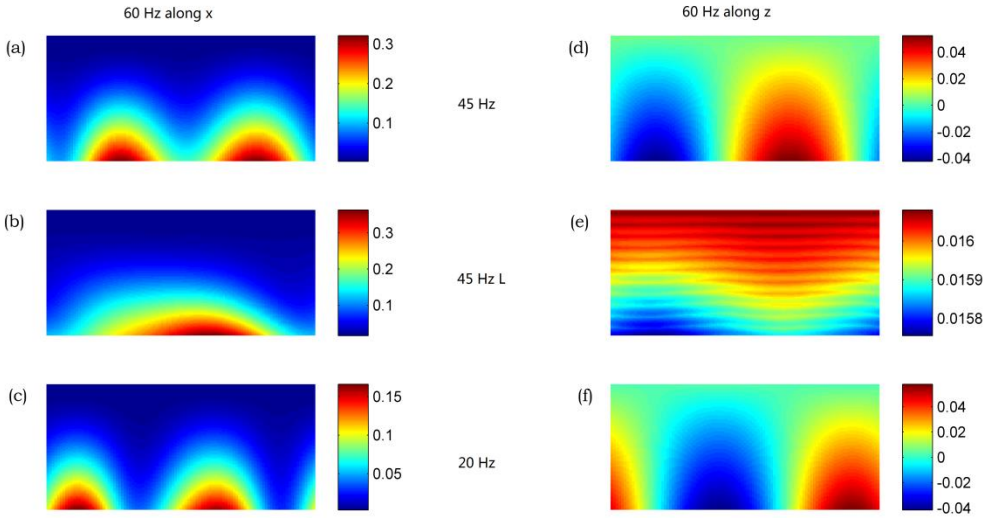

Figure 6-9. Robustness of low frequency transition against 60 Hz magnetic fields.

Transition infidelity map measured in $2\left(1-\left|c_{+3}(T_p)\right|^2\right)$ *for 60 Hz fields along x (a-c) and along z (d-f). For each map, the vertical axis is magnetic field from 0 (top) to 10 μG (bottom), the horizontal axis is the relative phase (0~2π) between 60 Hz fields and the optimized waveform.*

6.2.4. Interference fringe contrast

After a free evolution time, the interferometric states pick a relative phase ϕ that is EDM sensitive. As the final part of the EDM measurement, we use a low frequency transition waveform to bring atoms back from $m_F = \pm 3$ to $m_F = 0$ and let them interfere. The fractional number of atoms returning to $m_F = 0$ will be $cos^2\left(\frac{\phi}{2}\right)$. The rest of the atoms will be left among all other $m_F \neq 0$ levels, with fractional populations that are proportional to $sin^2\left(\frac{\phi}{2}\right)$. Figure 6-10 (a) shows an ideal case for the low frequency transitions without transverse bias magnetic fields, the final pulse is identical to the initial low frequency pulse that is used to prepare the

superposition state, except it is reversed in time $B_x(t') = B_x(T_p - t)$. The performance of the time-reversed pulses is also identical to those described in section 6.2.3.

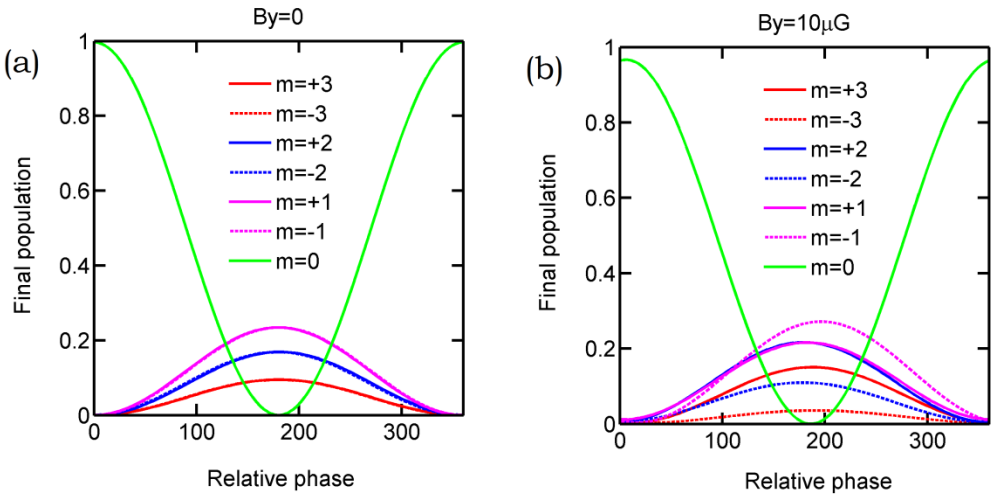

Figure 6-10. Final population as a function of interferometer phase.

(a) Ideal case without transverse magnetic fields; (b) with a transverse magnetic field of 10 μG, which lifts the degeneracy of the $\pm m_F$ states and but barely affects the $m_F = 0$ fringe contrast.

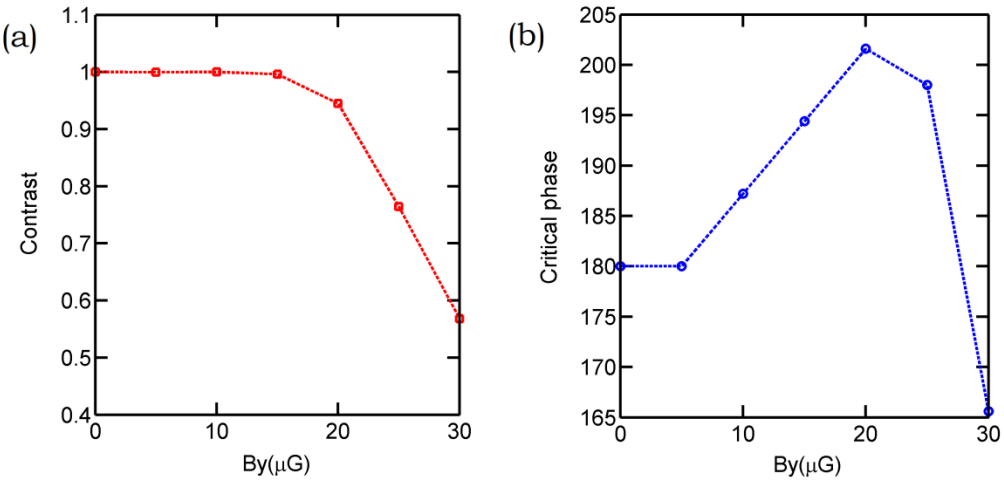

Figure 6-11. Contrast and critical phase as a function of transverse magnetic field.

The data is calculates from Figure 6-10 for various transverse magnetic field settings. Critical phase is an interferometer phase that corresponds to a minimum of the m_F=0 fringe.

In the presence of a transverse magnetic field, due to the state mixing effect demonstrated in Figure 6-1 (a), the $m_F = 0$ interference contrast will be degraded, and the interference signal minimum no longer occurs at $\phi_c = \pi$, because the $\pm m_F$ levels are no longer pure (energy eigenstates) in a large transverse magnetic field, as seen by the green curve in Figure 6-10(b).

Figure 6-11 shows the dependence of interference fringe contrast and critical phase ϕ_c on the transverse bias magnetic field B_y. Since in our experiment transverse fields are cancelled to a level of 3 μG or better, the transverse fields will only affect the fringe contrast at a level of less than 0.1%, as illustrated in Figure 6-11 (a).

6.3. References

[1] S. Ulzega *et. al*., *Measurement of the forbidden electric tensor polarizability of Cs atoms trapped in solid ^4He*, Phys. Rev. A **75**, 042505 (2007).

[2] C. Cohen-Tannoudji, B. Diu, F. Laloe, *Quantum Mechaincs*, Wiley-VCH, Vol. **1**, p659, (1992).

[3] J. Werschnik and E. K. U. Gross, *Quantum optimal control theory*, J. Phys. B: At. Mol. Opt. Phys. **40** R175 (2007).

[4] A. Assion *et. al*., *Control of Chemical Reactions by Feedback-Optimized Phase-Shaped Femtosecond Laser Pulses*, Science **282**, 919 (1998).

[5] R. J. Levis, G. M. Menkir, H. Rabitz, *Selective Bond Dissociation and Rearrangement with Optimally Tailored Strong-Field Laser Pulses*, Science **292**, 709 (2001).

[6] S. T. Merkel *et. al*., *Quantum control of the hyperfine-coupled electron and nuclear spins in alkali-metal atoms*, Phys. Rev. A **78**, 023404 (2008).

[7] S. T. Merkel *et. al*., *Constructing general unitary maps from state preparations*, Phys. Rev. A **80**, 023424 (2009).

[8] H. A. Rabitz, M. M. Hsieh, and C. M. Rosenthal, *Quantum Optimally Controlled Transition Landscapes*, Science **303**, 1998 (2004).

[9] S. G. Schirmer, A. I. Solomon and J. V. Leahy, *Degrees of controllability for quantum systems and application to atomic systems*, J. Phys. A: Math. Gen. **35**, 4125 (2002).

[10] M. Hsieh, R. Wu, and H. Rabitz, *Topology of the quantum control landscape for observables*, J. Chem. Phys. **130**, 104109 (2009).

[11] P. Kr á, I. Thanopulos, and M. Shapiro, *Coherently controlled adiabatic passage*, Rev. Mod. Phys. **79**, 53 (2007).

Chapter 7

Sensitivity, noises and systematics

The experiment is designed to be insensitive to particular types of noise and to minimize certain types of systematic errors, with the powerful and unique features already discussed in Chapter 2, section 2.2. We will discuss possible noise and systematic errors that can affect the eEDM measurement in this Chapter. Calculations of noise and systematic errors in many cases have already been performed by Fang ([1], p. 30-45) and by Solmeyer ([2], p. 137-159). I shall not repeat the work when this is the case, but will summarize the important conclusions for the sake of structural completeness. Detailed calculations in a few special cases, like the Linear Stark interference in section 7.2.3, which has not yet been discussed in the exact configuration of our experiment, will be included for the first time. The noise and systematic error estimates will provide insights about what experimental factors really matter and what needs to be achieved in order to meet our projected eEDM sensitivity.

The interferometric signal in our experiment is the fractional population of atoms returning to the $m_F = 0$ state (see section 1.2, section 2.1.4 and 6.2.4)

$$\frac{n_0}{n} = cos^2\left[\frac{g_F m_F \tau}{\hbar}(dE + \mu B)\right], \tag{7.1}$$

which is determined by the relative phase between the $m_F = +3$ and $m_F = -3$ interferometric states that is accumulated during the free evolution time τ. The fractional populations of atoms for the other 6 Zeeman sublevels (Figure 6-10) are also detected in order to calculate the total atom number and normalize the signals. The noise on the signal described by Eq. (7.1) may originate from noise in the preparation, preservation and measurement of the interferometric

states, as well as from noise on the interferometer phase. Section 7.1 discusses the effects of various sources of noise.

The shot noise level is the uncertainty in the final measurement imposed by quantum counting statistics [3], which can be reduced by repeated measurements. In our experiment, the signal described by Eq. (7.1) leads to a short noise limited sensitivity of the electron EDM for a single measurement [2]

$$\delta d_e^s = \frac{\hbar}{4ERm_F g_F \tau\sqrt{N}}, \tag{7.2}$$

with the projected DC electric field $E = 150\ kV/cm$, Cs enhancement factor $R = 120.5$, free evolution time $\tau = 3\ s$ and total atom number per shot $N = 1 \times 10^8$. If the shot noise per shot per group of atoms δd_e^g is considered, the number of atoms per group for 25 groups is then $N/25 = 4 \times 10^6$. When the measurement is repeated for $T = 24$ hours with a 50% duty cycle $D = 0.5$, the shot noise limited sensitivity can be improved to

$$\delta d_e^u = \frac{\hbar}{4ERm_F g_F \sqrt{NTD\tau}} \tag{7.3}$$

Eq. (7.3) gives the ultimate projected sensitivity of our eEDM experiment. It is often useful to express the sensitivity limits in terms of energy differences between the $m_F = +3$ and $m_F = -3$ interferometric states, or an equivalent bias magnetic field, in order to directly compare with the sizes of noise sources and systematic errors.

Unit	δd_e^u	δd_e^s	δd_e^g
δd_e	2.4×10^{-30} e-cm	2.9×10^{-28} e-cm	1.5×10^{-27} e-cm
$m_F = \pm 3$ energy	$h \times 16\ nHz$	$h \times 1.9\ \mu Hz$	$h \times 9.5\ \mu Hz$
Equivalent magnetic field	$7.5\ fG$	$0.9\ pG$	$4.5\ pG$

Table 7-1. Shot noise limited sensitivity.

The 2nd to the 4th column are: δd_e^u shot noise limited ultimate sensitivity, δd_e^s shot noise per shot, δd_e^g shot noise per shot per group.

The estimated sensitivities to the electron EDM in all three units are listed in Table 7-1. From Eq. (7.3), it is seen that the sensitivity can be improved by having larger electric fields, longer measurement, longer coherence time, and larger total atom number per measurement. These parameters cannot be made arbitrarily large, for either technical/physical reasons or limited ability to control systematics. Thus the numbers quoted in Table 7-1 are based on practical experimental parameters and our best estimates of noise and systematic errors.

Systematic errors are effects that mimic an eEDM and will be indistinguishable from an actual eEDM signal. The effects would be correlated with the reversal of the electric field throughout the entire run of the experiment. Unlike effects of various noise sources they will never be averaged out. Hence they need to be smaller than the shot noise limited ultimate sensitivity quoted in Table 7-1.

Equipped with the powerful features described in Chapter 2, our experiment has three possible remaining systematic effects: leakage currents across the electric field plates and their mounting accessories, imperfect electric field reversals leading to a shifted position of the atoms in a magnetic field gradient, and a linear Stark interference effect resulting from third-order laser-atom interactions [4]. In section 7.2, those systematic effects will be studied in details.

7.1. Sources of noises

7.1.1. Magnetic field noises

Magnetic field noise during free evolution will affect the interferometer phase in Eq. (7.1) directly. In our experiment, magnetic noise may come from residual ambient fields leaking through the magnetic shields, residual magnetization of the magnetic shields, Johnson noise induced by conductors near the measurement chamber, noise in thermoelectric currents from

dissimilar metals used in the high voltage systems and the 60 Hz field plate pick-up noises. All of these will presumably be uncorrelated with the polarity switching of the DC electric field and to the extent that they are in the z direction, different for the two cavities, and different from one shot to the next. They should be compared directly to the shot noise per shot of ~1 pG.

Johnson noise is the magnetic field noise created by thermal agitation of electrons in a conductor [5, 6]. This is the motivation behind our maximal use of insulating materials (both glass and plastics) and keeping good conductors (when possible) away from the atoms in our experiment. The root-mean-square Johnson noise magnetic field at the location (x,y,z) from an arbitrarily shaped conductor with a volume V'(x',y',z') is given by [2, 6]

$$B_z^{rms}(x,y,z) = \frac{\mu_0}{4\pi}\sqrt{4\sigma k_B T}\cdot\left(\iiint_{V'} dx'dy'dz' \frac{(x-x')^2+(y-y')^2}{\left((x-x')^2+(y-y')^2+(z-z')^2\right)^3}\right)^{1/2} \quad (7.4)$$

Where σ is the conductivity and T is the temperature of the conductor. Equation (7.4) is used throughout the design of the experiment to calculate the Johnson noise from parts like the inner magnetic shield, small titanium screws used for the plastic mirror mounts, titanium clamps for plate mounting, and the magnetic field coils inside the shield, etc., which will largely be common mode between the two lattices but will not be completely canceled out. However, in all cases, the calculated values fall below the shot noise limit. The thin ITO coating on the field plates will likely produce a fluctuating magnetic field that is different for the two lattices. Using the coating thickness of 150 nm and the sheet resistance of 100 **Ω**/■, Equation (7.4) gives around 8 $pG/\sqrt{Hz}$, which is about the size of the shot noise limit per shot for a 3 sec evolution time.

Thermoelectric current from an ITO-titanium interface is about 36 $\mu V/K$ [7]. In our high voltage field plate system ([2], p. 113), the current in the large loop formed by the connections to the top and the bottom of the plates is suppressed by the 2 MΩ resistors in that path; the smaller loop formed by the two ground plates (~460 Ω) is potentially more problematic because of the

difficulty of inserting high vacuum compatible resistors into that loop. Nevertheless, it could only potentially cause a problem when the temperature of the system does not equilibrate to better than $0.1\ K$ ([2], p.153). This is unlikely to happen, since the apparatus temperature is actively stabilized to within 0.03 K. Furthermore, calculations of uniform Joule heating of field plates during plates charging and discharging followed by thermal conduction and surface radiation cooling show that the plate temperature will have a maximum increase of 0.015 K.

The double-sided high voltage electric connections to the field plates, which is designed to minimize leakage currents through the plates (section 7.2.1), leads to a large pick-up loop with 60 Hz, 2 nA current through the plates ([2], p.153 and Fig. 6-14). Additional suppression of this noise source can occur when the experimental timing is triggered on the 60 Hz line, so that the magnetic field produced from the 60 Hz line is the same during each shot of the experiment and cancels out in the differential measurement that compares one shot to the next.

7.1.2. Trapping light related noises

The 1064 nm optical lattice trapping light can destroy the coherence in the interferometric states and lead to a reduction in fringe contrast. With an atom temperature of $10\ \mu K$ after polarization gradient cooling, we expect the operating trap depth for the EDM measurement to be about $20\ \mu K$. At this trap depth, atoms are scattered from the lattice light at a rate of once every 5 seconds. The noise on the fringe contrast will be a fraction of this depending on the intensity fluctuations of the cavity on the timescale of the measurement time. Currently the intensity fluctuations of the cavity have an amplitude of about 1%, but the drift of the average intensity over the measurement time will be much less than this. The lattice intensity noise is mostly uncorrelated between the two cavities.

Vector light shifts (discussed in detail and measured in Chapter 5, section 5.4) act like fictitious magnetic fields in our experiment. The inhomogeneous part of the vector light shifts is about 0.2 Hz for a 20 μK trap depth, and can lead to dephasing of the coherent atom ensemble. However, the fictitious field is along the y direction, so it is a transverse field. Its effect is greatly suppressed by a power-law scaling factor in the EDM measurement, where the DC electric field defines the quantization axis (Chapter 6, section 6.1).

Tensor light shifts for Cs atoms in a 1064 nm trap are [4]

$$\Delta v_T = v_T U(3cos^2\phi - 1)m_F^2,\ v_T = 0.0035\ Hz/\mu K, \tag{7.5}$$

where $\phi = 0$ is the angle between the linear polarization axis of the trapping light and the quantization axis. The tensor light shifts depend linearly on the trapping light intensity and shift the $m_F = \pm 3$ levels equally. Thus it will not affect the interferometer phase. At a trap depth of 20 μK, the tensor light shift is 1.3 Hz for $|m_F| = 3$ states. Fluctuations in the trapping light intensity (~1%) could affect the fidelity of the low frequency transitions used in EDM interferometric state preparation and measurement. According to the calculations in section 6.2.3, Figure 6-6 (b), the fluctuations in tensor light shifts (~0.01 Hz) will only affect the low frequency transition fidelity at a negligible level of much less than 1%.

7.1.3. Collisional frequency shifts

Atom-atom collisions result in dephasing of the interferometer, which is the motivation behind the design requirement that we have a large effective trapping volume (25 mm^3). The collisional frequency shift for $|m_F| = 3$ atoms in our experiment can be estimated according to [8]

$$\delta v_c = \frac{1}{2\pi} nV\left|\lambda_{3,3}\right|\left(\rho_{3,+3} - \rho_{3,-3}\right), \tag{7.6}$$

where the atom density is $n{\sim}10^{10}\ cm^{-3}$, the root-mean-square velocity is $V{\sim}2.5\ cm/s$, the collisional cross section is $|\lambda_{3,3}|{\sim}10^{-12}\ cm^2$ (for a 10 μK atom ensample) and the population difference is $\rho_{3,+3} - \rho_{3,-3}$. To keep the frequency shift below shot noise limited frequency resolution per group of atoms (~10 μHz), the population imbalance must be kept below 0.25%, which is achievable according to the numerical calculations in Chapter 6, section 6.2.3.

7.1.4. Measurement noises

Atom number fluctuations could come from atom processing (~20% intensity drift in the cooling beams due to etaloning from the glass cell) and atom loss (6 sec 1/e lifetime) due background gas collisions. However, both of these effects can be avoided by measuring the total number of atoms in each shot including the atoms returning to $m_F = 0$ and 6 other Zeeman sublevels, and normalizing the interferometer signal with the total atom number. Thus the measurement noise is dominated by the noise from detecting each Zeeman sublevel. Noise in the detection systems were analyzed in detail at the end of section 3.3.2, Chapter 3. Currently, with a total atom number of $N_A = 5 \times 10^6$ we have achieved a signal-to-noise ratio of SNR~1.7x10^3. In comparison, the atom shot noise per group (for effectively 10 subgroups) limited SNR is 7.1x10^2. Since the fluorescence detector has a fixed electronic noise level, an increase in total atom number will increase the SNR linearly.

In conclusion, noise can come from effects that alter the atom number or the phase of the interferometer. The types of noises described above will affect the measurement differently, and seem to fall within the requirements for the EDM measurement.

7.2. Systematic effects

7.2.1. Leakage currents

Leakage currents in the high voltage field plate system are potential systematic error sources since they generate magnetic fields that reverse sign upon high voltage polarity switching. In our experiment, the field plates are designed to reduce the leakage currents running through the plates directly by a geometric factor of 10, by making electric connections on both ends of the field plates (see Chapter 6 in ref. [2]). Depending on the geometry, there are three types of leakages currents in the system: leakage from the 4 mm plate spacers, from vertical high voltage rods and through ITO coatings on the plate surfaces. The former two types of leakage currents are at least 10 cm away from the atoms, while the ITO leakage is as close as 2 mm to the atoms. The magnetic fields generated from those leakage currents in the regions where atoms are trapped must be kept below 7.5 fG (see Table 7-1).

Due to the unpredictable nature of leakage currents running through spacers, the worst case is when the leakage current goes along a cylindrical spacer while picking up a "winding phase" of 2π. Since currents along z do not contribute to B_z, the overall effect of such current is equivalent to a magnetic dipole $\boldsymbol{m} = I_S \times \pi R^2 \hat{\boldsymbol{z}}$, where I_S is the size of the leakage current and R=4.76 mm. The magnetic field generated from the dipole $\boldsymbol{m}$ is

$$\boldsymbol{B}(\boldsymbol{r}) = \frac{\mu_0}{4\pi} \frac{[3\hat{\boldsymbol{r}}(\hat{\boldsymbol{r}}\cdot\boldsymbol{m}) - \boldsymbol{m}]}{r^3}. \tag{7.7}$$

At a distance $d = 10\ cm \gg R$ away, the z component of the field is approximately

$$B_z = \frac{\mu_0}{4} \frac{I_S R^2}{d^3}. \tag{7.8}$$

Assuming the worst case, the contributions from 4 spaces add constructively, and the ultimate sensitivity of 7.5 fG corresponds to a leakage current of $I_S = 26\ pA$ per spacer.

The magnetic fields from vertical leakage currents through 2 high voltage center rods and 8 ground rods can be calculated directly using the Biot-Savart Law, which yields $B_z = 0.02\ fG/pA$ per rod. Assuming that the contributions of 10 rods add constructively, the ultimate sensitivity of 7.5 fG corresponds to a leakage current of $I_V \approx 37.5\ pA$ per rod. Therefore, the leakage currents through high voltage and ground titanium are a less stringent constraint than that of the plate spacers.

Leakage currents through the 3 field plates are the most important one among the three kinds because they can be very close to the atoms. We consider a single ITO rectangular sheet (with length $L = 20\ cm$ and width $W = 4\ cm$) centered at the origin, and assume the leakage current I_P flows uniformly from the top to the bottom. The current density, magnetic vector potential and magnetic fields resulting from the sheet current are

$$\begin{aligned} \boldsymbol{J}(\boldsymbol{r}) &= \frac{I_P}{W}\delta(z)\hat{\boldsymbol{y}} \\ \boldsymbol{A}(\boldsymbol{r}) &= \frac{\mu_0}{4\pi}\int \frac{\boldsymbol{J}(\boldsymbol{r}')}{|\boldsymbol{r}-\boldsymbol{r}'|}d^3r' \\ \boldsymbol{B}(\boldsymbol{r}) &= \boldsymbol{\nabla}\times\boldsymbol{A}(\boldsymbol{r}). \end{aligned} \tag{7.9}$$

Note that $A_x = A_z = 0$, and therefore $B_y = 0$ and

$$\begin{aligned} B_z(x,y,z) = \partial_x A_y &= \frac{\mu_0 I}{4\pi W}\int_{-W/2}^{W/2} dx' \int_{-L/2}^{L/2} dy' \frac{x-x'}{\left[(x-x')^2+(y-y')^2+z^2\right]^{3/2}} \\ B_x(x,y,z) = -\partial_z A_y &= -\frac{\mu_0 I}{4\pi W}\int_{-W/2}^{W/2} dx' \int_{-L/2}^{L/2} dy' \frac{z}{\left[(x-x')^2+(y-y')^2+z^2\right]^{3/2}} \end{aligned} . \tag{7.10}$$

A notable special case is $B_z(0,y,z) = 0$, which implies that if the atoms are centered along the x direction with respect to the field plates, the only non-zero component is B_x. This provides a plausible way to reduce the systematic effects of leakages current by fine tuning the lattice beam positions along the x direction. If the atoms are offset from the center of the plates in the x direction by Δx mm, then Eq. (7.10) gives $B_z \approx 4.7\Delta x\ \frac{fG}{pA}$, which depends linearly on Δx and

remains nearly constant along the atom pancake stack. Assuming that the contributions of the 3 field plates add constructively, and we have a 1 mm alignment error ($\Delta x = 1$), the ultimate sensitivity of 7.5 fG corresponds to a leakage current of $I_P = 1.9\ pA$ per field plate.

Given the measured leakage current – high voltage relation of $1{\sim}2\ pA/kV$ ([2], p. 118), if the leakage currents follows the same linear scale up to designed maximum high voltage, the total maximum leakage current is about $50{\sim}100\ pA$. Since leakage currents will most likely take the minimal resistance paths via the glass plate spacers, the measured leakage currents will marginally meet the requirement set by the ultimate sensitivity. Furthermore, because leakage currents result in spatially dependent magnetic fields, resolving independent groups of trapped atoms (see Chapter 4, section 4.3) provide an extra handle on the systematic errors due to leakage currents.

7.2.2. Atoms shift in magnetic field gradients

The combination of a non-uniform DC electric field $E_s(\boldsymbol{r})$ along the z direction and an imperfect field reversal of the DC electric field $E_+ + E_- = \Delta E \neq 0$ leads to the second systematic effect in our experiment. For atoms in the 1064 nm trapping potential $U_{AC}(y,\rho) = -U_0 cos^2(ky) exp(-\rho^2/w^2)$, combined with a DC Stark potential $U_{DC}(\boldsymbol{r}) = -\frac{1}{2}\alpha_{DC}E_S^2(\boldsymbol{r})$, the equilibrium location for the atoms is set by the forces determined by the curvatures of the potentials [1]

$$\boldsymbol{\nabla} U_{DC} = \boldsymbol{\nabla} U_{AC} \tag{7.11}$$

In our experiment, atoms are most likely shifted along the transverse directions (the z direction and the x direction) in a DC electric gradient $\boldsymbol{\nabla} E_s(\boldsymbol{r})$ due to the tight confinement of optical lattice along the y direction. However, because the DC Stark effect depends on $E_S^2(\boldsymbol{r})$, the

atoms would be shifted to the same place in a positive and negative electric field. If the positive applied electric field is different in amplitude from the negative applied electric field, then the atoms will experience a slightly different force and will be displaced in the trap by different amounts depending on ΔE. A slight displacement in the trap becomes a problem for the measurement if there is a gradient of the z-component of the magnetic field ($\frac{dB_z}{dx}$ or $\frac{dB_z}{dz}$), because the atoms will move upon reversing the electric field and will hence experience a different magnetic field. This effect would be perfectly correlated with the electric field reversal and would mimic an EDM.

Electric field gradients could stem from plate imperfections or pinholes in the ITO coating. The gradients produced by imperfections smaller than the scratch-dig of the plates will only cause local effects and will not be a problem, since for example, the fractional electric field change at a distance d ($\geq 2\ mm$) away from a dig diameter of R ($\leq 50\ \mu m$) is scaled as $\frac{3R^4}{16d^4}$ due to charge redistribution around the imperfections. The ITO coating is done with a low to no-pinhole process by Evaporated coatings Inc.. Another possible way to create an electric field gradient is a wedge on the field plates. From the interferometric measurements of plate separations in Chapter 3, section 3.4.2, we determine the maximum wedge of the current plates is $\sim 1 \times 10^{-4}$, which would create a transverse displacement in the optical lattice traps of $26\ \mu m$ [1, 2]. From the test data in section 3.4.1, we expect a DC electric field polarity reversal to within $|\Delta E/E_+| \leq 2 \times 10^{-5}$. In order to meet the systematic sensitivity to the magnetic field of 7.5 fG, this imposes the requirement for the gradient of the magnetic field in the z direction to be smaller than 140 nG/cm. This level of magnetic field gradient seems achievable. Furthermore, spatial array of independent groups of atoms will also provide an extra handle on the systematic errors due to local magnetic field gradients and electric field gradients.

7.2.3. Linear Stark interference

Linear Stark interference (LSI) for atoms in optical lattices traps (which have laser electric and magnetic fields $\boldsymbol{E}_L$ and $\boldsymbol{B}_L$) and a large DC electric field $\boldsymbol{E}_S$ could also lead to a systematic error. Both the calculation [9] and a measurement [10] of the LSI effect in ^{85}Rb have been performed in Dr. Norval Fortson's group. The atomic theory prediction agrees well with the experimental result within the ~10% measurement uncertainty [10]. The same group has also predicted the size of the LSI in ^{133}Cs [4], but to the author's knowledge no measured values have been reported. Notably, linear Stark interference effect has also been studied both theoretically [11] and experimentally [12] for an EDM search in ^{199}Hg. In this section we will follow ref. [4] to derive a complete set of equations for the LSI effect that applies to our experimental configurations, which provides a design guide throughout the experiment.

Due to parity mixing by the DC electric field $\boldsymbol{E}_S$, two types of transitions contribute to the linear Stark effect in Cs. The first type depends on a magnetic dipole transition (Fig. 12 in [4]), with the Hamiltonian H_{MD} and linear frequency shift $\Delta v^{MD}_{F=I\pm1/2}$ given by

$$\begin{aligned} H_{MD} &\propto (-\boldsymbol{d}\cdot\boldsymbol{E}_L)(-\boldsymbol{d}\cdot\boldsymbol{E}_S)(-\mu\cdot\boldsymbol{B}_L) \\ \Delta v^{MD}_{F=I\pm1/2} &= \mp[v_1^{MD}(\boldsymbol{B}\cdot\boldsymbol{\sigma})(\boldsymbol{E}\cdot\epsilon_S)+v_2^{MD}(\boldsymbol{B}\cdot\epsilon_S)(\boldsymbol{E}\cdot\boldsymbol{\sigma})], \end{aligned} \tag{7.12}$$

where $\boldsymbol{d}$ (μ) is the electric (magnetic) dipole moment, $\boldsymbol{\sigma}$ is the quantization axis, and ϵ_S is the linear polarization axis of the optical lattice beams. The second type depends on an electric quadruple transition (Fig. 14 in [4]), with the Hamiltonian H_{EQ} and linear frequency shift $\Delta v^{EQ}_{F=I\pm1/2}$ given by

$$\begin{aligned} H_{EQ} &\propto (-\boldsymbol{d}\cdot\boldsymbol{E}_L)(-\boldsymbol{d}\cdot\boldsymbol{E}_S)(-\frac{1}{6}\boldsymbol{Q}\vdots\boldsymbol{\nabla}\boldsymbol{E}_L) \\ \Delta v^{EQ}_{F=I\pm1/2} &= \pm\big[v_1^{EQ}(\boldsymbol{B}\cdot\boldsymbol{\sigma})(\boldsymbol{E}\cdot\epsilon_S)+v_2^{EQ}(\boldsymbol{B}\cdot\epsilon_S)(\boldsymbol{E}\cdot\boldsymbol{\sigma})\big], \end{aligned} \tag{7.13}$$

where $\boldsymbol{Q}$ is the electric quadruple moment of Cs atoms. At $U_0 = 100\ \mu K\ (1064\ nm), E = 100\ kV/cm$, the LSI coefficients (Fig.13 and Fig.15 in [4]) are $v_1^{MD} \approx 0.202\ Hz, v_2^{MD} \approx 0.030\ Hz$, $v_1^{EQ} \approx 0.237\ Hz$, $v_2^{EQ} \approx 0.003\ Hz$.

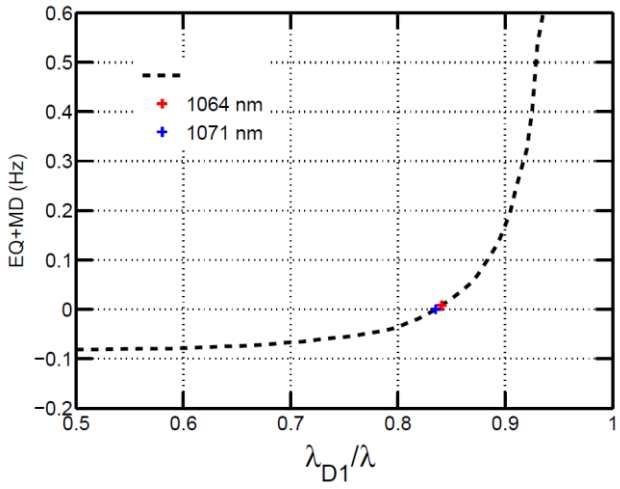

Figure 7-1. Magic wavelength for the linear Stark interference effect in Cs.

The combined frequency shift (MD+EQ) versus rescaled trap wavelength λ (with wavelength of Cs D1 line $\lambda_{D1} \approx 894.593\ nm$), plotted using data combined from Fig.13 and Fig.15 in ref. [4] for 100 μK trap depth and 100 kV/cm electric field. At λ =1064 nm (+), the linear frequency shifts from magnetic dipole transitions and electric quadruple transitions have an opposite sign and largely cancel out to 0.008 Hz. At λ ~1071 nm (+), the total shift is zero.

For the Cs F=3 hyperfine ground state, the linear frequency shifts from magnetic dipole transitions and electric quadruple transitions have opposite signs and largely cancel out. The cancellation occurs in Cs largely due to the near degeneracy of the 6P and 5D atomic states [13]; for ^{85}Rb the LSI is dominated by v^{MD}, since v^{EQ} is about 10 times smaller [10]. The combined LSI frequency shift for Cs has a coefficient of $\sim 8 \times 10^{-7}\ Hz$ per μK per kV/cm for 1064 nm light traps. A magic wavelength near 1071 nm seems to exist (Figure 7-1) such that two contributions exactly cancel out to zero, according to predictions based on Fig.13 and Fig.15 in ref. [4]. The accuracy of LSI coefficients in Cs remains unknown [4] and cries out for more precise theoretical calculations. In comparison, similar calculations for Rb based on central

potentials have <1% uncertainty in $v_{1,2}^{MD}$ and at least 5% uncertainty in $v_{1,2}^{EQ}$ [9]. The magic wavelength for Cs might be ultimately experimentally determined, at the cost of a high power tunable laser system that might not be readily accessible.

We now focus on the angular dependences, $(\boldsymbol{B}\cdot\boldsymbol{\sigma})(\boldsymbol{E}\cdot\epsilon_S)$ and $(\boldsymbol{B}\cdot\epsilon_S)(\boldsymbol{E}\cdot\boldsymbol{\sigma})$, of the third-order laser-atom interactions. For simplicity, let's choose the trap light as the coordinate system. This is slightly different from our usual convention, where we take the quantization axis to be **z** and where misaligned laser polarization is slightly rotated with respect to **z**. First, assume we have a pure linear polarization along **z**. The electric and magnetic field of the trapping laser light then reads

$$\begin{aligned}\boldsymbol{E} &= (\kappa+\varepsilon)sin(ky-\omega t)\boldsymbol{z}+\kappa sin(ky+\omega t)\boldsymbol{z}\\ \boldsymbol{B} &= (\kappa+\varepsilon)sin(ky-\omega t)\boldsymbol{x}+\kappa sin(ky+\omega t)(-\boldsymbol{x}).\end{aligned} \tag{7.14}$$

As a sanity check, the above definition satisfies the Maxwell's equations $\boldsymbol{B}=\boldsymbol{k}\times\boldsymbol{E}$ and $\boldsymbol{\nabla}\times\boldsymbol{E}=-\frac{\partial\boldsymbol{B}}{\partial t}$. The 1st term corresponds to **k**=**y** and the 2nd term corresponds to **k**=-**y**. In the limit $\varepsilon=0$, Eq. (7.14) is reduced to a perfect standing wave (intensity balanced); In the limit $\kappa=0$, it is an up going traveling wave. We can rewrite the fields in a standing wave format:

$$\begin{aligned}\boldsymbol{E} &= [2\kappa cos(\omega t)sin(ky)+\varepsilon sin(ky-\omega t)]\boldsymbol{z}\\ \boldsymbol{B} &= [-2\kappa sin(\omega t)cos(ky)+\varepsilon sin(ky-\omega t)]\boldsymbol{x}.\end{aligned} \tag{7.15}$$

Assume the DC electric field and quantization axis are close to **z** but not exactly parallel to **z** ($\phi\approx 0,\theta\approx 0$):

$$\boldsymbol{\sigma}=\epsilon_S=cos\theta cos\phi\boldsymbol{z}+cos\theta sin\phi\boldsymbol{x}+sin\theta\boldsymbol{y}. \tag{7.16}$$

After straight-forward algebra, the angular dependence of the 3rd order interaction is given by

$$\begin{aligned}\Delta^{(3)} &= (\boldsymbol{B}\cdot\boldsymbol{\sigma})(\boldsymbol{E}\cdot\epsilon_S)=(\boldsymbol{B}\cdot\epsilon_S)(\boldsymbol{E}\cdot\boldsymbol{\sigma})\\ &= \frac{sin2\phi}{2}cos^2\theta[-I_\downarrow sin(2\omega t)sin(2ky)+(I_\uparrow-I_\downarrow)sin^2(ky-\omega t)]\end{aligned} \tag{7.17}$$

Note that the upward and downward lattices beam intensities are $I_{\downarrow} = \kappa^2$ and $I_{\uparrow} = (\kappa + \varepsilon)^2$, respectively.

Now let's look at the time averages (over a oscillation cycle of the trapping laser) for various functions defined as $\langle f(t)\rangle = \frac{1}{\tau}\int_0^{\tau} f(t)dt\,, \tau = \lambda/c$. Following this definition, $\langle sin^2(ky - \omega t)\rangle = \frac{1}{2}, \langle sin(2\omega t)\rangle = 0$. The time-averaged intensity of the lattice is

$$I = -(4\kappa^2)sin^2(ky)\langle cos^2(\omega t)\rangle = -\frac{1}{2}(4\kappa^2)sin^2(ky) \tag{7.18}$$

Finally, from the time average of Eq. (7.17) one gets the functional form for the 3rd order shift

$$\begin{aligned} \Delta^{(3)} &= \frac{sin2\phi}{2} cos^2\theta\{-I_{\downarrow}\langle sin(2\omega t)\rangle sin(2ky) + [I_{\uparrow} - I_{\downarrow}]\langle sin^2(ky - \omega t)\rangle\} \\ &= \tfrac{sin2\phi}{4} cos^2\theta \cdot (I_{\uparrow} - I_{\downarrow}). \end{aligned} \tag{7.19}$$

In the limit of $I_{\uparrow} - I_{\downarrow} = 0$ (perfect intensity balance) or $\phi = 0$ (perfect parallel), the 3rd order shift goes to zero.

Since atoms are trapped around places where $U_{trap} \propto -sin^2(ky)$ is minimized, the $sin(2ky)$ factor in Eq. (7.19) is an odd function around the trap center and spatially averages to zero. One could imagine that gravity on average will shift the atoms away from the center, and then the term won't spatially average to zero, which suggests the possibility of canceling the 2nd term due to beam imbalance. This is not the case, however, since the temporal average in the first term (red) in Eq. (7.19) is always zero, regardless of where the atoms are trapped, and gravity-induced small shifts in atom locations do not matter.

There is only one relevant angle ϕ for the 3rd order shifts, namely the angle between the laser E field and the quantization axis. The requirement that the laser wave vector k be perpendicular to the quantization axis is not a sufficient condition to cancel out $\Delta^{(3)}$, because

even if that is true one can still have $\phi \neq 0$ and a nonzero LSI. Nevertheless, when $\phi = 0$, it is automatically guaranteed that the laser wave vector k is perpendicular to the quantization axis.

In our experiment, with a trap depth of 20 μK and an applied DC electric field of $150\ kV/cm$, in order to suppress the linear Stark effect below our ultimate sensitivity limit, the design requirements are given by

$$\begin{aligned} &2m_F \cdot (8 \times 10^{-7}\ Hz\ \times 20 \times 150) \cdot \left[\frac{sin2\phi}{4} \times \frac{I_\uparrow - I_\downarrow}{(I_\uparrow + I_\downarrow)/2}\right] \leq 1.6 \times 10^{-8}\ Hz \\ &\rightarrow \phi \times \tfrac{I_\uparrow - I_\downarrow}{(I_\uparrow + I_\downarrow)/2} \leq 2.2 \times 10^{-6}. \end{aligned} \tag{7.20}$$

Namely, with the intensity imbalance $\frac{I_\uparrow - I_\downarrow}{(I_\uparrow + I_\downarrow)/2} \approx 2 \times 10^{-3}$ determined by the 1064 nm built-up cavities, the linear polarization axis must be parallel to the DC electric field to within $\phi \leq 1.1 \times 10^{-3}\ rad$, or equivalently 0.06^o, which is achievable by fine tuning the lattice polarization axis using precision rotation stages (section 3.1.2).

Now let's generalize the result to an arbitrary polarization ($\alpha \rightarrow 0$) with intensity imbalance. Similar to the previous derivation, we start by replacing Eq. (7.14) with

$$\begin{aligned} \boldsymbol{E} &= (\kappa + \varepsilon) sin(ky - \omega t)\left[cos(\alpha)\boldsymbol{z} + e^{i\delta} sin(\alpha)\boldsymbol{x}\right] \\ &\quad + \kappa sin(ky + \omega t)\left[cos(\alpha)\boldsymbol{z} + e^{i\delta} sin(\alpha)\boldsymbol{x}\right], \\ \boldsymbol{B} &= (\kappa + \varepsilon) sin(ky - \omega t)\left[cos(\alpha)\boldsymbol{x} - e^{i\delta} sin(\alpha)\boldsymbol{z}\right] \\ &\quad + \kappa sin(ky + \omega t)\left[-cos(\alpha)\boldsymbol{x} + e^{i\delta} sin(\alpha)\boldsymbol{z}\right] \end{aligned} \tag{7.21}$$

Straight forward algebra shows:

$$\begin{aligned} \Delta^{(3)} &= \tfrac{1}{2}[(\boldsymbol{B}^* \cdot \boldsymbol{\sigma})(\boldsymbol{E} \cdot \epsilon_S) + c.c.] = \tfrac{1}{2}[(\boldsymbol{B} \cdot \epsilon_S)(\boldsymbol{E}^* \cdot \boldsymbol{\sigma}) + c.c.] \\ \Delta^{(3)} &= \frac{I_\uparrow - I_\downarrow}{4} cos^2\theta \times [sin(2\phi)cos(2\alpha) - cos(\delta)cos(2\phi)sin(2\alpha)] \end{aligned} \tag{7.22}$$

Eq. (7.22) is a general expression that contains all possible imperfections: beam imbalance, beam misalignment and imperfect linear polarization.

First, let's focus on two special cases:

(i) Pure linear polarization δ=0

$$\Delta^{(3)} = \frac{I_\uparrow - I_\downarrow}{4} cos^2\theta \times sin2(\phi - \alpha) \tag{7.23}$$

This is a trivial case and identical to the result in Eq. (7.19) if one rotates the **E** axis by α.

(ii) Circular polarization component δ=π/2

$$\Delta^{(3)} = \frac{I_\uparrow - I_\downarrow}{4} cos^2\theta \times sin(2\phi) \times cos(2\alpha) \tag{7.24}$$

This case is interesting since $\Delta^{(3)}|_{\alpha=\pi/4} = 0$, which corresponds to pure circular polarized trapping light, gives the maximal vector light shift. From Eq. (7.24) one finds that a small fraction of circular component ($sin^2\alpha$ in fractional intensity) in the lattice beams will not change the linear Stark shift due to the $cos(2\alpha)$ dependence, which is very different from what happens with vector light shifts.

A general $\Delta^{(3)} = 0$ condition is $tan(2\phi) = cos(\delta)tan(2\alpha)$. For small ϕ and α, the condition is approximately $\phi/\alpha \approx cos(\delta)$. This provides a plausible but technically challenging way to cancel the non-parallelness by adding a controlled circular component.

In summary, the noise sources and systematic errors can be controlled to a level that will allow the eEDM to be measured with enough sensitivity to improve on the current experimental limit.

7.3. References

[1] F. Fang, *Progress toward a measurement of the electron electric dipole moment using ultra-cold atoms*, PhD dissertation, Penn State University, (2007).

[2] N. Solmeyer, *Progress toward an electron electric dipole moment measurement*

With laser-cooled atoms, PhD dissertation, Penn State University, (2013).

[3] W. M. Itano et al., *Quantum projection noise: Population fluctuations in two-level systems,* Phys. Rev. A **47**, 3554 (1993).

[4] M. V. Romalis and E. N. Fortson, *Zeeman frequency shifts in an optical dipole trap used to search for an electric-dipole moment,* Phys. Rev. A **59**, 4547 (1999). See also private communication with M. V. Romalis.

[5] H. Nyquist, *Thermal Agitation of Electric Charge in Conductors*, Phys. Rev. **32**, 110 (1928).

[6] T. Varpula and T. Poutanen, *Magnetic field fluctuations arising from thermal motion of electric charge in conductors*, J. Appl. Phys. **55**, 4015 (1984).

[7] S. R. S. Kumar and S. Kasiviswanathan, *A hot probe setup for the measurement of Seebeck coefficient of thin wires and thin films using integral method*, Rev. Sci. Instrum. **79**, 024302 (2008).

[8] Bijlsma et al., *Role of collisions in the search for an electron electric-dipole moment*, Phys. Rev. A **49**, R4285 (1994).

[9] J. Hodgdon, B. R. Heckel, and E. N. Fortson, *Calculation of a linear-Stark effect in D-line absorption in rubidium*, Phys. Rev. A **43**, 3343 (1991).

[10] X. Chen et al., Measurement of a linear Stark interference effect on the rubidium D1 absorption line, Phys. Rev. A **50**, 4729 (1994).

[11] K. Beloy, V. A. Dzuba, and A. Derevianko, *Calculation of Stark-induced absorption on the 6s6p 3P1–6s2 1S0 transition in Hg*, Phys. Rev. A **79**, 042503 (2009).

[12] T. H. Loftus et al., *Measurement of Linear Stark Interference in 199Hg*, Phys. Rev. Lett. **106**, 253002 (2011).

[13] D. Pappas et al., *A cesium resonance fluorescence imaging monochromator*, Opt. Comm. **191**, 263 (2001).

Chapter 8

Current status and outlook

Many aspects of the experiment and the apparatus development have been worked out (see the overview in Chapter 2, section 2.1). To demonstrate an EDM measurement, the only technical bottleneck to overcome is the generation of a large DC electric field such that the quadratic DC Stark shifts of the Zeeman sublevels are sufficiently large for the EDM spectroscopy to become feasible. The calculations in Chapter 6 imply that at least 20 kV high voltage must be sustained, or equivalently the DC Stark splitting between $m_F = 0$ and $m_F = \pm 1$ should be at least 5 Hz to begin the EDM spectroscopy.

The current field plate setup had an unfortunate breakdown at +10 kV, but not at -10 kV, the details of which have been described in section 6.4, pg. 119-123 of Dr. Solmeyer's dissertation [1]. Experiments with larger negative polarity high voltages were not conducted in order to protect the glass cell from being optically damaged from the coatings of the field plates that have experienced high voltage breakdown. The cause of failure has been identified as the inappropriate geometry of the transparent conductive (ITO) coating on the surfaces of the ground plates. In the very initial design of the field plates, the central area of the backside of the ground plates was not coated with ITO out of concern that ITO might severely limit the transmission of the ground plates. It was based on the incorrect assumption that the electric fields on the backside of the ground plates are not large enough to become a limiting factor. This has been proven to be not the case. With optimized multilayer dielectric anti-reflection coating together with the ITO, the reflection per surface has been made as small as 1%. The 30 nm-thin ITO coating on the backsides of the ground plates in fact generates large enough electric fields to cause unsustainable field emission and trigger a breakdown at +10 kV.

At the time of writing this dissertation, manufacturing a new set of field plates with full coverage of ITO coating and a factor of 5 increase in ITO thickness is in progress, and the apparatus is partially disassembled in preparation for remounting the new field plates. According to the previous high voltage test results with prototype ITO plates (pg. 48-55 in ref. [2]) and COMSOL Multiphysics simulations of the electric fields around the field plates (pg. 119-123 in ref. [1]), the high voltage rating of the new field plates should be improved by a large factor, the Stark splitting between $m_F = 0$ and $m_F = \pm 1$ is then at least 20 Hz, which is large enough to begin an EDM measurement. When the new plates are mounted in the experiment, besides the high voltage tests, the mystery with small vector light shifts can be resolved (see section 5.4 and 5.5 in Chapter 5, and magnetic fields (especially along z direction) can be zeroed to a much better level.

Several known improvements can be made to improve the EDM sensitivity. Atom number per shot in the measurement chamber can be improved by an order of magnitude by adding transverse cooling to the atomic beam in the Zeeman slower and boosting the intensity of horizontal cooling beams near the glass cell. Once EDM signals with light induced systematic errors are measured and identified, precision alignment of lattice beam polarizations so that they are made parallel to the direction of DC electric fields becomes feasible (section 7.2.3 in Chapter 7). Finally, in the long term, measurements with laser cooled Rb can be done by interfacing 780 nm laser systems to the existing dichroic optics for ultimate check of systematic errors.

In conclusion, most of the important experimental steps and apparatus developments have been completed for an EDM measurement using laser-cooled Cs atoms. With powerful control of noises and systematics, 1~2 orders of magnitude improvement over the current eEDM limit is expected.

8.1. References

[1] N. Solmeyer, *Progress toward an electron electric dipole moment measurement With laser-cooled atoms*, PhD dissertation, Penn State University, (2013).

[2] F. Fang, *Progress toward a measurement of the electron electric dipole moment using ultra-cold atoms*, PhD dissertation, Penn State University, (2007).

Appendix A

Setup and test of the built-up cavities

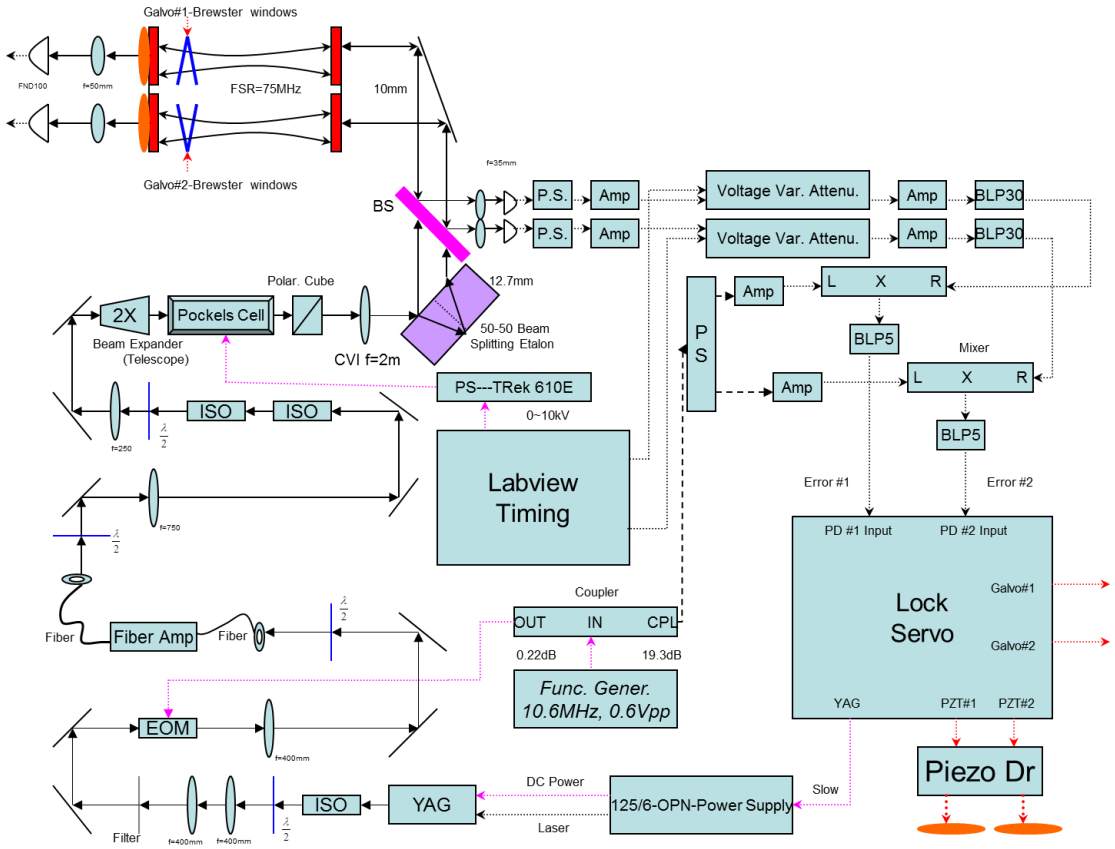

Figure A-1. Complete electronic and optic map of the optical lattice system.

A temperature stabilized YAG laser (Lightwave Electronics part #126-1064-100) seeds a fiber amplifier (IPG Photonics part #YAR-LP-SF) with an input power of 2~4 mW. The 10 W output power from the fiber amplifier is sent through a Pockels cell and a Glan laser polarizer which control the cavity power during the experiment. The output is then split into two parallel, equal power beams, used as input to the two cavities.

The YAG laser and fiber amplifier output have the TEM_{00} spatial mode. The YAG laser temperature set point can be adjusted so that it avoids a dual-longitudinal mode in lasing

frequency, which occurs at the crossover of the two frequency bands occasionally (set by the YAG laser NPRO crystal). According to the user manual from the manufacture, when the dual longitudinal output modes occur, shifting the temperature set point of the YAG laser by 0.5 ^{o}C will park the laser in the middle of a single frequency band. By keeping the YAG laser temperature controller on all the time (even when the laser output is turned off), the dual longitudinal mode does not occur very often.

Each cavity is frequency stabilized using a separate PDH locking circuit. The detailed circuit for the RF signal mixing is shown in Figure A-1, and the circuit for the lock servo is shown in Appendix-B of Dr. Solmeyer's dissertation. The electronic design for the PZT driver is shown in Figure A-4.

The electro-mechanical responses of the PZT-mirror system mounted onto various mirror mounts are shown in Figure A-2. The response functions (mirror displacements corresponding to PZT input voltages) are measured using a standard Michelson interferometer. Four types of mirror mount (Thorlabs #KS1D, Siskiyou #IXF.75ti, LINOS LEES #LM2, and Siskiyou industrial extreme #IXM100.P3) have been tested. The Siskiyou industrial extreme mounts has the flattest response and least number of large resonance peaks.

The effect of a 9 mm glass spacer on the mirror mount plate is seen in Figure A-3. After the hole is cut for cavity power monitoring, the mechanical response of the PZT-mirror system is degraded. Attempted recovery solutions included: adding a thick transparent glass plate to the backside of the mirror mount plate, or cutting an asymmetric hole (instead of a circular one) to suppress the mechanical resonances, and finally filling the hole with a glass spacer. The last solution has been proven to be the best.

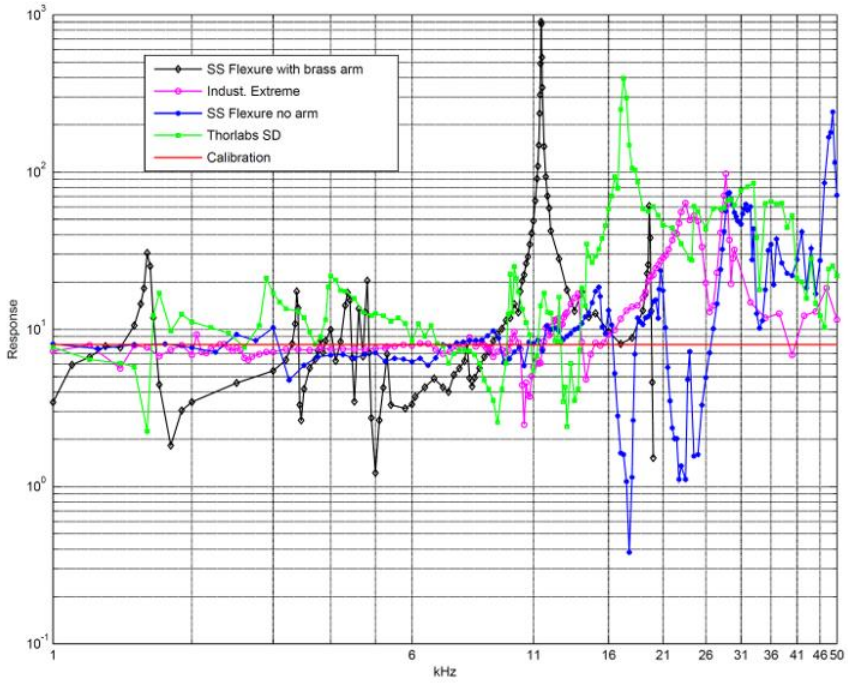

Figure A-2. Interferometric tests and selection of the cavity mirror mounts.

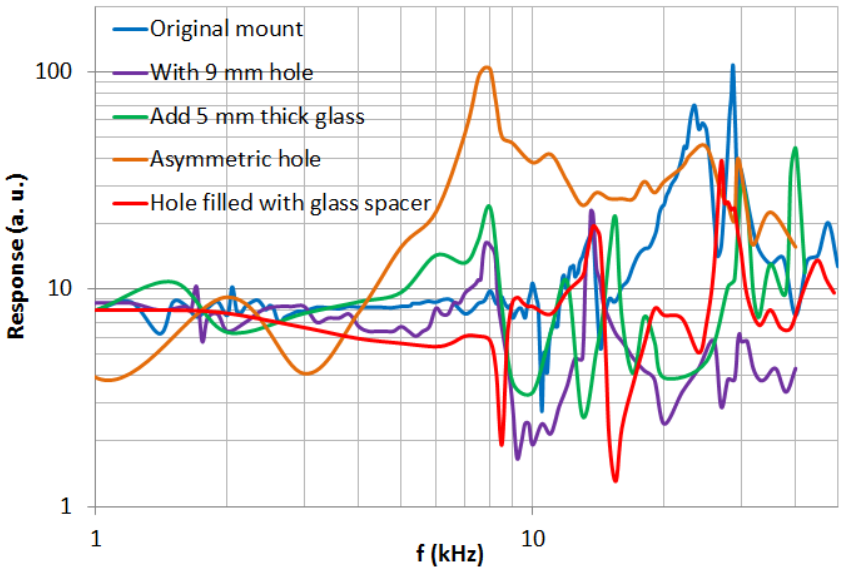

Figure A-3. Optimizing the mechanical performance of the cavity mirror mounts.

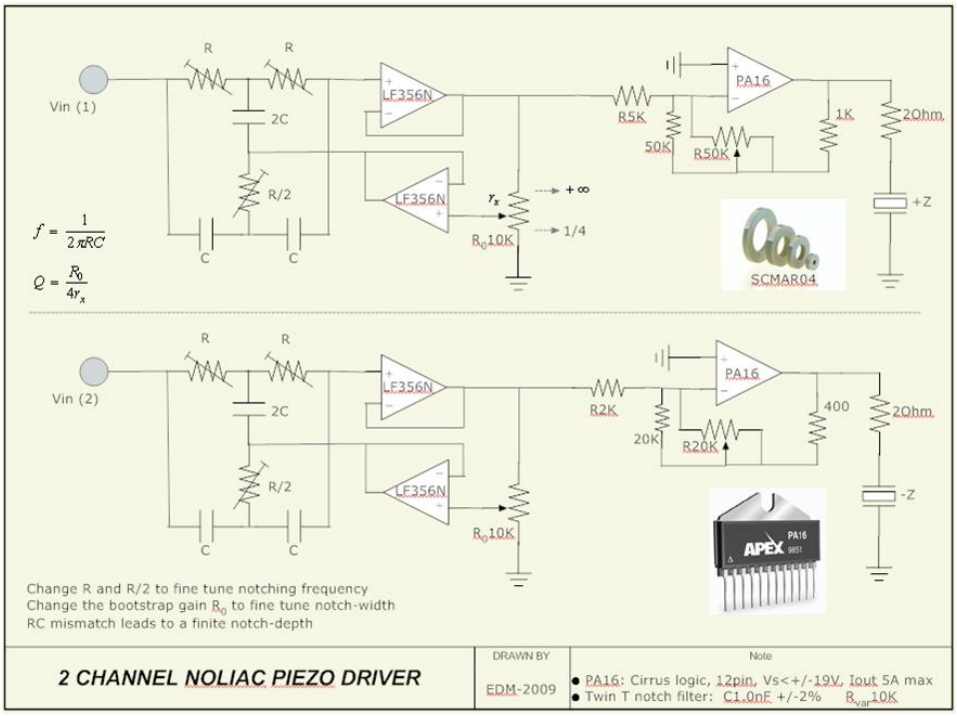

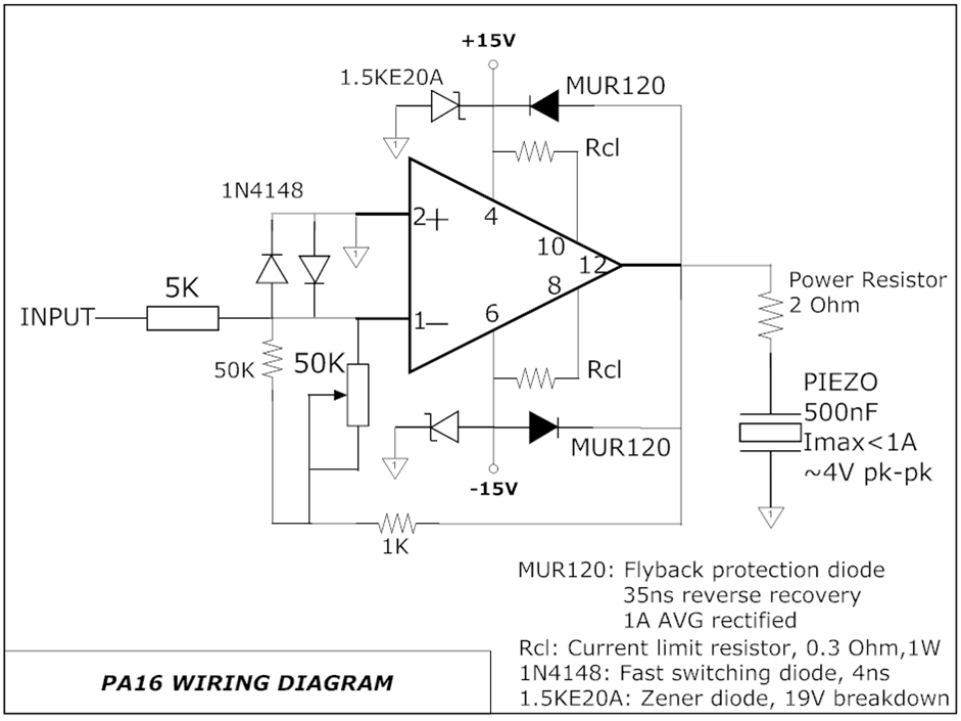

Figure A-4. The PZT driver electronics design for cavity stabilization.

Appendix B

Electronic design of the microwave system

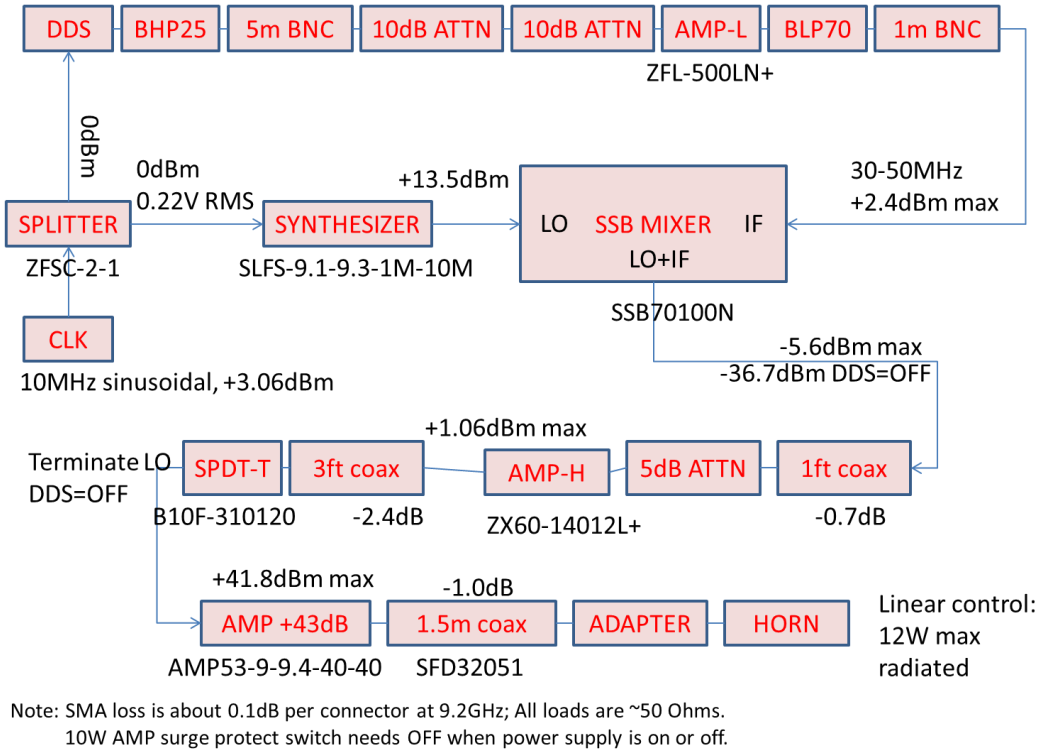

Figure B-1. Complete map of the microwave system.
The map contains every component of the microwave system, with RF powers matched to within the best working range of every element. A complete list of manufactures and part numbers are enumerated below:

Part name	**Part number**	**Manufacture**
Realtime DDS control board	PCI-6534	National Instruments
DDS	NA	Homemade
9.152 GHz synthesizer	SLFS-9.1-9.3-1M-10M	Miteq Inc.
Single sideband mixer	SSB70100N	Polyphase Microwave Inc.
Microwave SPDT switch	B10F-310120	Charter Engineering, Inc.
10 Watt amplifier	AM53-9-9.4-40-40	Microwave Amps Ltd.
Low loss coaxial cable	SFD32051	A-INFO, Inc
Rectangular horn antenna	JXTXLB-112-10-6793-C-SF	A-INFO, Inc
Misc. Filters, amplifiers, attentuators, adpaters	See Figure B-1	Mini-Circuit

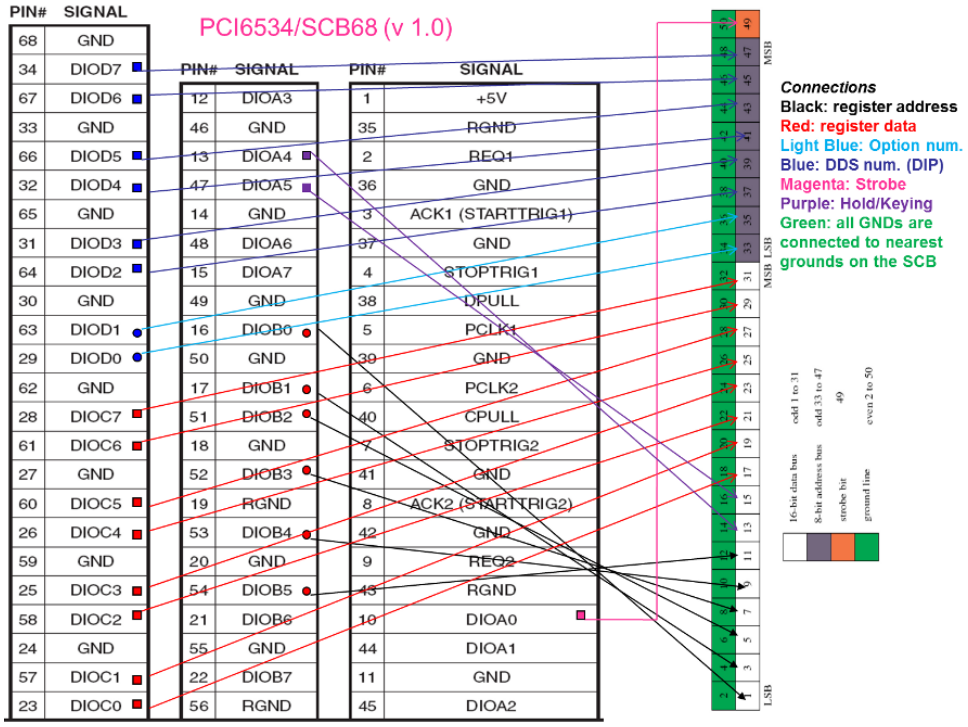

Figure B-2. Electric connections for the DDS control.
This map shows the connections between the 32-channel DIO board NI PCI-6534 breakout ports SCB68 to the 25-pin connector on the homemade DDS.

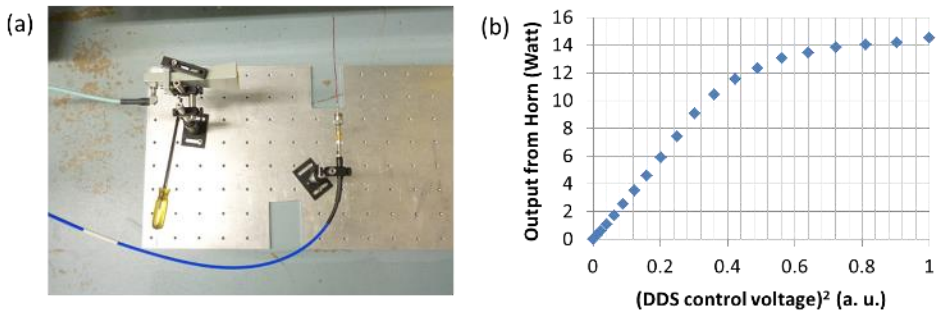

Figure B-3. Microwave system power measurement.
(a)A natural way to measure the gain of a high power microwave amplifier. The input (either signal before or after the 10-Watt amplifier) is sent to a horn antenna and a pick up dipole antenna is installed at a fixed distance away from the horn. As long as the geometry of the horn and the dipole antenna are fixed during all measurements, the setup gives a natural attenuation to prevent any possibility of to damage to the costly microwave power measurement device, a spectrum analyzer or a power meter. (b)Measured output power as a function of DDS control voltage. A attenuator is then placed after the DDS output to limit the maximum output power to 10 Watts.

Appendix C

Electrical connections for the PDA imaging system

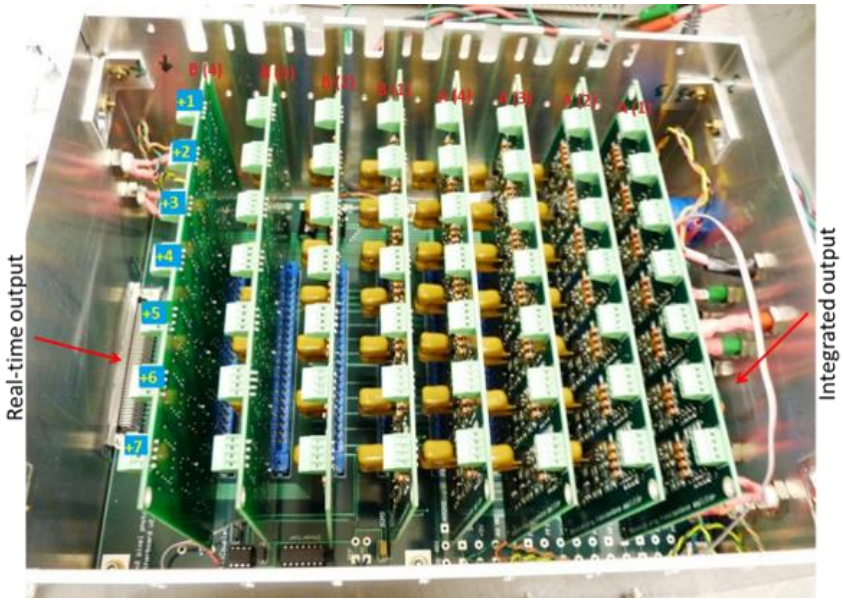

Channel/board mapping to PCI-6071E connector pin-out
(use this to program in any order for data acquisition)

Board Channel	+1	+2	+3	+4	+5	+6	+7
A (1)	INT:AI0 RT:AI54	INT:AI1 RT:AI53	INT:AI2 RT:AI52	INT:AI3 RT:AI51	INT:AI4 RT:AI50	INT:AI5 RT:AI49	INT:AI6 RT:AI48
A (2)	INT:AI8 RT:AI62	INT:AI9 RT:AI61	INT:AI10 RT:AI60	INT:AI11 RT:AI59	INT:AI12 RT:AI58	INT:AI13 RT:AI57	INT:AI14 RT:AI56
A (3)	INT:AI16 RT:AI38	INT:AI17 RT:AI37	INT:AI18 RT:AI36	INT:AI19 RT:AI35	INT:AI20 RT:AI34	INT:AI21 RT:AI33	INT:AI22 RT:AI32
A (4)	INT:AI24 RT:AI46	INT:AI25 RT:AI45	INT:AI26 RT:AI44	INT:AI27 RT:AI43	INT:AI28 RT:AI42	INT:AI29 RT:AI41	INT:AI30 RT:AI40
B (1)	INT:AI32 RT:AI22	INT:AI33 RT:AI21	INT:AI34 RT:AI20	INT:AI35 RT:AI19	INT:AI36 RT:AI18	INT:AI37 RT:AI17	INT:AI38 RT:AI16
B (2)	INT:AI40 RT:AI30	INT:AI41 RT:AI29	INT:AI42 RT:AI28	INT:AI43 RT:AI27	INT:AI44 RT:AI26	INT:AI45 RT:AI25	INT:AI46 RT:AI24
B (3)	INT:AI48 RT:AI6	INT:AI49 RT:AI5	INT:AI50 RT:AI4	INT:AI51 RT:AI3	INT:AI52 RT:AI2	INT:AI53 RT:AI1	INT:AI54 RT:AI0
B (4)	INT:AI56 RT:AI14	INT:AI57 RT:AI13	INT:AI58 RT:AI12	INT:AI59 RT:AI11	INT:AI60 RT:AI10	INT:AI61 RT:AI9	INT:AI62 RT:AI8

"INT:AIx" Integrated out analog input channel x "RT:AIx" Realtime out analog input channel x

Figure C-1. Electronic and programming interface of the 56-channel PDA amplifier.

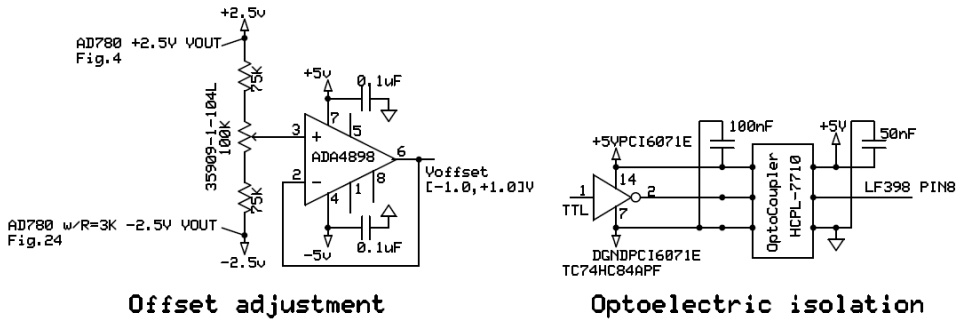

Figure C-2. The accessory circuit on the PDA motherboard.

Appendix D

High voltage system lock circuit

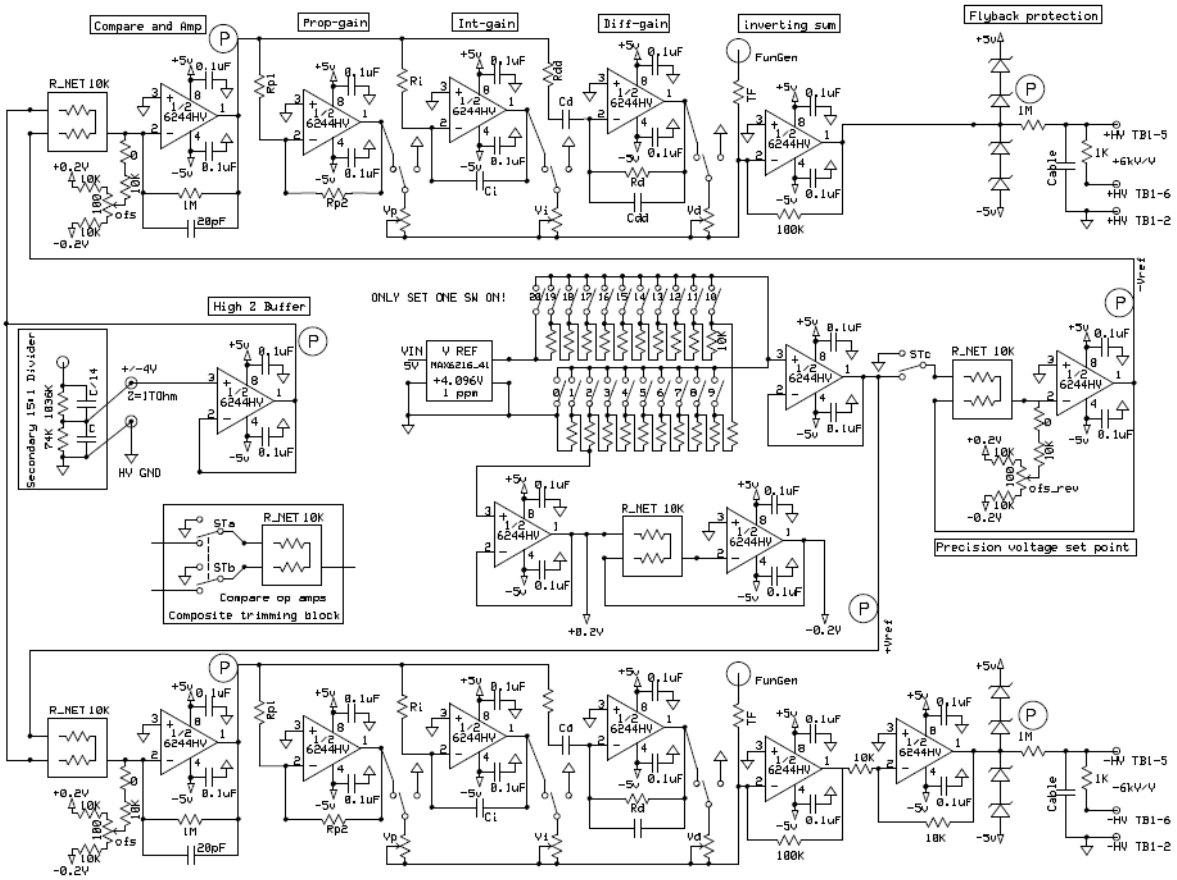

Figure D-1. The lock circuit for the high voltage system.

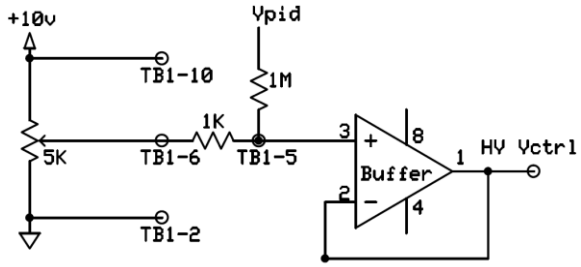

Figure D-2. The high voltage power supply interface and internal circuit.
TBx-y stands for the high voltage power supply terminal block index. We are slightly modifying the HV Vctrl by adding the Vpid, which is the feedback signal from the HV PID circuit. The 1000:1 voltage limiting ratio corresponds to 30 V maximum correction to the power supply.

Appendix E

Mastermind software special functions

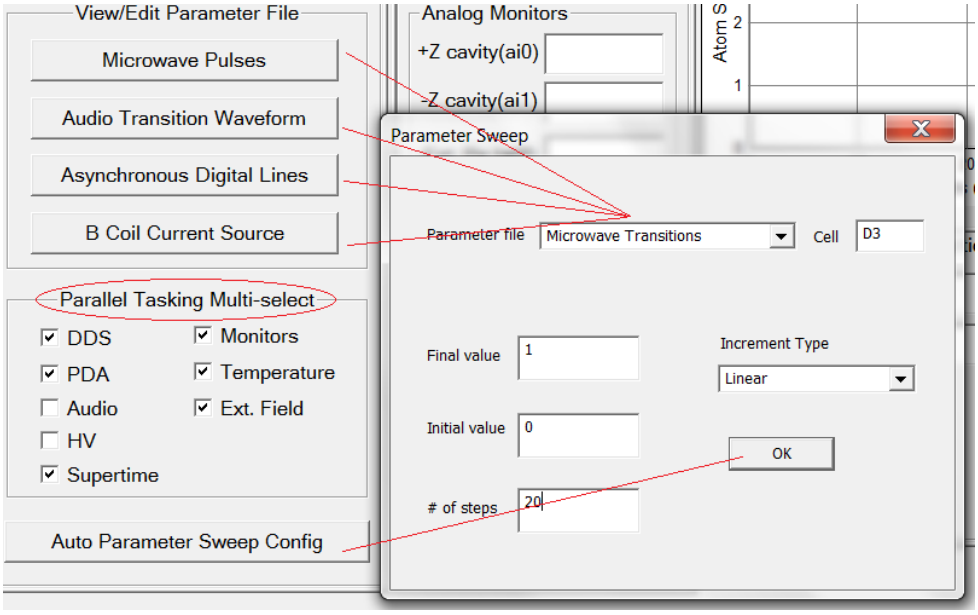

Figure E-1. Multi-choice parallel tasking with parameter sweep.

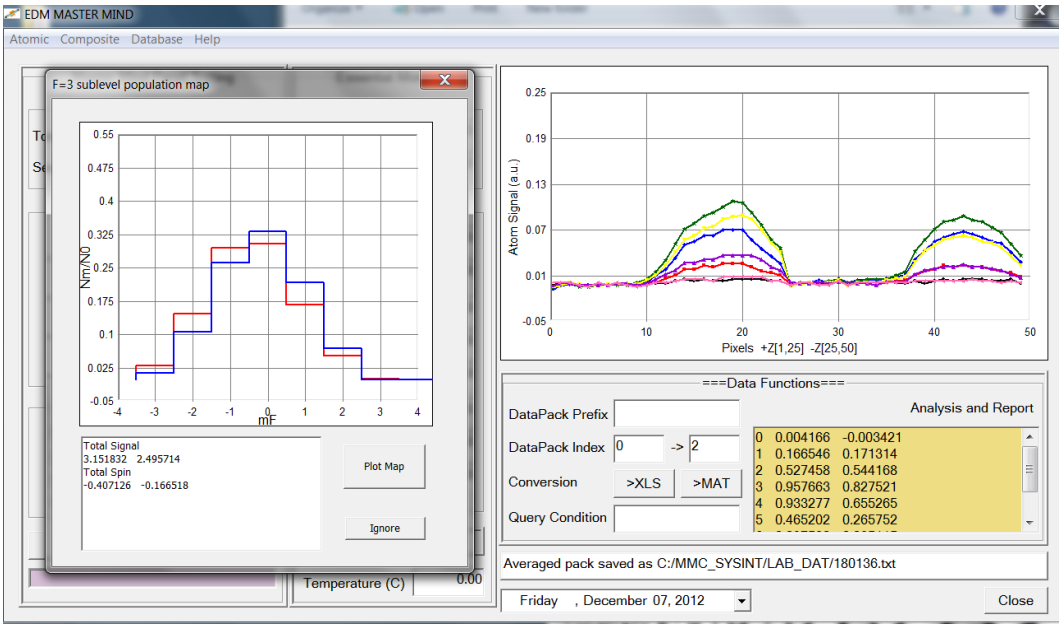

Figure E-2. Data function for imaging and analysis of 7 Zeeman sublevels.

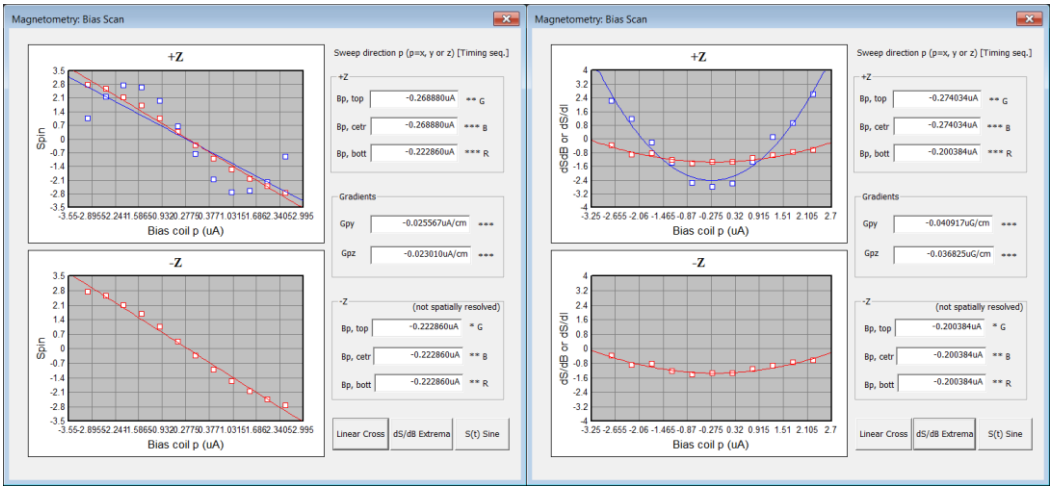

Figure E-3. Data function for magnetic bias scan in atomic magnetometry experiments.

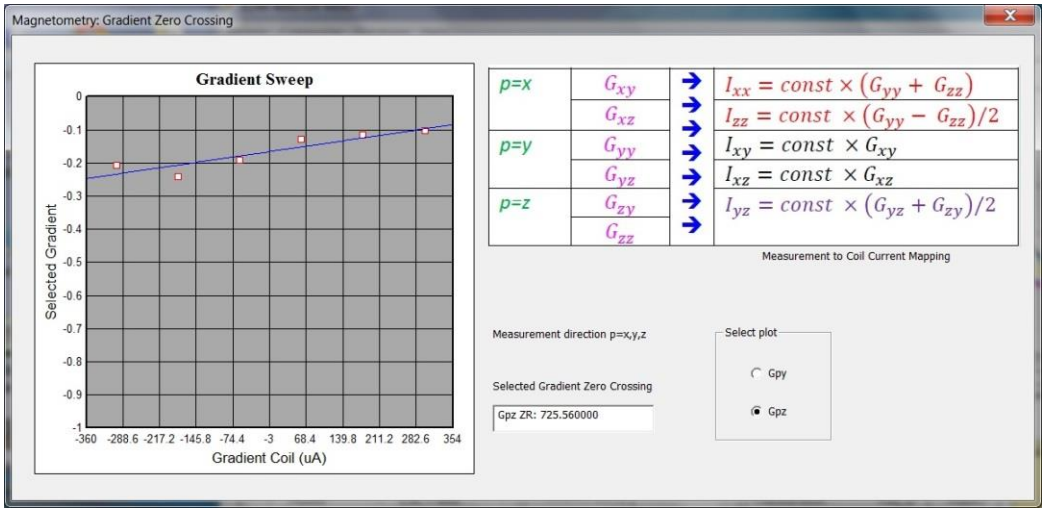

Figure E-4. Data function for magnetic gradients scan in atomic magnetometry experiments. *The mapping between measured magnetic field gradients and the magnetic gradient coil current settings is shown on the right.*

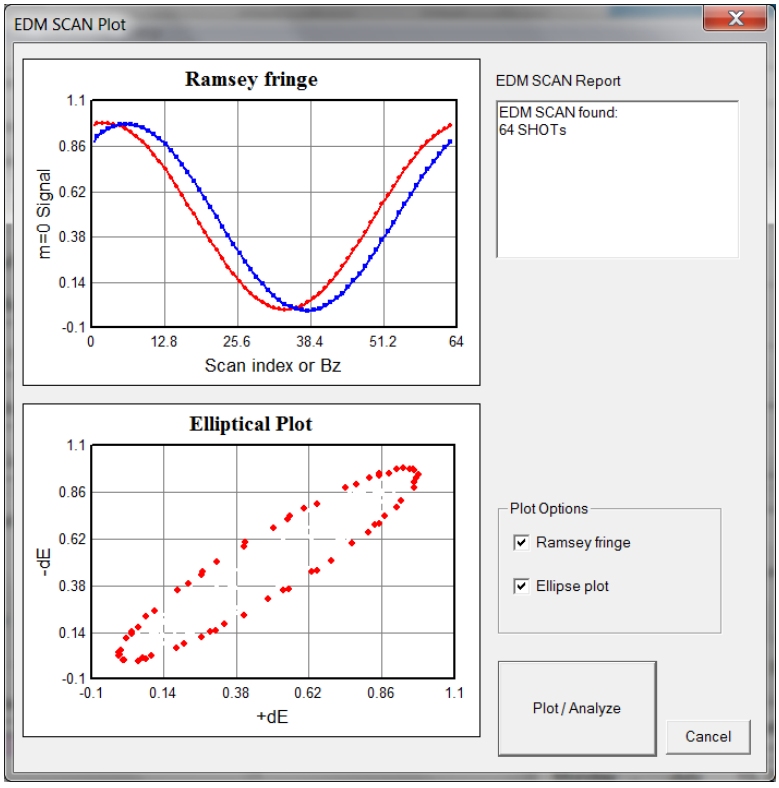

Figure E-5. Dialog for displaying data packs from a single EDM SCAN.

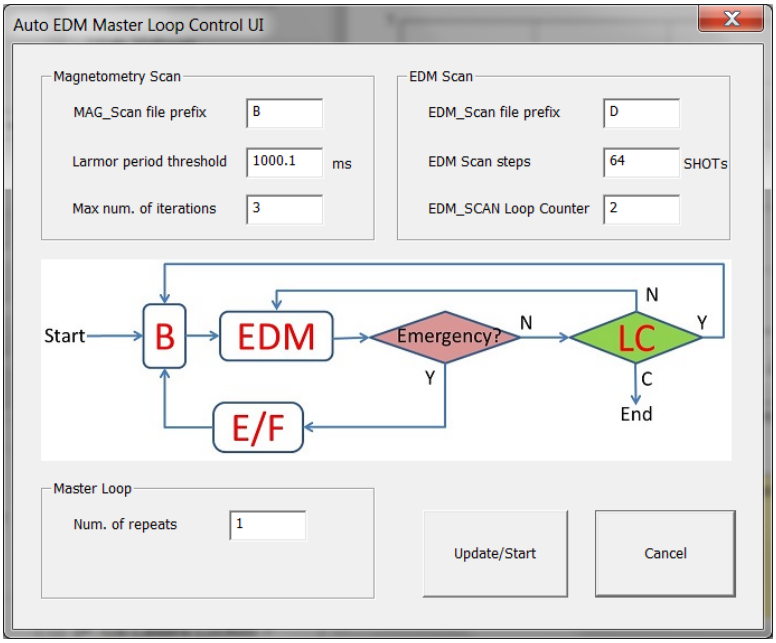

Figure E-6. Dialog for configuring an automated EDM measurement master loop.

Appendix F

Thermally induced birefringence in thin optical windows

In this section we derive a complete set of equations to estimate the thermally induced birefringence in thin (thickness $l \ll$ diameter) optical windows. We start with a model from ref. [1, 2], where the optical distortion and birefringence in a heated trigonal crystal rod with a rectangular cross section is studied. We extend the model to the case of isotropic crystals which have either cylindrically symmetric or asymmetric temperature profiles, due to heating from circular or elliptical high intensity laser beams.

The incident laser beam is taken to be linearly polarized along x axis, as shown in Figure F-1. The input beam can be represented by the Jones vector

$$\boldsymbol{E}_i = \begin{pmatrix} 1 \\ 0 \end{pmatrix} \tag{F.1}$$

Due to local thermal stress, the indicatrix ellipsoid of the thin window is rotated by a spatially dependent angle $\alpha(x, y)$. The transformation between the local principle axes (x',y') and the (x,y) coordinate are

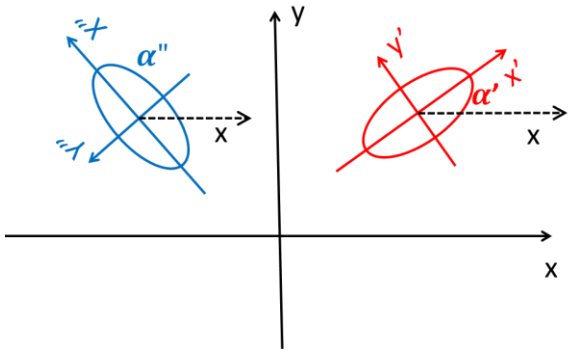

Figure F-1. Coordinate system for the thermal stress induced rotation of indicatrix ellipsoid. *The laser beam is propagated along z direction and linearly polarized along x direction. The thin window is along the x-y plane. The refractive index ellipsoid of the thin window is rotated by local thermal stress by angle α, which is spatially varying across the beam and not unidirectional, as indicated by the red in the first quadrant and blue in the second quadrant.*

$$\begin{pmatrix} x \\ y \end{pmatrix} = \begin{bmatrix} cos\alpha & -sin\alpha \\ sin\alpha & cos\alpha \end{bmatrix} \begin{pmatrix} x' \\ y' \end{pmatrix} \tag{F.2}$$

The output laser beam is then represented by

$$\boldsymbol{E}_o = \begin{bmatrix} cos\alpha & -sin\alpha \\ sin\alpha & cos\alpha \end{bmatrix} \begin{bmatrix} \exp(i\Delta\phi_{x\prime}) & 0 \\ 0 & \exp(i\Delta\phi_{y\prime}) \end{bmatrix} \begin{bmatrix} cos\alpha & sin\alpha \\ -sin\alpha & cos\alpha \end{bmatrix} \boldsymbol{E}_i \tag{F.3}$$

Straightforward algebra shows

$$\boldsymbol{E}_o = \begin{bmatrix} \sqrt{cos^2\tau + sin^2\tau cos^2(2\alpha)}\, exp\{-tan^{-1}[\cos(2\alpha) tan\tau]\} \\ -i\sin(2\alpha) sin\tau \end{bmatrix}, \tag{F.4}$$

with the birefringence phase shift given by

$$\tau = \frac{1}{2}\left(\Delta\phi_{y\prime} - \Delta\phi_{x\prime}\right) = \frac{kl}{2}\left(\Delta n_{y\prime} - \Delta n_{x\prime}\right). \tag{F.5}$$

The fractional amount of light displaced into the y polarization is

$$FD = sin^2\tau cos^2(2\alpha). \tag{F.6}$$

If the rotation of the indicatrix ellipsoid is unidirectional such as in wave plates, Eq. (F.6) is reduced to the well-known Malus law. By aligning the input linear polarization along the principle axes, one can minimize the fractional depolarization (FD). Thermally induced stress and rotations of indicatrix ellipsoid typically vary across the laser beam, which leads to a spatially dependent FD with a mode profile that is different from the input laser beam. The equation of the elliptical cross section of the indicatrix ellipsoid in the two coordinate systems is given by

$$\frac{x\prime^2}{n_{x\prime}^2} + \frac{y\prime^2}{n_{y\prime}^2} = 1 \leftrightarrow \left(\frac{1}{n_0^2} + \Delta B_1\right) x^2 + \left(\frac{1}{n_0^2} + \Delta B_2\right) y^2 + 2\Delta B_6 xy = 1, \tag{F.7}$$

where the ΔB_i are the variations in the relative dielectric impermeability tensor elements caused by the stresses, written in matrix notation. Eq. (F.7) is the elliptical cross section of the indicatrix ellipsoid that is normal to the optical axis z. Using the coordinate transformation from Eq. (F.2), Eq. (F.7) becomes

$$\frac{1}{n_{x'}^2}-\frac{1}{n_0^2}=\Delta B_1 cos^2\alpha+\Delta B_2 sin^2\alpha+\Delta B_6\sin(2\alpha)$$

$$\frac{1}{n_{y'}^2}-\frac{1}{n_0^2}=\Delta B_1 sin^2\alpha+\Delta B_2 cos^2\alpha-\Delta B_6\sin(2\alpha) \quad \text{(F.8)}$$

$$2\alpha=tan^{-1}\left(\frac{2\Delta B_6}{\Delta B_1-\Delta B_2}\right).$$

Assuming the stress-induced variations in refractive indices are small, then

$$\Delta n_{x'}\approx-\frac{n_0^3}{2}[\Delta B_1 cos^2\alpha+\Delta B_2 sin^2\alpha+\Delta B_6\sin(2\alpha)]$$

$$\Delta n_{y'}\approx-\frac{n_0^3}{2}[\Delta B_1 sin^2\alpha+\Delta B_2 cos^2\alpha-\Delta B_6\sin(2\alpha)]. \quad \text{(F.9)}$$

Using Eq. (F.5) and Eq. (F.9), we get the birefringence phase shift

$$\tau=\frac{kn_0^3 l}{4}\sqrt{(\Delta B_1-\Delta B_2)^2+(2\Delta B_6)^2}. \quad \text{(F.10)}$$

Eq. (F.6), Eq. (F.8) and Eq. (F.10) thus form a complete set for calculating the FD.

The relation between ΔB_i coefficients and stress for an isotropic crystal is given in Nye's convention [3] by

$$\begin{pmatrix}\Delta B_1\\ \Delta B_2\\ \Delta B_3\\ \Delta B_4\\ \Delta B_5\\ \Delta B_6\end{pmatrix}=\begin{pmatrix}\multicolumn{6}{c}{Isotropic}\\ \multicolumn{6}{c}{\text{ 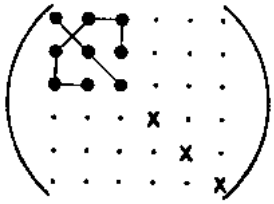 }}\end{pmatrix}\begin{pmatrix}\sigma_1\\ \sigma_2\\ \sigma_3\\ \sigma_4\\ \sigma_5\\ \sigma_6\end{pmatrix} \quad \text{(F.11)}$$

Where σ_1, σ_2, and σ_3 are the tensile stresses in the x, y, and z directions, respectively, and σ_4, σ_5 , and σ_6 are the shear stresses in the yz, xz, and xy planes, respectively. For fused silica, the diagonal connected dots are stress-optic coefficient $q_{11}=q_{||}$, the off-diagonal connected dots are $q_{12}=q_{\perp}$, the diagonal crosses are $\frac{1}{2}(q_{11}-q_{12})$ and the rest are zeros. For thermal stress on a thin window, $\sigma_3\approx\sigma_4\approx\sigma_5\approx 0$, therefore

$$\begin{pmatrix} \Delta B_1 \\ \Delta B_2 \\ 0 \\ 0 \\ 0 \\ \Delta B_6 \end{pmatrix} = \begin{pmatrix} q_{||}\sigma_1 + q_{\perp}\sigma_2 \\ q_{\perp}\sigma_2 + q_{||}\sigma_2 \\ 0 \\ 0 \\ 0 \\ \frac{1}{2}(q_{||} - q_{\perp})\sigma_6 \end{pmatrix} \tag{F.12}$$

Using the ΔB_i coefficients, we can write the FD in terms of stresses as

$$FD = \frac{4\sigma_6^2}{(\sigma_1 - \sigma_2)^2 + 4\sigma_6^2} sin^2\tau \tag{F.13}$$

We now focus on calculations of stresses for an arbitrary temperature distribution, $T(x, y)$. When the temperature distribution is mirror symmetric, namely $T(x, y) = T(-x, y) = T(x, -y)$, the stresses are related to strains by Young's modulus E and the Poisson's ratio ν

$$\begin{gathered} \sigma_1 - \sigma_2 \approx \frac{E}{1+\nu}(\varepsilon_1 - \varepsilon_2) \\ \sigma_6 \approx \frac{E}{2(1+\nu)}\varepsilon_6 \end{gathered} \tag{F.14}$$

Where $\varepsilon_1, \varepsilon_2$ and ε_6 are strains defined as derivatives of the deformation displacements, u and v

$$\varepsilon_1 = \frac{\partial u}{\partial x}; \varepsilon_2 = \frac{\partial v}{\partial y}; \varepsilon_6 = \frac{\partial u}{\partial y} + \frac{\partial v}{\partial x} \tag{F.15}$$

Note u is along x direction and v is along y direction. The term $\sigma_1 - \sigma_2$ in Eq. (F.14) has ignored the corrections from the thin window boundary [2], which are very small since the boundary is far away from the center of the laser beam and the temperature profile does not change rapidly at the boundary (see Figure 5-17 (a) for example).

Introducing the thermo-elastic displacement potential Ψ, the deformation displacements can be written as

$$\begin{gathered} u = \frac{\partial \Psi}{\partial x}; v = \frac{\partial \Psi}{\partial y}; \\ \varepsilon_1 + \varepsilon_2 = \nabla^2 \Psi = \frac{1+\nu}{1-\nu}\alpha_T T \end{gathered} \tag{F.16}$$

Eq. (F.16) is a Poisson equation, which is analogous to the problem of solving internal "electric" fields (u, v) from a "charge" distribution (T). Furthermore, the total strain $\varepsilon_1 + \varepsilon_2$ has the same shape as the temperature profile. The Poisson equation can be solved using the 2D Green function, which yields

$$\Psi = \frac{1+\nu}{1-\nu}\frac{\alpha_T}{2\pi}\iint T(\xi,\eta) ln\rho d\xi d\eta\,,\ \ \rho = \sqrt{(x-\xi)^2+(y-\eta)^2} \tag{F.17}$$

The solution for the thermo-elastic displacement potential allows one to evaluate the strains

$$\begin{aligned} \varepsilon_1 - \varepsilon_2 &= \frac{\partial u}{\partial x} - \frac{\partial v}{\partial y} = \frac{1+\nu}{1-\nu}\alpha_T \times TC(x,y); \\ \varepsilon_6 &= \frac{\partial u}{\partial y} + \frac{\partial v}{\partial x} = \frac{1+\nu}{1-\nu}\alpha_T \times TS(x,y) \end{aligned} \tag{F.18}$$

with integral temperatures defined as

$$\begin{aligned} TC(x,y) &= -\frac{1}{\pi}\iint T(\xi,\eta)\frac{(x-\xi)^2-(y-\eta)^2}{\rho^4}d\xi d\eta\,; \\ TS(x,y) &= -\tfrac{1}{\pi}\iint T(\xi,\eta)\tfrac{2(x-\xi)(y-\eta)}{\rho^4}d\xi d\eta. \end{aligned} \tag{F.19}$$

Note that $TC(x,y)$ has the same symmetry as $T(x,y)$ whereas $TS(x,y)$ reverses the symmetry, that is $-TS(x,y) = T(-x,y) = T(x,-y)$.

Direct numerical integration of the temperatures $TC(x,y)$ and $TS(x,y)$ is unsuitable because the term $\rho = \sqrt{(x-\xi)^2+(y-\eta)^2}$ diverges as $x \to \xi$, $y \to \eta$. Nevertheless, the kernels of $TC(x,y)$ and $TS(x,y)$ do not have singularities and have finite contributions depending on the structure of computing unit cell [2]. A practical integration method is to divide regions of interest on the thin windows to finite-size cells and sum over contributions from all cells. For instance,

$$TS(x,y) \approx -\frac{a^2}{\pi}\sum_{i\neq i*,j\neq j*} T(\xi_i,\eta_j)\frac{2(x_{i*}-\xi_i)(y_{j*}-\eta_j)}{\left[(x_{i*}-\xi_i)^2+(y_{j*}-\eta_j)^2\right]^2} \tag{F.20}$$

where we have chosen a square unit cell $(a \times a)$ and excluded the "self points" $(i = i*, j = j*)$. It is proven in ref. [2] that "self points" contributions from square unit cells are zero. We have

numerically tested multiple choices of unit cell sizes and the differences in resulting integral temperatures are less than 1%.

Figure F-2 shows plots of temperatures and fractional depolarization for the vacuum windows, using the parameters from Chapter 5, section 5.4.2.2 and the cylindrically symmetric temperature distribution Eq. (5.25). The fractional depolarization well agrees with the analytical results [4, 5] as described by Eq. (5.29) for cylindrically symmetric laser heating. Furthermore, birefringence phase distortions which produce the FD have an intrinsic odd symmetry built into them that is similar to $TS(x, y)$, namely the 1st and 3rd quadrant across the beams have opposite signs compared to the 2nd and 4th quadrant. Therefore the birefringence phase distortions averaged across the beams are zero.

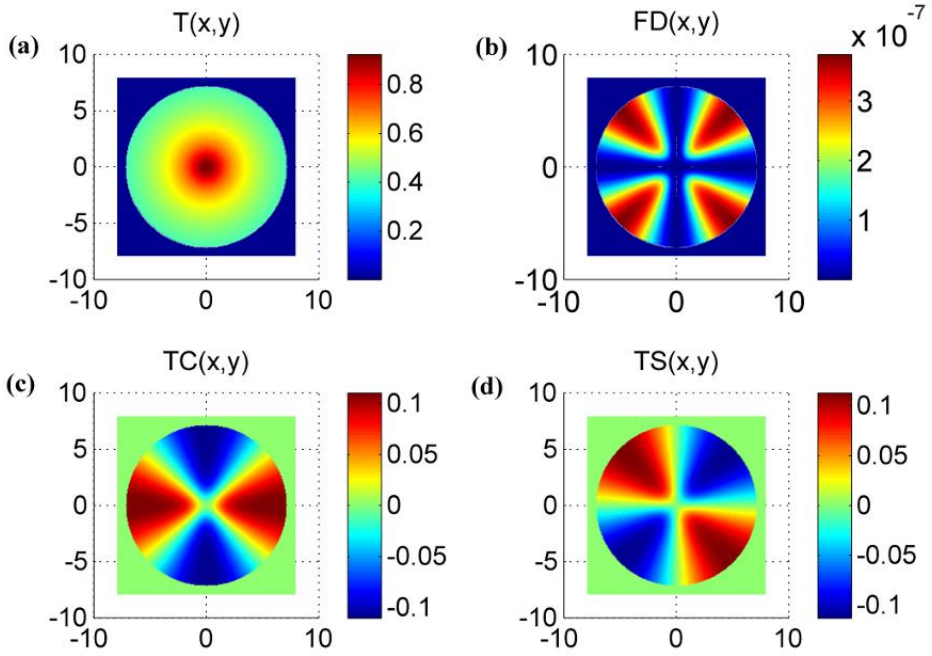

Figure F-2. Temperatures and fractional depolarization of the vacuum windows.
All temperatures are in unit of Kelvin and x, y dimensions are in unit of laser beam waist radius.

Due to the elliptical projection (at Brewster's angle θ_B) of the laser beams at the Brewster plates, the local heating rate of the Brewster plates has an aspect ratio of $1: cos\theta_B \approx 1: 0.56$.

Using the cylindrically symmetric temperature distribution Eq. (5.25), the temperature for the Brewster plates can be approximately written by

$$T_{BP}(x,y,t) \approx T\left[\sqrt{\left(\frac{x}{cos\theta_B}\right)^2 + y^2}, t\right] \tag{F.21}$$

Where x is along the major axis of the Brewster plates and the projection of the linear polarization axis is along x. Eq. (F.21) is constructed in a way that for a fixed distance d away from the center, $T_{BP}(d,0,t) < T_{BP}(0,d,t)$.

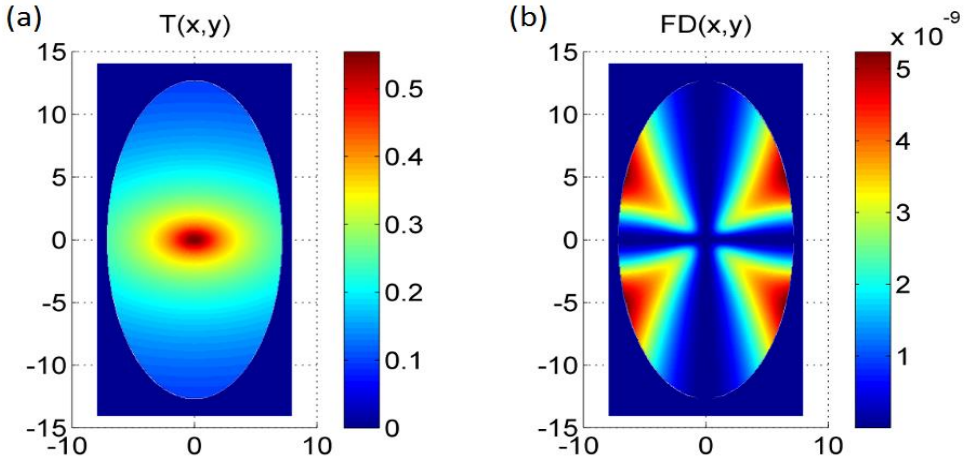

Figure F-3. Temperature and fractional depolarization of the Brewster plates.
All temperatures are in unit of Kelvin and x, y dimensions are in unit of laser beam waist radius. Major axis is along x and minor axis is along y.

Figure F-3 and Figure F-4 shows plots of temperatures and estimated fractional depolarization for the Brewster plates, using the parameters from Chapter 5, section 5.4.2.2. The maximum FD of Brewster plates is ~1/72 of that of vacuum windows, since the vacuum windows are 6 times thicker and have higher internal absorption. Similar to the case of vacuum windows, heating the Brewster plates will also produce an odd symmetric birefringence phase distortion, but the four-leaved structure in FD no longer has the C_4 symmetry. Precision alignment of laser beam polarization along the major axis does not avoid the thermally induced birefringent depolarization, because of the spatial dependence of thermal stresses across the laser beams.

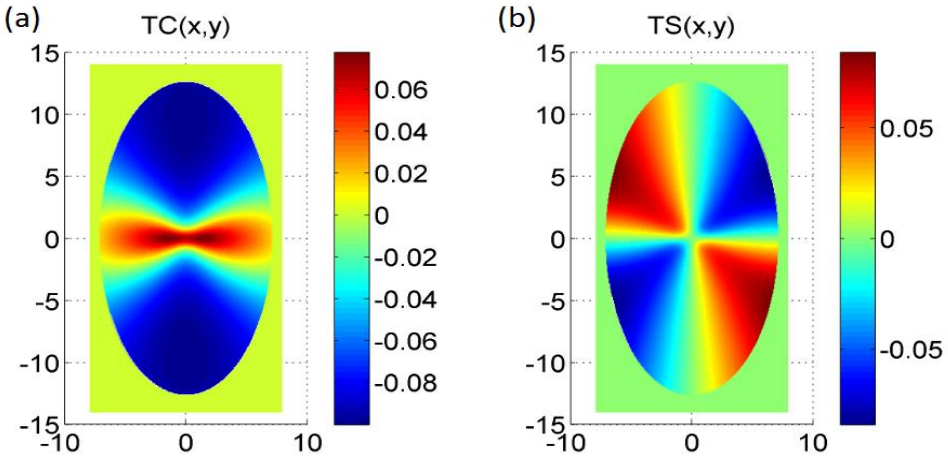

Figure F-4. The integral temperatures TC(x,y) and TS(x,y) of the Brewster plates.

In summary, the numerical results presented in this Appendix provide an estimate of the magnitude and the spatial dependence of the thermally induced stress birefringence in our optical lattice system. Without considering the cancellation mechanism due to the C_4 symmetry, the maximum birefringent phase shift from the vacuum windows is about 22 times smaller than what is needed to account for the 40 Hz VLS. The birefringent phase shift from the Brewster plates is ~12% of that of the vacuum windows. Therefore, the thermally induced stress birefringence in our optical lattice system is too small to cause the 40 Hz coherent Larmor precession.

[1] C. E. Greninger, *Optical distortion and birefringence in a heated trigonal crystal rod*, J. Appl. Phys. **85**, 7037 (1999).

[2] C. E. Greninger and S. E. Rodriguez, *Thermal stress in a trigonal crystal rod*, J. Appl. Phys. **85**, 3159 (1999).

[3] J. F. Nye, *Physical Properties of Crystals*, Oxford University Press, Chap. VIII, (1985).

[4] C. E. Greninger and S. E. Rodriguez, *Thermal stress, optical distortion, and birefringence in a heated cylindrical trigonal crystal rod*, J. Appl. Phys. **87**, 8545 (2000).

[5] L. C. Malacarne, N. G. C. Astrath, and M. L. Baesso, *Unified theoretical model for calculating laser-induced wavefront distortion in optical materials*, J. Opt. Soc. Am. B **29**, 1772 (2012).

VITA

Kunyan Zhu

Kunyan Zhu was born in Shiyan, China, an industrial city known for the Dongfeng Motor Corporation and the Wudang Mountains (Taoist center). He received a Bachelor's degree in theoretical physics from Lanzhou University in 2007. During the summer of 2006, he was a visiting Chun-Tsung scholar at the National Tsing-Hua University, supported by the T. D. Lee foundation. Since fall 2007, he has been a graduate student at The Pennsylvania State University and conducted research on the precision measurement of the electron electric dipole moment using laser-cooled alkali atoms. During his graduate study, he received the David C. Duncan Graduate Fellowship in 2010 and 2011, and the Peter Eklund Memorial Lectureship in 2013.